

Multi-orbital quantum phenomena: from magnetic impurities to lattice models with strong Hund's coupling



DISSERTATION ZUR ERLANGUNG DES NATURWISSENSCHAFTLICHEN DOKTORGRADES DER
JULIUS-MAXIMILIANS-UNIVERSITÄT WÜRZBURG

vorgelegt von

Alexander Anton Kowalski

aus Ochsenfurt

Würzburg, 2023



Eingereicht am 04. August 2023
bei der Fakultät für Physik und Astronomie

1. Gutachter: Prof. Dr. Giorgio Sangiovanni
 2. Gutachter: Prof. Dr. Fakher Assaad
- der Dissertation

Vorsitzender: Prof. Dr. Karl Brunner

1. Prüfer: Prof. Dr. Giorgio Sangiovanni
 2. Prüfer: Prof. Dr. Fakher Assaad
 3. Prüfer: Prof. Dr. Friedrich Reinert
- im Promotionskolloquium

Tag des Promotionskolloquiums: 29. November 2023
Doktorurkunde ausgehändigt am:

Abstract

Strong correlations caused by interaction in systems of electrons can bring about unusual physical phenomena due to many-body quantum effects that cannot properly be captured by standard electronic structure methods like density functional theory. In this thesis, we apply the state-of-the-art continuous-time quantum Monte Carlo algorithm in hybridization expansion (CT-HYB) for the strongly correlated multi-orbital Anderson impurity model (AIM) to the solution of models of magnetic impurities on metallic surfaces and, via dynamical mean-field theory (DMFT), to the solution of a lattice model, the multi-orbital Hubbard model with Hund's coupling.

A concise introduction to the theoretical background focuses on information directly relevant to the understanding of applied models, methods, and the interpretation of results. It starts with a discussion of the AIM with its parameters and its solution in the path integral formalism, the basis of the CT-HYB algorithm. We consider its derivation and implementation in some detail before reviewing the DMFT approach to correlated lattice models and the interpretation of the single-particle Green's function.

We review two algorithmic developments for the CT-HYB algorithm that help to increase the performance of calculations especially in case of a complex structure of the interaction matrix and allow the precise calculation of self-energies and vertex functions also at intermediate and higher frequencies.

Our comparative analysis of Kondo screening in the cobalt on copper impurity system points out the importance of an accurate interaction matrix for qualitatively correct Kondo temperatures and the relevance of all d -orbitals in that case. Theoretical modeling of cobalt impurities in copper "atomic wires" fails to reproduce variations and partial absence of Kondo resonances depending on the wire size. We analyze the dependence of results on parameters and consider possible reasons for the discrepancy. Different Kondo temperatures of iron adatoms adsorbed on clean or oxygen-reconstructed niobium in the normal state are qualitatively reproduced, with the adsorption distance identified as major factor and implications for the superconducting state pointed out.

Moving on to lattice problems, we demonstrate the connection between Hund's coupling, shown to cause first-order character of the interaction-driven Mott transition at half-filling in the two-orbital Hubbard model, and a phase separation zone ending in a quantum critical point at finite doping. We touch on similarities in realistic models of iron-pnictide superconductors. We analyze the manifestation of the compressibility divergence at the finite-temperature critical points away from half-filling in the eigenbasis of the two-particle generalized susceptibility. A threshold for impurity susceptibility eigenvalues that indicates divergence of the DMFT lattice compressibility and distinguishes thermodynamic stability and instability of DMFT solutions is determined.

Deutsche Zusammenfassung

Wechselwirkungsbedingt stark korrelierte Elektronensysteme können wegen Mehrteilcheneffekten ungewöhnliche Physik aufweisen, die Standardmethoden für elektronische Struktur wie die Dichtefunktionaltheorie nicht erfassen. Diese Dissertation handelt von der Anwendung des Quanten-Monte Carlo Algorithmus in kontinuierlicher Zeit mit Reihenentwicklung in der Hybridisierung (CT-HYB), aktuellster Stand der Technik für das stark korrelierte Anderson-Modell für Störstellen (AIM), auf magnetische Adatome auf Metalloberflächen und, im Rahmen der dynamischen Molekularfeldtheorie (DMFT), auf das Mehrorbital-Hubbard-Modell mit Hundscher Kopplung.

Eine kurze Einführung fokussiert den für das Verständnis der Modelle, Methoden, und Interpretationen relevanten theoretischen Hintergrund. Sie beginnt mit dem AIM, seinen Parametern, und seiner Lösung im Pfadintegralformalismus, welche Grundlage des CT-HYB Algorithmus ist. Wir betrachten dessen Herleitung und Implementation im Detail, bevor wir einen Überblick über den DMFT-Zugang zu korrelierten Gittermodellen und die Interpretation der Einteilchen-Greenschen Funktion geben.

Wir berichten von zwei algorithmischen Entwicklungen für CT-HYB, die helfen, die Geschwindigkeit der Rechnungen besonders in Fällen einer lokalen Wechselwirkung komplexer Form zu erhöhen und die präzise Berechnung von Selbstenergien und Vertexfunktionen auch bei mittleren und höheren Frequenzen erlauben.

Unsere Analyse der Kondo-Abschirmung in Kobalt-Adatomen auf Kupfer weist auf die Bedeutung einer akkuraten Wechselwirkungsmatrix für korrekte Kondo-Temperaturen und die Relevanz aller d -Orbitale hin. Die Variation der Kondo-Resonanz von Kobalt in "atomaren Drähten" aus Kupfer mit der Anzahl der Atome kann unsere theoretische Modellierung nicht nachvollziehen. Wir untersuchen die Abhängigkeit der Ergebnisse von Parametern und diskutieren mögliche Ursachen. Kondo-Temperaturen von Eisen-Adatomen auf sauberer oder Sauerstoff-rekonstruierter Niob-Oberfläche werden im Normalzustand qualitativ reproduziert, der Adsorptionsabstand als wichtiger Faktor identifiziert, und auf die Folgen für den supraleitenden Zustand hingewiesen.

Wir wenden uns dem Hubbard-Modell eines Gitters mit zwei Orbitalen pro Platz zu und zeigen den Zusammenhang zwischen Hundscher Kopplung, Ursache der Diskontinuität des Mott-Übergangs bei halber Füllung, und einer Phasenseparationszone endend in einem quantenkritischen Punkt bei endlicher Dotierung. Wir reißen Parallelen in realistischeren Eisenpniktid-Modellen an. Zuletzt sehen wir, wie sich die Kompressibilitätsdivergenz an den kritischen Punkten bei endlicher Temperatur abseits halber Füllung in den Eigenwerten der verallgemeinerten lokalen Suszeptibilität ausprägt und bestimmen für sie eine Schwelle, an der die DMFT-Gitterkompressibilität divergiert und deren Unterschreitung eine thermodynamisch instabile DMFT-Lösung anzeigt.

Contents

1	Introduction	9
2	Background	13
2.1	The Anderson impurity model	13
2.2	Continuous-time quantum Monte Carlo in hybridization expansion . . .	18
2.3	Dynamical mean-field theory	32
2.4	Interpretation of Green's functions	35
3	Algorithmic developments	43
3.1	Superstate and state sampling	43
3.1.1	Local weight calculation	43
3.1.2	CT-HYB updates	45
3.1.3	Results and performance	49
3.1.4	Application to a Hund's metal with low coherence temperature .	51
3.1.5	Conclusions	54
3.2	Symmetric improved estimators	56
3.2.1	Self-energies in CT-HYB	56
3.2.2	Definitions	57
3.2.3	One-particle symmetric improved estimators	58
3.2.4	Two-particle symmetric improved estimators	61
3.2.5	CT-HYB replacement moves for equal-time worm operators . . .	65
3.2.6	Results	68
3.2.7	Conclusions	71
4	Magnetic impurities on metallic surfaces	73
4.1	Analysis of the influence of the interaction parameterization on Kondo screening in cobalt adatoms	73
4.1.1	Kondo effect in cobalt impurities on copper surfaces	73
4.1.2	First principles DFT+AIM approach	76
4.1.3	Outline of the resulting picture	78
4.1.4	Spin susceptibility and moment	80
4.1.5	Charge and spin fluctuations	85

4.1.6	Spectral function and self-energy	89
4.1.7	Interaction terms	92
4.1.8	Conclusions	96
4.2	Kondo effect of a cobalt atom embedded into linear clusters of copper atoms on a Cu(111) surface	98
4.2.1	Introduction	98
4.2.2	Experimental results	99
4.2.3	Density functional theory	101
4.2.4	Continuous-time quantum Monte Carlo simulations	103
4.2.5	Conclusions	108
4.3	Dependence of spin screening on the adsorption site in iron impurities on partially oxygen-reconstructed niobium surfaces	110
4.3.1	Introduction	110
4.3.2	Experimental results	111
4.3.3	Density functional theory	115
4.3.4	Continuous-time quantum Monte Carlo simulation	118
4.3.5	Conclusions	121
5	DMFT analysis of the doped two-orbital Hubbard model with Hund's coupling	123
5.1	Mott quantum critical point at finite doping	123
5.1.1	Mott transition in the Hubbard model: background and methods	124
5.1.2	Half-filling case	131
5.1.3	Doped case	138
5.1.4	Physical origin of the first-order transition at half-filling	147
5.1.5	Conclusion, contextualization and outlook	158
5.2	Detection of thermodynamic instabilities from quantities on the two-particle level	163
5.2.1	The physics of response functions and vertex divergences	163
5.2.2	Background on two-particle quantities	168
5.2.3	Compressibility enhancement and divergence in the two-orbital Hubbard model	182
5.2.4	Connection between generalized susceptibility eigenvalues and thermodynamic quantities	192
5.2.5	Conclusion and outlook	199
6	Conclusion	201
A	Fourier transforms between imaginary time and Matsubara frequencies	203

B Equation of motion for the AIM Green's function	207
Bibliography	217

1 Introduction

The quantum mechanical laws that govern the behavior of atoms and electrons in a solid and give rise to the properties of materials have essentially been known for almost a century. As Dirac already noted in 1929 [1], what is left to do as far as their theoretical description is concerned is rather the development of methods that allow some amount of abstract insight into the behavior of macroscopically large systems. The exact solutions of the equations describing such amounts of particles may forever remain out of reach, leaving aside the question how well such results would even be interpretable in terms of measurable quantities. Direct numerical *exact diagonalization* of the Hamiltonian suffers from exponential scaling of the Hilbert space and consequently resource usage with the system size. The enormous increase of computational performance [2] in the last half-century has actually enabled the productive use of even this method for small models. In the context of the many-body problem in condensed matter physics [3, 4], this however restricts its applicability to model Hamiltonians that only try reproduce interesting features rather than the full complexity of real systems [5].

In contrast, a numerical method that has become extremely successful for calculations in solid state physics, materials science, and even chemistry is the density functional theory (DFT) [6, 7]. Already in the year after Dirac made his famous remark cited above [8], he described the Thomas-Fermi [9, 10] model as a practical approximation for the solution of the many-electron problem. It is formulated in terms of just the electron density, one scalar function of position in three-dimensional space, rather than a many-body wave function. Without additional potentially inaccurate approximations as e.g. in the Hartree-Fock approach [11–14] the full many-body wave function is in general a function of a position in a space whose dimension scales with the particle number. DFT is based on the Hohenberg-Kohn theorem [15] proving the existence of a functional of the electron density of a system of electrons in an external potential whose minimum is the correct ground state energy, and the ground state density for which that minimum is attained also determines the ground state wave functions [6]. The density functional can be decomposed into terms one of which is the exchange-correlation energy [16]. It cannot be evaluated exactly, but commonly used approximations are sufficiently good to make DFT the standard method for electronic structure calculations in

periodic solids [17]. There are however also various cases where these approximations fail, and one of them are correlated systems and their interesting quantum many-body physics that they cannot describe even qualitatively [7].

Strongly correlated electron systems include particularly materials with partially filled d - or f -shells hosting well localized electrons, such as compounds of transition metal, rare-earth and actinide elements [18–20]. These systems exhibit a wide range of partially unusual behaviors such as ferro- and antiferromagnetism, metal-insulator transitions [21–23], high-temperature unconventional superconductivity [23–27], the Kondo effect [28], large effective electron masses in “heavy-fermion” systems [29], and colossal magnetoresistance [23, 30] to name a few. In this thesis, we investigate the behavior of strongly correlated systems in the form of both realistic transition metal impurities as well as the multi-orbital Hubbard model [31]. The multi-orbital Anderson impurity model (AIM) [32] is directly able to represent transition metal impurities, which we do in a first-principles way by using DFT to set its parameters. In order to deal with a multi-orbital model of interacting electrons on a lattice instead, we make use of dynamical mean-field theory (DMFT) [33]. This method describes the lattice model in terms of an auxiliary AIM for a single site embedded in a self-consistently determined bath. We use the continuous-time quantum Monte Carlo algorithm in hybridization expansion (CT-HYB) [34] to perform calculations for the Anderson impurity model and also present algorithmic improvements that increase performance and allow the calculation of quantities with lower high-frequency errors.

In Chapter 2, we introduce the theoretical framework and algorithms that we use for our investigations. We discuss the multi-orbital Anderson impurity model, including the choice of parameters and its solution in the coherent state path integral formalism. Building on this, we thoroughly describe the evaluation of the solution in the continuous-time quantum Monte Carlo algorithm in hybridization expansion and continue with the dynamical mean-field theory and the iterative solution procedure yielding its self-consistent result. We finish with a discussion of the interpretation of single-particle Green’s functions particularly in the case of correlated systems, as they are one of the main result quantities that we obtain in our calculations.

In Chapter 3, we discuss algorithmic improvements to the continuous-time quantum Monte Carlo algorithm in hybridization expansion. In Section 3.1, we present the state and superstate sampling algorithms, which enable calculations of approximately the same statistical quality with a measured performance increase in our best test case with a full spherical Coulomb interaction for five orbitals at moderately high temperatures by a factor of almost one thousand. As an application example, we revisit a three-orbital model with a suspected quantum phase transition to a “frozen moment” phase [35] and demonstrate the restoration of Fermi-liquid behavior at sufficiently low temperatures.

In Section 3.2, we introduce symmetric improved estimators that allow self-energies and vertex functions to be obtained from CT-HYB with constant rather than diverging error at high Matsubara frequencies. We derive the equations of motion expressing the one- and two-particle Green's function in terms of higher-order correlation functions and discuss the measurement of these higher order correlation functions in CT-HYB using worm sampling.

In Chapter 4, we consider the Kondo effect in three cases of transition metal impurities on metallic surfaces by solving multi-orbital AIMs we construct for them using parameters from first-principles DFT calculations. In Section 4.1, we show that the accuracy of the parameterization of the local interaction has a significant influence on the estimated Kondo temperature in the prototypical case of a cobalt adatom on a copper Cu(001) surface by calculating spin susceptibilities and moments, charge and spin fluctuations, and spectra. We reveal that an approximation of the local interaction of the impurity $3d$ -shell orbitals beyond the full (spherically symmetric) Coulomb interaction leads to qualitatively incorrect results, and that a two-orbital description as it is occasionally found in the literature is at most appropriate with approximate interactions, as all five orbitals are relevant with the full Coulomb interaction. In Section 4.2, we report experiments of our collaborators with cobalt adatoms on copper surfaces surrounded by linear "atomic wire" clusters of a varying number of further copper atoms, where a variation of the Kondo temperature as a function of the cluster length and in two cases a total absence of the Kondo resonance are found. We attempt to reproduce the variations by running CT-HYB calculations for the cobalt impurities parameterized by DFT results for such atomic wires, but find that our results are at most qualitatively right. Since quantitative variations—and most importantly the absence of the Kondo effect in two cases—are not captured correctly, we analyze the dependence of the results on structural and interaction parameters in search of possible reasons for the discrepancies between experiment and the solution of a first-principles description in terms of an AIM. In Section 4.3, we report experiments of our collaborators finding different normal-state Kondo temperatures and superconducting-state Yu-Shiba-Rusinov resonance positions in iron adatoms deposited on a niobium surface depending on the adsorption site. DFT reveals that the adatoms on the clean surface are more distant than those adsorbed on patches with oxygen impurities, which causes a stronger hybridization with the substrate. This is shown to be one of the main causes of the different temperature scales of spin screening in CT-HYB calculations that qualitatively reproduce the Kondo temperatures.

In Chapter 5, our focus moves from atomic impurities to lattice models of correlated electrons. We investigate the Mott metal-insulator transition and its continuation as metal-metal transition and crossover in the doped two-orbital Hubbard model with

Hund's coupling using DMFT. In Section 5.1, we present our CT-HYB results at finite temperatures and NRG results of our collaborators that demonstrate the existence of a phase separation region in the phase diagram extending from half-filling to finite doping and down to zero temperature. The main finding is that the phase separation zone terminates in a line of critical points at finite temperature ending at a finite-doping quantum critical point at zero temperature. The presence of the phase separation zone and quantum critical point is connected to the first-order character of the transition at half-filling, whose cause we identify in the excitation structure of the single-site Hamiltonian using a perturbative analysis. In Section 5.2, we calculate generalized susceptibilities of the auxiliary AIM in the region of parameter space around the critical point we found in the previous section. The compressibility divergence at the critical point originates from the contribution of a single diverging eigenvalue in the eigenbasis of the DMFT generalized lattice susceptibility, whose eigenbasis representation can be directly related to that of the generalized impurity susceptibility. Thus we determine a threshold that an eigenvalue of the generalized local susceptibility needs to reach to cause that divergence of the uniform lattice charge response. The approach of that eigenvalue to the threshold is identified as the cause of the compressibility enhancement in the crossover region and it is found to fall below the threshold for unstable solutions in the phase separation region. We discuss the relation of the eigenvalues to thermodynamic derivatives and empirically find the eigenvalue threshold to distinguish stable solutions with no eigenvalue below it from unstable ones where an eigenvalue has crossed it.

We summarize our main conclusions in Sec. 6 and have a more detailed look at the Fourier transform to the Matsubara axis in Appendix A and the equations of motion of the AIM Green's function in Appendix B.

2 Background

2.1 The Anderson impurity model

The physical systems considered in this thesis are magnetic impurity atoms and the Hubbard model, which was introduced to describe systems with narrow energy bands [31]. Both of these types of systems share the property that a treatment in terms of quasi-free electrons is insufficient due to strong correlation of the well localized electrons on partially filled d -shells [31, 32]. For the case of magnetic impurities, P. W. Anderson introduced a model that includes a continuum of free electronic states representing mostly s - and p -shell states of the host metal as well as a localized state representing a d -state of the transition metal or rare-earth impurity atom, where the Hamiltonian contains a correlation term for the repulsion between two electrons of opposite spin on the same orbital as well as a hybridization or hopping term connecting the localized state to the free states [32].

A generalized multi-orbital version of this “Anderson impurity model” (AIM) not only directly serves as the description for the magnetic impurities we consider as well, but is also the auxiliary model employed in the dynamical mean-field theory (DMFT) approximation (see Sec. 2.3) for the solution of the Hubbard model [33]. As such, the computation of numerical solutions for the AIM is the basis for most of the results we present in the following, and we present a short review of the model as well as the method we use to solve it.

The Hamiltonian of the generalized AIM in the notation of second quantization is

$$\begin{aligned}
 H = & \underbrace{\sum_{\alpha,\beta} E_{\alpha\beta} c_{\alpha}^{\dagger} c_{\beta}}_{H_{loc,0}} + \underbrace{\sum_{\alpha,\beta,\gamma,\delta} \frac{U_{\alpha\beta\gamma\delta}}{2} c_{\alpha}^{\dagger} c_{\beta}^{\dagger} c_{\delta} c_{\gamma}}_{H_{loc,int}} + \underbrace{\sum_{\mathbf{k},\rho} \varepsilon_{\mathbf{k}\rho} a_{\mathbf{k}\rho}^{\dagger} a_{\mathbf{k}\rho}}_{H_{bath}} + \underbrace{\sum_{\mathbf{k},\alpha,\rho} V_{\mathbf{k}\rho,\alpha} a_{\mathbf{k}\rho}^{\dagger} c_{\alpha} + V_{\mathbf{k}\rho,\alpha}^{*} c_{\alpha}^{\dagger} a_{\mathbf{k}\rho}}_{H_{hyb}}, \\
 & \hspace{20em} (2.1)
 \end{aligned}$$

cf. Ref. [36], where we identify the distinct terms as the level structure of the non-interacting bath H_{bath} , the level structure of the impurity $H_{loc,0}$, the interaction between impurity electrons $H_{loc,int}$ and the hybridization term H_{hyb} between the bath states and the impurity states. We write $a_{\mathbf{k},\alpha}^{\dagger}$ and $a_{\mathbf{k},\alpha}$ for the operators creating and annihilating, respectively, an electron in the bath state with momentum \mathbf{k} and other degrees of

freedom α and c_α^\dagger and c_α for the operators creating and annihilating, respectively, an electron in the impurity state with degrees of freedom α . The matrix $E_{\alpha\beta}$ describes the (single-particle) level structure of the impurity, $U_{\alpha\beta\gamma\delta}$ the interactions between electrons on the impurity, $V_{a\beta}$ the hopping amplitudes between bath and impurity states, and the vector $\varepsilon_{\mathbf{k},\rho}$ the level structure of the bath. We shall in general try to use Greek indices for combined indices or spin indices and Latin indices for orbital indices in the following unless clarity requires otherwise.

In an orbital basis whose representations as wave functions in real space are known, it is in principle possible for us to calculate the matrix elements

$$U_{ijkl} = \int \phi_i^*(\mathbf{r})\phi_j^*(\mathbf{r}') \frac{e^2}{|\mathbf{r} - \mathbf{r}'|} \phi_k(\mathbf{r})\phi_l(\mathbf{r}') \, d\mathbf{r} \, d\mathbf{r}' \quad (2.2)$$

of the Coulomb interaction between the orbitals. In practice our orbital basis must be small enough to be suitable for actual numerical calculations, at most five in the calculations we shall consider in this thesis, and is therefore usually chosen as the subset of well localized orbitals with strongly correlated electrons. Due to screening by other electrons, we can not use the bare Coulomb interaction since the effective Coulomb interaction differs considerably [37, 38]. The constrained random phase approximation (cRPA) employed in these comparisons [37, 38] is a first-principles method that can be used to calculate the effective Coulomb interaction U_{ijkl} , but we use simpler forms of the interaction matrix.

The most complex form of the interaction matrix we use for our calculations is the full spherically symmetric Coulomb interaction, whose calculation and matrix elements are discussed in Sec. 4.1.7. The simplest form on the other hand is the “density-density” interaction [39, 40]

$$H_{\text{int,d-d}} = \frac{1}{2} \sum_{i,j,\sigma} U_{ij} n_{i\sigma} n_{j\bar{\sigma}} + \frac{1}{2} \sum_{i \neq j, \sigma} (U_{ij} - J_{ij}) n_{i\sigma} n_{j\sigma}, \quad (2.3)$$

where $\bar{\sigma}$ stands for the spin index opposite to σ , $n_{i\sigma} = c_{i\sigma}^\dagger c_{i\sigma}$ are densities, and the matrices $U_{ij} = U_{ijij}$ of direct integrals and $J_{ij} = U_{ijji}$ of exchange integrals together account for the largest elements of the Coulomb matrix [39]. Because this form of the interaction contains only densities, it does not change states it is applied to, which makes its use advantageous or mandatory for some numerical algorithms. Even if U_{ij} and J_{ij} are constructed under the assumption of spherical symmetry, this form consisting of densities can however not be invariant under arbitrary rotations in space. The addition of “spin flip” and “pair hopping” is necessary to restore spin- $SU(2)$ symmetry for

instance and arrive at the Kanamori form [20, 39–41]

$$H_{\text{int,Kanamori}} = H_{\text{int,d-d}} + \frac{1}{2} \sum_{i \neq j, \sigma} J_{ij} \left(c_{i\sigma}^\dagger c_{j\bar{\sigma}}^\dagger c_{i\bar{\sigma}} c_{j\sigma} - c_{i\sigma}^\dagger c_{i\bar{\sigma}}^\dagger c_{j\sigma} c_{j\bar{\sigma}} \right). \quad (2.4)$$

This interaction contains e.g. already all possible terms for the t_{2g} triplet of d -shell orbitals [20], but that is not the case in general and using it for the full d -shell can significantly affect results, cf. Sec. 4.1. When we use the density-density or Kanamori form of the interaction, we may use the full U_{ij} and J_{ij} matrices such that the interaction matrices only differ from that of the full spherically symmetric Coulomb interaction by lacking some elements, or we may use orbitally uniform matrices like in (5.2). In the latter case, we need to specify only the intraorbital repulsion U (also ‘‘Hubbard- U ’’) for the diagonals U_{ii} , interorbital repulsion U' for the offdiagonals U_{ij} , and the spin-aligning [42] Hund’s coupling J for the (exclusively relevant) offdiagonal elements J_{ij} [20, 39], where we choose $U' = U - 2J$ which makes the Kanamori interaction fully (spin and orbital) rotationally invariant in the case of t_{2g} orbitals [20].

In our calculations, the impurity level matrix $E_{\alpha\beta}$ is usually diagonal, i.e. there is no on-site hopping, and consists of the chemical potential μ and the crystal field, which e.g. comes from density functional theory (DFT) results for the impurity systems considered in Sec. 4. The information corresponding to the bath levels $\varepsilon_{\mathbf{k},\rho}$ and the hopping $V_{\alpha\beta}$ between bath and impurity is usually given in the form of a hybridization function $\Delta_{\alpha\beta}$, introduced below and defined in (2.10). This also comes from DFT for the real physical impurity systems considered in Sec. 4 and is self-consistently determined during the calculation to describe the effect of the rest of the lattice for the auxiliary impurity model used in DMFT.

While the AIM Hamiltonian (2.1) completely defines the model in a form that allows us to solve it when numerical values for the parameters are also specified, e.g. by means of exact diagonalization [4] if the dimensions permit, we shall proceed toward an expression that is amenable to treatment using continuous-time quantum Monte Carlo methods [36]. Using the formalism of imaginary-time coherent state path integrals as presented e.g. in Ref. [43], we write the thermodynamic partition function $Z = \text{Tr}(\exp(-\beta(H - \mu N)))$ of the AIM at inverse temperature β and chemical potential μ as

$$Z = \int \mathcal{D}(a^\dagger, a, c^\dagger, c) \exp(-S_{\text{AIM}}) \quad (2.5)$$

with the action

$$S_{\text{AIM}} = \int_0^\beta d\tau \sum_{\alpha, \beta, \gamma, \delta, \rho, \mathbf{k}} c_\alpha^\dagger(\tau) \delta_{\alpha\beta} (\partial_\tau - \mu) c_\beta(\tau) + a_{\mathbf{k}\rho}^\dagger(\tau) (\partial_\tau - \mu) a_{\mathbf{k}\rho}(\tau) \quad (2.6)$$

$$\begin{aligned}
& + H(a_{\mathbf{k}\rho}^\dagger(\tau), a_{\mathbf{k}\rho}(\tau), c_\alpha^\dagger(\tau), c_\beta(\tau)) \\
= & \int_0^\beta d\tau \sum_{\alpha,\beta,\gamma,\delta,\rho,\mathbf{k}} c_\alpha^\dagger(\tau) (\delta_{\alpha\beta} \partial_\tau - \delta_{\alpha\beta} \mu + E_{\alpha\beta}) c_\beta(\tau) \\
& + \frac{U_{\alpha\beta\gamma\delta}}{2} c_\alpha^\dagger(\tau) c_\beta^\dagger(\tau) c_\delta(\tau) c_\gamma(\tau) \\
& + a_{\mathbf{k}\rho}^\dagger(\tau) (\partial_\tau - \mu + \varepsilon_{\mathbf{k}\rho}) a_{\mathbf{k}\rho}(\tau) \\
& + V_{\mathbf{k}\rho,\alpha} a_{\mathbf{k}\rho}^\dagger(\tau) c_\alpha(\tau) + V_{\mathbf{k}\rho,\alpha}^* c_\alpha^\dagger(\tau) a_{\mathbf{k}\rho}(\tau),
\end{aligned} \tag{2.7}$$

where a^\dagger , a , c^\dagger , and c in the context of a path integral are to be understood as Grassmann variables rather than operators in second quantization. For the bath degrees of freedom, the path integral contains the local level term quadratic in the bath variables and the hybridization terms (“source terms”) linear in the bath variables (and the impurity variables), so the path integral is of Gaussian form and can be performed explicitly using

$$\int \mathcal{D}(a^\dagger, a) \exp\left(-\sum_{\rho,\theta} a_\rho^\dagger B_{\rho\theta} a_\theta + \sum_\rho c_\rho^\dagger a_\rho + a_\rho^\dagger c_\rho\right) = \det(B) \exp\left(\sum_{\rho,\theta} c_\rho^\dagger B_{\rho\theta}^{-1} c_\theta\right) \tag{2.8}$$

as given in Ref. [43], where all degrees of freedom including imaginary times are combined into a single index each and the individual impurity operators have to be identified with the summation over hybridization matrix elements and impurity operators in our action (2.7). Here, only the new term for the impurity action is relevant, as the factor $\det(B)$ multiplying the partition function cancels in the calculation of any observables. We thus obtain the effective action

$$\begin{aligned}
S_{\text{AIM}} = & \int_0^\beta d\tau d\tau' \sum_{\alpha,\beta,\gamma,\delta} c_\alpha^\dagger(\tau) (\delta(\tau - \tau') (\delta_{\alpha\beta} \partial_\tau - \delta_{\alpha\beta} \mu + E_{\alpha\beta}) + \Delta_{\alpha\beta}(\tau - \tau')) c_\beta(\tau') \\
& + \frac{U_{\alpha\beta\gamma\delta}}{2} c_\alpha^\dagger(\tau) c_\beta^\dagger(\tau) c_\delta(\tau) c_\gamma(\tau).
\end{aligned} \tag{2.9}$$

where $B^{-1} = (\partial_\tau - \mu + \varepsilon)^{-1}$ is calculated in frequency representation as $(-i\nu_n - \mu + \varepsilon)^{-1}$, which together with the source terms and absorbing μ in the levels ε results in the hybridization function

$$\Delta_{\alpha\beta}(i\nu) = \sum_{\rho,\mathbf{k}} \frac{V_{\mathbf{k}\rho\alpha}^* V_{\mathbf{k}\rho\beta}}{i\nu - \varepsilon_{\mathbf{k}\rho}} \tag{2.10}$$

on fermionic Matsubara frequencies $\nu_n = \frac{(2n+1)\pi}{\beta}$, $n \in \mathbb{Z}$ [44–47] and can be Fourier

transformed to obtain the β -antiperiodic hybridization function on imaginary time [36]

$$\Delta_{\alpha\beta}(\tau) = \sum_{\rho, \mathbf{k}} \frac{V_{\mathbf{k}\rho\alpha}^* V_{\mathbf{k}\rho\beta}}{\exp(\varepsilon_{\mathbf{k}\rho}\beta) + 1} \times \begin{cases} -\exp(-\varepsilon_{\mathbf{k}\rho}(\tau - \beta)) & 0 < \tau < \beta \\ \exp(-\varepsilon_{\mathbf{k}\rho}\tau) & -\beta < \tau < 0 \end{cases}. \quad (2.11)$$

Under the ‘‘solution’’ of the AIM as specified by its Hamiltonian (2.1) or effective action (2.9) we understand the calculation of primarily the one-particle Green’s function for the impurity states [36, 47]

$$G_{\alpha\beta}(\tau) = -\left\langle T_{\tau} c_{\alpha}(\tau) c_{\beta}^{\dagger}(0) \right\rangle, \quad (2.12)$$

where T_{τ} is the time-ordering symbol [48] on imaginary time, and occasionally also higher-order correlation functions such as the double occupancies $\langle n_{\alpha}(0)n_{\beta}(0) \rangle$ and others that we will define before their use. From the one-particle Green’s function, we in particular also get orbital occupations as the special case $\tau = 0$, and from its imaginary part on the real axis, proportional to the spectral function, information on the one-particle excitations of the system [47]. Without interaction between electrons on the impurity, the one-particle Green’s function for the AIM can simply be calculated as $\mathbf{G}_0(i\nu) = (i\nu - \mathbf{E} - \Delta(i\nu))^{-1}$ [36], and to capture the change introduced by the interaction, we define the self-energy [36, 47]

$$\mathbf{\Sigma} = \mathbf{G}_0^{-1} - \mathbf{G}^{-1} \quad (2.13)$$

such that $\mathbf{G}(i\nu) = (\mathbf{G}_0^{-1}(i\nu) - \mathbf{\Sigma}(i\nu)) = (i\nu - \mathbf{E} - \Delta(i\nu) - \mathbf{\Sigma}(i\nu))^{-1}$, where we have used matrix-valued quantities indicated by bold letters for clarity rather than writing indices explicitly as before.

The calculation of the correlation functions of the AIM can be done using a variety of algorithms and approximations. We shall consider the continuous-time quantum Monte Carlo (CT-QMC) algorithm in hybridization expansion (CT-HYB) [34], which was used to obtain the majority of the results presented in this thesis, in more detail in Sec. 2.2. It uses Monte Carlo integration to sum up diagrammatic contributions to the relevant path integral expressions after expansion of the exponential of the hybridization part of the action into a power series. Other CT-QMC algorithms [36] such as CT-INT [49] and CT-AUX [50] differ in the term of the action whose exponential is expanded into a power series, which allows calculations with more orbitals but can be problematic depending on the strength and form of the interaction. As far as QMC is concerned, there is also the older Hirsch-Fye QMC algorithm [51], which requires discretization of imaginary time into slices and discrete Hubbard-Stratonovich transformations [52, 53] to deal with the interaction.

Other algorithms apart from QMC that are commonly used to solve the AIM include the aforementioned exact diagonalization (ED) [4], which however requires a bath consisting of a discrete number of states and therefore suffers from discretization errors when fitting hybridization functions that are not representable in this way, as they may e.g. occur in DMFT in general. ED results are used as reference values free from statistical error in Sec. 3.2. Further, there are the density matrix renormalization group (DMRG) [54–56] and numerical renormalization group (NRG) [57, 58] algorithms, which are methods based on truncation and iterative diagonalization. Zero-temperature results in Sec. 5.1 were obtained using NRG and complemented by ED results. Several methods of a more approximative nature have also been in use, cf. Refs. [36, 59], such as e.g. perturbative expansions [60–64] the “Hubbard-I” [31, 65] and “Hubbard-III” approximations [66], and the non- (NCA) and one-crossing approximation (OCA) [67–69], to name a few. In the context of DMFT, solution by second-order perturbation theory [60–62] has been significant, which is known in that combination as “iterated perturbation theory” (IPT) [70].

2.2 Continuous-time quantum Monte Carlo in hybridization expansion

Continuous-time quantum Monte Carlo in hybridization expansion (CT-HYB) was introduced in Ref. [34], with the generalizations and optimizations of Refs. [71–74] also relevant for our introductory discussion here. It is a diagrammatic Monte Carlo algorithm based on the idea of a technique introduced earlier for bosonic systems [75, 76], the Monte Carlo integration of a formal perturbation expansion of the path integral expression for the partition function, and is particularly similar to the method now called CT-INT that was previously developed for the AIM [49, 77] and differs only in expanding the interaction term instead.

Path integral expansion

Using the path integral expression (2.5) for the partition function of the AIM with the effective action (2.9), we obtain the perturbation expansion by expanding the exponential in $S_{\text{hyb}} = c_{\alpha}^{\dagger}(\tau)\Delta_{\alpha\beta}(\tau - \tau')c_{\beta}(\tau')$, with the remaining part of the action being the local terms for levels and interaction S_{loc} ,

$$Z = \sum_{k=0}^{\infty} \int \mathcal{D}(c^{\dagger}, c) e^{-S_{\text{loc}}} \frac{(-1)^k}{k!} \int_0^{\beta} d\tau_i d\tau'_i \sum_{\alpha_i, \beta_i} \prod_{i=1}^k c_{\alpha_i}^{\dagger}(\tau_i) \Delta_{\alpha_i \beta_i}(\tau_i - \tau'_i) c_{\beta_i}(\tau'_i) \quad (2.14)$$

$$\begin{aligned}
&= \sum_{k=0}^{\infty} \int \mathcal{D}(c^\dagger, c) e^{-S_{\text{loc}}} \int_{\tau_{i-1}}^{\beta} d\tau_i \int_{\tau'_{i-1}}^{\beta} d\tau'_i \sum_{\alpha_i, \beta_i} \det\left(\left(\Delta_{\alpha_i \beta_j}(\tau_i - \tau'_j)\right)_{ij}\right) \prod_{i=1}^k c_{\beta_i}(\tau'_i) c_{\alpha_i}^\dagger(\tau_i) \\
&= \sum_{k=0}^{\infty} \int_{\tau_{i-1}}^{\beta} d\tau_i \int_{\tau'_{i-1}}^{\beta} d\tau'_i \sum_{\alpha_i, \beta_i} \underbrace{\text{Tr}\left(T_\tau e^{-\beta H_{\text{loc}}} \prod_{i=1}^k c_{\beta_i}(\tau'_i) c_{\alpha_i}^\dagger(\tau_i)\right)}_{=:w_{\text{loc}}} \underbrace{\det\left(\left(\Delta_{\alpha_i \beta_j}(\tau_i - \tau'_j)\right)_{ij}\right)}_{=:w_{\text{bath}}},
\end{aligned} \tag{2.15}$$

where sums over the $2k$ creator indices $\alpha_{i \in \{0, \dots, k\}}$ and annihilator indices $\beta_{i \in \{0, \dots, k\}}$ run over all possible operator “flavors”, i.e. in our case orbitals and spins, integrals over the $2k$ creator times $\tau_{i \in \{0, \dots, k\}}$ and annihilator times $\tau'_{i \in \{0, \dots, k\}}$ run from 0 to β in the first line and from the time of the previous creator resp. annihilator to β in the second and third lines, and we separate the integrand into the local weight w_{loc} and bath weight w_{bath} .

From the second to the third line, we change back from path integral to operator formalism as that lends itself more obviously to implementation because matrices can be used to represent operators with occupation number states as basis and allow products, exponential functions and traces to be performed numerically as matrix operations. The details of the step from the first to the second line are more involved. Due to the expansion of $e^{-S_{\text{hyb}}}$, we have a factor of $(-1)^k/k!$ in the first line from the coefficients of the exponential series. Because each factor of the hybridization term that we get by expanding is independent, we also have $k!$ duplicates of every possible contribution that differ only by permutations of the indices i . Imposing the time order $\tau_1 < \dots < \tau_k$ and $\tau'_1 < \dots < \tau'_k$ in the second line removes these $k!$ duplicates, because permuting the indices i would violate this ordering, allowing us to remove the factor $1/k!$.

However, this change alone would also remove all contributions that we get by permuting either only the creators’ or only the annihilators’ indices, such that e.g. the contribution where the first creator is paired with the last annihilator is missing. Because we still have contributions with all different possible choices of times and flavors and the path integral results in a time-ordered expectation value anyway, the only part of the expression that actually meaningfully “pairs” the creators with the annihilators are the hybridization function factors. We can therefore compensate for the “overzealous” removal of the unordered pairs by replacing the single hybridization function product in each contribution with the determinant $\det\left(\left(\Delta_{\alpha_i \beta_j}(\tau_i - \tau'_j)\right)_{ij}\right)$ of a “hybridization matrix” Δ , where each row i is associated with a specific creator and each column j with a specific annihilator as far as the arguments of the hybridization function entries are concerned. This matrix contains hybridization function values for every possible pairing of a creator with an annihilator and the determinant ensures that each product

corresponds to pairing each creator with exactly one annihilator while also taking care of the negative signs brought about by the commutation of Grassmann variables, as each exchange of two creators or two annihilators requires an odd number of commutations.

Finally, since we get k pairs of creators and annihilators from the expansion of the exponential, we exchange the “formal” order of the creator and the annihilator in all the k factors of $-S_{\text{hyb}}$, which removes the factor $(-1)^k$ due to the total anticommutation of Grassmann variables and brings us to the final expression (2.15). Note that the time-ordering symbol is defined to include a sign factor due to the necessary commutation of fermionic operators from this original formal ordering of operators to the time order used for actual calculation. Since this can meaningfully change the sign of the contribution, it must be taken into account by the implementation.

In Refs. [34, 71], a hybridization function $F(\tau)$ defined differently from ours was introduced, to which our definition (2.10) is related by $\Delta_{\alpha\beta}(\tau) = -F_{\beta\alpha}(\beta - \tau)$ [78], or, equivalently, $\Delta_{\alpha\beta}(i\nu) = F_{\beta\alpha}(-i\nu)$. From the structure of the definition of the hybridization function $F(\tau - \tau')$ as $\langle T_{\tau} a^{\dagger}(\tau)a(\tau') \rangle$ in Ref. [71], where the bath is not integrated out using the path integral formalism, we can see that for $\tau > 0$ it is a Green’s function describing the propagation of a hole through the bath [47] and associated with an impurity operator pair $c(\tau)c^{\dagger}(\tau')$ describing propagation of electron on the impurity. Our definition $\Delta(\tau)$ on the other hand is associated with the propagation of a hole on the impurity, as recognizable in (2.14), and thus the propagation of an electron through the bath, which allows us to give an illustrative interpretation to its contribution to the effective action (2.9): it is that term of the action associated with the electrons that leave the impurity at some point and return after time τ .

The Monte Carlo method

The expression (2.15) is now in a form that can be evaluated by using the Monte Carlo method to perform the summations and integrations over the expansion order, flavor indices, and times, one specific choice of which we collectively call the (Monte Carlo) configuration. The Monte Carlo method, covered e.g. in textbooks and review articles such as Refs. [79–81], is a stochastic method that allows integrations (and simulations) to be performed through calculations involving a sample of random numbers, in practice usually pseudorandom numbers generated by deterministic algorithms, from a suitable probability distribution. In the simplest case, we may imagine e.g. taking a sample of pairs of random coordinates uniformly distributed between zero and one that we interpret as points inside a square of unit area. We expect the square of unit area to be covered uniformly by the points in the limit of an infinitely large sample and

every part of it to eventually contain a number of points proportional to its area. If we take the ratio of points with a distance of less than one from the origin to the size of the entire sample, we therefore get an estimate of the ratio of the area of a quarter of the circle of unit radius around the origin to the area of the unit square, or in other words $\pi/4$ by definition [80]. This is a very simple example of integration by direct sampling from a probability distribution, more formally and in one dimension the law of large numbers states that the average of function values $f(x_i)$ evaluated at N discrete random numbers x_i uniformly distributed on an interval $[a, b]$ will converge to the average calculated as the normalized value of the integral of the function in the limit of a large number N of random numbers [79],

$$\frac{1}{N} \sum_{i=1}^N f(x_i) \rightarrow \frac{1}{b-a} \int_a^b f(x) dx, \quad (2.16)$$

where we can recognize that the sum to the left would just correspond to the rectangle rule or a Riemann sum for perfectly equidistant numbers x_i .

An important practical improvement over such a Monte Carlo integration by direct sampling is the use of importance sampling. If the value of the integrand varies strongly over the domain of integration, the Monte Carlo estimate will suffer from a larger uncertainty than in the optimal case that each random point contributes equally [79]. Sampling points from a probability distribution close to the integrand rather than uniformly can improve the uncertainty in such cases, formally this corresponds to a change of integration variables [79] or a reweighing [36, 80]. Taking the example of the expectation value of a physical quantity A [36],

$$\langle A \rangle_p := \frac{1}{Z} \int_C A(x) p(x) dx, \quad \text{with } Z = \int_C p(x) dx, \quad (2.17)$$

where $x \in C$ are states in the physical configuration space C , $p(x)$ the probability distribution of states, and $A(x)$ a suitable function representing A , we can calculate a Monte Carlo estimate as

$$\langle A \rangle_{\text{MC}} = \frac{1}{N} \sum_{i=1}^N A(x_i) \quad (2.18)$$

where x_i are N random states sampled according to the probability distribution $p(x)/Z$ [36].

In the case that we need to sample states with a different probability distribution

$q(x)$, it is necessary to reweigh the expectation value according to [36]

$$\langle A \rangle_p = \frac{1}{Z} \int_C A(x) p(x) dx = \frac{\int_C A(x) \frac{p(x)}{q(x)} q(x) dx}{\int_C \frac{p(x)}{q(x)} q(x) dx} = \frac{\langle Ap/q \rangle_q}{\langle p/q \rangle_q}. \quad (2.19)$$

Looking at the “weight” proportional to our “ideal” probability distribution,

$$w(x) = \text{Tr} \left(T_\tau e^{-\beta H_{\text{loc}}} \prod_{i=1}^k c_{\beta_i}(\tau'_i) c_{\alpha_i}^\dagger(\tau_i) \right) \det \left((\Delta_{\alpha_i \beta_j}(\tau_i - \tau'_j))_{ij} \right) = w_{\text{loc}} w_{\text{bath}}, \quad (2.20)$$

which is the integrand of (2.15) with states $x = \{k, \alpha_i, \beta_i, \tau_i, \tau'_i\}_{i \in 1, \dots, k} \in C$, we note the problem that the weight is not necessarily positive and thus $w(x)$ not actually an admissible probability distribution even if we could normalize it. We will therefore have to use its absolute value $|w(x)|$ instead and reweigh according to (2.19) with $p = w, q = |w|, p/q = \text{sign}(w)$, which shall be implied in all expressions for Monte Carlo estimates of expectation values given below. Due to the indefinite sign of the weight from which a necessity for reweighing follows, calculations for fermionic systems may suffer from a “sign problem” as the relative error of the sign in general grows exponentially with decreasing temperature and increasing system size [36], but our calculations are only significantly affected in cases where we use the full Coulomb interaction on the impurity.

It is further entirely impractical in our case to directly sample states even with probability density $|w|$ from our configuration space of in general high and varying number of dimensions. This problem can be overcome by sampling states along a Markov chain [82, 83] whose stationary probability distribution p corresponds to the one of our states. Instead of absolute probabilities, we then only need to provide transition probabilities w_{xy} from one state x to another state y that fulfill the *balance* or *stationarity* condition $\int_C p_x w_{xy} dx = p_y$ and the *ergodicity* or *irreducibility* condition that every state is reachable from all the other ones in a finite amount of steps [36, 84]. Due to the correlation of subsequent states (“autocorrelation”), sampling along a Markov chain does however change the statistical errors of observables compared to direct sampling unless only states separated by sufficiently many steps are used [84]. Further, a certain amount of “warm-up” states sampled from the first Markov chain iterations of a calculation before it reaches equilibrium may be overly influenced by the initial probability distribution and should not be used either [84].

We generate the transition probabilities by using the Metropolis-Hastings algorithm [82, 83], a two-step algorithm which requires us to randomly choose a transition from the current configuration x to another one y from all the possible transition processes

we have “designed” (constrained only by the need for ergodicity and practicality) and prescribes the rule that we should take the target state as next state, i.e. actually “accept the proposed transition”, only with the acceptance probability

$$w_{xy}^{\text{acc}} = \min \left(1, \frac{p_y w_{yx}^{\text{prop}}}{p_x w_{xy}^{\text{prop}}} \right), \quad (2.21)$$

and otherwise “reject the transition” and take the *current* state as next state again, with w_{xy}^{prop} being the probability for the choice of the specific random transition proposal, w_{yx}^{prop} the probability for the proposal of the reverse transition, and p_x and p_y the probabilities of the states according to the desired stationary probability distribution, of which we only ever need the ratio. The total transition probability is just $w_{xy} = w_{xy}^{\text{prop}} w_{xy}^{\text{acc}}$, and this rule satisfies not only the balance condition but even the sufficient but unnecessary *detailed balance* or *reversibility* condition $p_x w_{xy} = p_y w_{yx}$, i.e. equality of the probability flows in both directions between any two configurations [83]. In fact, avoiding detailed balance can lead to more efficient algorithms [85] such as the class of event-chain Monte Carlo algorithms [86, 87].

Let us also note that the stochastic nature of Monte Carlo methods makes an estimate of the statistical error possible by running multiple calculations with different sequences of pseudorandom numbers. Using resampling methods such as the jackknife [88] or bootstrap [89, 90] method, the errors of arbitrary quantities calculated from the QMC results can be estimated.

Updates in CT-HYB

In the *w2dynamics* implementation of CT-HYB [40], we propose several different kinds of transitions between configurations, also “updates”, “steps” or “moves”. All updates not individually discussed in Sec. 3.1 or 3.2 are listed in Tab. 2.1 with symbolic representations of exemplary configurations connected by them and proposal probability ratios $R_{xy}^{\text{prop}} = w_{yx}^{\text{prop}} / w_{xy}^{\text{prop}}$ for the general case of nonzero flavor-offdiagonal entries of the hybridization function and without considering window sampling [73] discussed below.

Let us first consider the insertions and removals of impurity operators with accompanying entries in the hybridization matrix into (2.15), which change the expansion order k . Insertions and removals of one pair are always necessary for ergodicity [34] and insertions and removals of four impurity operators are necessary for ergodicity in some cases [92, 93]. In general, the proposal probability density for the insertion carries a factor of $d\tau_i / \beta$ per operator for its uniformly distributed random imaginary time argument and a factor of $1/N_{\text{fl}}$ per operator for its uniformly distributed random

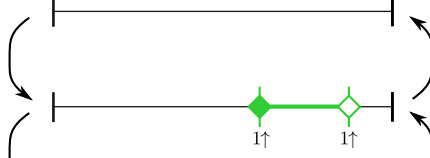
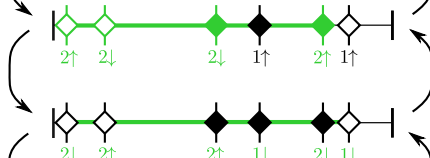
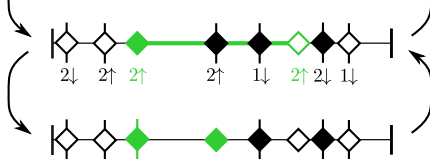
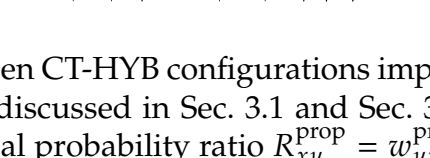
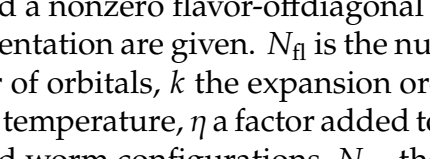
name (down)	R^{prop} (down)	symbolic representation	R^{prop} (up)	name (up)
pair insertion	$\frac{N_{\text{fl}}^2 \beta^2}{(k+1)^2}$		$\frac{k^2}{N_{\text{fl}}^2 \beta^2}$	pair removal
quadruplet insertion	$\frac{4N_{\text{fl}}^4 \beta^4}{(k+2)^2 (k+1)^2}$		$\frac{k^2 (k-1)^2}{4N_{\text{fl}}^4 \beta^4}$	quadruplet removal
flavor permutation	$\frac{2N_{\text{fl}}!}{2N_{\text{fl}}!}$		$\frac{2N_{\text{fl}}!}{2N_{\text{fl}}!}$	flavor permutation
worm insertion	$\eta \beta^{N_{\text{op}}}$		$\frac{1}{\eta \beta^{N_{\text{op}}}}$	worm removal
worm replacement	$\frac{N_{\text{op}} k_{\text{fl}}}{N_{\text{op}} k_{\text{fl}}}$		$\frac{N_{\text{op}} k_{\text{fl}}}{N_{\text{op}} k_{\text{fl}}}$	worm replacement

Table 2.1: Transitions between CT-HYB configurations implemented in *w2dynamics* excluding changes discussed in Sec. 3.1 and Sec. 3.2. For each transition, the name, the proposal probability ratio $R_{xy}^{\text{prop}} = w_{yx}^{\text{prop}} / w_{xy}^{\text{prop}}$ assuming no window sampling and a nonzero flavor-offdiagonal hybridization function, and a symbolic representation are given. N_{fl} is the number of flavors equal to two times the number of orbitals, k the expansion order of the source configuration, β the inverse temperature, η a factor added to balance the amount of partition function and worm configurations, N_{op} the number of extra operators in worm space, and k_{fl} the number of operators associated with hybridization of the same flavor and type as the selected worm operator. In the symbolic representation, impurity operators are depicted as filled (creators) and empty (annihilators) diamonds with orbitals and spins written below them and vertical line segments indicating associated entries in the hybridization matrix on a horizontal line representing the imaginary time axis from 0 to β . Every transition (left half) can also be performed in reverse (right half), which are not equivalent in those cases where the number of operators is changed. Changed and added parts of the configuration and the time segment needing recalculation in a matrix-vector implementation for the down direction are colored green. The dotted line separates partition function configurations above and worm configurations below, here specifically from the space of diagonal single-particle Green's function configurations for orbital 2 and spin up. Adapted from Tab. 2.4 of Ref. [91], cf. Tab. 2 of Ref. [40].

flavor argument. For the case of flavor-diagonal hybridization functions, which we usually consider, the weight is zero if creators and annihilators of same flavor cannot be paired up, so only one factor of $1/N_{\text{fl}}$ per pair of inserted operators is necessary if

we avoid unacceptable proposals. If we enable window sampling, the factors of $1/\beta$ require modification because we restrict the first time argument of an operator pair to a subinterval of β and impose a maximum pair distance that restricts the second time argument even further, see Ref. [73]. The proposal probability for the removal of operators is $\binom{k}{i}^{-2}$ with the expansion order k and number of removed pairs i . Let us note that time evolution on the AIM does not connect states with different numbers of electrons, so the number of creators and annihilators must always be the same and therefore insertions and removals must always remove the same number of each of them. The binomial coefficient takes into account that the removal move does not distinguish by “order” of operator selection, and it is squared because the choice of the removed annihilators and removed creators is independent. If however the hybridization function is flavor-diagonal and unacceptable selections are avoided or the selection is restricted due to window sampling, this factor is in general the number of distinct permissible choices of operators [73]. Taking into account that the expansion order of the *source* configuration is relevant for the removals, leading to $k + 1$ etc. instead of k , we arrive at the ratios R_{xy}^{prop} given in Tab. 2.1.

The next type of moves are global permutations of the flavors (orbitals and spins) of all operators [94], including possibly an exchange of creators and annihilators. These moves are supposed to connect regions of configuration space that are hard to reach through sequences of individual insertions and removals of operators that are local in imaginary time, such as e.g. configurations with opposite spins or orbital occupations in calculations that are strongly polarized in this respect. Using only standard CT-HYB [71] without such techniques as Wang-Landau sampling [50, 95–97], expansion order zero is unlikely to be revisited at sufficiently low temperatures on practical timescales and the weight of intermediate configurations with mixed flavors may be low enough to be practically unreachable as well [98]. The proposal probability for a uniformly random permutation is $2N_{\text{fl}}!$, twice the factorial of the number of flavors $N_{\text{fl}} = 2N_{\text{orb}}$ to account for all possible mappings from one flavor to another and the possibility of swapping creators for annihilators and vice versa. As the proposal of the reverse is equally likely, R_{xy}^{prop} is one. In practice, *w2dynamics* divides the total proposal probability of global moves into a part for totally random permutations and parts for permutations more likely to be accepted in usual cases, such as flips of all spins. The division of the total proposal probability among “classes” of moves requires no further modifications of the probability ratios if all these classes contain the inverse of every move they contain, which e.g. also applies to the user-configurable probabilities of the proposal classes (i.e. per line of Tab. 2.1).

Finally, two further types of moves are used in the context of a technique known as worm sampling [74, 76, 99, 100]. Using the weight (2.20), we are actually performing

importance sampling with respect to the magnitude of diagrammatic contributions to the partition function, while the quantity we are most interested in is the Green's function. We will see the expression for the Green's function estimator based on partition function configurations below, but it may be unacceptably inefficient or even give wrong results [101, 102] in some limiting cases such as the atomic limit, i.e. high temperature and interaction strength leading to low expansion order, or for certain hybridization functions corresponding to discrete baths. Beyond the one-particle Green's function, higher-order correlation functions may not have usable estimators based on partition function configurations at all [74]. In that case, we can directly sample configurations that represent diagrammatic contributions to the quantities of interest, and from the expression [74]

$$\langle O_{\gamma_1 \dots \gamma_n}(\tau_{o,1} \dots \tau_{o,n}) \rangle = Z^{-1} \sum_{k=0}^{\infty} \int_{\tau_{i-1}}^{\beta} d\tau_i \int_{\tau'_{i-1}}^{\beta} d\tau'_i \sum_{\alpha_i, \beta_i} \text{Tr} \left(T_{\tau} e^{-\beta H_{\text{loc}}} O_{\gamma_1 \dots \gamma_n}(\tau_{o,1} \dots \tau_{o,n}) \prod_{i=1}^k c_{\beta_i}(\tau'_i) c_{\alpha_i}^{\dagger}(\tau_i) \right) \det \left((\Delta_{\alpha_i \beta_j}(\tau_i - \tau'_j))_{ij} \right), \quad (2.22)$$

for the expectation value of some n -point correlation function $O_{\gamma_1 \dots \gamma_n}(\tau_{o,1} \dots \tau_{o,n})$ we see that they differ from partition function configurations (2.15) by including additional impurity operators in the trace over impurity states w_{loc} that have no corresponding entries in the hybridization matrix and so no influence on the bath weight w_{bath} .

In order to transition between such configurations and partition space configurations, which we continue to sample for normalization [74], we need moves that insert and remove the additional impurity operators. In current versions of *w2dynamics*, we sample configurations for different components of correlation functions separately, so in the simple cases assumed for the ratios given in Tab. 2.1, we have N_{op} extra operators with a different uniformly random imaginary time argument each and externally fixed flavors, such that the proposal weight for an insertion consists of N_{op} factors of β and a factor η used to balance the number of configurations sampled from worm configuration space $C_{O_{\gamma_i}}$ and partition function configuration space C_Z (previously just C). In case of multiple operators at equal time, the number of factors of β may differ from N_{op} and in case of summations over internal flavor indices that are performed stochastically, additional factors of N_{fl} and coefficients may enter, cf. Sec. 3.2. The proposal probability for a worm removal is just η^{-1} because every worm configuration contains exactly one set of worm operators. Since performing calculations with just insertion and removal moves suffers from practical ergodicity problems [74], as insertions of impurity operator pairs with imaginary time distances around $\beta/2$ are unlikely [72–74, 103], we additionally perform replacement moves that exchange the roles of a worm

operator and an operator that differs from it only in its imaginary time argument and associated hybridization. These moves change only the bath weight by replacing the time of the latter operator in the hybridization matrix entries with that of the former, such that the former worm operator becomes the one associated with hybridization instead, making larger distances of the worm operators in imaginary time more likely [74].

Estimators in worm and partition function sampling

In order to obtain an estimate for e.g. the one-particle Green's function from worm sampling, it is only necessary to take the normalized time difference of the worm operators [74],

$$G_{\gamma_1\gamma_2}(\tau) = \frac{N_{G_{\gamma_1\gamma_2}}}{\eta_{G_{\gamma_1\gamma_2}} N_Z} \langle \delta(\tau, \tau_{o,1} - \tau_{o,2}) \rangle_{MC}, \quad (2.23)$$

where $N_{G_{\gamma_1\gamma_2}}$ is the number of configurations sampled from the worm space of $G_{\gamma_1\gamma_2}$, N_Z is the number of configurations sampled from the partition function configuration space, and $\eta_{G_{\gamma_1\gamma_2}}$ the balancing factor for the worm space. The relevant weight w is the worm space configuration weight found in the second line of (2.22) including the minus sign found in the definition (2.12) of G and contributions for negative τ are instead counted for $\tau + \beta$ with opposite sign due to antiperiodicity. This can be binned as desired or alternatively

$$G_{\gamma_1\gamma_2}(i\nu) = \frac{N_{G_{\gamma_1\gamma_2}}}{\eta_{G_{\gamma_1\gamma_2}} N_Z} \langle \exp(i\nu(\tau_{o,1} - \tau_{o,2})) \rangle_{MC}, \quad (2.24)$$

can be used instead to directly collect the contributions per Matsubara frequency without any systematic errors from binning [74]. For more efficiency, values of a window function centered on the time differences at a small number of the nearest points on an equispaced oversampled grid can be collected instead to perform the adjoint non-equispaced discrete Fourier transform to Matsubara frequencies by using an FFT algorithm at the end of the calculation [104–106]. The worm sampling estimators for other quantities are entirely analogous, with the only difference being the different expressions for w_{loc} and possibly multiple imaginary time arguments requiring multidimensional binning or a multidimensional NFFT.

The one-particle Green's function estimator in partition function sampling is by comparison more involved. As we have just seen, in worm sampling, where the configurations are distributed according to their contributions to the Green's function, we essentially just need to count them. If we sample according to contributions to the partition function instead, we need to make sure to generate all possible Green's function con-

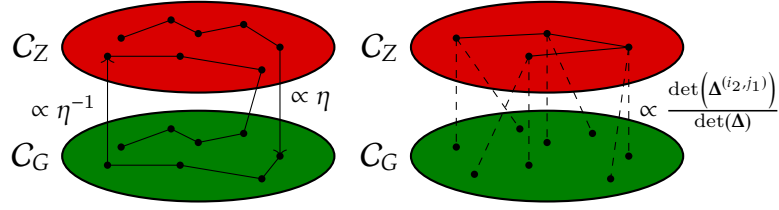


Figure 2.1: Illustration of the difference between worm sampling (left panel) and partition function sampling (right panel). Black dots represent configurations in the partition function (Z) space C_Z and the Green's function (G) worm space C_G . The Markov chain follows the solid line, i.e. the weights of the configurations represented by these dots is the probability density used for importance sampling. In worm sampling, the proposal probability of transitions from and into worm space carries a factor of η to balance sampling as different average weights might otherwise lead to unbalanced sampling and increase the statistical error, but the G estimator effectively just "counts" worm configurations grouped by distance in τ . In partition function sampling, the Markov chain does not visit G configurations, but for every Z configuration the G estimator collects contributions from all G configurations reachable by "cutting a hybridization line", which are those at the ends of the dashed lines, weighted by the ratio of bath weights, where $\det(\Delta^{(i_2, j_1)})$ is the determinant of the hybridization matrix with row i_2 and column j_1 removed. Inspired by Fig. 1 of Ref. [74].

tributions in some way and take the different weights into account. The difference in sampling and estimators is symbolically represented in Fig. 2.1. In the standard procedure [34, 36, 71, 72], contributions from all Green's function configurations that can be generated from the current partition function configuration by selecting a pair of a creator and an annihilator and disassociating them from hybridization with the bath are collected. Except for unusual models [102], every Green's functions configuration can be reached, as the associated partition function configuration differs from it only by having a hybridization matrix with one row and column more. Rather than just counting it, we also need to take the weight ratio of the Green's function configuration and the actually sampled partition function configuration into account. Since the local weight does not change, this is just the ratio $\det(\Delta^{(i_2, j_1)}) / \det(\Delta)$ of the two hybridization matrices where $\Delta^{(i_2, j_1)}$ denotes the hybridization matrix obtained by removing the column j_1 associated with the annihilator of flavor γ_1 at time $\tau_{o,1}$ and the row i_2 associated with the creator of flavor γ_2 at time $\tau_{o,2}$. This ratio is equal to the element $(\Delta^{-1})_{i_2 j_1}$ of the inverse of the hybridization matrix [36, 91, 107, 108], resulting in the expression

$$G_{\gamma_1 \gamma_2}(\tau) = -\frac{1}{\beta} \left\langle \sum_{i,j=1}^k (\Delta^{-1})_{ij} \delta(\tau, \tau'_j - \tau_i) \delta_{\gamma_1 \beta_j} \delta_{\gamma_2 \alpha_i} \right\rangle_{\text{MC}}, \quad (2.25)$$

with further processing the same as for the worm estimator.

Substituting the inverse hybridization matrix elements for the ratio of determinants differing by single rows and columns, many of which are used not only for the Green's function estimator but also to calculate the bath part of the weight ratio p_x/p_y entering the acceptance probability (2.21) for pair insertions and removals, actually comes with a performance advantage. Using the Sherman-Morrison formula [109], a special case of the Woodbury identity [110, 111], the change of the inverse of a matrix due to a change of one row and column of the matrix can be calculated with complexity $O(k^2)$, while the direct calculation of a determinant or inverse is asymptotically slower with $O(k^3)$ [36]. Since the calculation of such determinant ratios is such a central part of the continuous-time quantum Monte Carlo algorithms [36] and it is only those ratios we need, keeping the inverse hybridization matrix in memory and updating it is the primary way in which these values are calculated, although e.g. global moves may necessitate full recomputation.

Details of the local trace calculation

With this algorithm providing the bath weight ratios and the known proposal ratios as given in Tab. 2.1, we further only require the calculation of ratios of traces w_{loc} of products of impurity creators, annihilators, and time evolution. A numerical evaluation is obviously possible using matrices in a basis of many-body occupation number states, but given that this part of the calculation effectively corresponds to an exact diagonalization of the local part of the impurity problem and therefore scales exponentially with the number of orbitals, it is usually the computationally most expensive part of a CT-HYB calculation [36, 71, 72] and should accordingly be optimized. If the interaction involves only terms of density-density form, the sampling and trace calculation can be performed very efficiently using a "segment" representation [34, 71], though this is not necessarily faster than an optimized general implementation [91] and we will not consider it here.

A considerable optimization is possible by reducing the size of the matrices that need to be considered at a time, i.e. splitting an operation on large matrices into multiple operations on smaller matrices, since the computational effort of the matrix product scales with the third power of the matrix dimension [36]. This can be achieved by block-diagonalizing the Hamiltonian employing either conserved quantum numbers [72, 112], since blocks with different values of them are by definition not mixed by time evolution and that is the exponential of the Hamiltonian, or an automatic partitioning algorithm [93, 113, 114]. Depending on the exact form of the Hamiltonian useful quantum numbers [72] may be the total occupation N , the spin z -component S_z (w. l.

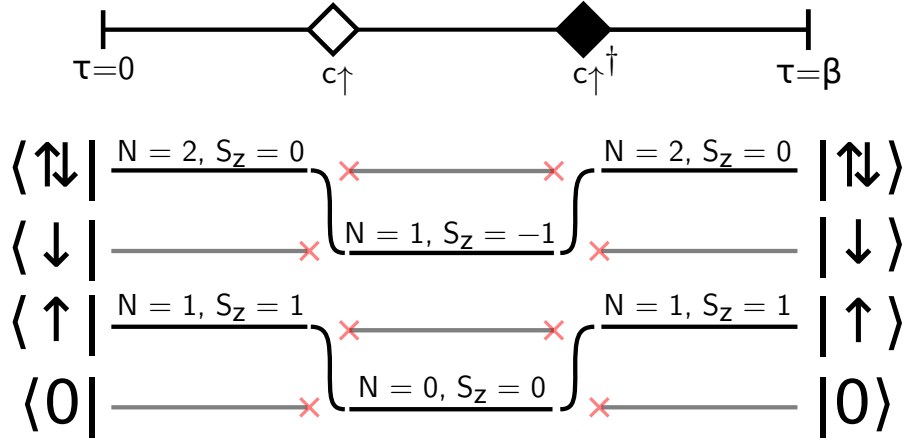


Figure 2.2: The “switchboard” picture illustrates how block-diagonalizing the Hamiltonian using superstates found by employing quantum numbers or automatic partitioning reduces the dimensions of the involved matrices and allows quick checks to be performed. Below the symbolic representation of the configuration we can see how the states at the ends, which are all put into different superstates according to occupation N and spin S_z , are mapped to other superstates by the application of operators along the imaginary time axis. At the red crosses, application of the operator results in zero, which happens to two of our superstates when we try to remove an up-spin electron that is not there and means that no explicit calculation is necessary in those cases. Inspired by Fig. 2.5 of Ref. [91]

o. g.), the occupation n_α per flavor α for density-density interaction, or the pattern of singly occupied orbitals for an interaction of Kanamori form [115]. We further require the blocks that block-diagonalize the Hamiltonian to be chosen such that a creator or annihilator connects each block with at most one other one and merge blocks that do not fulfill this condition [93, 114], obtaining the “superstates” of Ref. [72]. Otherwise, we would not be able to perform all matrix products using just one block of each matrix, but might have a situation where a state from one block is taken to two different ones along the trace, complicating the implementation [114].

Considering the concrete evaluation of the local weight as found in (2.15),

$$\begin{aligned}
 w_{\text{loc}} &= \text{Tr}(\hat{\mathcal{L}}) & \text{with } \hat{\mathcal{L}} &= T_\tau e^{-\beta H_{\text{loc}}} \prod_{i=1}^k c_{\beta_i}(\tau'_i) c_{\alpha_i}^\dagger(\tau_i) \\
 &= \sum_s \langle s | \hat{\mathcal{L}} | s \rangle \\
 &= \sum_{\mathcal{S}} \sum_{s \in \mathcal{S}} \langle s | \hat{\mathcal{L}} | s \rangle, \tag{2.26}
 \end{aligned}$$

where \mathcal{S} runs over all superstates and s in the second line runs over all many-body

basis states, breaking up the sum into a sum over superstates not only allows us to use matrices of reduced size to calculate $\hat{\mathcal{L}}$, but also allows us to perform a quick check first to see whether the calculation is even necessary in the first place [72]. The application of a creator or annihilator to a state in one specific superstate may not only take it to one specific other superstate, but also result in zero, e.g. when an annihilator is applied to a state with $N = 0$. With block connections for each operator stored, we can see whether a state in \mathcal{S}_i ends up back in \mathcal{S}_i after applying all the operators in $\hat{\mathcal{L}}$ without actually performing the matrix product, which is faster but can still tell us that the contribution of a superstate to the trace is zero if an operator application results in zero along the way or the state ends up in a different superstate \mathcal{S}_j at the end. A simple switchboard-like diagram can illustrate the principle of this “quantum number checking” [91]: In Fig. 2.2, we split the four-dimensional space of possible states for one orbital into four one-dimensional superstates using the quantum numbers N and S_z , turning a product of 4×4 matrices into four products of scalars, two of which we do not even need to perform if we follow the connections mediated by the operators, where red crosses mean that the application results in zero.

Sliding window sampling [73] further allows us to skip both calculation and quantum number checking in large parts of imaginary time if β is large by limiting the positions where pair insertions and removals can be done to a small window that only slowly moves from $\tau = 0$ to $\tau = \beta$. Since *w2dynamics* is a “matrix-vector” [36, 91, 116] implementation, calculating the trace contributions by taking each state s in (2.26) and applying the matrices to it rather than multiplying the matrices themselves, we can start calculations from both $\tau = 0$ and $\tau = \beta$ [72] and perform the scalar product somewhere in between. If we cache the states resulting from operator applications along the way, the window will ensure that most of the time, cached states outside of the window stay usable [73] and only a part of the trace inside the window needs to be recalculated. On the other hand, storing intermediate matrix products in a tree [50] or skip list [103], which cuts the number of products that need to be performed on an update from linear in the expansion order down to the logarithm of the expansion order, is not possible with a matrix-vector implementation.

Concluding the discussion of the trace calculation, let us also note that we compute time evolution and operator products in the eigenbasis of the Hamiltonian, which makes time evolution diagonal and creator and annihilator matrices dense. There are faster options for the trace calculation for large numbers of orbitals [73, 116] that we do not currently employ, as well as other optimizations of it like lazy trace calculation [103], which we do not implement either, but assume to be partially redundant with our state and superstate sampling technique [117] discussed in Sec. 3.1.

2.3 Dynamical mean-field theory

Apart from magnetic impurities, the other physical system we consider in this thesis is the multi-orbital Hubbard model, a model for narrow electron bands in a lattice, such as those arising from the d - and f -orbitals of transition metals in particular [31, 41, 118, 119]. The model describes electrons in a lattice that are able to hop between sites, but that are subject to strong correlations and thus not adequately described by an approximation in terms of independent electrons [23, 120]. Its Hamiltonian is of the form [20, 119]

$$H = - \sum_{\langle i,j \rangle, m, \sigma} t_{ij}^m c_{im\sigma}^\dagger c_{jm\sigma} + \sum_{i\alpha\beta\gamma\delta} \frac{U_{\alpha\beta\gamma\delta}}{2} c_{i\alpha}^\dagger c_{i\beta}^\dagger c_{i\delta} c_{i\gamma} \quad (2.27)$$

with site index i , site index j of nearest neighbors of site i , orbital index m , spin index σ , and combined orbital and spin indices α, β, γ , and δ , where t_{ij}^m is the hopping matrix between sites and $U_{\alpha\beta\gamma\delta}$ a matrix describing electron interactions on a site of a form that we leave unspecified for now for simplicity.

In the limit $U \rightarrow 0$, only the hopping term survives and we have a tight-binding Hamiltonian resulting in a dispersion relation $\varepsilon(\mathbf{k})$ consisting of sums of cosines [121, 122]. It is in particular metallic at half-filling, where the Fermi level lies in the middle of a band and excitations of infinitesimal energy are possible. Considering the “opposite” limit $t \rightarrow 0$, we are left with the interaction only. With a simple density-density interaction $\sum_{im} U n_{im\uparrow} n_{im\downarrow}$ [31] the ground state has one electron on each site at half-filling and the lowest excited state has one double occupation of a site costing a finite energy of U , so the system is insulating.

For intermediate t/U , where neither of the terms may be disregarded, an exact solution is not possible in general and only the development of the dynamical mean-field theory (DMFT) method, also known as local impurity self-consistent approximation (LISA), made it possible to capture the behavior of a lattice model while treating both of these terms on an equal footing [33]. The development of this method was preceded by the discovery that an infinite-dimensional limit of the Hubbard model exists that describes a non-trivial system of correlated electrons, which retains the competition between hopping and on-site interaction but admits a drastically simplified diagrammatic treatment due to the suppression of non-local contributions to the self-energy [33, 122–125]. Considerable interest into investigations of infinite-dimensional fermionic lattices was raised by these results, leading first to the solution of the simpler Falicov-Kimball model [126] by mapping to an atomic model in a time-dependent field [127–129], which is equivalent to a kind of mean-field solution that becomes exact in infinite dimensions [130, 131]. Subsequently, a mean-field approximation of the Hubbard

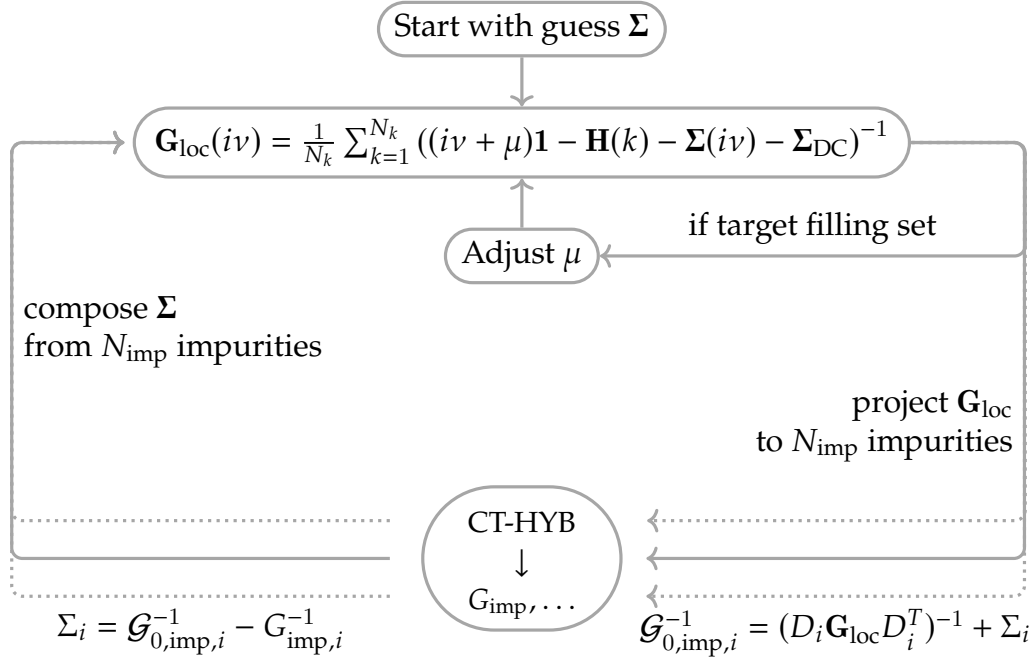


Figure 2.3: DMFT cycle implemented by *w2dynamics* in its general form: At the start, we guess a trial self-energy Σ , e.g. 0 or the Hartree self-energy. Using the self-energy, we calculate the local lattice Green’s function. If a target filling is set, we try to use that chemical potential in the expression for the local lattice Green’s function that allows us to achieve that filling. For each of the N_{imp} impurities, we project the local lattice Green’s function onto the space of the interacting orbitals assigned to the impurity, obtain the non-interacting impurity Green’s function through Dyson’s equation, run the CT-HYB impurity solver to obtain the full impurity Green’s function and calculate the new impurity self-energy using Dyson’s equation. We compose all impurity self-energies into the new lattice self-energy, using zero or the Hartree self-energy for “non-interacting” orbitals, and repeat the process by using the mixed new self-energy to calculate the new local Green’s function.

model that becomes exact in infinite dimensions¹ was shown to be based on the solution of an auxiliary Anderson impurity model [70, 132, 133] with Georges and Kotliar formulating the self-consistency equations of DMFT in Ref. [70]. While the solution of the Hubbard model by means of the DMFT self-consistency equations treats non-local correlations on a mean-field level and is thus only an approximation for finite-dimensional systems, it treats all local correlations exactly and non-perturbatively.

DMFT has e.g. been used to quantitatively study the Hubbard model in infinite dimensions [33, 134–138] and in particular to demonstrate the existence of a Mott transition [21] in the infinite-dimensional case [33, 135, 139]. Apart from such analyses of

¹as opposed to the Hartree-Fock mean-field theory, which does not become exact even in the limit of infinite dimensions

model Hamiltonians, DMFT has however also been used as an approximation for the finite-dimensional case with considerable success, e.g. in combination with Hamiltonians derived from density functional theory (DFT) [6, 15, 16] in suitable localized bases [140] as a method for first-principles (“ab initio”) electronic structure calculations for strongly correlated materials [19, 59, 65, 141–144].

For our DMFT calculations, we employ the very comprehensive numerical implementation in *w2dynamics* [40], which includes a CT-HYB solver for the impurity model. The full self-consistency equations [40, 59] applied in the iteration process we discuss in the next paragraph are

$$\mathbf{G}_{\text{loc}}(i\nu) = \frac{1}{N_k} \sum_{j=1}^{N_k} \mathbf{G}_{\text{latt}}(\mathbf{k}_j, i\nu) = \frac{1}{N_k} \sum_{j=1}^{N_k} ((i\nu + \mu)\mathbf{1} - \mathbf{H}(\mathbf{k}_j) - \boldsymbol{\Sigma}(i\nu) - \boldsymbol{\Sigma}_{\text{DC}})^{-1} \quad (2.28a)$$

$$\mathcal{G}_{0,\text{imp},i}(i\nu) = \left(D_i \mathbf{G}_{\text{loc}}(i\nu) D_i^T \right)^{-1} + \boldsymbol{\Sigma}_i(i\nu) \quad (2.28b)$$

$$\boldsymbol{\Sigma}(i\nu) = \sum_{i=1}^{N_{\text{imp}}} \left(D_i^T \underbrace{\left(\mathcal{G}_{0,\text{imp},i}^{-1}(i\nu) - \mathbf{G}_{\text{imp},i}^{-1}(i\nu) \right)}_{=\boldsymbol{\Sigma}_i(i\nu)} D_i \right), \quad (2.28c)$$

where \mathbf{G}_{loc} is the full local lattice Green’s function, \mathbf{G}_{latt} the full momentum-dependent lattice Green’s function, \mathbf{k} a lattice momentum argument, $i\nu$ a fermionic Matsubara frequency argument, N_k the number of points in momentum space, μ the chemical potential, $\mathbf{H}(\mathbf{k})$ the quadratic part of the lattice Hamiltonian in momentum space, $\boldsymbol{\Sigma}$ the full self-energy of the lattice, which is local in DMFT, $\boldsymbol{\Sigma}_{\text{DC}}$ the double-counting correction, N_{imp} the number of impurities, $\mathcal{G}_{0,\text{imp},i}$ the non-interacting Green’s function of the AIM for impurity i (also called “Weiss function” as dynamical analogon of the Weiss mean field), $\mathbf{G}_{0,\text{imp},i}$ the full Green’s function of the AIM with interaction for impurity i obtained from the impurity solver separately for each impurity, $\boldsymbol{\Sigma}_i$ the self-energy of the AIM for impurity i , and D_i the $N_{\text{orb},\text{imp},i} \times N_{\text{orb},\text{total}}$ matrix that projects from the local Green’s function in the basis of all $N_{\text{orb},\text{total}}$ orbitals to the $N_{\text{orb},\text{imp},i}$ interacting orbitals belonging to impurity i , used together with its transpose D_i^T to take the block for impurity i out of the full \mathbf{G}_{loc} in (2.28b) and put the self-energy block $\boldsymbol{\Sigma}_i(i\nu)$ in the space of interacting orbitals of impurity i at its right place in an otherwise empty self-energy matrix $D_i^T \boldsymbol{\Sigma}_i D_i$ in the space of all orbitals in (2.28c). This admits e.g. the inclusion of multiple impurities, “non-interacting” orbitals², and a double-counting correction.

²in the sense that they are not treated by the CT-HYB impurity solver and therefore assigned a simpler self-energy of either zero or their Hartree self-energy, but if the quadratic Hamiltonian originates from DFT, it partially incorporates the interaction of these orbitals

Let us summarize the calculation cycle performed by the implementation to reach the self-consistent solution of (2.28), which is depicted in Fig. 2.3 and described in Ref. [40]. We start by initializing the self-energy with zero, the Hartree self-energy, or a self-energy from a similar previous calculation. Using the initial self-energy or in subsequent iterations one mixed from the results of the preceding iterations, cf. Ref. [145], we calculate the local Green's function of the lattice. For a Hamiltonian given in momentum space, e.g. one obtained from a DFT calculation, this is done by summing the momentum-dependent lattice Green's function over all momenta in the Brillouin zone, but for e.g. the Bethe lattice in the limit of infinite coordination, an analytic formula exists. If we want to target a specific total filling n rather than set a fixed chemical potential μ , we determine our best estimate of μ to reach that filling. This is usually done by numerically solving the filling $n = \beta^{-1} \sum_m e^{-i\nu_m 0^-} \text{Tr}(\mathbf{G}_{\text{loc}}(i\nu_m))$ evaluated as the sum over fermionic Matsubara frequencies ν_m of the trace of the local Green's function for μ , which occurs in $\mathbf{G}_{\text{loc}}(i\nu)$. Alternatively, the root solver based on Broyden's method potentially used for mixing self-energies by solving the DMFT fixed-point problem [145] can additionally simultaneously solve for the value of μ necessary to get a difference of zero between target filling and actual filling using values of μ and n from preceding iterations [146]. Next, for each of the N_{imp} impurities we consider, we project the full local Green's function to the subset of that impurities' interacting orbitals. We can solve the impurity Dyson equation for the non-interacting Green's function of the auxiliary AIM, i.e. the mean field, in terms of the projection of the local Green's function and the self-energy, which is local in DMFT. In the form of the corresponding hybridization function and local levels, the mean field enters into a CT-HYB calculation for the impurity together with the local interaction. From the resulting full Green's function of the impurity, we can calculate the impurity self-energy using the impurity Dyson equation again. The self-energies obtained in this way for each impurity in the basis of the interacting orbitals of that impurity are composed into a total self-energy in the basis of all orbitals, which is then used as the self-energy of the lattice in the next iteration for the calculation of the local lattice Green's function, closing the cycle. The approximation of DMFT in finite dimensions consists in using the local self-energy as self-energy of the lattice, while the true self-energy of the lattice would depend on momentum in finite dimensions.

2.4 Interpretation of Green's functions

In Sec. 2.1, we mentioned that when we "solve" the Anderson impurity model, it is particularly the computation of the one-particle Green's function (2.12) that we are interested in and in DMFT we may equivalently be particularly interested in the momentum-

dependent lattice Green's function or the local Green's function as found in (2.28a). In addition to giving access to all single-particle observables such as occupations (since the corresponding single-particle operators are bilinear in creators and annihilators), the full single-particle Green's function also contains information about the ground-state energy, cf. Ref. [147] or Ref. [148] and appendix B, and importantly the spectrum of single-particle excitations as well, cf. Refs. [148, 149] and textbooks such as Refs. [43, 46, 47, 147, 150].

In order to see how, let us follow Ref. [47] in considering a retarded fermionic Green's function on the real time and frequency axis defined as

$$G_{\alpha}^R(t) = -i\theta(t) \langle \{c_{\alpha}(t), c_{\alpha}^{\dagger}(0)\} \rangle, \quad (2.29)$$

where $\{A, B\} = AB + BA$ is the anticommutator and $\theta(t)$ the Heaviside step function, which is one for $t > 0$ and zero for $t < 0$. By inserting representations of unity $\sum_n |n\rangle\langle n|$, where n runs over all eigenstates $|n\rangle$ with eigenenergies E_n of the full interacting Hamiltonian H invariant under translations in time, the thermal expectation value $\langle A \rangle = Z^{-1} \text{Tr}(e^{-\beta H} A)$ with inverse temperature β and partition function $Z = \text{Tr}(e^{-\beta H})$ in (2.29) can be evaluated to obtain the spectral or Lehmann [149] representation of the Green's function

$$G_{\alpha}^R(t) = -i\theta(t)Z^{-1} \sum_{nm} e^{-\beta E_n} \left(\langle n|c_{\alpha}|m\rangle\langle m|c_{\alpha}^{\dagger}|n\rangle e^{i(E_n-E_m)t} + \langle n|c_{\alpha}^{\dagger}|m\rangle\langle m|c_{\alpha}|n\rangle e^{-i(E_n-E_m)t} \right). \quad (2.30)$$

By Fourier transforming this to real frequencies $\omega + i\eta$ with an infinitesimal factor $\eta \rightarrow 0^+$, which is necessary to ensure convergence of the integral because the retarded Green's function does in general not decay to zero at large times, we obtain

$$\begin{aligned} G_{\alpha}^R(\omega) &= \int_0^{+\infty} \exp(i(\omega + i\eta)t) G_{\alpha}^R(t) dt \\ &= Z^{-1} \sum_{nm} e^{-\beta E_n} \left(\frac{\langle n|c_{\alpha}|m\rangle\langle m|c_{\alpha}^{\dagger}|n\rangle}{\omega + E_n - E_m + i\eta} + \frac{\langle n|c_{\alpha}^{\dagger}|m\rangle\langle m|c_{\alpha}|n\rangle}{\omega - E_n + E_m + i\eta} \right) \\ &= Z^{-1} \sum_{nm} \frac{\langle n|c_{\alpha}|m\rangle\langle m|c_{\alpha}^{\dagger}|n\rangle}{\omega + E_n - E_m + i\eta} \left(e^{-\beta E_n} + e^{-\beta E_m} \right). \end{aligned} \quad (2.31)$$

This expression shows that the retarded Green's function has a pole infinitesimally below each real frequency ω equal to the energy difference between a many-body state $|n\rangle$ and another many-body state $|m\rangle$ with exactly one particle more [43]. These frequencies therefore correspond to the excitation energies of the system [147]. Using the

identity

$$\lim_{\eta \rightarrow 0^+} \frac{1}{\omega \pm i\eta} = \mathcal{P} \frac{1}{\omega} \mp i\pi\delta(\omega) \quad (2.32)$$

(also known as Sokhotski-Plemelj theorem [151] and related to the Kramers-Kronig relations and the Hilbert transform) that holds in a distributional sense [47, 147, 148], where $\delta(\omega)$ is the Dirac delta distribution and integrals of the \mathcal{P} -term are to be evaluated in terms of their Cauchy principal value, we can define and evaluate the spectral function

$$\begin{aligned} A_\alpha(\omega) &:= -\frac{1}{\pi} \text{Im}(G_\alpha^R(\omega)) \\ &= Z^{-1} \sum_{nm} \langle n|c_\alpha|m\rangle \langle m|c_\alpha^\dagger|n\rangle \left(e^{-\beta E_n} + e^{-\beta E_m} \right) \delta(\omega + E_n - E_m), \end{aligned} \quad (2.33)$$

which consists of delta contributions at the excitation energies of the system. For this reason the spectral function can be seen as the extension of the density of states to interacting systems [47]. For a *non-interacting* system, it can easily be seen that the two functions coincide. The local Green's function of a lattice system without interaction with a density of states $D(\varepsilon) = \sum_{\mathbf{k}} \delta(\varepsilon - \varepsilon_{\mathbf{k}})$, where $\varepsilon_{\mathbf{k}}$ is the dispersion, can be calculated as Hilbert transform of the density of states $G^R(\omega) = \int_{-\infty}^{+\infty} \frac{D(\varepsilon)}{\omega - \varepsilon + i\eta} d\varepsilon$, cf. Ref. [33]. Taking the imaginary part to get the spectral function returns exactly the density of states as inserting (2.32) shows explicitly. This follows since for a function analytic on the upper complex half-plane, the Hilbert transform takes real and imaginary parts evaluated for arguments slightly above the real axis into each other.

If we integrate the spectral function $A_\alpha(\omega)$ as defined in (2.33) over the entire real frequency axis, $\int_{-\infty}^{+\infty} A_\alpha(\omega) d\omega$, we are left with the sum in (2.33) without delta distribution factors in its terms. By reidentifying this sum as thermal expectation value $\langle \{c_\alpha, c_\alpha^\dagger\} \rangle$, which is exactly one due to the fermionic anticommutation relations, we obtain the sum rule

$$\int_{-\infty}^{+\infty} A_\alpha(\omega) d\omega = 1 \quad (2.34)$$

for the spectral function [47].

Due to the addition of interactions to a non-interacting problem, the Green's function changes in a way that is entirely captured by the self-energy Σ as given for a local problem in (2.13), which is the Dyson equation solved for the self-energy. For a lattice problem, the Green's functions and self-energies in (2.13) should additionally be evaluated at the same momentum, which they take as additional argument in that context. Let us consider how the low-energy effect of interactions can be characterized by closely following a derivation detailed in Ref. [47], cf. also Refs. [147, 152]. We start with the general form of the retarded Green's function for a lattice system on the real

axis

$$G_\alpha^R(\mathbf{k}, \omega) = \left(\omega - \varepsilon_{\mathbf{k}} - \Sigma_\alpha^R(\mathbf{k}, \omega) \right)^{-1}, \quad (2.35)$$

where $\varepsilon_{\mathbf{k}} = \frac{\mathbf{k}^2}{2m} - \mu$ is the energy of free electrons with momentum \mathbf{k} and (free) electron mass m relative to the Fermi level or chemical potential μ and $\Sigma_\alpha^R(\mathbf{k}, \omega)$ the retarded self-energy on the real frequency axis. For the low-energy behavior of a system, which includes in particular the existence or absence of excitations at arbitrarily low energy that makes the system conducting or insulating, it is primarily wave vectors at the edge of the Fermi sea that interest us, as states sufficiently far away from it are essentially always full or empty. Therefore, we expand most of the inverse of the full Green's function only up to first order in ω and $k - \tilde{k}_F$ (neglecting the possibility of anisotropy) where \tilde{k}_F corresponds to the Fermi wave vector or radius of the Fermi surface after the introduction of interactions given by the implicit equation $\varepsilon_{\tilde{k}_F} + \text{Re}(\Sigma_\alpha^R(\tilde{k}_F, \omega = 0)) = 0$. Going beyond the zeroth order for the imaginary part of the self-energy is not necessary for this consideration, so we do not do that but separate the real and imaginary part of the self-energy to get the expression

$$G_\alpha^R(\mathbf{k}, \omega) = \left(\omega - \left(\varepsilon_{\mathbf{k}} + \text{Re}(\Sigma_\alpha^R(\mathbf{k}, \omega)) \right) - i \text{Im}(\Sigma_\alpha^R(\mathbf{k}, \omega)) \right)^{-1} \quad (2.36)$$

in which we expand the first two terms and just take the contribution of order zero in the last one. This results in

$$\begin{aligned} G_\alpha^R(\mathbf{k}, \omega) = & \left(\omega - \omega \partial_\omega \text{Re}(\Sigma_\alpha^R(\tilde{k}_F, \omega)) \right) \\ & - \left(k - \tilde{k}_F \right) \partial_k \left(\varepsilon_{\mathbf{k}} + \text{Re}(\Sigma_\alpha^R(\mathbf{k}, 0)) \right) \\ & - i \text{Im}(\Sigma_\alpha^R(\tilde{k}_F, \omega = 0)) \right)^{-1}, \end{aligned} \quad (2.37)$$

where the first two terms are of first order in ω , the second term is of first order in $k - \tilde{k}_F$, and the last term is the only one of order zero due to the definition of \tilde{k}_F . We clearly bring out the ω -dependence equal to that of the free Green's function by factoring out the *quasiparticle weight* (not to be confused with the partition function)

$$Z_\alpha := \left(1 - \partial_\omega \text{Re}(\Sigma_\alpha(\tilde{k}_F, \omega)) \Big|_{\omega=0} \right)^{-1} \quad (2.38)$$

to get

$$G_\alpha^R(\mathbf{k}, \omega) = Z_\alpha \left(\omega - \left(k - \tilde{k}_F \right) Z_\alpha \partial_k \left(\varepsilon_{\mathbf{k}} + \text{Re}(\Sigma_\alpha^R(\mathbf{k}, 0)) \right) - i Z_\alpha \text{Im}(\Sigma_\alpha^R(\tilde{k}_F, 0)) \right)^{-1}$$

$$= \frac{Z_\alpha}{\omega - \tilde{\varepsilon}_\alpha(k) + i\Gamma_\alpha} = \frac{Z_\alpha(\omega - \tilde{\varepsilon}_\alpha(k)) - iZ_\alpha\Gamma_\alpha}{(\omega - \tilde{\varepsilon}_\alpha(k))^2 + \Gamma_\alpha^2} \quad (2.39)$$

where we cast the second term in the form of a first-order approximation of the *free* dispersion around \tilde{k}_F but with an *effective* mass m_α^* collecting the remaining factors of the second term to result in the effective energy $\tilde{\varepsilon}_\alpha(k) := \frac{1}{m_\alpha^*}(k - \tilde{k}_F)\tilde{k}_F$ and identify the imaginary part of the self-energy as the inverse of the quasiparticle lifetime $\tilde{\tau}_\alpha(\mathbf{k}, \omega)$, the scattering rate Γ_α . Explicitly we define

$$\tilde{\varepsilon}_\alpha(k) := \frac{(k - \tilde{k}_F)\tilde{k}_F}{m_\alpha^*}, \quad (2.40)$$

$$m_\alpha^* := \frac{m}{Z_\alpha} \left(1 + \frac{m}{\tilde{k}_F} \partial_k \text{Re} \left(\Sigma_\alpha^R(k, 0) \right) \Big|_{k=\tilde{k}_F} \right)^{-1}, \quad (2.41)$$

$$\Gamma_\alpha := -Z_\alpha \text{Im} \left(\Sigma_\alpha^R(\tilde{k}_F, 0) \right), \quad (2.42)$$

where the first term in the parenthesis in the definition of the effective mass originates from the derivative of $\varepsilon_{\mathbf{k}}$ and we should note that the value of Γ_α with this explicit sign is positive such that the pole of the retarded Green's function (2.39) correctly lies in the lower complex half-plane. The connection between Γ_α and a lifetime can be recognized by considering how it changes the time-dependent retarded Green's function (2.30). Since it appears in the same position as the infinitesimal factor η introduced in (2.31) to make the integral converge, we can infer that it represents an additional factor $e^{-\Gamma_\alpha t}$ in the time-dependent retarded Green's function $G_\alpha^R(t)$ and causes it to decay exponentially for large times [148] in contrast to the Green's function of a free particle.

From (2.39), the spectral function

$$A_\alpha(\mathbf{k}, \omega) = \frac{Z_\alpha\Gamma_\alpha}{(\omega - \tilde{\varepsilon}_\alpha(k))^2 + \Gamma_\alpha^2} \quad (2.43)$$

follows. In contrast to the non-interacting spectral function we have seen before, it does not consist of delta peaks any more, but of Lorentzian distribution functions centered around the effective energies $\tilde{\varepsilon}_\alpha(k)$. This results from the presence of a non-infinitesimal Γ_α that shifts the poles significantly away from the real axis. Another change in the interacting case can be seen if we assume for a moment that Γ_α is infinitesimal, which would give the spectral function

$$A_\alpha(\mathbf{k}, \omega) = Z_\alpha \delta(\omega - \tilde{\varepsilon}_\alpha(k)) \quad (2.44)$$

instead [47]. Due to the presence of the quasiparticle weight Z_α with a value between zero and one this spectral function does not fulfill the sum rule (2.34) and we must

assume that apart from this peaked and therefore particle-like *quasiparticle* contribution a total spectral weight of $(1 - Z)$ originates from some incoherent, not quasiparticle-like contribution.

Low-energy excitations in metallic systems of interacting electrons can often be satisfactorily represented by effectively free renormalized quasiparticles [47, 150, 153, 154], whose physical behavior can be described by the Fermi liquid theory developed by Landau and others [154–158]. This theory applies when a perturbative description of electronic interaction is possible, but this is not a necessary condition. In particular, it also applies to the non-perturbative low-temperature behavior of the Kondo problem [159], although not necessarily in the multi-orbital case [160–162]. Therefore, the Anderson impurity models considered in this thesis, including the auxiliary models describing metallic solutions of DMFT, usually exhibit Fermi-liquid-like low-temperature behavior. In the low-energy and low-temperature case, the imaginary part of the retarded self-energy of a Fermi liquid near the Fermi level scales as $\text{Im}(\Sigma^R(\omega, T)) \propto \omega^2 + \pi^2 T^2$ [47, 163, 164], i.e. the scattering rate goes quadratically to zero and the quasiparticle lifetime diverges.

In quantum Monte Carlo calculations, we obtain time-ordered Matsubara Green's functions $G_\alpha(i\omega_n)$ rather than the retarded Green's functions on the real frequency axis $G_\alpha^R(\omega)$ we have considered in this section so far. Some properties characterizing an interacting system can still be obtained relatively easily, the quasiparticle weight (2.38) for example can be written as the derivative

$$Z_\alpha = (1 - \partial_\omega \text{Im}(\Sigma_\alpha(i\omega))|_{\omega=0})^{-1} \quad (2.45)$$

of an imaginary frequency function by application of the Cauchy-Riemann equations for derivatives of complex differentiable functions, although the accuracy with which we can compute this is limited by the discrete set of Matsubara frequencies depending on the temperature of the system. This factor limiting how close we can get to zero with positive fermionic Matsubara frequencies also means that our data does not “automatically” give us $\text{Im}(\Sigma_\alpha(i\omega = 0))$, which is together with the quasiparticle weight necessary for the computation of the scattering rate Γ_α . We can however extrapolate the imaginary part of the Matsubara self-energy from the lowest fermionic Matsubara frequencies to zero frequency to do that. While a value at zero Matsubara frequency does exist and is physically distinguished as static response for bosonic functions, for fermionic functions this is not the case and so this extrapolation to zero can be done without issue.

Behavior of the Green's or spectral function on the real frequency axis off zero frequency can be determined from the Matsubara frequency data using analytic continu-

ation. While quite accurate results are possible for sufficiently precise Matsubara frequency data [165, 166], the problem of analytically continuing Green's functions is in general ill conditioned [167, 168] because the integral kernel $K(\tau, \omega) = e^{-\tau\omega}/(1 + e^{-\beta\omega})$ for the expression $G(\tau) = \int_{-\infty}^{+\infty} K(\tau, \omega)A(\omega) d\omega$ of the imaginary-time Green's function in terms of the spectral function exponentially suppresses the influence of the spectral function at high frequencies. There are therefore many different spectral functions that would agree with the calculated imaginary-time Green's function within its statistical error, and additional criteria must be applied to select the best estimate [168].

A standard method currently used for analytic continuation of CT-QMC Green's functions [36] is the maximum entropy method (also MEM or MaxEnt) [168–171]. It replaces the normal objective function to be minimized for a least-squares fit, $\chi^2/2 = \sum_{j,k}(G_j - K_{jk}A_k)^2/(2\sigma_j^2)$ with discretized versions of the kernel K_{jk} , real-frequency spectrum A_k , imaginary-time Green's function G_j , and statistical Monte Carlo error σ_j of the Green's function in the case of diagonal covariance [168, 170], by the objective function $\chi^2/2 - \alpha S$ [168, 170]. Here, $S = -\int A(\omega) \log(A(\omega)/m(\omega))$ is the information entropy [172] of the spectrum A relative to a featureless default model m and α a hyperparameter to be set in an appropriate way [168, 170]. When we show real-frequency spectra obtained by analytical continuation, we use Bryan's method [173], which averages over α by its probability, as implemented in Ref. [174]. We also compared some of the results to continuations obtained with α selected at the crossover between the information- and noise-fitting regime [175] using the implementation described by Refs. [151, 176] and using the reference implementation of the SpM-Padé method [177, 178], a combination of the sparse modeling approach [179] with Padé approximants [180], without noticing qualitative differences from the original MaxEnt results in either case.

3 Algorithmic developments

3.1 Superstate and state sampling

In this section, we consider an optimization of the trace calculation that splits the entire calculation into parts that are sampled individually using the Monte Carlo method. The strong concentration of the local weight of the standard configurations onto few outer superstates and states allows us to sample according to the largest contributions while mostly avoiding to calculate the smaller ones at all. We describe the improved sampling procedure in detail, measure the performance improvements that we find to be particularly large in the case of many orbitals with general interactions like the full Coulomb interaction, and consider DMFT calculations for the bad metallic state in a degenerate three-orbital Hubbard model with Hund’s coupling as an example application.

The results presented in this section were previously partially covered in my Master’s thesis, Ref. [181], and the following published article, Ref. [117], which is also the source of the figures

*A. Kowalski, A. Hausoel, M. Wallerberger, P. Gunacker, and G. Sangiovanni,
“State and Superstate Sampling in Hybridization-Expansion Continuous-Time Quantum
Monte Carlo,”
Phys. Rev. B **99**, 155112 (2019)*

3.1.1 Local weight calculation

Let us take another look at one of the trace calculation optimizations we covered at the end of our introduction to CT-HYB presented in Sec. 2.2. In (2.26), we manipulate the trace of the impurity operator product $\hat{\mathcal{L}}$. The trace of a matrix is the sum of its diagonal elements, which we get by first multiplying it with the same basis state from the right and the left to take out one diagonal element and then summing over the outer basis states. This turns it into an explicit sum over all many-body basis states s , which can be grouped together into superstates \mathcal{S} , diagonal blocks of the Hamiltonian mapped to (at most) one other superstate each by the application of a creator or annihilator and thus the smallest “convenient” blocks into which the product of the original larger matrices

in the full many-body basis can be decomposed. If we insert that expression for w_{loc} back into the expression for the partition function (2.15), we get

$$\sum_{k=0}^{\infty} \int_{\tau_{i-1}}^{\beta} d\tau_i \int_{\tau'_{i-1}}^{\beta} d\tau'_i \sum_{\alpha_i, \beta_i} \sum_{\mathcal{S}} \sum_{s \in \mathcal{S}} \langle s | \hat{\mathcal{L}} | s \rangle \det(\Delta). \quad (3.1)$$

The integrals and sums here are partially performed stochastically using Monte Carlo integration, summing the significantly contributing parts with importance sampling, and partially by exact summation. We might wonder whether it is actually necessary to perform any of these summations exactly, or whether we can instead use importance sampling for all of them to gain performance benefits [91].

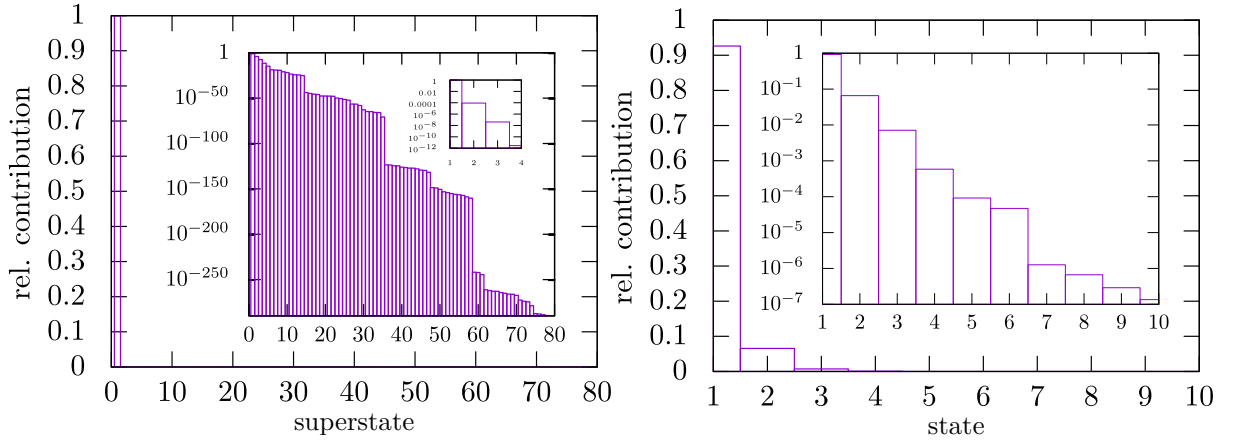


Figure 3.1: Left panel: Average relative contributions of outer superstates to the total local weight per configuration ordered by contribution per configuration. Since the order of contributions depends on the configuration, the superstate index on the x -axis does not refer to one specific *superstate*, but to one specific *position in the contribution list* per configuration. Right panel: Average relative contribution of outer states to the contribution of their outer superstate to the local weight of a configuration, ordered by the contribution. Obtained using the conventional sampling procedure for a five-orbital model (for Co/Cu(001), cf. Refs. [182, 183] and Sec. 4.1) with interaction of Kanamori form.

We found that this is in fact possible and can be used to accelerate the trace computation even further with usually at most minor deterioration of the mean sign and the autocorrelation time. This seems reasonable when we consider the relative average contributions per outer superstate and per individual outer state to the full local weight in the conventional CT-HYB sampling, shown in Fig. 3.1 for an exemplary five-orbital model (for a cobalt impurity on copper, Co/Cu(001), cf. Refs. [182, 183] and Sec. 4.1 for details) with a non-uniform interaction of Kanamori form¹ with average

¹obtained by removing elements not included in the Kanamori form from the full Coulomb interaction

intraorbital repulsion $U = 5.03$ eV, average Hund's coupling $J = 0.64$ eV, average interorbital repulsion $U' = U - 2J$, inverse temperature $\beta = 30$ eV⁻¹, a target filling of 8, and a hybridization function obtained from DFT. There is on average one superstate that contributes an overwhelming amount of the local weight per configuration and one outer state per superstate that is responsible for a still considerable majority of that contribution, and that already at a relatively high temperature. Heuristically, we can argue that as the inverse temperature β increases and the average expansion order with it [72], the higher number of operators and thus of occasions for sending a superstate to zero gradually reduces the number of outer superstates that “survive” quantum number checking until there is only one left at sufficiently low temperature. We therefore expect the small relative contributions to only shrink with decreasing temperature and the sum over all states to be better approximated by its largest contribution. If we manage to mostly sample “extended” configurations containing the outer superstate and outer state responsible for these largest contributions, the only significant change should be less computational effort because we can avoid the matrix products or at least quantum number checking for the other superstates and states. This should work particularly well at low temperatures, but the heuristic argument also implies that it will be mostly quantum checking that we avoid in that case rather than the usually much more calculation-intensive matrix products.

Depending on whether just the outer superstates or the individual outer states are summed stochastically, we call our technique superstate or resp. state sampling. In superstate sampling, the Monte Carlo configurations are extended by a stochastically sampled outer superstate \mathcal{S}_o to $\{\mathcal{S}_o, k, \alpha_i, \beta_i, \tau_i, \tau'_i\}_{i=1,\dots,k} \in \mathcal{C}_{\text{sst}}$, and the local weight of the configuration is just

$$w_{\text{loc,sst}} = \sum_{s \in \mathcal{S}_o} \langle s | \hat{\mathcal{L}} | s \rangle \quad (3.2)$$

instead of (2.26), while in state sampling we have configurations with an additional stochastically sampled outer state $s_o \in \mathcal{S}_o$, i.e. of the form $\{\mathcal{S}_o, s_o, k, \alpha_i, \beta_i, \tau_i, \tau'_i\}_{i=1,\dots,k} \in \mathcal{C}_{\text{st}}$, and the local weight

$$w_{\text{loc,st}} = \langle s_o | \hat{\mathcal{L}} | s_o \rangle. \quad (3.3)$$

3.1.2 CT-HYB updates

In order to sample the outer superstate and outer state ergodically, we need to change the usual CT-HYB updates, cf. Tab. 2.1, or add new ones. Let us first consider only the case of superstate sampling, as we modify all the updates for state sampling in the same simple way. Note also that we choose the initial outer superstate and state

tensor

randomly weighted by the full local time evolution from 0 to β , which avoids possibly long thermalization if we picked one of the many highly excited ones with local weight close to zero.

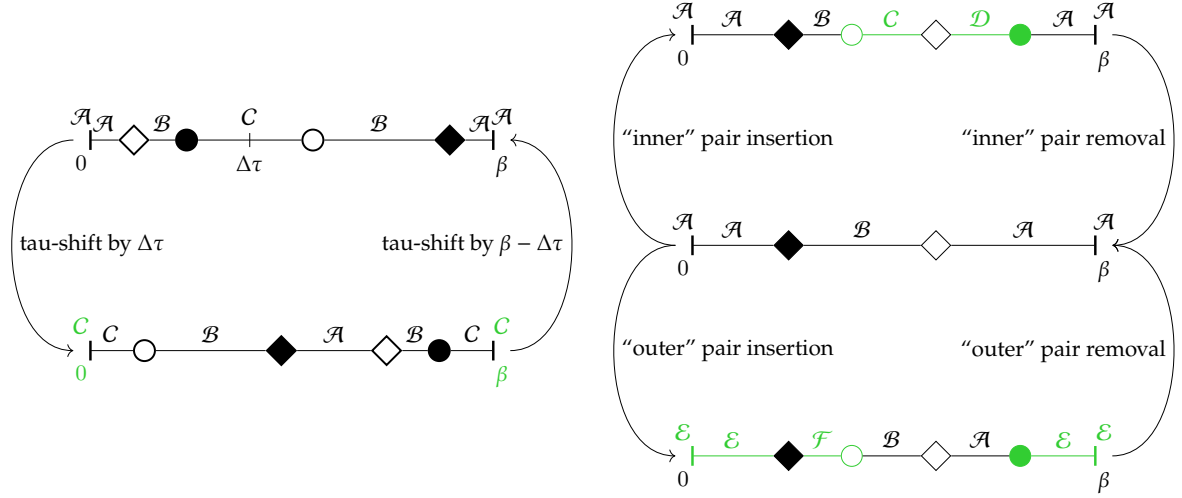


Figure 3.2: Symbolic representation of configurations connected by a global τ -shift move by a random distance $\Delta\tau$ (left panel) or by the two types of pair moves we define for use with superstate sampling (right panel). The outer superstate that is part of the configuration is indicated by the calligraphic letters at $\tau = 0$ and $\tau = \beta$, and the other calligraphic letters over segments of imaginary time indicate the superstate that the state at this time belongs to. This is not explicitly part of the configuration, but the superstate after application of any sequence of impurity operators follows directly from the outer superstate by the definition of superstates. Changed operators and the changed part of the “superstate sequence” are indicated in green; in the case of the τ -shift move, we do not consider the sequence as fundamentally changed as it is only cyclically shifted.

The primary method we use for changing the outer superstate is a new global τ -shift move that shifts all operators by one fixed uniformly random imaginary time distance $\Delta\tau$ along the imaginary time axis with periodic boundary conditions, i.e. with new times positive modulo β . Equivalently, we can consider this as a cyclical shift of the imaginary time axis itself. The outer superstate, which is part of the configuration, by the definition of superstates also uniquely determines the superstate at any point in imaginary time including at $\Delta\tau$, which is the one that we propose as outer superstate of the new configuration. If we only allow moves in one direction w. l. o. g. due to cyclicity, the reverse of a move by $\Delta\tau$ is another τ -shift move by $\beta - \Delta\tau$, which has the same proposal probability and so the proposal ratio is one. A symbolical representation is shown in the left panel of Fig. 3.2. In conventional sampling, such a move would change the local weight by at most a minus sign from time order since the trace is cyclical. In

fact, the same is also true in superstate sampling, and the total weight does not change at all in both techniques; the acceptance probability is therefore one.

Let's sketch the proof for the local weight. The local weight in superstate sampling has only one contribution to the trace, that of the outer superstate. We can also consider it as the trace with projection operators projecting to the outer superstate inserted as first and last operators. The projection operators commute with arbitrary time evolution operators because superstates are blocks that diagonalize the Hamiltonian. The other property of superstates, which is that creators and annihilators send states from one superstate to at most one specific other superstate, presents us with a way to exchange a projection operator with a creator or annihilator. If we do that, we just also need to change the target superstate of the projection operator to the one the original target superstate would get sent to by the creator or annihilator. The projection operators can thus be moved to an arbitrary point $\Delta\tau$ in imaginary time as long as we change them to project to the one unique superstate at that point compatible with the current outer superstate. Bringing the projection operators back to the ends by using the cyclicity of the trace shows that this is the local weight of the configuration after τ -shift by $\Delta\tau$ with the exception of possibly a minus sign due to time ordering, which we save for the bath weight.

Proceeding with the bath weight, let us note that equal time shifts applied to creator and annihilator times cancel. Due to periodic boundary conditions, one time may however be shifted by an additional amount of β , which results in a minus sign for all elements in one row or column of the hybridization matrix due to β -antiperiodicity of the hybridization function, giving one minus sign for its determinant per affected operator. The reordering of the hybridization matrix rows and columns into the time order of the corresponding annihilators and creators possibly also results in an additional minus sign in total. Careful accounting of the minus signs due to changes in the hybridization matrix and the one we might have kept from the time ordering of local operators would show that no total minus sign remains, which is explained in slightly more detail in an appendix of Ref. [117].

We may also wonder about the utility of the τ -shift move, since it basically only changes the outer superstate by moving a different point of time "outside" and does nothing else, which is also the reason for the acceptance probability of one. The former is however precisely what it is useful for, since we primarily propose pair insertions and removals highly local in time, which therefore at most change "inner" superstates. Combining them with the τ -shift move allows us to use them to change the superstate at any point in time, including the outer superstate.

This covers the only significant new move we introduce. In case the current expansion order is zero, which could occur often for certain choices of parameters, we do

not perform meaningless τ -shift moves but propose a transition to a randomly chosen outer superstate with normalized full local time evolution as proposal probability. Apart from these, all other moves are just extensions of the standard moves in Tab. 2.1 with regard to how the outer superstate of the proposed configuration is to be determined. For the global flavor permutation, we propose one of the outer superstates that pass quantum number checking with uniform proposal probability. In some cases, particularly ones close to the atomic limit, it might also be necessary to use such a choice with worm insertions and removals in order to avoid systematic errors in the worm estimators. For all other moves, we usually propose no change in the outer superstate, i.e. only the part of the superstate sequence between the changed operators can change (which might however be moved “outside” by some subsequent τ -shift move). Since insertion and removal moves are particularly likely to be accepted for short time distances of the involved operators [73], which cause a smaller change of the contributions to the full local trace than long time distances, the outer superstate with the largest contribution before the move will usually also be the one with the largest contribution after the move and our choice of usually not proposing a change should therefore be relatively efficient.

For pair moves, we also tried a different prescription, which fixes the part of the superstate sequence between the operators instead. By continuing the superstate sequence from there to the outside, we get a unique new outer superstate for the proposal. We call this an “outer” pair insertion or removal since it changes the outer part of the superstate sequence, in contrast to our preferred prescription to keep the old outer superstate and thus change the inner part of the superstate sequence, giving the corresponding “inner” moves. A symbolic representation of both types of moves is shown in Fig. 3.2, which also illustrates the difference as the depicted moves are equal in all other respects.

The same configuration transition caused by an outer move can also be realized through a combination of a τ -shift move, inner move, and another τ -shift move inverse to the first one. Since pair moves with short time distances are exponentially more likely to be accepted and actually the only ones proposed if sliding window sampling [73] is used, putting a window partially “around $\tau = 0$ and $\tau = \beta$ ” (covering time segments at both ends) would be important to get an acceptable acceptance probability for outer moves. This would complicate the implementation and not lead to any significant improvements as we have just seen that a simulation with inner moves and τ -shift moves can reach all the same configurations. We therefore do not use outer pair moves by default in *w2dynamics*, although they can be enabled using a configuration parameter by a user with the caveat that they will usually suffer from bad acceptance probabilities due to our implementation of window sampling. A proof sketch demon-

strating ergodicity when inner pair moves and either outer pair moves or τ -shift moves are available is given in an appendix of Ref. [117].

When we perform state sampling rather than superstate sampling, we additionally also need to consider how to select and change the outer state, the one specific state in the outer superstate that is used for the local weight calculation. Since even single outer states can turn into states with multiple nonzero components at some other point in imaginary time, there is no equivalent of the superstate sequence determined by the outer superstate for single states, and e.g. a τ -shift move can not really “naturally” pick any specific one of the states at the chosen $\Delta\tau$. We therefore use a simple procedure for the next proposed outer state: In all cases where we keep the outer superstate fixed, we keep the outer state fixed for the same reason that most moves are local and only change contributions slightly. In all other cases, we propose a random outer state. Since we have seen that even in a single superstate, the contribution to the local weight is usually dominated by a single state, proposing them uniformly would however be inefficient.

Our technique therefore uses a part of the local weight as proposal probability, specifically the part that is easiest to calculate: As we use a single eigenstate as outer state in state sampling, time evolution from $\tau = 0$ to the first operator and from $\tau = \beta$ to the last operator is just one exponential, and this is what we use as proposal probability. Whenever it is possible without disproportional increase of computational effort, this strategy of “moving” factors of the weight into the proposal probability can be helpful, as terms present in both the proposal probability and weight cancel in the Metropolis-Hastings acceptance probability (2.21). The concrete normalized proposal probability for the outer state s_o is

$$p^{\text{prop}}(s_o) = \frac{\exp(-(E_{s_o} - E_0) \cdot (\tau_f + \beta - \tau_l))}{\sum_{k \in \mathcal{T}} \exp(-(E_s - E_0) \cdot (\tau_f + \beta - \tau_l))}, \quad (3.4)$$

where E_{s_o} is its eigenenergy, E_0 that of the ground state, E_s that of state k which is summed over, τ_f the imaginary time variable of the first impurity operator, τ_l the imaginary time variable of the last impurity operator, and \mathcal{T} the set of all possible target outer states, i.e. all states from all possible target outer superstates.

3.1.3 Results and performance

With the description of superstate sampling and state sampling concluded, let us have a look at the performance improvements achieved by their use. For this purpose, we implement them in *w2dynamics* and compare with an older version that only implements the conventional sampling. The Co/Cu(001) five-orbital model (cf. Refs. [182, 183] and Sec. 4.1) we have previously considered serves as our example again, and this

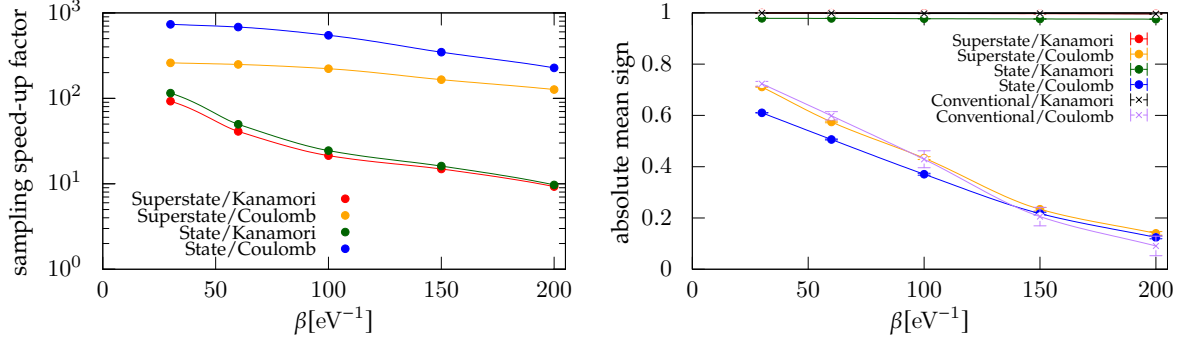


Figure 3.3: Left panel: Sampling speed-up due to superstate sampling or state sampling as a function of inverse temperature for the case of Coulomb interaction (larger superstates) and Kanamori interaction (smaller superstates). Right panel: Mean sign as a function of the inverse temperature for conventional, superstate and state sampling for both Coulomb interaction, which suffers from the sign problem, and Kanamori interaction, for which usually no noticeable deterioration of the sign with decreasing temperature can be observed. Curves in both panels are monotonicity-preserving cubic spline interpolations.

time we use full Coulomb interaction in addition to the non-uniform Kanamori interaction at various different temperatures. The two different interactions are supposed to show the dependence of performance improvements on the size of superstates, as the blocks obtained for the full Coulomb interaction using automatic partitioning are not as small as those that can be obtained for an interaction of Kanamori form using appropriate quantum numbers. The results are shown in the left panel of Fig. 3.3. We observe significant speed-up factors from slightly below 10 up to almost 1000 when superstate or state sampling are used compared to the conventional method. As expected, with decreasing temperature the speed-up shrinks as higher expansion orders cause quantum number checking to fail for more superstates, so the matrix products are not necessary anyway and we can only avoid less costly quantum number checking. The effect of improvements to the local weight calculation is further necessarily expected to decrease for sufficiently low temperature due to the worse computational complexity of the bath weight, which scales like β^3 , while that of the local weight only scales like β^2 [36]. The additional speed-up due to the switch from superstate to state sampling is also significantly smaller for Kanamori interaction with smaller superstates than for Coulomb interaction with larger superstates. We find a larger speed-up for Coulomb interaction in general than for Kanamori interaction, suggesting that although the total number of superstates is smaller, usually a larger number of superstates would pass quantum number checking and require calculation for Coulomb interaction than for Kanamori interaction.

We do not detect any deterioration in the quality of the results, and for a simpler two-orbital model we find agreement with exact diagonalization. The absolute mean sign for the previously considered model is shown in the right panel of Fig. 3.3. While no significant deterioration can be found for superstate sampling, consistent with our prior observation that contributions due to a single outer superstate were found to be overwhelming, a slight decrease with state sampling is visible. We find that the relative deterioration decreases slightly at lower temperatures in the case of Coulomb interaction, where a sign problem is found, which is consistent with the expected stronger concentration of contributions at lower temperatures. As far as the autocorrelation time of the Green’s function is concerned, we find an increase of about 10% for superstate sampling and about 3% for state sampling compared to the conventional method, which we expect to partially result from the now necessary use of τ -shift moves, which leave the value of the estimator unchanged.

3.1.4 Application to a Hund’s metal with low coherence temperature

Finally, let us consider a system whose low-temperature behavior is numerically hard to access as an application of superstate sampling in conjunction with sliding window sampling [73], which was introduced simultaneously in *w2dynamics* [40] since superstate sampling slightly simplifies its implementation. We shall perform DMFT calculations for a degenerate three-orbital Hubbard model on a Bethe lattice first investigated using DMFT with a CT-HYB solver in Ref. [35], using an interaction of Kanamori form [20] with Hund’s coupling $J = U/6$ and interorbital interaction $U' = U - 2J$ fixed relative to the intraorbital Hubbard- U . In Ref. [35], an incoherent metallic state with frozen moments was found that persisted down to the lowest temperature reachable in the calculations. While similar models were later shown to merely have a very low but non-zero coherence temperature as discussed below, it was therefore concluded in Ref. [35] that the model undergoes a quantum (i.e. $T = 0$) phase transition termed “spin freezing” between a paramagnetic Fermi liquid state and that incoherent metallic state. This was based on an insufficiently fast decay of the imaginary time spin-spin correlation function at $\tau = \beta/2$ and a non-zero intercept and non-Fermi-liquid exponent of the imaginary part of the self-energy on the Matsubara axis.

In the meantime, the bad metal state termed “frozen moment phase” there has become known as the “Hund’s metal” state [20, 184–188]. This strongly correlated metallic state that is found in multi-orbital models with Hund’s coupling in the vicinity of the Mott transition at half-filling is reached via a crossover across a roughly parabolic curve in the phase diagram (cf. Fig. 3.4) emanating from the Mott transition point at half-filling. In Ref. [35] for example, primarily the crossover at constantly high Hub-

bard interaction strength parameter $U = 8t$ relative to hopping t from a weakly correlated good metal at high doping $n \lesssim 2$ to a strongly correlated metallic state closer to half-filling $n = 3$ is considered. As observed in Ref. [35], while screening of the orbital degrees of freedom still happens at higher temperatures in that state, it is characterized by local moments and non-Fermi-liquid behavior down to much lower temperatures than were reached there; screening of the spin degrees of freedom and Fermi liquid behavior do however in fact set in at a very low coherence temperature before reaching zero temperature [187, 189, 190], and this difference by orders of magnitude between the scales of spin and orbital screening is also known as “spin-orbital separation” [190–192]. We review this in slightly more detail in Sec. 5.1.1, the introduction to the first section in which we ourselves take a close look at that same region in the parameter space of a two-orbital Hubbard model with Hund’s coupling [193, 194].

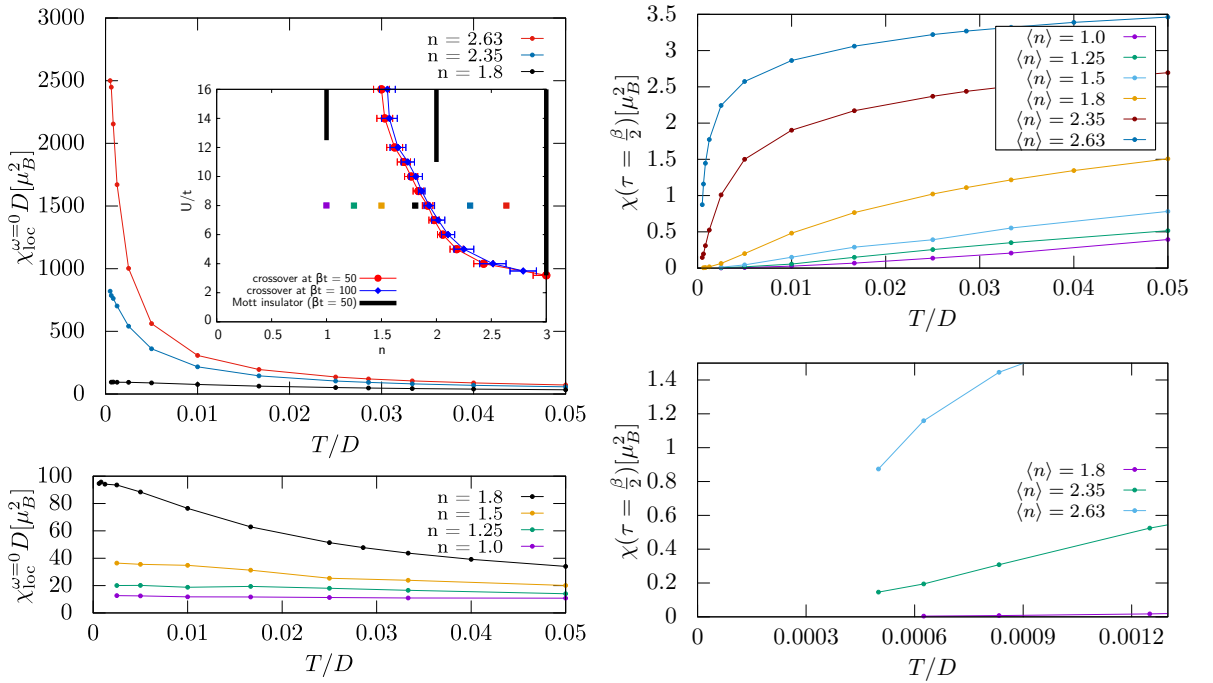


Figure 3.4: Left panels: Static local spin susceptibilities as functions of temperature for a series of points going across the bad metal or “spin freezing” crossover, which are also marked in the same colors in the inset showing the phase diagram adapted from Ref. [35]. For the two bad metal cases, a Curie-like behavior $\propto T^{-1}$ approximately persists down to the lowest temperatures, while a Pauli-like constant behavior clearly eventually sets in for the other ones at low T . Right panels: Local spin susceptibility in imaginary time at $\tau = \beta/2$ as a function of temperature for the same points, where it is clearly recognizable that even in all the bad metallic cases, the value sharply drops for sufficiently low temperatures.

For now, let us follow Ref. [35], but to considerably lower temperatures with the

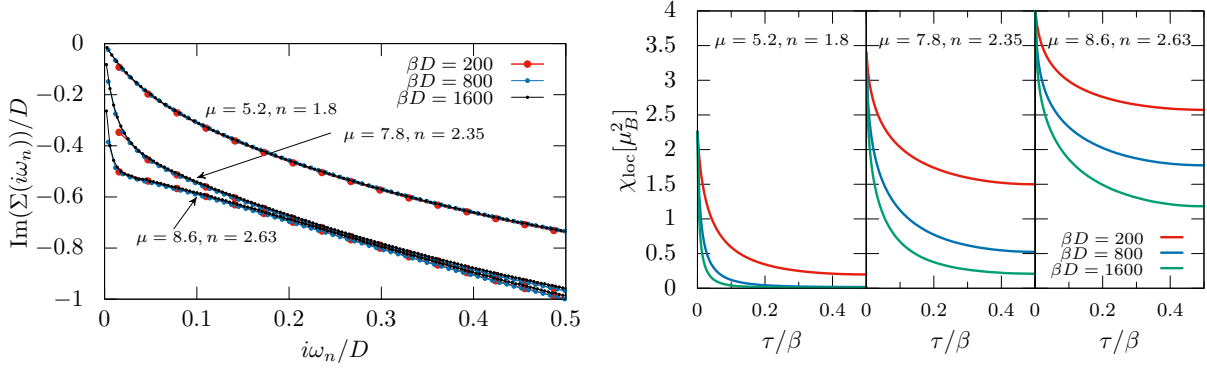


Figure 3.5: Left panel: Imaginary part of the self-energy on the Matsubara axis with curves obtained at three different temperatures overlaid for three fillings, the higher two ones of which are in the “frozen moment” / bad metal regime. In the bad metal cases the curves come close to Fermi liquid behavior only for the lowest temperatures and rather abruptly at the lowest Matsubara frequencies. Right panel: Local spin susceptibility in imaginary time (only one of symmetric halves shown) for the same three temperatures and fillings as the self-energy. At higher temperature, the high plateau at $\tau = \beta/2$ in the bad metal cases points to unscreened local moments, but for sufficiently low temperatures the susceptibility drops significantly even there.

help of the current version of *w2dynamics*. The local moment physics is clearly visible in our results for the static local spin susceptibility $\chi_{\text{loc}}^{\omega=0}(T) = \int_0^\beta d\tau \chi_{\text{loc}}(\tau)$ with $\chi_{\text{loc}}(\tau) = g^2 \sum_{ij} \langle S_z^i(\tau) S_z^j(0) \rangle$ shown in the left panels of Fig. 3.4. The parameters of our calculations are for orientation marked in an inset containing the phase diagram of Ref. [35] with the transition curves that mark the position of the “good metal” to “bad metal” crossover. For the two points in the “frozen moment” regime closest to half-filling we observe Curie behavior $\propto T^{-1}$ down to low temperatures as typical for Hund’s metals [192] with no clear crossover to constant Pauli behavior recognizable yet. In contrast to that, we already reach Pauli behavior for our next value of doping $n = 1.8$ just across the crossover line as well as for all other fillings below that at constant interaction. We reach a minimum temperature of $\beta D = 1600$ for the three points closer to half-filling, one eighth of $\beta D = 2\beta t = 200$, which is the lowest temperature reached in Ref. [35] with the Bethe lattice half-bandwidth D or hopping $t = D/2$ as reference energy scale.

Let us compare the local spin susceptibilities at imaginary time $\tau = \beta/2$ shown in the right panels of Fig. 3.4 next, which are expected to drop as T^2 in a Fermi liquid and were found to be constant in the “frozen moment” regime by Ref. [35]. We instead find that they actually do drop considerably even there as the temperature is lowered,

though at much lower temperatures than for higher doping and with the scaling at our lowest temperatures still quantitatively different from exact Fermi liquid behavior. If we e.g. take the inflection point as an indicator of the coherence temperature, since T^2 curves upward with increasing T while the curves in the “frozen moment” curve downward for most of the temperature range, we were just about able to reach the coherence temperature for $n = 2.35$ while we are not quite there yet for $n = 2.63$.

Looking at the imaginary time dependence of the local spin susceptibilities in the upper right panel of Fig. 3.5, we observe that the $\tau = 0$ susceptibility rises upon approaching half-filling, but the $\tau = \beta/2$ value does markedly decrease with temperature in all cases. This is required to eventually reach the constant Pauli behavior, in which case the total integral over imaginary time yielding the static local susceptibility remains constant as β is increased. This only happens much slower for the higher fillings, pointing to the lower coherence temperatures in these cases, cf. also Refs. [195, 196].

Correspondingly, the imaginary part of the self-energy on the Matsubara frequency axis shown in the left panels of Fig. 3.5 that seems to clearly target a non-zero intercept at higher temperatures in the “frozen moment” regime also takes a sharp turn at the lowest frequencies as the temperature is reduced considerably below $\beta D = 200$ to abruptly come much closer to the expected behavior for a Fermi liquid [195, 197]. For the doping of $n = 1.8$ on the other hand, the behavior at low Matsubara frequencies does not significantly change in the considered temperature range, the data just becomes denser on the Matsubara axis according to $\omega_n = (2n + 1)\pi T$ as the temperature is reduced. Considering just the change of the value at the first Matsubara frequency $\text{Im}(\Sigma(i\omega_0))(T)$, we can easily observe scaling linear in T in that case as described by the “first-Matsubara-frequency rule” for Fermi liquids following from the proportionality of the scattering rate to T^2 [164], which is only restored at lower temperatures in the “frozen moment” cases.

All the quantities we have looked at serve as clear indicators of a surprisingly sharp drop of the coherence temperature as the line found in Ref. [35] is crossed, which was later quantitatively clearly identified as such in e.g. high-precision calculations using the numerical renormalization group [189, 191].

3.1.5 Conclusions

In conclusion, we find that the strong concentration of contributions to the full local weight in CT-HYB on few outer superstates and outer states due to the exponential damping of contributions of excited states by imaginary time evolution allows the sum over outer superstates and states to be efficiently performed stochastically. This leads to considerable increases in sampling performance without a significant negative im-

pact on the results, especially in calculations with large numbers of orbitals and few good quantum numbers such as realistic calculations for transition metal impurities treating five orbitals with full Coulomb interaction. As an example, we consider how optimization techniques like superstate and state sampling can contribute to our ability to reach lower temperatures in CT-HYB calculations as it is e.g. necessary to get closer to the Fermi liquid state in Hund's metals.

3.2 Symmetric improved estimators

In this section, we derive generalized equations of motion for the one- and two-particle Green’s function of the Anderson impurity model. Rather than just computing the derivative with respect to one time argument, we differentiate them “symmetrically” with respect to all of their time arguments and obtain expressions for the one-particle Green’s function in terms of up to a three-particle Green’s function and for the two-particle Green’s function in terms of up to a six-particle Green’s function with partially contracted time arguments. We show that using these expressions and CT-HYB measurements of the higher-order correlation functions, whose efficient sampling we discuss, in order to calculate one- and two-particle Green’s function yields results with asymptotically lower errors than their standard estimators in CT-HYB. When these improved estimators are used to obtain the self-energy and higher-order vertex functions, their errors do not diverge with increasing Matsubara frequency but remain constant.

This section covers results previously published in the following article, Ref. [198], which is also the source of the figures, and also discussed in Ref. [176]

*J. Kaufmann, P. Gunacker, A. Kowalski, G. Sangiovanni, and K. Held,
“Symmetric Improved Estimators for Continuous-Time Quantum Monte Carlo,”
Phys. Rev. B **100**, 075119 (2019)*

3.2.1 Self-energies in CT-HYB

Self-energies calculated from CT-HYB results for Green’s functions using the Dyson equation show a level of noise that rapidly increases with the Matsubara frequency to such an extent that it is hard to capture the high frequency behavior accurately [199]. This is in stark contrast to the so-called weak coupling methods CT-INT and CT-AUX, in which the Green’s function is measured as a correction to the non-interacting Green’s function that rapidly decreases for high frequencies, giving the right asymptotic behavior [36, 199]. Efforts have been directed at working around this problem since CT-HYB is the QMC solver of choice for impurities with strong interactions of a complicated form and a small to moderate number of orbitals, which includes such physically relevant cases as transition metal impurities, DMFT for strongly interacting Hubbard models with multiple orbitals or in small clusters, and especially “ab initio” calculations for correlated materials like transition metal compounds [36, 200].

While the convergence of DMFT itself for example is not particularly sensitive to noise at high frequencies², quantities evaluated by performing numerical summations

²although we have observed that difficult cases, such as convergence to unstable solutions using improved non-linear mixing [145] with a phase space extension [146] that we performed in Sec. 5.1

over Matsubara frequencies such as energies could be severely affected [201]. Proposed countermeasures include the use of orthogonal polynomial expansions, in which statistical error and actual information are more clearly separated to high and low coefficients respectively than on Matsubara frequencies [201], the use of more precisely determinable moments and asymptotic behaviors at high frequencies [36, 202–206], causal optimization [207], and the use of improved estimators [200, 208, 209] based on equations of motion, cf. e.g. Ref. [47].

The improved estimators used in CT-HYB so far were based on equations of motions obtained by differentiating the one- or two-particle Green’s function with respect to only one of their two or four time arguments, which results in expressions relating them to higher-order correlation functions [200, 208, 209]. We carry the procedure further here by differentiating them with respect to their other time arguments as well [210], deriving “symmetric improved estimators” for the self-energy and four-leg vertex function in terms of correlation functions of even higher order. Using these estimators ameliorates the asymptotic scaling of the statistical error of the results sufficiently to make it constant with increasing Matsubara frequency, which we derive and demonstrate using exemplary CT-HYB calculation results.

3.2.2 Definitions

For the definition of the Hamiltonian (2.1) of the Anderson impurity model and the hybridization function (2.10) in the context of the derivations in this section, we refer back to Sec. 2.1. Let us however explicitly repeat the form of the non-interacting Green’s function

$$\mathcal{G}_{0,\alpha\beta}^v = \frac{1}{i\nu\delta_{\alpha\beta} - E_{\alpha\beta} - \Delta_{\alpha\beta}(i\nu)} \quad (3.5)$$

and of the general full one-particle Green’s function with two time arguments

$$G_{\alpha\beta}(\tau_1, \tau_2) = -\left\langle T_\tau c_\alpha(\tau_1)c_\beta^\dagger(\tau_2) \right\rangle \quad (3.6)$$

and introduce the two-particle Green’s function with four time arguments

$$G_{\alpha\beta\gamma\delta}(\tau_1, \tau_2, \tau_3, \tau_4) = \left\langle T_\tau c_\alpha(\tau_1)c_\beta^\dagger(\tau_2)c_\gamma(\tau_3)c_\delta^\dagger(\tau_4) \right\rangle, \quad (3.7)$$

whose properties are considered in some more detail in Sec. 5.2.2. Due to the invariance of the AIM Hamiltonian under time translations, it is in principle possible to remove one time argument from each of the Green’s functions by specifying only time

and Sec. 5.2, may be impacted by the diverging noise and require working around it by e.g. mixing another quantity than the self-energy on Matsubara frequencies

differences. We also define the Fourier transforms to fermionic Matsubara frequencies $\nu_m = (2m + 1)\pi\beta^{-1}$, $m \in \mathbb{Z}$ of the Green's functions as

$$G_{\alpha\beta}^{\nu_1\nu_2} = \beta^{-1} \int_0^\beta e^{i(\nu_1\tau_1 - \nu_2\tau_2)} G_{\alpha\beta}(\tau_1, \tau_2) d\tau_1 d\tau_2 \quad (3.8)$$

and

$$G_{\alpha\beta\gamma\delta}^{\nu_1\nu_2\nu_3\nu_4} = \beta^{-2} \int_0^\beta e^{i(\nu_1\tau_1 - \nu_2\tau_2 + \nu_3\tau_3 - \nu_4\tau_4)} G_{\alpha\beta\gamma\delta}(\tau_1, \tau_2, \tau_3, \tau_4) d\tau_1 d\tau_2 d\tau_3 d\tau_4, \quad (3.9)$$

where the time-translational invariance is reflected in energy conservation in the form that we can use a single frequency $\nu_1 = \nu_2 =: \nu$ for the one-particle Green's function and have the relation $\nu_1 + \nu_3 = \nu_2 + \nu_4$ for the two-particle Green's function that in principle allows us to remove one of its frequency arguments as well. Details on the Matsubara frequency transforms and the removal of one of the redundant frequency arguments can be found in Appendix A, which however uses slightly different definitions.

3.2.3 One-particle symmetric improved estimators

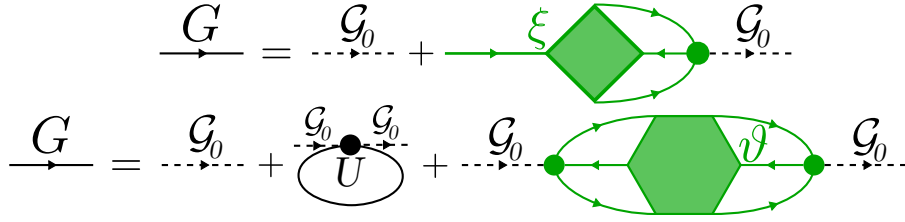


Figure 3.6: Diagrammatic representation of the evaluation of the full one-particle Green's function G drawn as solid line using improved estimators, where sections of the diagrams marked in green are multi-operator correlation functions individually measured in CT-HYB, interaction factors are represented by thick dots, and the non-interacting Green's function by dashed lines. Top panel: Diagram using the "normal" improved estimator $G = \mathcal{G}_0 + \mathcal{G}_0 \xi$ with four-operator correlation function ξ with three equal times [200]. Bottom panel: Diagram using the symmetric improved estimator, which represents the equation $G = \mathcal{G}_0 + \mathcal{G}_0 U n \mathcal{G}_0 + \mathcal{G}_0 \vartheta \mathcal{G}_0$ with a six-operator correlation function ϑ with twice three equal times.

Let us start by reviewing the result for the simple improved estimator for the single-particle Green's function [200, 208, 209, 211], which we encounter during the derivation of the symmetric improved estimator anyway. The improved estimator equation for the

single-particle Green's function obtained by differentiating (3.6) with respect to τ_1 is

$$G_{\alpha\beta}^v = \sum_{\gamma} \mathcal{G}_{0,\alpha\gamma}^v (\delta_{\gamma\beta} + \xi_{\gamma\beta}^v), \quad (3.10)$$

where

$$\xi_{\alpha\beta}^v = \beta^{-1} \int_0^{\beta} e^{iv(\tau_1 - \tau_2)} \left\langle -T_{\tau} q_{\alpha}(\tau_1) c_{\beta}^{\dagger}(\tau_2) \right\rangle d\tau_1 d\tau_2 \quad (3.11)$$

is a four-operator correlation function with three operators at equal times, expressed using the operators

$$q_{\alpha} := \sum_{\beta\gamma\delta} U_{[\alpha\beta]\gamma\delta} c_{\beta}^{\dagger} c_{\delta} c_{\gamma} \quad (3.12a)$$

$$q_{\alpha}^{\dagger} := \sum_{\beta\gamma\delta} U_{\gamma\delta[\alpha\beta]}^* c_{\gamma}^{\dagger} c_{\delta}^{\dagger} c_{\beta}, \quad (3.12b)$$

where we employ a commutator-like bracket notation in the indices of the interaction matrix to abbreviate

$$U_{[\alpha\beta]\gamma\delta} := \frac{1}{2} (U_{\alpha\beta\gamma\delta} - U_{\beta\alpha\gamma\delta}) \quad (3.13a)$$

$$U_{\alpha\beta[\gamma\delta]} := \frac{1}{2} (U_{\alpha\beta\gamma\delta} - U_{\alpha\beta\delta\gamma}). \quad (3.13b)$$

The full derivation can be found in Appendix B, and a representation of the improved estimator equation (3.10) in terms of Feynman diagrams [212] is shown in the top panel of Fig. 3.6. By comparing (3.10) to the Dyson equation $G_{\alpha\beta}^v = \mathcal{G}_{0,\alpha\beta}^v + \mathcal{G}_{0,\alpha\gamma}^v \Sigma_{\gamma\eta}^v G_{\eta\beta}^v$, obtained from (2.13) by multiplying with \mathcal{G}_0 from the left and G from the right, we can identify ξ with the product ΣG , which leads to the notations ΣG and $G\Sigma$ for this quantity in the literature [200, 209]. In the general case, we can measure the quantity ξ as well as all further correlation functions we define in this chapter in CT-HYB using worm sampling [209].

Since the non-interacting Green's function is free of error as far as only CT-HYB is concerned (and not e.g. DMFT convergence) and assuming an error for all measured quantities that is approximately constant as a function of the Matsubara frequency particularly in the high-frequency limit [91], we can use formal error propagation to compute the asymptotic scaling of the error of the self-energy. We use the expression $\Sigma = \xi/G$ for that purpose but consider only the error in ξ because it is clear that when we insert (3.10) into the Dyson equation (2.13) for the actual calculation, ξ is the only quantity with statistical error. For the error of the self-energy, the error propagation formula thus yields $\sigma_{\Sigma} = \sqrt{|G|^{-2} \sigma_{\xi}^2}$, which we can further evaluate using the high-

frequency asymptotic behavior $|G| \propto \nu^{-1}$ of the Green's function to get $\sigma_\Sigma \propto \nu\sigma_\xi$. Therefore, the error of the self-energy calculated by means of the improved estimator grows linearly with the Matsubara frequency. Using the improved estimator thus indeed constitutes an improvement over the direct insertion of a Green's function obtained using the standard estimator into the Dyson equation, which results in a self-energy with an error of $\sigma_\Sigma \propto \nu^2\sigma_G$ that instead scales quadratically with the frequency. This is the disadvantage of having to compute differences involving quantities subject to numerical error rather than ratios, as in the former case absolute errors propagate while it is only relative errors in the latter case. Particularly if the result of the difference is small, the relative error may increase considerably, as it has already been noted for the case of the self-energy calculated using the Dyson equation by Refs. [200, 211].

Let us proceed to the symmetric improved estimator for the single-particle Green's function. We now differentiate $\xi(\tau_1, \tau_2)$ in (3.10) with respect to the time argument τ_2 of the single fermionic creator as shown in Appendix B to obtain the symmetric improved estimator equation

$$G_{\alpha\beta}^v = \sum_\gamma \mathcal{G}_{0,\alpha\gamma}^v \left(\delta_{\gamma\beta} + \sum_\delta \left(2 \sum_{\mu\rho} U_{[\gamma\mu][\delta\rho]} \langle c_\mu^\dagger c_\rho \rangle + \vartheta_{\gamma\delta}^v \right) \mathcal{G}_{0,\delta\beta}^v \right), \quad (3.14)$$

where

$$\vartheta_{\alpha\beta}^v = -\beta^{-1} \int_0^\beta e^{i\nu(\tau_1-\tau_2)} \langle T_\tau q_\alpha(\tau_1) q_\beta^\dagger(\tau_2) \rangle d\tau_1 d\tau_2 \quad (3.15)$$

is a six-operator correlation function with twice three operators at equal times and $\langle c_\mu^\dagger c_\rho \rangle$ is a density $n_\mu \delta_{\mu\rho}$ if the hybridization function is diagonal. In the symmetric improved estimator equation, we have not only the contribution of the non-interacting Green's function and that including the six-operator correlator, but now also such a density-dependent contribution to the full Green's function. It can be diagrammatically represented by a single interaction vertex with a loop, which is known as the Hartree self-energy [47]. While this diagram is included in contributions of ξ to the improved estimator, it is not included in those of ϑ to the symmetric improved estimator. The diagrammatic representation of the symmetric improved estimator equation is found in the bottom panel of Fig. 3.6. A similar relation has previously been found in a slightly different context [213].

We repeat our calculation of the asymptotic error of the self-energy for the symmetric improved estimator. After inserting (3.14) into (2.13) and some elementary arithmetic, we arrive at the expression $\Sigma = (2Un + \vartheta)/(1 + \mathcal{G}_0(2Un + \vartheta))$ for the self-energy in terms of the quantities ϑ and n carrying statistical error. We focus on only that of the six-operator correlator ϑ since a static quantity like the density can be measured with

very high precision by comparison. The derivative of the self-energy with respect to ϑ is $(1 + \mathcal{G}_0(2Un + \vartheta))^{-2}$, which is equal to one in the high-frequency limit due to the high-frequency asymptotic behavior of \mathcal{G}_0 . The error of the self-energy calculated by means of the symmetric improved estimator therefore scales with the frequency like the error of ϑ , which is approximately independent of the frequency. This constitutes an improvement over even the conventional improved estimator with its linear scaling of the error.

3.2.4 Two-particle symmetric improved estimators

The diagrammatic equation shows the evaluation of the connected part G_{conn} of the two-particle Green's function. On the left, a square vertex labeled F is connected to four external lines, with the label G_{conn} below it. This is equal to a sum of terms. The first line includes a thick dot U , a term with two green ovals labeled ϑ , a term with two green ovals labeled ϑ and a thick dot, and four terms with green squares labeled ξ . The second line includes two groups of terms in parentheses: the first group has terms with green ovals labeled ϕ and f , and the second group has terms with green ovals labeled ψ and g . Finally, a term with a green circle labeled h is added.

Figure 3.7: Diagrammatic representation of the evaluation of the connected part G_{conn} of the two-particle Green's function, which is a full vertex F with full one-particle Green's functions G drawn as solid lines at its legs, using the symmetric improved estimator. In the diagrams connected sections marked in green are multi-operator correlation functions measured individually in CT-HYB, dashed lines represent the non-interacting Green's function and thick dots factors of the interaction. The first line of the equation contains terms with insertions of the correlation functions from single-particle improved estimators, the second those representing essential two-particle terms with terms reducible in the same channel grouped in parentheses. Terms with Hartree-like factors ($\propto n$ in the equation) are not depicted.

With the presentation of one-particle improved estimators concluded, we proceed to the two-particle Green's function, where we need to perform derivatives with respect to all four time arguments. Since there are both far more terms originating from the derivatives of the theta functions than in the case of the single-particle Green's functions and they actually also involve some rather “non-standard” correlation functions themselves, this leads to considerably more unwieldy expressions than we have seen so far. We limit ourselves to the results and only a short summary of the derivation, while the full derivation can be found in Appendix B of Ref. [198]. Further we assume a diagonal hybridization and thus diagonal single-particle Green's function as it is done

there from here on. By abstracting slightly over the details of the derivation we can collect terms in the expression for the two-particle Green's function

$$G_{\alpha\beta\gamma\delta}^{v_1v_2v_3v_4} = \mathcal{G}_{0,\alpha}^{v_1} \left(-R_{1,\alpha\beta\gamma\delta}^{v_1v_2v_3v_4} + \mathcal{G}_{0,\beta}^{v_2} \left(R_{2,\alpha\beta\gamma\delta}^{v_1v_2v_3v_4} + \mathcal{G}_{0,\gamma}^{v_3} \left(-R_{3,\alpha\beta\gamma\delta}^{v_1v_2v_3v_4} + \mathcal{G}_{0,\delta}^{v_4} \left(R_{4,\alpha\beta\gamma\delta}^{v_1v_2v_3v_4} + \frac{h_{\alpha\beta\gamma\delta}^{v_1v_2v_3v_4}}{\beta} \right) \right) \right) \right). \quad (3.16)$$

Here we see the general structure of the expansion that we obtain when we in each step explicitly perform the time derivative of a single creator or annihilator in the term that collected an extra factor of q or q^\dagger in the previous step (and thus is the term with the most of these factors at that point) and just name the other term with a delta function and anticommutator $R_{i,\alpha\beta\gamma\delta}^{v_1v_2v_3v_4}$. With $S_{i,\alpha_1\alpha_2\alpha_3\alpha_4}^{\dots v_i\tau_{i+1}\dots}$ the term with the most factors of q and q^\dagger at step i , which is exactly i factors such that $S_{0,\alpha_1\alpha_2\alpha_3\alpha_4}^{\tau_1\tau_2\tau_3\tau_4} = G_{\alpha_1\alpha_2\alpha_3\alpha_4}^{\tau_1\tau_2\tau_3\tau_4}$, we can express this as $S_{i,\alpha_1\alpha_2\alpha_3\alpha_4}^{\dots v_i\tau_{i+1}\dots} = \mathcal{G}_{0,\alpha_i}^{v_i} \left((-1)^{i+1} R_{i+1,\alpha_1\alpha_2\alpha_3\alpha_4}^{\dots v_{i+1}\tau_{i+2}\dots} + S_{i+1,\alpha_1\alpha_2\alpha_3\alpha_4}^{\dots v_{i+1}\tau_{i+2}\dots} \right)$, where the alternating minus sign in front of R_{i+1} is caused by the alternation of annihilators and creators in the two-particle Green's function and we also performed additional Fourier transforms for all remaining time arguments that we had not already needed to Fourier transform during the derivation before.

After four steps, we end up with the twelve-operator correlation function h with four times three operators at equal times defined in (3.18e), as well as several other terms in R_i of a less regular form. In general, we need to evaluate (anti-)commutators by applying the fermionic anticommutation relations, removing two operators each, and differentiate with respect to time arguments of remaining sole creators and annihilators, giving additional factors of q and q^\dagger . As previously mentioned, a more detailed summary of the derivation can be found in Appendix B of Ref. [198], which gives us to the expressions

$$R_{1,\alpha\beta\gamma\delta}^{v_1v_2v_3v_4} = -\delta_{12}G_\delta^{v_4} + \delta_{14}G_\beta^{v_2}, \quad (3.17a)$$

$$R_{2,\alpha\beta\gamma\delta}^{v_1v_2v_3v_4} = -\delta_{12}\mathcal{G}_{0,\gamma}^{v_3} 2 \sum_\rho U_{[\alpha\rho][\alpha\rho]} n_\rho - \delta_{14}\xi_\delta^{v_4}, \quad (3.17b)$$

$$-\frac{2}{\beta}\mathcal{G}_{0,\gamma}^{v_3}\mathcal{G}_{0,\delta}^{v_4} \left(-U_{[\alpha\gamma][\beta\delta]} + \sum_\rho \left(U_{[\alpha\rho][\beta\delta]}\xi_{\gamma\rho}^{v_3} + U_{[\alpha\gamma][\beta\rho]}\xi_{\delta\rho}^{v_4} \right) - 2\phi_{\alpha\beta\gamma\delta}^{v_4-v_3} + f_{\gamma\delta\alpha\beta}^{v_3,(v_3-v_4)} \right),$$

$$R_{3,\alpha\beta\gamma\delta}^{v_1v_2v_3v_4} = \delta_{12}\mathfrak{D}_\alpha^{v_1} \quad (3.17c)$$

$$+ \beta^{-1}\mathcal{G}_{0,\delta}^{v_4} \left(2 \sum_\rho \left(U_{[\rho\gamma][\beta\delta]}\xi_{\alpha\rho}^{v_1} + U_{[\alpha\gamma][\rho\delta]}\xi_{\beta\rho}^{v_2} \right) \right) \quad (3.17d)$$

$$\begin{aligned}
& - \psi_{\alpha\beta\gamma\delta}^{v_1+v_3} + 4\phi_{\alpha\delta\gamma\beta}^{v_1-v_4} + 2f_{\alpha\delta\gamma\beta}^{v_1,(v_1-v_4)} - g_{\delta\gamma\beta\alpha}^{v_4v_2} \Big), \\
R_{4,\alpha\beta\gamma\delta}^{v_1v_2v_3v_4} &= \beta^{-1} \left(2f_{\gamma\beta\alpha\delta}^{v_3,(v_4-v_1)} + g_{\alpha\beta\gamma\delta}^{v_1v_3} - 2f_{\alpha\beta\gamma\delta}^{v_1,(v_1-v_2)} \right), \tag{3.17e}
\end{aligned}$$

where $\delta_{12} = \delta_{\alpha\beta}\delta_{\gamma\delta}\delta_{v_1v_2}\delta_{v_3v_4}$, $\delta_{34} = \delta_{\alpha\delta}\delta_{\beta\gamma}\delta_{v_1v_4}\delta_{v_2v_3}$, single indices for quantities that should carry multiple ones refer to diagonal elements, ξ and ϑ are the correlation functions we have already encountered in the improved estimators for the single-particle Green's function given in (3.11) and (3.15), full single-particle Green's functions G in R_1 are to be evaluated by means of the symmetric improved estimator equation (3.14), and we defined some additional correlation functions appearing on the right-hand sides,

$$\phi_{\alpha\beta\gamma\delta}^\omega = \beta^{-1} \int_0^\beta e^{i\omega(\tau_1-\tau_2)} \langle T_\tau (Un)_{\alpha\beta}(\tau_1)(Un)_{\gamma\delta}(\tau_2) \rangle d\tau_1 d\tau_2, \tag{3.18a}$$

$$\psi_{\alpha\beta\gamma\delta}^\omega = \beta^{-1} \int_0^\beta e^{i\omega(\tau_1-\tau_2)} \langle T_\tau (Ucc)_{\alpha\gamma}(\tau_1)(Uc^\dagger c^\dagger)_{\beta\delta}(\tau_2) \rangle d\tau_1 d\tau_2, \tag{3.18b}$$

$$f_{\alpha\beta\gamma\delta}^{v\omega} = \beta^{-1} \int_0^\beta e^{iv(\tau_1-\tau_2)+i\omega(\tau_2-\tau_3)} \langle T_\tau q_\alpha(\tau_1)q_\beta^\dagger(\tau_2)(Un)_{\gamma\delta}(\tau_3) \rangle d\tau_1 d\tau_2 d\tau_3, \tag{3.18c}$$

$$g_{\alpha\beta\gamma\delta}^{vv'} = \beta^{-1} \int_0^\beta e^{iv(\tau_1-\tau_3)+iv'(\tau_2-\tau_3)} \langle T_\tau q_\alpha(\tau_1)q_\gamma(\tau_2)(Uc^\dagger c^\dagger)_{\beta\delta}(\tau_3) \rangle d\tau_1 d\tau_2 d\tau_3, \tag{3.18d}$$

$$h_{\alpha\beta\gamma\delta}^{v_1v_2v_3v_4} = \beta^{-1} \int_0^\beta e^{i(v_1\tau_1-v_2\tau_2+v_3\tau_3-v_4\tau_4)} \langle T_\tau q_\alpha(\tau_1)q_\beta^\dagger(\tau_2)q_\gamma(\tau_3)q_\delta^\dagger(\tau_4) \rangle d\tau_1 d\tau_2 d\tau_3 d\tau_4, \tag{3.18e}$$

with fermionic Matsubara frequencies $\nu = (2n+1)\pi\beta^{-1}$, $n \in \mathbb{Z}$, bosonic Matsubara frequencies $\omega = 2n\pi\beta^{-1}$, $n \in \mathbb{Z}$, and abbreviations

$$(Un)_{\alpha\beta} := \sum_{\rho\mu} U_{[\alpha\rho][\beta\mu]} c_\rho^\dagger c_\mu, \tag{3.19a}$$

$$(Uc^\dagger c^\dagger)_{\alpha\beta} := \sum_{\rho\mu} U_{\rho\mu[\alpha\beta]} c_\rho^\dagger c_\mu^\dagger, \tag{3.19b}$$

$$(Ucc)_{\alpha\beta} := \sum_{\rho\mu} U_{[\alpha\beta]\rho\mu} c_\mu c_\rho. \tag{3.19c}$$

By inserting the evaluated R_i given in (3.18) into the symmetric improved estimator equation for the two-particle Green's function (3.16), we can collect similar terms to obtain

$$G_{\alpha\beta\gamma\delta}^{v_1v_2v_3v_4} = (\delta_{12} - \delta_{14})G_\alpha^{v_1}G_\gamma^{v_3} - \overbrace{\beta^{-1}\mathcal{G}_{0,\alpha}^{v_1}\mathcal{G}_{0,\beta}^{v_2}\mathcal{G}_{0,\gamma}^{v_3}\mathcal{G}_{0,\delta}^{v_4}\mathcal{F}_{\alpha\beta\gamma\delta}^{v_1v_2v_3v_4}}^{G_{\text{conn}}}. \tag{3.20}$$

Here we separate the contributions due to disconnected propagation of two particles in the first term and the connected contribution G_{conn} in the second term with four non-interacting legs attached to a sum of correlation functions similar to a full vertex, cf. [214],

$$\begin{aligned}
\mathcal{F}_{\alpha\beta\gamma\delta}^{v_1v_2v_3v_4} &= \beta(\delta_{12} - \delta_{14}) \left(2 \sum_{\rho} U_{[\alpha\rho][\alpha\rho]} n_{\rho} + \vartheta_{\alpha}^{v_1} \right) \left(2 \sum_{\rho} U_{[\gamma\rho][\gamma\rho]} n_{\rho} + \vartheta_{\gamma}^{v_3} \right) \quad (3.21) \\
&+ 2U_{[\alpha\gamma][\beta\delta]} + 2 \sum_{\rho} \left(U_{[\rho\gamma][\beta\delta]} \xi_{\alpha\rho}^{v_1} + U_{[\alpha\gamma][\rho\delta]} \xi_{\beta\rho}^{v_2} + U_{[\alpha\rho][\beta\delta]} \xi_{\gamma\rho}^{v_3} + U_{[\alpha\gamma][\beta\rho]} \xi_{\delta\rho}^{v_4} \right) \\
&\underbrace{+ 4\phi_{\alpha\beta\gamma\delta}^{v_4-v_3} + 2f_{\alpha\beta\gamma\delta}^{v_1,(v_1-v_2)} + 2f_{\gamma\delta\alpha\beta}^{v_3,(v_2-v_1)}}_{\mathcal{F}_{2,ph}} \\
&\underbrace{+ 4\phi_{\alpha\delta\gamma\beta}^{v_1-v_4} - 2f_{\alpha\delta\gamma\beta}^{v_1,(v_1-v_4)} - 2f_{\gamma\beta\alpha\delta}^{v_3,(v_4-v_1)}}_{\mathcal{F}_{2,\overline{ph}}} \\
&\underbrace{+ -\psi_{\alpha\beta\gamma\delta}^{v_1+v_3} - g_{\alpha\beta\gamma\delta}^{v_1v_3} - g_{\alpha\beta\gamma\delta}^{v_4v_2}}_{\mathcal{F}_{2,pp}} + \underbrace{h_{\alpha\beta\gamma\delta}^{v_1v_2v_3v_4}}_{\mathcal{F}_{2,\text{irred.}}},
\end{aligned}$$

where the underbraced terms can be identified as essential two-particle contributions that can be decomposed into $\mathcal{F}_{2,ph}$ reducible in the particle-hole channel, $\mathcal{F}_{2,\overline{ph}}$ reducible in the transverse particle-hole channel, $\mathcal{F}_{2,pp}$ reducible in the particle-particle channel, and fully irreducible $\mathcal{F}_{2,\text{irred.}}$, cf. [214]. A diagrammatic representation of the symmetric improved estimator decomposition (3.20) of the connected part G_{conn} of the two-particle Green's function is shown in Fig. 3.7, with contributions with insertions of correlation functions of the one-particle symmetric improved estimator in the first line and the essential two-particle contributions in the second line, grouped by parentheses according to reducibility as just discussed.

For the scaling of the error in two-particle quantities, we want to consider a quantity similar to the one-particle self-energy that suffers from statistical error diverging at high frequencies using standard CT-HYB estimators [36, 200, 204] for the two-particle Green's function. In a certain sense, the closest two-particle analogon to the self-energy are the irreducible vertex functions, cf. Sec. 5.2.2. Since they are related to the two-particle Green's function³ by the Bethe-Salpeter equation, which is analogous to the Dyson equation in form and function, it follows that these quantities have diverging statistical error from error propagation just as it did for the self-energy calculated using

³actually to generalized susceptibilities, which differ from the two-particle Green's function by subtraction of a disconnected contribution of a product of single-particle Green's functions, cf. Sec. 5.2.2 and Ref. [214]

the Dyson equation. We have explicitly considered that case before and data confirming the scaling of the error of the irreducible vertex functions can be found in Refs. [91, 209]. We will for simplicity consider the full vertex F defined by

$$G_{\alpha\beta\gamma\delta}^{v_1v_2v_3v_4} = (\delta_{12} - \delta_{14})G_{\alpha}^{v_1}G_{\gamma}^{v_3} - \beta^{-1}G_{0,\alpha}^{v_1}G_{0,\beta}^{v_2}G_{0,\gamma}^{v_3}G_{0,\delta}^{v_4}F_{\alpha\beta\gamma\delta}^{v_1v_2v_3v_4} \quad (3.22)$$

instead. Assuming that the error of the two-particle Green's function is independent of the Matsubara frequency in the limit of high frequencies and considering just its error for error propagation, the error of the vertex scales with the fourth power of the frequency because we need to divide four times by the one-particle Green's function that is inversely proportional to the frequency in the high-frequency limit. Numerical CT-HYB results demonstrate this bad scaling of the error of the full vertex [206]. The full vertex can be decomposed into fully irreducible contributions and contributions reducible in one of the three channels according to the parquet equation [214], and differs from a vertex that is irreducible in one of the channels by just the contributions reducible in that channel. It plays a role e.g. in certain diagrammatic techniques [215] and extensions to DMFT [216] and the Bethe-Salpeter equations for the irreducible vertices can also be formulated in terms of the full vertex rather than the generalized susceptibilities [214].

From the expression (3.22) for the full vertex F in terms of full one- and two-particle Green's functions we recognize by comparison to the symmetric improved estimator equation (3.20) that the full vertex can be expressed in terms of the vertex-like combination of correlation functions \mathcal{F} given in (3.21) as

$$F_{\alpha\beta\gamma\delta}^{v_1v_2v_3v_4} = \frac{\mathcal{G}_{0,\alpha}^{v_1}\mathcal{G}_{0,\beta}^{v_2}\mathcal{G}_{0,\gamma}^{v_3}\mathcal{G}_{0,\delta}^{v_4}}{G_{0,\alpha}^{v_1}G_{0,\beta}^{v_2}G_{0,\gamma}^{v_3}G_{0,\delta}^{v_4}}\mathcal{F}_{\alpha\beta\gamma\delta}^{v_1v_2v_3v_4}. \quad (3.23)$$

In the high-frequency limit, the asymptotic behavior of full and non-interacting Green's functions in the error propagation cancels, so the error of the vertex computed from symmetric improved estimators scales like that of \mathcal{F} , which is composed of correlation functions measured directly in Monte Carlo only whose error is independent of the frequency.

3.2.5 CT-HYB replacement moves for equal-time worm operators

As we have previously mentioned, all correlation functions can in principle be measured using worm sampling. In contrast to that, measuring correlation functions with multiple operators at equal time in partition function sampling is in general not possible as the insertion of local operators is not ergodic in CT-HYB [36]. For the case of

the conventional improved estimator [200], the worm sampling procedure has previously been discussed in Ref. [209], where it was implemented in *w2dynamics* [40] and shown to indeed reduce the asymptotic error in the resulting self-energies and vertex functions in numerical tests. For the practical use of symmetric improved estimators, it is important to be able to measure the necessary multi-operator correlation functions found in (3.11), (3.15), and (3.18) efficiently in CT-HYB.

We first need to add additional worm spaces for each component $k_{\alpha_1 \dots \alpha_n}$ of each correlation function k and have to perform sampling runs in the combined spaces $C_Z \oplus C_{k_{\alpha_1 \dots \alpha_n}}$ for all $k_{\alpha_1 \dots \alpha_n}$ that are necessary to evaluate the symmetric improved estimator equations, which are the components of \mathfrak{D} in the case of the symmetric improved estimator for the one-particle Green's function and additionally those of the correlation functions in (3.11) and (3.18) for the two-particle Green's function. The local weight in worm space is calculated as the trace in (2.22) with $O_{\gamma_1 \dots \gamma_n}$ representing the relevant correlation function, and measurement is then performed by simply counting configurations in analogy to (2.23). As usual the sampling steps in C_Z are used for normalization, which requires an appropriate relative weight factor $\eta_{k_{\alpha_1 \dots \alpha_n}}$ between the configurations of partition function and worm space to achieve a low relative error, conventionally chosen such that the amount of steps is balanced.

In principle, the ‘‘granularity’’ of worm space can be chosen in different ways too. We could e.g. have allowed worm insertions of arbitrary flavors to sample all components $k_{\alpha_1 \dots \alpha_n}$ of a correlation function k at once. Using the example of $\mathfrak{D}_{\alpha\rho}^{\tau_1\tau_2} = \sum_{\beta\gamma\delta\mu\pi\zeta} U_{[\alpha\beta]\gamma\delta} U_{\pi\zeta[\rho\mu]} \left\langle T_\tau c_\beta^\dagger c_\delta c_\gamma c_\pi^\dagger c_\zeta^\dagger c_\mu \right\rangle$, where we have inserted the definitions of the operators q and q^\dagger from (3.12), we currently restrict sampling to single choices of α and ρ per sampling run. This is not necessary, but considering an increase rather than decrease of granularity, it is not necessary to perform the sum $\sum_{\beta\gamma\delta\mu\pi\zeta}$ over internal indices stochastically either. While this at least has the advantage of integrating the prefactors of U directly in the weight, preferring configurations with larger contributions over those with lower ones, we could also do a separate sampling run for each choice of these internal indices instead and perform the linear combination with coefficients of the interaction afterward. The advantage of a high granularity is that different components do not necessarily have the same value and so the number of configurations for which the estimator is evaluated (N_{meas} in *w2dynamics*) that is required to e.g. get a uniform relative error for the entire quantity might be different for each component. Choosing different values is only possible if the sampling is performed separately because the relative amount of configurations per component will otherwise be stochastically chosen roughly according to their relative weights.

An important matter to consider is however that of which moves to perform to ensure ergodic sampling. For a correlation function like ϕ , which consists of two density

operators at two different times and is therefore easy to insert in all positions that lead to non-zero weight, worm insertions and worm removals in addition to the standard moves in partition function sampling (cf. Tab. 2.1) may be sufficient for ergodic sampling. For general correlation functions such as even already a one-particle Green's function itself, it was however shown that using only worm insertions and removals but no replacements leads to ergodicity problems in practice [74]. The reason is the acceptance probability of pair insertion and removal moves, which exponentially decreases with the distance of the operator pair in imaginary time due to quantum number violations [72–74, 103]. The same is also necessarily the case for a function like ϑ , which also inserts operators at two different times in such a way that the superstate sequence is changed, which happens for all operators that are not of the form of a density. The replacement moves described in Tab. 2.1 that fix the ergodicity problems for Green's functions are not directly applicable to worm configurations with multiple operators at equal imaginary time, as replacing one of them with an operator associated with hybridization would change the number of worm operators at equal time and thus not lead to a configuration corresponding to a valid contribution to the measured correlation function.

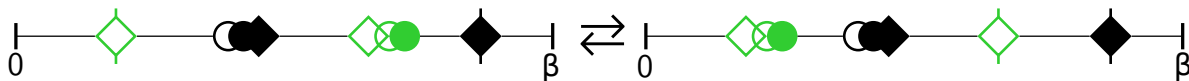


Figure 3.8: Symbolic representation of a replacement move for worm spaces with operators at equal times in the style of the diagrams in Tab. 2.1 with the changed operators marked in green. The three partially overlapping symbols represent a combination of three operators at equal time and different shapes of the operator symbols indicate potentially different flavors. The new replacement move not only exchanges the “worm status” (indicated by short segments at the top and bottom of the symbols representing connection to hybridization events) of the two operators represented by diamonds, but also moves the two other operators at equal time from the former worm operator to the proposed new worm operator.

We therefore introduce new moves analogous to worm replacements that can be used for worm configurations with operators at equal times. Rather than just proposing an exchange of the “worm status” between a randomly chosen worm operator and a randomly chosen operator with hybridization [74], we propose a new configuration by proposing this exchange combined with a shift of all the other worm operators at equal time to the time of the chosen operator with hybridization, symbolically depicted in Fig. 3.8. This effectively swaps the position of the chosen operator with hybridization with the entire combination of operators at equal time by reconstructing the latter at the position of the former. While the change of the bath weight is the same as for a

conventional worm replacement move because none of the worm operators contribute to it and so the combination with a worm shift does not change it, now the local weight changes as well. This could cause a lower acceptance of these moves compared to the conventional worm replacements, but particularly in cases where the other operators may be density-like, such as a replacement of $q = c^\dagger c c$ where one of the annihilators is chosen for the exchange of worm status as in Fig. 3.8, the acceptance rate may be acceptable. In practice, we find that the moves alleviate ergodicity problems in the cases we tested.

3.2.6 Results

In order to demonstrate the correctness and asymptotically smaller statistical error at high frequencies of our implementation of symmetric improved estimators compared to other estimators, we perform calculations for a small system with a discrete bath. This allows us to show the correctness of our results by comparison to those from exact diagonalization, where the Lehmann representations of the correlation functions can be directly evaluated. The statistical error can be determined as the difference of our results for the self-energies and vertex functions to the more precise results from exact diagonalization, which we do for self-energy and full vertex function obtained using the Dyson equation from the one- and two-particle Green's functions determined by means of the naive worm estimator (2.24) and its two-particle equivalent, for the self-energy obtained using the improved estimator (3.10), and for the self-energy and vertex function obtained using the symmetric improved estimators (3.14) and (3.20).

The small system under consideration is an Anderson impurity model with one impurity orbital with zero eigenenergy, a repulsive local intra-orbital interaction of $U = 2$, and a hybridization amplitude $V = 0.3$ with one bath orbital with eigenenergy $\varepsilon = 0.5$ at a chemical potential of $\mu = -0.1$ and inverse temperature of $\beta = 10$, all given in arbitrary internally consistent units. The resulting occupation of the impurity orbital per spin is approximately $n = 0.307$.

For the calculation of the self-energy, we use CT-HYB worm sampling implemented in *w2dynamics* to get the Green's function G and the improved estimator correlation functions ξ and ϑ by measuring 1.44×10^9 configurations each. The results for the self-energy are shown in the left panel of Fig. 3.9 and the difference between each of these results and the exact diagonalization result as a measure of statistical error in the right panel. Note that the statistical error of the QMC results could also be estimated by e.g. calculating the standard error for a number of uncorrelated results, e.g. from multiple runs using different seeds for the random number generator. We can observe that the result obtained using symmetric improved estimators indeed has a statistical error

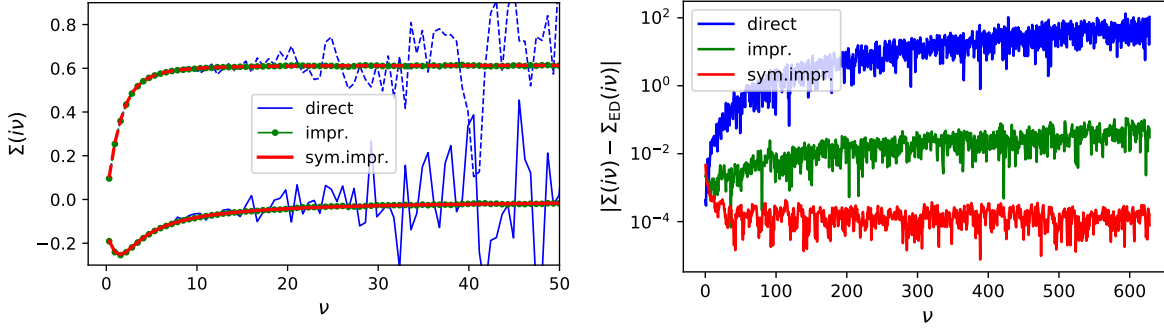


Figure 3.9: Left panel: Self-energy (top: real part, bottom: imaginary part) on the Matsubara frequency axis of the one-orbital Anderson impurity model described in the text calculated using a Green’s function obtained from CT-HYB worm sampling of the standard Green’s function estimator (“direct”), the improved estimator (“impr.”), and the symmetric improved estimator (“sym. impr.”). Right panel: Absolute difference between the self-energies $\Sigma(i\nu)$ from CT-HYB and the self-energy $\Sigma_{ED}(i\nu)$ calculated using exact diagonalization on a logarithmic axis as a measure of the statistical error. In the left panel only the result from direct measurement clearly has an error increasing with the frequency and those from improved and symmetric improved estimators appear visually almost identical on the range of frequencies shown, but the error shown in the right panel clearly increases for the improved estimator and even faster for the standard estimator and is larger than the approximately constant one for the symmetric improved estimator except at a few of the lowest frequencies.

that is approximately independent of the frequency in the high-frequency limit, while those of the conventional improved estimator and standard estimator results increase with the frequency as our scaling analysis using error propagation would suggest. Additionally, for the same number of measurements the error of the symmetric improved estimator result is also smaller by orders of magnitude than either of the other ones except for a small number of the lowest frequencies. There we find instead that the standard estimator result has a smaller error than either of the improved estimator results for the same number of measured configurations. While often just the very first Matsubara frequency is affected and the error of the improved estimator results are also not extraordinarily large, results from the standard worm or even partition function sampling estimator could be used in combination with improved estimators to improve the results, e.g. by replacing the first few frequencies or performing a weighted average. Since we sample in combined worm and partition function configuration space anyway for normalization, the standard partition function sampling estimator for the Green’s function can even be evaluated in the same sampling run.

We further measure the two-particle Green’s function G and the seven correlation

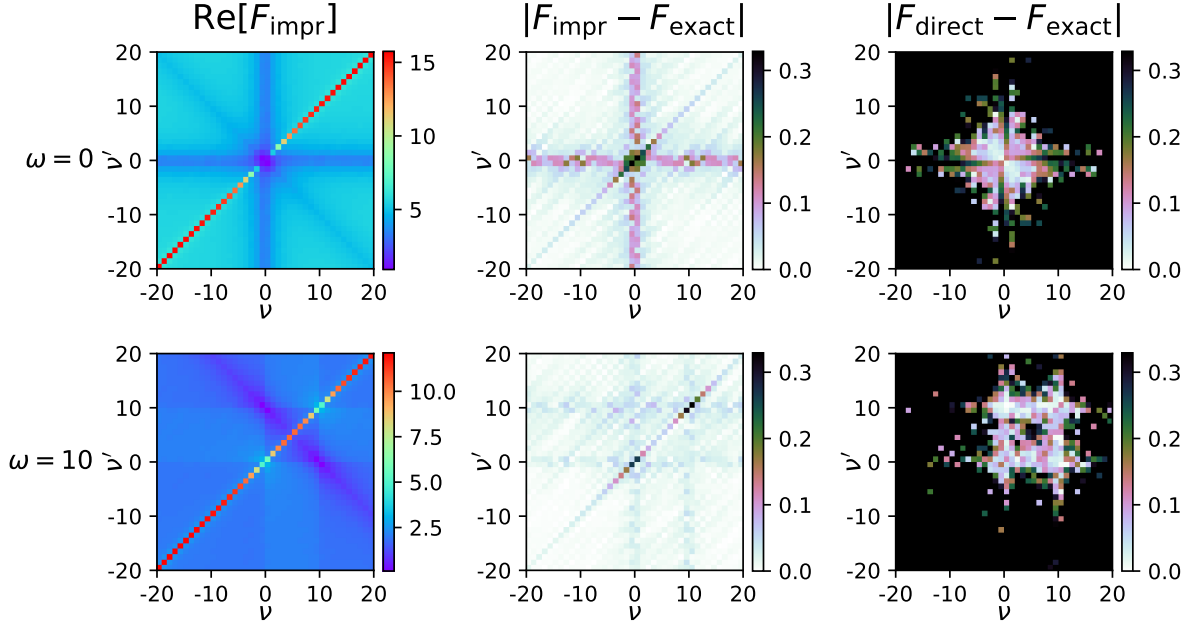


Figure 3.10: Real parts with symmetric improved estimators (left panels), absolute differences between symmetric improved estimator results and exact diagonalization results (middle panels), and absolute differences between standard estimator results and exact diagonalization results of the full vertex function $F_{\uparrow\uparrow\downarrow}^{v\nu'\omega} = F_{\uparrow\uparrow\downarrow}^{v,(v-\omega),(v'-\omega),\omega}$ from CT-HYB measurement as a color grid plot of matrix values with the fermionic Matsubara frequency arguments ν and ν' as axes for bosonic Matsubara frequency argument $\omega = 0$ (top panels) and the tenth positive bosonic Matsubara frequency $\omega = 20\pi/\beta$ (bottom panels). In the vertex function obtained using symmetric improved estimators, there is no visually recognizable noise and its statistical error, i.e. the absolute difference from the exact result, is approximately constant for high Matsubara frequencies. The error of the vertex function obtained using the standard two-particle Green's function estimator increases with the frequency instead. The error of the symmetric improved estimator result seems to have systematic features that are likely caused by different statistical errors of the contributions to the estimator depending on which of the seven measured correlation functions they originate from.

functions $\xi, \vartheta, \phi, \psi, f, g, h$ entering into the symmetric improved estimator expression (3.20) to get the full vertex according to (3.22). Results and their statistical errors are shown in Fig. 3.10, where we consider the full vertex $F_{\uparrow\uparrow\downarrow}^{v\nu'\omega}$ as a function of three frequency arguments, related to the vertex as a function of four frequency arguments by $F_{\uparrow\uparrow\downarrow}^{v\nu'\omega} = F_{\uparrow\uparrow\downarrow}^{v,(v-\omega),(v'-\omega),\omega}$, at two fixed bosonic frequencies and show the matrix elements of the real part of the symmetric improved estimator result as well as of its statistical error and of the statistical error of the result obtained using the standard estimator as color-coded image with the two Matsubara frequencies as axes. As expected from

our scaling considerations, the statistical error of the result obtained using the standard estimator quickly diverges for higher Matsubara frequencies while the error of the symmetric improved estimator result does not increase for higher frequencies. The error with symmetric improved estimators seems to be slightly higher for the lowest frequencies just like for the self-energy and additionally, there seem to be systematic patterns in the error related to prominent features of the vertex function. The cause of this is likely a significantly different statistical error for different contributions to the vertex, as the prominent features at positions distinguished by symmetry are more likely to come from the reducible contributions that are calculated from several of the various measured correlation functions.

3.2.7 Conclusions

In conclusion, we found that the bad scaling of CT-HYB self-energy and vertex results in the high-frequency limit can be corrected by the use of symmetric improved estimators. We calculated equations of motions for the one- and two-particle Green's function by differentiating with respect to all time arguments to derive the symmetric improved estimator equations and showed how to perform efficient worm sampling for the occurring correlation functions in CT-HYB. We find a frequency-independent and mostly significantly reduced error, but standard estimators seem to converge slightly faster than improved estimators for a small number of the lowest frequencies.

4 Magnetic impurities on metallic surfaces

4.1 Analysis of the influence of the interaction parameterization on Kondo screening in cobalt adatoms

In this section, we analyze a prototypical example of a system exhibiting the Kondo effect: cobalt impurities on a copper surface. Using density functional theory we parameterize an Anderson impurity model that we solve using continuous-time quantum Monte Carlo as a first-principles approach to the problem. We perform calculations using multiple parameterizations of the local interaction in a temperature range around the experimentally determined Kondo temperature and find a remarkably strong influence of the form of the interaction on the screening. Depending on the used interaction, the Kondo temperatures range from values in the right order of magnitude in the case of the most realistic full spherical Coulomb interaction to values at least two orders below it. In the most realistic case, we find that the picture of just two d -orbitals aligned by Hund's coupling forming a local spin-1 moment often assumed in the literature is inaccurate and instead, the contribution of other orbitals is significantly enhanced by the inclusion of more interaction terms.

This section is based on the following article, Ref. [183], which is also the source of the figures

*A. Valli, M. P. Bahlke, A. Kowalski, M. Karolak, C. Herrmann, and G. Sangiovanni,
"Kondo screening in Co adatoms with full Coulomb interaction,"
Phys. Rev. Res. 2, 033432 (2020)*

4.1.1 Kondo effect in cobalt impurities on copper surfaces

The Kondo effect was first observed in the 1930s as an increase of the resistivity of metals toward zero temperature [217] and later explained by Kondo in 1964 [28]. It occurs in metals hosting magnetic impurities due to enhanced scattering of conduction electrons off the impurities below a Kondo temperature T_K , with a scattering amplitude

that diverges to leading order of perturbation theory as the temperature is reduced [28]. The many-body ground state at low temperatures is a collective bound state in which the local spin of the impurity is coupled with opposite conduction electron spins to a singlet [218–221], which effectively screens the magnetic moment of the impurity. In the microscopic physics of an impurity, the Kondo effect manifests itself in the appearance of the Abrikosov-Suhl (or Kondo) resonance [222–224], a spectral feature pinned to the Fermi level that originates from the renormalization of the level on the impurity through quantum many-body effects [225]. In an effort to improve upon perturbative descriptions of the Kondo problem, renormalization-based techniques such as Anderson’s “poor man’s” scaling theory [226] and Wilson’s numerical renormalization group [57] were later applied to the problem. Particularly the latter is able to provide a precise solution including e.g. the functional form of the susceptibility. Due to the local magnetic moment, it is a Curie-Weiss susceptibility at high temperatures that crosses over to a constant Pauli susceptibility as the moment is screened and effectively disappears around the Kondo temperature. Changes in the magnetic response and spectrum of the impurity are therefore indicators of the Kondo effect, which we will consider in our investigation. Due to its nature as a low-temperature quantum many-body effect with strong electron correlation, the theoretical treatment of realistic Kondo systems such as transition metal impurities with electrons in the localized $3d$ -shell carrying a moment is numerically difficult [36].

Among the most investigated cases of the Kondo effect believed to be both experimentally and theoretically relatively well understood are single cobalt impurity atoms on metallic surfaces. Using scanning tunneling microscopy (STM), studies of cobalt impurities on surfaces such as copper [227–230], gold [231], and silver [232] have been performed. With this kind of experimental setup, it has become possible to detect the resonance at the Fermi level directly by tunneling into it rather than inferring its existence from the decrease in the conductance of a metallic sample with impurities due to enhanced scattering [231, 233, 234]. The Kondo resonance is generally expected to manifest itself in a spectrum measured with an STM in the form of a Fano line shape [235, 236] in the differential conductance at zero bias [227–232, 237–239], although there are indications that a recent alternative interpretation of this feature in terms of spin excitations and proposed “spinaron” quasiparticles resulting from their interactions with electrons, strongly affected by spin-orbit coupling, may be more appropriate [240–242].

For the case of a cobalt impurity adsorbed on a Cu(001) copper surface (a cobalt *adatom*) that we consider here, previous theoretical studies have demonstrated a particular importance of two of the five cobalt $3d$ -orbitals [243–245]. These so-called Kondo-active orbitals d_{xy} and d_{z^2} are close to half-filling and therefore most responsible for the magnetic moment of the impurity, while the other orbitals are full and so relatively

inert at a total filling of eight electrons in the $3d$ -shell. The observed STM line shapes and Kondo temperatures do however have a strong dependence on various factors, from the environment of the impurity [246, 247] dependent e.g. on the type of surface, exemplified by the differences between the Cu(001) and the Cu(111) surfaces [230, 243, 245], to the occupation of the $3d$ -shell [228, 230, 232, 239, 244], which is connected to material and setup properties like the adatom adsorption distance and STM tip distance [182, 229, 230, 239, 245]. Such influences on the Kondo temperature can make its theoretical prediction difficult since it depends on system parameters exponentially [248].

Theoretical calculations for cobalt impurities have so far indicated a $S = 1$ high-spin state on both the Cu(001) and the Cu(111) surface [244, 245], which was actually shown in a scaling calculation by Nevidomskyy and Coleman [249] to be associated with a reduction of the Kondo temperature by orders of magnitude compared to the $S = 1/2$ case in agreement with the experimentally known relation between impurity spin and Kondo temperature [250]. Some of the recent calculations do however indicate different Kondo temperatures for each of the two involved orbitals [244, 245], pointing to an underscreened Kondo effect instead [244], with estimated Kondo temperatures that are in rough qualitative agreement with experimental ones [244, 245], found to be 88 K for the system on the Cu(001) surface with the STM tip distance in the tunneling regime specifically [228].

There are indications that actually the entire $3d$ -shell may be important for Kondo screening in cobalt on copper [251] and that a simplified parameterization of the local interaction may be insufficient [252], but these results originate from calculations performed for temperatures considerably above the Kondo temperature. We are not aware of any more careful analysis of such effects since then, and in fact many of the theoretical studies of the system since then would not have been suitable anyway because they e.g. focused on the two “Kondo-active” orbitals only [245], used an approximative solution of the Anderson impurity model (AIM) [244], or were performed for lower but possibly still insufficient temperatures [239]. Our interest in this investigation is to follow up on the earlier indications with a comprehensive account of Kondo screening in a cobalt impurity on a Cu(001) surface that treats the entire local $3d$ -shell using numerically exact continuous-time quantum Monte Carlo calculations for temperatures at and below the experimentally determined Kondo temperature. We compare the influence of different interaction parameterizations on the contribution of the whole $3d$ -shell to the spin moment, its screening, and on the spin and charge correlations between the orbitals and discuss the consequences for the description of the Kondo effect in this system.

4.1.2 First principles DFT+AIM approach

For our calculations, we employ a first-principles approach that uses density functional theory (DFT) in the local density approximation (LDA) to provide a realistic parametrization of an Anderson impurity model [253] describing the cobalt adatom as impurity coupled to the surface via the hybridization term. Local correlations on the impurity atom, which DFT alone cannot capture, are treated numerically exactly using CT-HYB as implemented in *w2dynamics*. This DFT+AIM approach [182], cf. also the procedures used in e.g. Refs. [239, 251, 254, 255] and others, may be considered as similar in spirit to other methods called DFT++ in the literature [65], but we should carefully note that it is distinct from and not to be confused with DFT+DMFT in particular. This approach, more traditionally associated with the term DFT++, has a different goal, namely to improve the DFT lattice solution by including the effect of strong correlations. This may also involve the CT-HYB solution of an AIM, but that model is just an iteratively updated auxiliary model onto which the lattice is mapped, turning one site of the lattice into a correlated impurity coupled to the rest of the lattice sites as bath. As discussed in Sec. 2.3, such an application of DMFT to a finite-dimensional lattice is only an approximation.

For the numerically exact solution of the cobalt adatom system, we instead extract parameters for an AIM modeling an actual impurity problem, where the impurity and bath are physically different parts of a real system instead of an auxiliary division. CT-HYB performs the solution of correlation effects on just the part selected as impurity, which is also fixed instead of self-consistently updated and does not have any feedback into the lattice model.

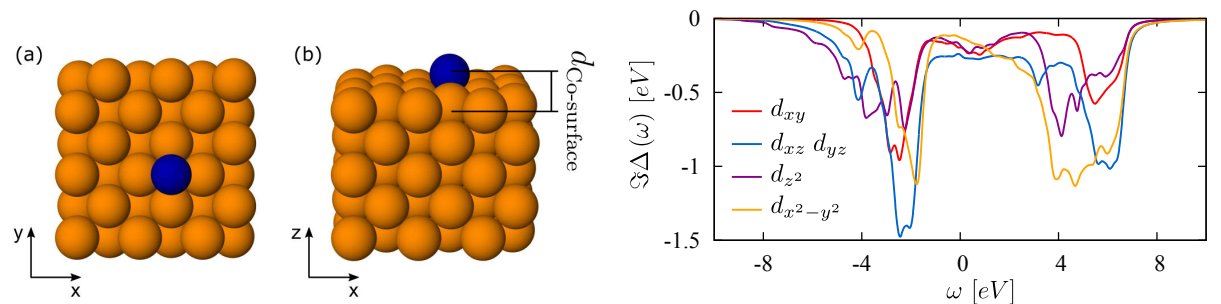


Figure 4.1: Left panels: Unit cell used for DFT calculations with the Cu(001) surface (orange) with the Co adatom (blue) viewed from the top (a) and the side (b). Right panel: Imaginary part of the orbital-resolved (diagonal) hybridization function on real frequencies extracted from DFT calculation as input for the CT-HYB impurity solver.

VASP [256, 257] with the projector-augmented plane wave (PAW) [257, 258] basis set was used to perform DFT calculations for a supercell of $4 \times 4 \times 1$ unit cells of five surface

orbital	crystal field $\epsilon_i + \text{Re}(\Delta_i(\infty))(\text{eV})$	$\Gamma_i(\text{eV})$
d_{xy}	-0.226	0.196
d_{xz}	-0.403	0.244
d_{z^2}	-0.295	0.180
d_{yz}	-0.403	0.244
$d_{x^2-y^2}$	-0.221	0.128

Table 4.1: Effective crystal field and coupling to the substrate (Fermi level value of the full hybridization shown in Fig. 4.1) determined for the localized $3d$ -orbitals included in the AIM for the Co impurity using DFT.

layers of Cu atoms and a Co impurity in the fourfold-hollow position, shown in the left panel of Fig. 4.1. The experimentally determined [259] lattice constant of 3.615 \AA was used for copper and an adsorption distance optimized in a previous DFT++ study [182] of 1.52 \AA consistent with other ab initio determinations [243] was used for the distance of the cobalt impurity to the topmost layer of the Cu(001) surface. A dense k -mesh of $100 \times 100 \times 1$ points around the zone center was used because a closer examination showed slow convergence of the resulting hybridization functions with the size and qualitative differences in CT-HYB self-energies at low temperatures for a too sparse mesh, cf. Appendix A of Ref. [183]. The hybridization function on real frequencies and the quadratic part of the impurity Hamiltonian, i.e. effectively something like crystal field splitting, are determined from $g_{ij}(\omega)$, the projection of the DFT real-frequency Green's function onto the subspace of localized orbitals of the impurity, according to $g_{ij}(\omega) = ((\omega + i0^+)\delta_{ij} - \epsilon_{ij} - \Delta_{ij}(\omega))^{-1}$ [182, 260, 261]. The energy levels from the crystal field are given in Tab. 4.1 and the imaginary parts of the hybridization function are shown in the right panel of Fig. 4.1 and agree with previously used ones [244].

With the hybridization function transformed to Matsubara frequencies and the local levels, the only remaining part of the AIM to be specified is the local electron-electron interaction of the cobalt $3d$ orbitals. We employ three different levels of complexity (and thus accuracy, but also numerical effort) of the interaction in order to investigate the impact of an approximated interaction on the physical results. The form of the interaction has already been shown to be quantitatively important in a study of a similar system, but calculations were performed far above the Kondo temperature [252] in contrast to the low temperatures we are able to reach. The three forms of the interaction we use are the density-density interaction consisting of density operators only, an interaction of Kanamori form [41] that additionally includes spin-flip and pair-hopping terms, and the full spherically symmetric Coulomb interaction without any further approximation. These were previously discussed in Sec. 2.1, and their matrix elements and the processes associated with them are more closely considered later in Sec. 4.1.7.

The former two interactions are specified by the intraorbital repulsion U_{ii} , opposite-spin interorbital repulsion U_{ij} and Hund's coupling J_{ij} . Since we assume a spherically symmetric interaction for the orbitals of the cobalt impurity atom, which excludes potential further effects specific to the copper substrate, the full Coulomb interaction for the d -shell can be specified in terms of the first three Slater radial integrals F^0 , F^2 and F^4 [262, 263]. Additionally, we use $F^4/F^2 \approx 5/8$ as a good approximation for $3d$ orbitals, cf. Refs. [39, 264–267], such that we have a total of two parameters for our full Coulomb interaction, $U_S = F^0$ and $J_S = \frac{1}{14}(F^2 + F^4)$, cf. Refs. [39, 268]. These are not to be confused with other U and J (or U_K and J_K) parameters occasionally used, cf. Refs. [39, 268]. We generate our interaction matrix using values of $U_S = 4.0$ eV and $J_S = 0.9$ eV, cf. e.g. [38, 269] and in agreement with the elements for this specific system computed within the ab initio constrained random phase approximation (cRPA) [37] in Ref. [244]. Matrices for the less complex Kanamori and density-density interactions are obtained by not including matrix elements of the full Coulomb interaction matrix associated with processes not contained in the simpler interactions, cf. Sec. 4.1.7. Since the form of the double counting correction, which takes into account the correlation energy that was already included in the DFT calculation, is not known, we usually choose to apply a chemical potential of $\mu_{\text{DC}} = 28.0$ eV to fix the occupation of the cobalt $3d$ -orbitals [260] to $n_d = 8.0$. This was determined by first-principles calculations [243] and is connected to a $S = 1$ spin state of the impurity [244, 245, 270], but we also discuss the influence of slight deviations from this filling on the screening properties [244].

4.1.3 Outline of the resulting picture

Since high-spin configurations of the impurity dominate, Hund's coupling J is expected to have a significant influence on the behavior of the system. As the effect of Hund's coupling depends particularly on the form of the interaction, cf. e.g. [271, 272], we are led to a systematic analysis of the differences in the Kondo screening mechanism due to the interaction parameterization. Our core results, which we later present in detail, are collected in the schema shown in Fig. 4.2 with complexity and accuracy of the interaction parameterization increasing from top to bottom in the entire diagram.

Focusing first on the left panel, we consider the occupation of the $3d$ -shell. In the density-density interaction, a strong effect of Hund's coupling maximizes the spin and polarizes the orbital occupation. This results in half-filling of the Kondo-active orbitals d_{xy} and d_{z^2} (cf. Ref. [244, 245], but with a relative 45° rotation of the $x - y$ coordinate plane) while the others are full and not contributing to the Kondo physics. More complex interactions introduce additional matrix elements associated with processes that allow the electrons to hop, cf. Sec. 4.1.7, and lead to a more even spread of the

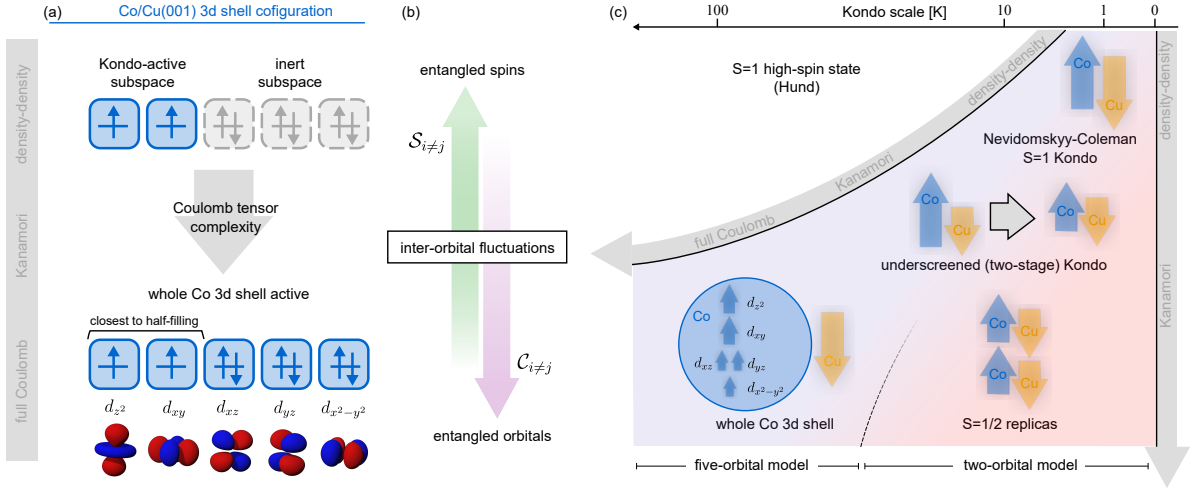


Figure 4.2: A schematic summary of our analysis of the influence of the interaction parameterization on the calculation results for the Co/Cu(001) impurity system, with complexity and accuracy of the interaction parameterization increasing from top to bottom. Left panel: For density-density interaction, the $3d$ -shell can relatively cleanly be separated into the Kondo-active half-filled d_{xy} and d_{z^2} orbitals and the other full orbitals. When more complex parameterizations are used, the exchange of electrons between orbitals increases and consequently the orbitals become less independent and the occupations less polarized. Middle panel: With density-density interaction, Hund's coupling maximizes the interorbital spin fluctuations $S_{i \neq j}$, while the additional interaction matrix elements of the more complex interaction parameterizations favor interorbital charge fluctuations $C_{i \neq j}$. Right panel: Kondo screening processes with different interactions leading to screening in different temperature regimes. With density-density interaction, Hund's coupling locks the two spins of the Kondo-active orbitals into a high spin state pushing the Kondo screened regime (colored background) down to very low temperatures as the Nevidomskyy-Coleman scaling theory for high spin explains [249]. As charge fluctuations increase with more complex interactions, we may have a description in terms of an underscreened or two-stage Kondo effect with higher T_K or a more complex Kondo effect due to the charge redistribution across the entire $3d$ -shell with concomitant enhancement of T_K in general. For a two-orbital model (that is not considered here), the upper limit of T_K is reached in the case of two independent replicas of the $S = 1/2$ Kondo effect.

occupation across the shell. In short, as symbolized by the middle panel, the simpler parameterization favors spin fluctuations and the more complex exchange terms favor charge fluctuations.

For the simple density-density interaction, the promotion of the high-spin $S = 1$ state by Hund's coupling pushes the Kondo temperature T_K down to very low temperatures as explained by the scaling theory of Nevidomskyy and Coleman [249], consistent with

the relationship between high spin and exponential reduction of the Kondo scale discovered earlier in experiments [250]. Consequently, the breakdown of the high-spin state induced by the enhancement of charge fluctuations and concomitant suppression of spin fluctuations (due to the introduction of further interaction matrix elements) enhances T_K . For more complex interactions, the Kondo effect must be explained by an alternative scenario and we might envisage several possibilities with the intention of identifying their signatures in the numerical results. A first observation is that Hund's coupling no longer locks the spins of the active orbitals, so we might instead have a two-stage Kondo effect with an underscreened regime [273] at intermediate temperatures, or the two orbitals might behave as two independent spin-1/2 replicas. Moreover, the previously inert orbitals are now also available, so we are no longer limited to just the two ones active in the density-density case. This could lead to a spin-orbital Kondo effect [274–276] with $SU(N)$ symmetry for some N depending on orbital degeneracy, which should result in a single and enhanced T_K [277]. All these proposed variants are in principle consistent with high $T_K = 70\text{--}100$ K determined in transport experiments using scanning tunneling microscopy [228, 229, 232].

4.1.4 Spin susceptibility and moment

As direct indicators of the Kondo screening, we shall consider quantities such as the imaginary time spin-spin correlation function that we can directly measure for the AIM in CT-HYB,

$$\chi_{ij}(\tau) = g^2 \langle S_{z,i}(\tau) S_{z,j}(0) \rangle, \quad (4.1)$$

with the electron g - or spin gyromagnetic factor g and $S_{z,i}(\tau)$ the spin z -component operator for impurity orbital i at imaginary time τ . We can integrate this quantity over imaginary time to get the orbital-resolved static spin susceptibility

$$\chi_{ii}^{\omega=0}(T) = \int_0^\beta \chi_{ii}(\tau) \quad (4.2)$$

that we previously considered in the exemplary application in Sec. 3.1, where $T = \beta^{-1}$ is the temperature.

We show the orbital-resolved static spin susceptibilities $\chi_i^{\omega=0}(T)$ of the orbitals d_{xy} and d_{z^2} closest to half-filling for all parameterizations of the interaction in Fig. 4.3 together with an inset showing $T\chi_i^{\omega=0}(T)$. This quantity is linear for the constant Pauli susceptibility [278] in the screened regime and approximately constant for Curie-Weiss [279] behavior $\propto (T + T_K)^{-1}$ of unscreened local moments above the Kondo temperature T_K [192, 280–282]. It is easily recognizable in the figure and its inset that the susceptibility in the case of density-density interaction is by far the closest to $\propto 1/T$ for both

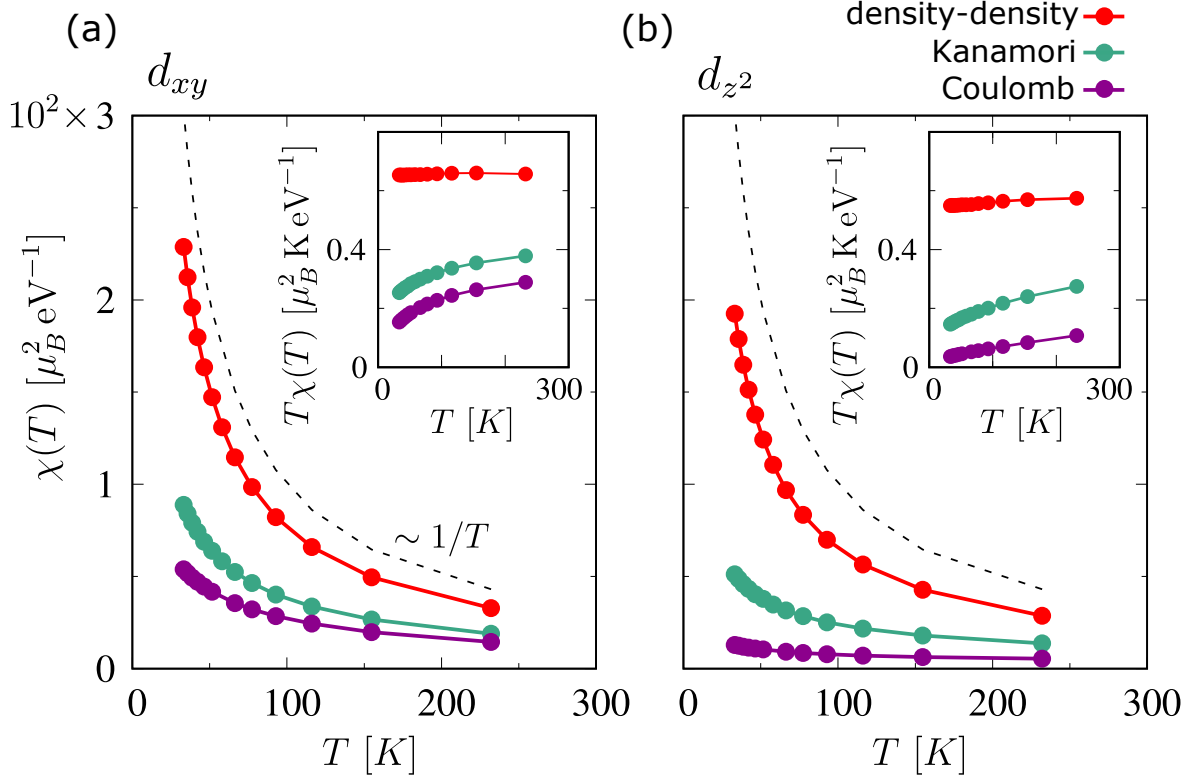


Figure 4.3: Diagonal orbital-resolved static spin susceptibility $\chi_{ii}^{\omega=0}(T)$ of the d_{xy} (left panel) and d_{z^2} (right panel) orbitals closest to half-filling. Calculated data for all parameterizations of the interaction are shown in addition to a Curie law curve $\propto 1/T$ for comparison. The inset shows $T\chi(T)$, which allows easy visual differentiation between Pauli ($T\chi_{ii}^{\omega=0}(T) \propto T$) and Curie-Weiss scaling ($T\chi_{ii}^{\omega=0}(T) \sim \text{const.}$).

orbitals and thus the Kondo scale the lowest, which is also reflected in only minimal deviations of $T\chi$ from constant behavior down to even the lowest temperatures we reach, about $T = 30$ K. From this we conclude that the Kondo temperature is considerably lower than 30 K in this case. As the accuracy of the interaction parameterization is increased, the local susceptibility is reduced considerably and Kondo screening becomes recognizable in the range of temperature we consider by the curvature of $T\chi$ toward the origin, i.e. crossover to Pauli susceptibility. For full Coulomb interaction, the scaling at the lowest temperatures is still clearly more linear than for Kanamori interaction, so the Kondo scale with full Coulomb interaction is the highest. As far as orbital dependence is concerned, we can observe that $T = 0$ extrapolations are closer to zero for the d_{z^2} orbital than for the d_{xy} orbital for all interactions, so the Kondo scale is lower for the latter.

With full Coulomb interaction, the d_{z^2} orbital even seems to have approximately reached Pauli behavior at the lowest temperatures indicating a Kondo temperature

around 30 K. We try to make a quantitative estimate of the Kondo temperatures by fitting the diagonal orbital-resolved static spin susceptibilities using Wilson’s numerical renormalization group result for the one-channel spin-1/2 Kondo problem in the intermediate temperature range around the Kondo temperature T_K [57, 268],

$$\chi(T) = \frac{\mu^2}{3k_B(T + 2T_K)}, \quad (4.3)$$

where μ is considered as the effective impurity spin of approximately the order of the Bohr magneton μ_B and we extract both μ and T_K from the fit. We separate out a factor of three in the denominator because we consider the correlation function of the spin z -component only [192], cf. our discussion of the moment below in this section. The fit results in Kondo temperatures below 1 K for the density-density interaction, Kondo temperatures of $T_K^{d_{xy}} = 8.5$ K and $T_K^{d_{z^2}} = 14$ K for Kanamori interaction, and $T_K^{d_{xy}} = 18$ K and $T_K^{d_{z^2}} = 40$ K for full Coulomb interaction. With the value for the d_{z^2} orbital obtained using the full interaction, we finally reach about the order of magnitude of the experimental value of $T_K = 70\text{--}100$ K [229].

A more differentiated analysis of the moment screening can be performed by considering the local spin susceptibility $\chi_{ij}(\tau)$ in imaginary time. While its value at $\tau = 0$ indicates the instantaneous magnetic moment, its value at its minimum at $\tau = \beta/2$ gives us information of the moment dynamically screened over long time scales [195, 196], which e.g. decays quickly to 0 for a Fermi liquid as T goes to zero and should remain high in the case of unscreened moments [283].

Apart from helping us to visualize the screening in a similar way to $T\chi(T)$, the individual elements of this matrix in orbital space also tell us to what extent the individual orbitals of the strongly correlated $3d$ -shell are contributing to the moment and its screening. We prepare this data in the form of (the square of) the magnetic moment with contributions from all orbitals and broken down into diagonal and offdiagonal contributions in the Kondo-active subspace only as well as an “effective spin” $S_{\text{eff}}(\tau)$ computed from the all-orbital magnetic moment, to be interpreted like a spin quantum number but not necessarily integer and including screening for $\tau = \beta/2$.

Importantly, it also makes the moments computed with the different interaction parameterizations comparable by factoring in the nature of the spin for density-density interaction as an “Ising spin” with \mathbb{Z}_2 symmetry in contrast to the “Heisenberg spins” with full $SU(2)$ rotational invariance for Kanamori and Coulomb interaction. Concretely, this means that while there is no distinguished direction for the latter and so the square of the magnetic moment is

$$m_{\text{Heisenberg}}^2 = g^2 \left(\langle S_x^2 \rangle + \langle S_y^2 \rangle + \langle S_z^2 \rangle \right) = 3g^2 \langle S_z^2 \rangle, \quad (4.4)$$

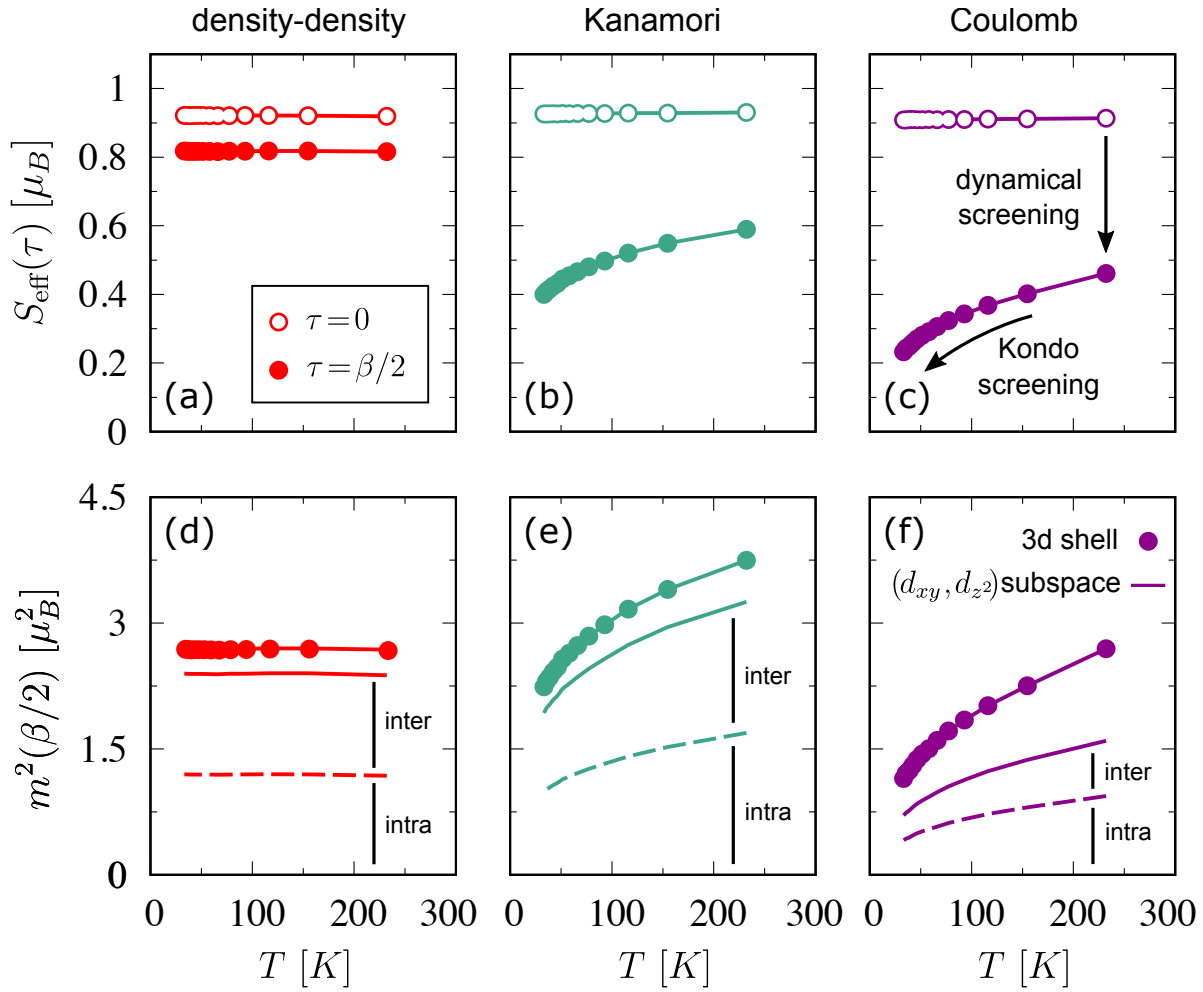


Figure 4.4: Unscreened instantaneous ($\tau = 0$) and dynamically screened ($\tau = \beta/2$) effective spin (top panels) and screened squared magnetic moment $m^2(\tau = \beta/2)$ (bottom panels) for density-density (left panels), Kanamori (middle panels) and full Coulomb (right panels) interaction parameterizations. Note the smaller moment but still comparable effective spin for density-density due to different Ising spin relations (4.5) and (4.7). The difference between $\tau = 0$ and $\tau = \beta/2$ values represents the dynamical screening of the moment by quantum fluctuations over long time scales, while the reduction of the screened moment with decreasing temperature is its Kondo screening, both of which are more effective with more accurate interactions. Symbols mark values obtained from all contributions of the entire $3d$ -shell. In the lower panels, the dashed lines give just the diagonal (intraorbital) contributions from the $\{d_{z^2}, d_{xy}\}$ subspace and the solid lines without symbols all contributions from that subspace including offdiagonal (interorbital) ones.

for the Ising spin only the component in z -direction is relevant, giving us

$$m_{\text{Ising}}^2 = g^2 \langle S_z^2 \rangle \quad (4.5)$$

with a difference by a factor of three. For the analysis of screening, we define a generalization of the square of the magnetic moment to arbitrary imaginary time differences as

$$m^2(\tau) = \xi \sum_{ij} \chi_{ij}(\tau), \quad (4.6)$$

where $\xi = 1$ for density-density interaction, $\xi = 3$ for rotationally invariant interaction, and the indices i and j run in general over all orbitals and for the contribution analysis just over the Kondo-active subspace $\{d_{z^2}, d_{xy}\}$ (for which we will occasionally still use that name even though its dominant role is significantly reduced with complex parameterizations of the interaction). Using either the equation

$$m^2(\tau) = g^2 S_{\text{eff}}^2(\tau) \quad (4.7)$$

in the case of the Ising spin for density-density interaction or the usual equation for a quantum mechanical spin

$$m^2(\tau) = g^2 S_{\text{eff}}(\tau)(S_{\text{eff}}(\tau) + 1) \quad (4.8)$$

in the other cases, we define the effective spin $S_{\text{eff}}(\tau)$ (as its positive solution) [283].

Values of the unscreened or instantaneous ($\tau = 0$) and screened ($\tau = \beta/2$) effective spin as well as the screened squared magnetic moment $m^2(\tau = \beta/2)$ are shown for all three interactions in the upper and, respectively, lower panels of Fig. 4.4. We find that the unscreened effective spin is just slightly above 0.9 as expected if the high-spin $S = 1$ configuration dominates [244] and independent of the temperature and interaction as we should reasonably expect due to the absence of screening. The agreement between the interaction parameterizations demonstrates the necessity of the different treatment of Ising and Heisenberg spins for comparability: although it can be inferred from the values of the dynamically screened moment $m^2(\tau = \beta/2)$ shown in Fig. 4.4 that the instantaneous moment $m^2(\tau = 0)$ is smaller for density-density interaction than for the others, the combination of the different formulas (4.4) and (4.5) for the moment and its different relations (4.8) and (4.7) to S_{eff} still results in the same unscreened effective spin.

Dynamical screening due to quantum fluctuations over long time scales reduces the effective spin drastically differently depending on the interaction parameterization. For density-density interaction, the screened effective spin remains at slightly more than 0.8, relatively close to the unscreened value, over the entire temperature range we consider. This is consistent with our observation of no Kondo screening at these temperature if density-density interaction is used. For the other interaction parameterizations on the other hand, we observe considerable dynamical screening compared to the in-

stantaneous effective spin even at our highest temperature around room temperature by about a third for Kanamori interaction and about half for Coulomb interaction. Furthermore, we observe a significant additional reduction as we go to lower temperatures, i.e. the effect of Kondo screening. Thus, while all cases exhibit an unscreened spin around one, only with the density-density interaction the strong suppression of T_K with spin as explained by Nevidomskyy and Coleman [249] actually sets in while the additional interaction matrix elements destabilize the high-spin state earlier. In agreement with our analysis of the static local susceptibility, the Kondo screening with full Coulomb interaction is more effective at higher temperatures than that with Kanamori interaction.

In the lower panels of Fig. 4.4 with the squared magnetic moment, we also show its decomposition into orbitally diagonal (intraorbital) and orbitally offdiagonal (interorbital) contributions in the Kondo-active $\{d_{z^2}, d_{xy}\}$ subspace and the rest. For density-density and only slightly less for Kanamori interaction, we find that the moment almost exclusively originates from the Kondo-active subspace with similar intra- and interorbital contributions. For the full Coulomb interaction, the contributions due to the two-orbital subspace only account for about two thirds of the total moment any more with the rest involving the other orbitals as well. In this case, the whole $3d$ -shell must be considered for an accurate description of the Kondo screening. We further find the interorbital contributions slightly reduced compared to the intraorbital ones. These effects of the full Coulomb interactions are explained by the tendency of its matrix elements to favor charge fluctuations and to suppress the spin-aligning effect of Hund's coupling, which we consider next.

4.1.5 Charge and spin fluctuations

In order to quantify the influence of the interaction parameterization on spin and charge fluctuations, we consider generalized double occupations of the form $\langle n_{i\sigma} n_{j\sigma} \rangle$ for parallel and $\langle n_{i\sigma} n_{j\bar{\sigma}} \rangle$ for antiparallel spins of orbitals i and j , symmetrized over spins and under exchange of orbitals $i \leftrightarrow j$. The diagonal elements for parallel spins further indicate the orbital-resolved occupations (since $n_{i\sigma}^2 = n_{i\sigma}$) and the diagonal elements for antiparallel spins the tendency toward double occupation of an orbital. A plot of the 5×5 matrix elements per interaction and relative orientation are shown in the form of heat maps in Fig. 4.5 for our lowest temperature data at approximately 33 K. We found no significant change with temperature over the entire range we considered. Our analysis should therefore hold for a considerable temperature range of at least about 30–300 K if not more.

Considering first the occupations, we find in the case of density-density interaction

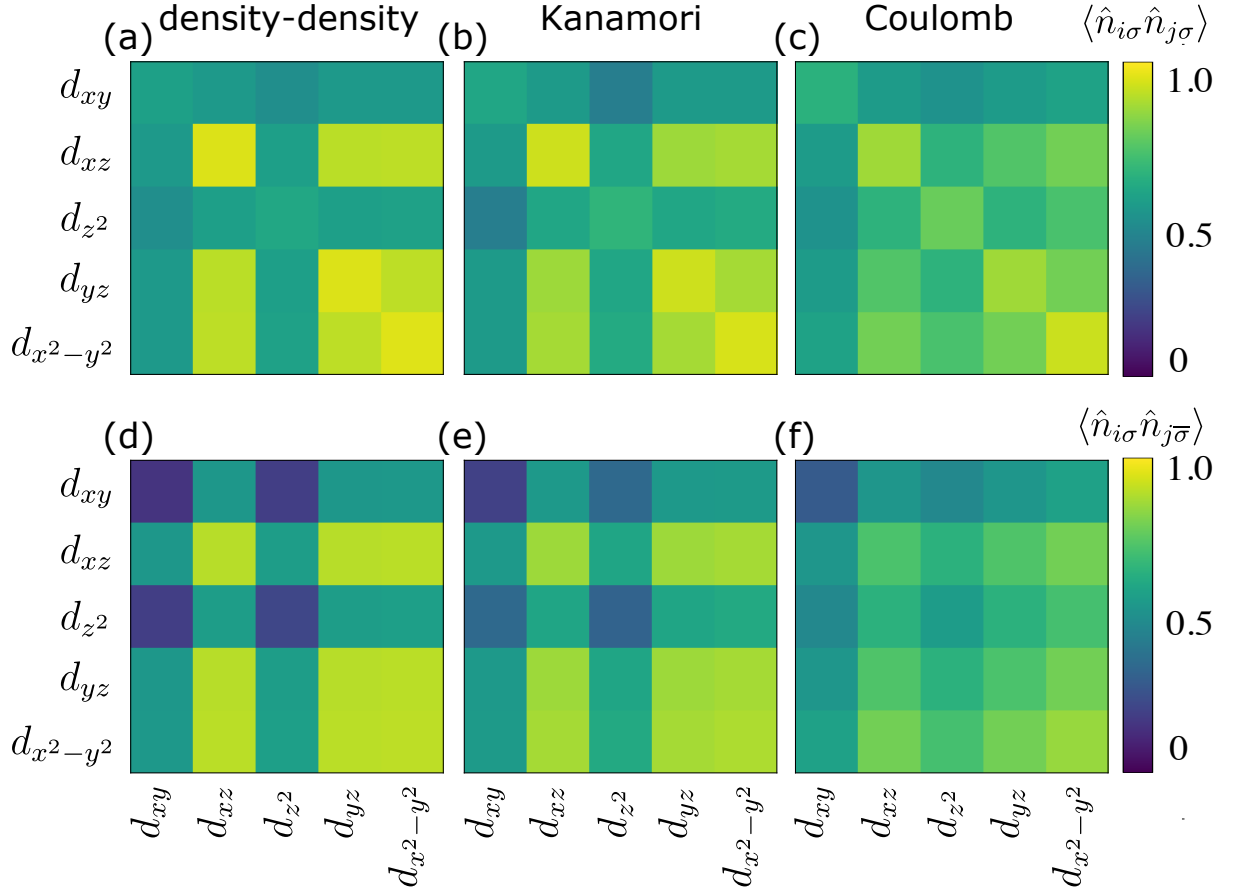


Figure 4.5: Double occupations $\langle n_{i\sigma} n_{j\sigma} \rangle$ for parallel spins (upper panels) and $\langle n_{i\sigma} n_{j\bar{\sigma}} \rangle$ for antiparallel spins (lower panels) between all orbitals of the Co $3d$ -shell, symmetrized over spins and under exchange of orbitals, for density-density (left panels), Kanamori (middle panels), and Coulomb (right panels) interaction at our lowest temperature of 33 K and approximately valid over our entire range of temperatures.

that the two Kondo-active orbitals are approximately half-filled and the others approximately full, confirming that it could be reasonable to consider the $\{d_{z^2}, d_{xy}\}$ subspace only [243, 245]. However, the occupations even out for Kanamori interaction, with those of the $\{d_{z^2}, d_{xy}\}$ subspace changing from $n_{d_{z^2}} = 0.60, n_{d_{xy}} = 0.57$ with density-density interaction to $n_{d_{z^2}} = 0.65, n_{d_{xy}} = 0.59$, and even more significantly for the spherical Coulomb interaction, reaching occupations of $n_{d_{z^2}} = 0.77, n_{d_{xy}} = 0.64$. The d_{xy} orbital remains significantly closer to half-filling than d_{z^2} , consistent with their previously determined hierarchy of Kondo temperature scales, and both of them still remain closer to half-filling than the previously inert other three orbitals, in agreement with their large contributions to the magnetic moment.

Considering the diagonal and offdiagonal elements in the $\{d_{z^2}, d_{xy}\}$ subspace, we find a confirmation of the tendency for spin alignment associated with the high-spin

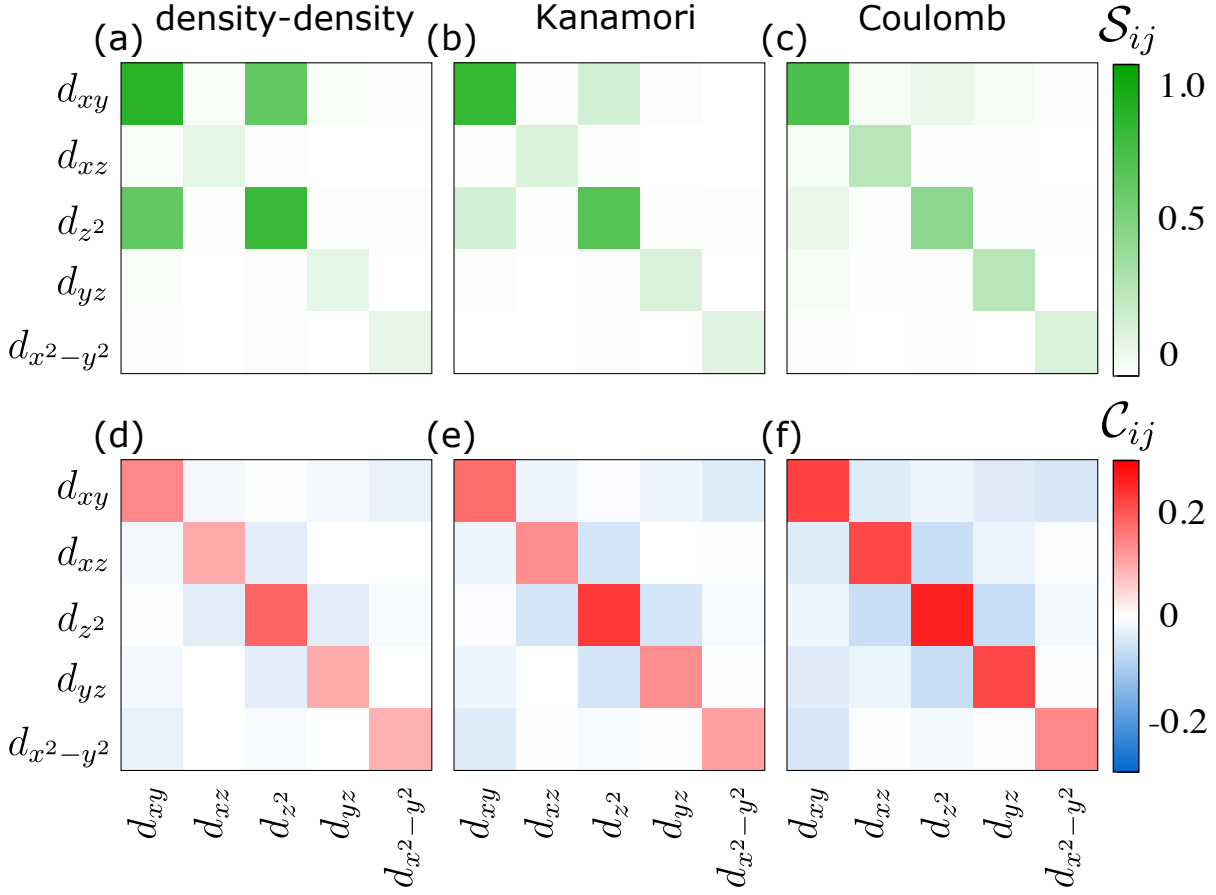


Figure 4.6: Purely correlated parts of the spin ($S_{ij} = \langle \sigma_i \sigma_j \rangle - \langle \sigma_i \rangle \langle \sigma_j \rangle$) correlation function (upper panels) and charge ($C_{ij} = \langle n_i n_j \rangle - \langle n_i \rangle \langle n_j \rangle$) correlation function (lower panels), whose off-diagonal elements indicate spin and charge fluctuations respectively, between all orbitals of the Co 3d-shell for density-density (left panels), Kanamori (middle panels), and Coulomb (right panels) interaction computed from single and double occupations at our lowest temperature of 33 K and approximately valid over our entire range of temperatures.

state $S = 1$ for density-density interaction in the much larger offdiagonals $\langle n_{d_{z^2}, \sigma} n_{d_{xy}, \sigma} \rangle$ for parallel spins compared to the suppressed values of $\langle n_{d_{z^2}, \sigma} n_{d_{xy}, \bar{\sigma}} \rangle$ for antiparallel spins. This tendency is considerably reduced for Kanamori interaction and Coulomb interaction, consistent with the reduction of the effective spin moment with the change of the parameterization. This change becomes even clearer when we do not consider the double occupations directly but the correlated part only of the spin correlation function, as we shall see in the following.

As indicators of spin and charge correlations and fluctuations, we define the corre-

lation functions

$$\mathcal{S}_{ij} = \langle \sigma_i \sigma_j \rangle - \langle \sigma_i \rangle \langle \sigma_j \rangle, \quad (4.9)$$

$$\mathcal{C}_{ij} = \langle n_i n_j \rangle - \langle n_i \rangle \langle n_j \rangle, \quad (4.10)$$

where $\sigma_i = n_{i\uparrow} - n_{i\downarrow}$ (without factor of $1/2$) and $n_i = n_{i\uparrow} + n_{i\downarrow}$, which we may imagine as a sort of rotation into a basis that lends itself to a more straight-forward interpretation. Since we subtract the factorized expectation values, a result of zero for the correlation functions indicates no correlation. The diagonal elements of \mathcal{S}_{ij} indicate the spin moment. The values of the correlation functions are displayed in Fig. 4.6 in a similar manner as the double occupations in Fig. 4.5. We use data from our lowest temperature again, but there are only minimal quantitative changes over the entire range we consider.

Looking at the spin correlation function, we can read off the change with the interaction parameterization in a more simple way than from the double occupations. We see that the offdiagonal elements in the $\{d_{z^2}, d_{xy}\}$ subspace that indicate alignment of the spins decrease with more complex interaction parameterization, pointing to the vanishing of the high-spin state. The diagonal elements in the subspace, which overwhelmingly dominate for density-density interaction, decrease as well with a more complex interaction and that of the d_{z^2} orbital does so faster, in agreement with its higher Kondo temperature scale. Concurrently, the other diagonal elements increase, indicating their higher contribution to the spin moment that becomes possible due to the redistribution of charge away from them and is a relevant contribution as we move away from the density-density interaction.

This is reflected in a significant increase of charge fluctuations, which e.g. particularly increase between the d_{z^2} and the d_{xz} and d_{yz} orbitals that belong to the inert subspace with density-density interaction and instead have a relevant contribution to the moment with the full Coulomb interaction. Within the density-density approximation, the spin alignment enforced by the strong influence of Hund's coupling decouples the orbitals [284, 285], but as we proceed to the more complex interactions, the suppression of the high-spin state makes charge fluctuations possible. Terms associated with the spin-flip processes in the Kanamori form of the interaction already contribute to that suppression, and further processes involving three or four different orbitals only occurring in the full spherical Coulomb interaction effectively counteract a strongly orbitally polarized occupation of the d -shell orbitals, such that neither the $S = 1$ Nevidomskyy-Coleman screening scenario [249] nor that of two independent $S = 1/2$ spins [244, 245] on just the $\{d_{z^2}, d_{xy}\}$ subspace can yield an accurate description of the real situation.

4.1.6 Spectral function and self-energy

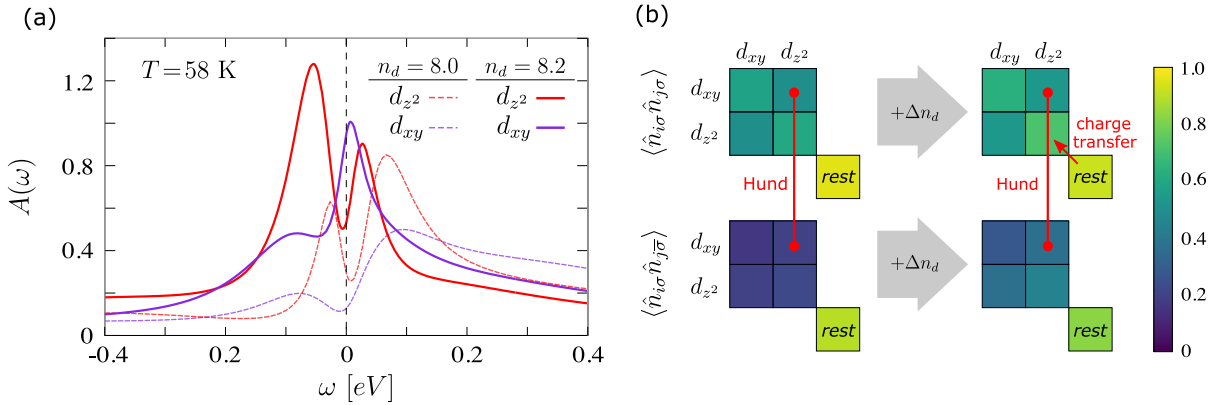


Figure 4.7: Left panel: Spectral functions calculated by maximum entropy analytic continuation for the orbitals of the Kondo-active $\{d_{z^2}, d_{xy}\}$ subspace with density-density interaction at a temperature of 58 K for total fillings of the cobalt $3d$ -shell of $n_d = 8.0$ (dashed curves) and $n_d = 8.2$ (solid curves). For our usual filling of $n_d = 8.0$, no Kondo resonance at the Fermi level is found at such a high temperature. Resonances do however develop as the filling is increased, indicating an enhancement of the Kondo temperature in that case. Right panel: Double occupations $\langle n_{i\sigma} n_{j\sigma} \rangle$ for parallel spins (upper half) and $\langle n_{i\sigma} n_{j\bar{\sigma}} \rangle$ for antiparallel spins (lower part) with density-density interaction at $n_d = 8.0$ (left half) and with an additional increase of filling by $\Delta n_d = 0.2$ (right half). The difference of the connected squares indicates spin alignment in the subspace caused by Hund’s coupling. When the filling is increased, a transfer of charge from the other orbitals of the $3d$ -shell, whose average is given by the “rest” square, to the orbitals in the subspace moves them away from half-filling and reduces the spin alignment, leading to a higher Kondo temperature like a more complex interaction would.

Finally we also consider indications of screening encoded in the Green’s function on the Matsubara axis computed by CT-HYB, first by looking at orbital-resolved spectral functions for the cobalt $3d$ -shell that we extract by numerical analytic continuation using the maximum entropy method [168, 170, 173, 174]. While it is in principle possible to estimate at least an apparent Kondo temperature from the width of the Kondo resonance [244, 245], we therefore restrict ourselves to qualitative observations in order not to depend on the quantitative accuracy of the continuation.

Spectral functions for the Kondo-active subspace with density-density interaction at a temperature of 58 K are shown in the left panel of Fig. 4.7. As expected from our previous results indicating no Kondo screening at this temperature for this interaction parameterization, we find no resonant features in the spectral functions at the Fermi energy at our usual filling of $n_d = 8.0$. We look at results for a slightly larger filling of $n_d = 8.2$ for comparison to investigate the effect of filling deviations, which the

Kondo temperatures were found to be quite sensitive to in Ref. [244]. Looking at the spectra shown in the same figure, we find that this change indeed causes the appearance of resonant features at the Fermi level, indicating a considerable increase of the Kondo temperature, which we previously estimated as below 1 K. This enhancement of the Kondo screening scale is mediated in the same way as when we change to a more complex interaction parameterization, which we can show with the aid of the double occupancies. In the right panel of Fig. 4.7, we visualize the double occupancies for both fillings in the same way as before in Fig. 4.5 with the exception that we replace the rows and columns associated with the orbitals $\{d_{xz}, d_{yz}, d_{x^2-y^2}\}$ with just a single square for their average occupation for compactness. We find that the change in total filling of $\Delta n_d = 0.2$ causes an even larger increase in the filling of just the $\{d_{z^2}, d_{xy}\}$ subspace from $n_{d_{z^2}} = 0.60, n_{d_{xy}} = 0.57$ per spin with density-density interaction and usual filling $n_d = 8.0$ to $n_{d_{z^2}} = 0.71, n_{d_{xy}} = 0.63$ with a total filling of $n_d = 8.2$, which is transferred from the other $3d$ -shell orbitals as it obviously must be. This shifts the filling of the subspace farther away from half-filling than a change to the more complex Kanamori parameterization of the interaction, though not quite as far as the full Coulomb one. If we look at the differences of parallel and antiparallel offdiagonal occupations in the subspace, which quantifies the spin alignment caused by Hund's coupling, we observe a significant reduction. Therefore the added total filling destabilizes the $S = 1$ state just as the more complex interactions do, leading to a larger T_K for the reasons previously discussed.

In the spectral functions calculated with the more complex full Coulomb interaction, shown in the left panel Fig. 4.8, we instead find resonances at the Fermi level clearly indicating the Kondo effect for both d_{z^2} and d_{xy} already at the usual filling of $n_d = 8.0$ at a temperature of $T = 36$ K as our other results would suggest. In fact, we even find small peaks at the Fermi energy in the spectra for the d_{xz} and d_{yz} orbitals, consistent with the significant contribution of other orbitals to the dynamical screening in the case of full Coulomb interaction. In the right panels of Fig. 4.8, spectral functions of d_{z^2} and d_{xy} at two different temperatures are overlaid for comparison. We find that resonances close to the Fermi level can already be found at temperatures as high as 93 K, but they become narrower, higher, and move closer to the Fermi level for lower temperature.

Apart from spectral functions, the self-energy on imaginary time calculated as difference of the inverses of non-interacting and interacting impurity Green's function can also tell us about the Kondo temperature, as the low-temperature state of a system exhibiting the Kondo effect is a Fermi liquid [159]. For a Fermi liquid, the self-energy at the lowest Matsubara frequency $\text{Im}(\Sigma(i\omega_0))$ must be proportional to the temperature, which is the so-called "first-Matsubara-frequency rule" [164]. If that is not the case at our lowest temperatures, we cannot have reached the Fermi-liquid state, so the

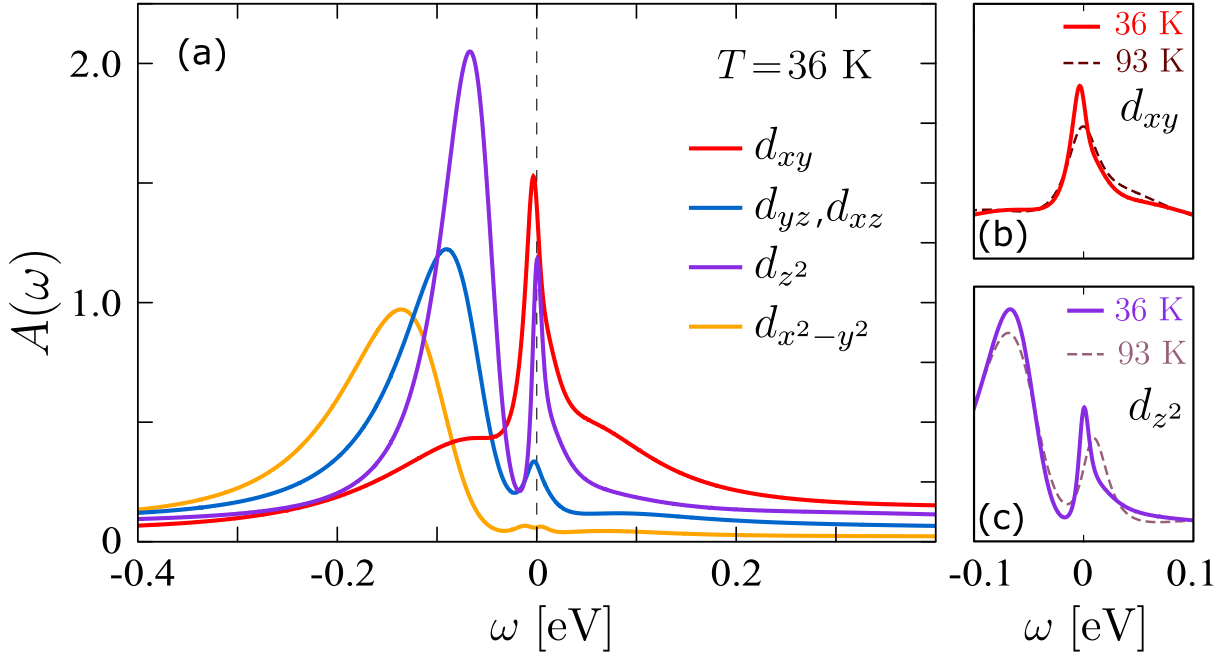


Figure 4.8: Left panel: Spectral functions calculated by maximum entropy analytic continuation for the orbitals of the cobalt $3d$ -shell with full Coulomb interaction at a temperature of 36 K for a total filling of the $3d$ -shell of $n_d = 8.0$. In the spectra of the orbitals d_{z^2} and d_{xy} , we can clearly recognize resonances at the Fermi level that point to the Kondo effect. We can even recognize resonances of a much lower height in the spectra of d_{xz} and d_{yz} suggesting the contribution of the entire $3d$ -shell to the Kondo effect for this parameterization of the interaction like our other results do. Right panels: Spectral functions for just the d_{z^2} (top) and d_{xy} (bottom) orbitals as shown in the left panel with additional data calculated for a higher temperature of 93 K (dashed lines) added for comparison. We can observe that the resonances near the Fermi level are already present at higher temperatures, but they become narrower, higher, and move closer as the temperature is lowered.

Kondo temperature must be below our temperature range. We show $\text{Im}(\Sigma(i\omega_0))$ as a function of temperature for the orbitals d_{z^2} and d_{xy} in Fig. 4.9, comparing all interaction parameterizations. As all other quantities also indicated, the d_{z^2} orbital with full Coulomb interaction seems to have the highest Kondo temperature since it follows the rule in our temperature range quite well already. For the other orbital and less complex interaction parameterizations, the curves still clearly extrapolate toward nonzero values of $\text{Im}(\Sigma(i\omega_0 \rightarrow 0))$ and are thus not Fermi-liquid states according to the first-Matsubara-frequency rule, which points to a Kondo scale below the temperature range we considered. In four of the other cases, the data curves toward the origin with lower temperature, but for the d_{z^2} orbital in the density-density approximation it even curves away from the origin instead, serving as a clear indication of a much lower Kondo scale.

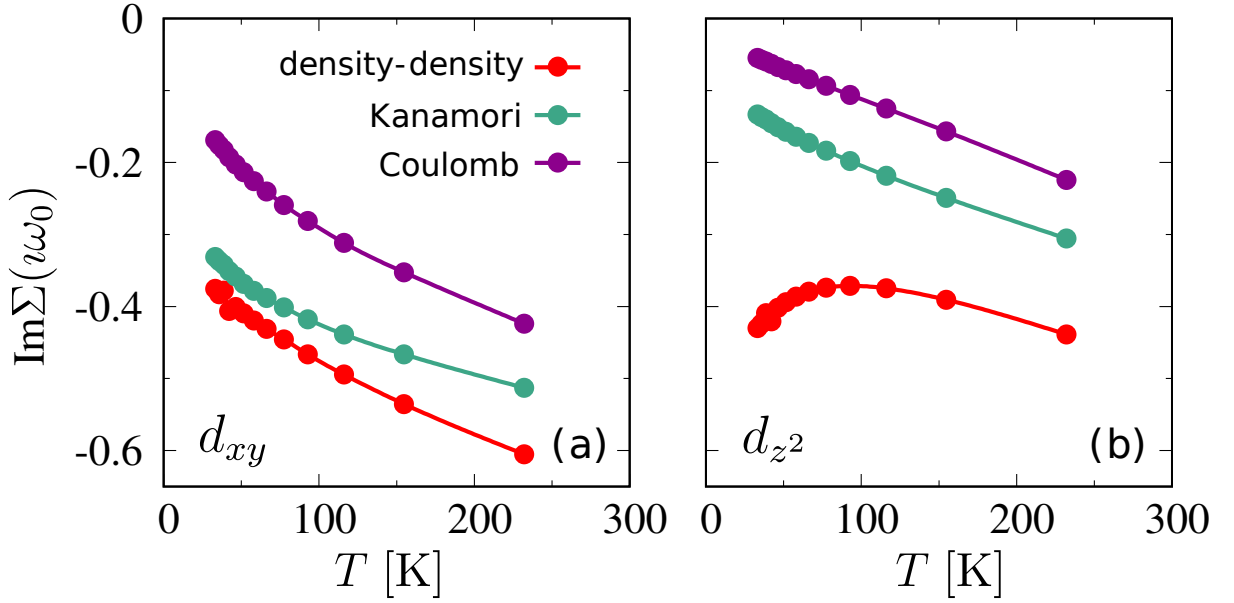


Figure 4.9: Imaginary part of the self-energy at the first Matsubara frequency ω_0 as a function of temperature for the d_{z^2} (right panel) and d_{xy} (left panel) orbital and all used parameterizations of the interaction. According to the “first-Matsubara-frequency” rule, this quantity is proportional to temperature in a Fermi liquid, which is the low-temperature state of a system exhibiting the Kondo effect. Since most curves still clearly extrapolate toward a nonzero value for $T \rightarrow 0$, we can conclude that the Kondo temperature in these cases is below our temperature range. The only curve with no recognizable deviation from the rule is that for the d_{z^2} orbital with full Coulomb interaction, which our previous observations indicate to be the one with the highest Kondo temperature.

4.1.7 Interaction terms

As we have seen, terms included in the more complex interaction parameterizations disrupt the strong orbital polarization of the occupation and spin alignment that result from just the density-density terms. Let us consider the individual interaction terms and the processes they represent to gain some insight into this effect.

We derive all forms of interaction that we use from the full spherical Coulomb interaction for the $3d$ -shell, which is given by

$$H_{\text{int}} = \frac{1}{2} \sum_{mm'm''m'''\sigma\sigma'} U_{mm'm''m'''} c_{m\sigma}^\dagger c_{m'\sigma'}^\dagger c_{m'''\sigma'} c_{m''\sigma} \quad (4.11)$$

with orbital magnetic quantum numbers $m, \dots, m''' \in -2, -1, \dots, 2$ and spins σ, σ' . In the spherically symmetric case, the matrix elements in the basis of spherical harmonics

are known to have the form [39, 262, 263]

$$U_{mm'm''m'''} = \sum_{k=0}^{2l} a_k(m, m'; m'', m''') F^k, \quad (4.12)$$

with the Slater radial integrals F^k over the radial part of the atomic wave functions and angular integrals a_k over the spherical harmonics, expressible in terms of Wigner 3- j symbols [39]. In this form, the interaction separately conserves total spin, which the only two independent spin indices in (4.11) ensure, and total angular momentum [263], which is equivalent to the condition $m + m' = m'' + m'''$ for nonzero matrix elements.

In practice, we change our basis into the cubic harmonics K_l^m however, expressed as [39]

$$K_l^m = \frac{1}{\sqrt{2}} \left((-1)^m Y_l^m + Y_l^{-m} \right), \quad (4.13)$$

$$K_l^0 = Y_l^0, \quad (4.14)$$

$$K_l^{-m} = \frac{-i}{\sqrt{2}} \left((-1)^m Y_l^m - Y_l^{-m} \right), \quad (4.15)$$

for orbital quantum number $l = 2$ for d -orbitals, positive magnetic quantum numbers m and spherical harmonics Y_l^m . The d -shell orbitals in terms of cubic harmonics K_2^m are named d_{xy} , d_{yz} , d_{z^2} , d_{xz} , and $d_{x^2-y^2}$ for increasing m from -2 to 2 [39].

Let us now have a look at the matrix elements in this basis and the processes they represent, for which we shall refer to their schematic depictions in Fig. 4.10 which show electrons as spin arrows in orbital boxes in black in their final states after the application of the corresponding term of H_{int} and in white in their initial states (if they differ). Considering the terms with the fewest different indices first, we start with the intraorbital repulsion element U_{iiii} for double occupation of a single orbital shown in panel (a), which we can show to be a density-density term by commuting operators. Next, we have four different types of elements with two orbital indices. For opposite spins, we have an interorbital repulsion of density-density form shown in panel (b) with matrix element $U_{ijij} = (U_{iiii} + U_{jjjj})/2 - 2U_{ijji}$ related to the intraorbital average and Hund's coupling U_{ijji} [244]. The interorbital repulsion for parallel spins shown in panel (c) has an additional density-density term with Hund's coupling U_{ijji} as matrix element. These three terms are the only ones that we preserve in the density-density form of the interaction (2.3). Notably, a Hamiltonian containing only these terms is diagonal in the basis of many-body states as it only counts occupations and time evolution with this interaction does therefore not mix states. In CT-HYB this has the advantage that the occupation per orbital and spin is a good quantum number and we can choose

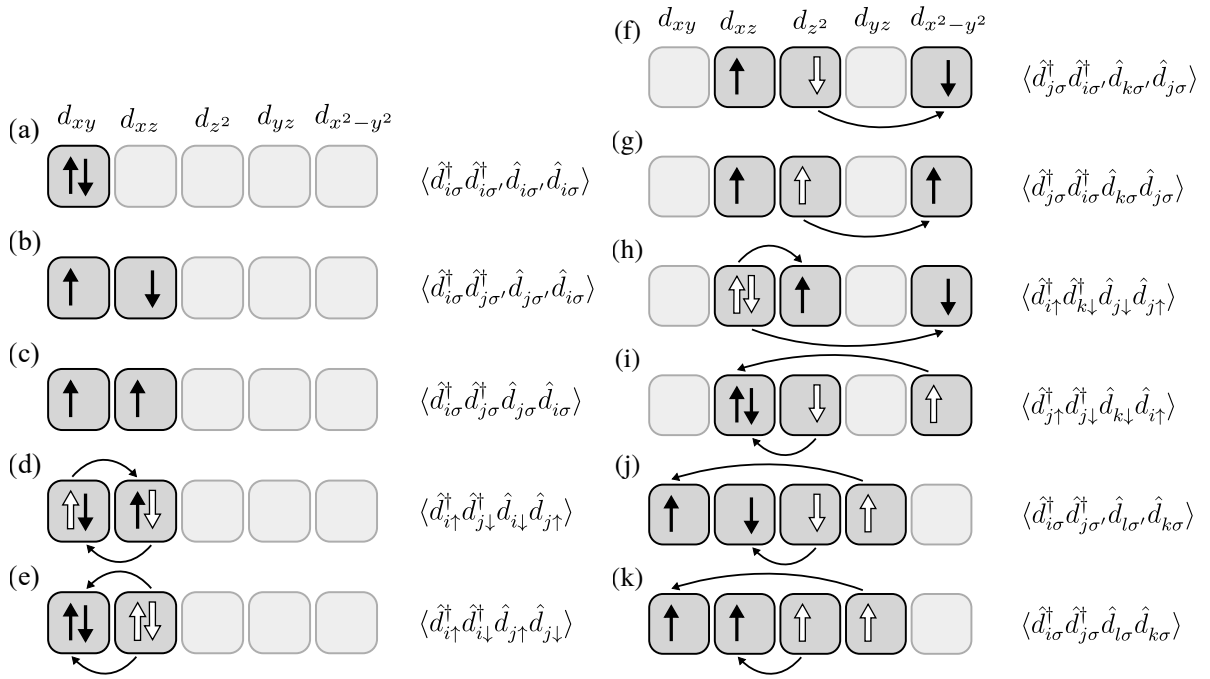


Figure 4.10: Diagrams representing one exemplary process for each type of interaction term included in the full spherical Coulomb interaction for the $3d$ -shell in the basis of cubic harmonics. Electrons are represented by spin arrows in boxes representing the individual orbitals, with black arrows indicating final states after the application of the interaction term and white arrows indicating different initial states. Arrows outside the boxes indicate which electron moves where in that case. The terms are the density-density (a) intraorbital interaction, (b) interorbital interaction for opposite spins, and (c) interorbital interaction for parallel spins with exchange term, followed by (d) spin flip and (e) pair hopping terms additionally included in the Kanamori form, followed by four three-orbital terms and two four-orbital terms included in the full Coulomb interaction only, (f) and (g) “correcting” the interorbital terms including a simultaneous interorbital hopping, (h) and (i) as creation and annihilation of an intraorbital pair (by hopping from or to two different other orbitals), and (j) and (k) for two simultaneous hopping events involving four different orbitals.

superstates of size one (or use the original “segment” representation of the algorithm [34]).

The term with matrix element U_{ijji} but opposite spins is the “spin flip” term, shown in panel (d), and the final term with at most two different orbital indices is the “pair hopping” shown in panel (e) with matrix element U_{iijj} . Adding these two terms to density-density interaction, we obtain the Kanamori form of the interaction (2.4). Time evolution under this interaction is able to flip spins and change the occupation of orbitals. As we have seen, it does however not redistribute charge in the entire shell quite

as effectively as the full Coulomb interaction, since that would lead to more significant contributions from the d_{xz} , d_{yz} and $d_{x^2-y^2}$ orbitals, cf. Figs. 4.4 and 4.5. We might suspect that the reason for this is that the pair hopping processes need one full and one empty orbital to move charge and none of the orbitals are preferentially empty, whereas the full interaction includes terms for processes in which orbitals gain or lose a single electron only. In CT-HYB we can in general not choose superstates of size one, but assuming no mixing by the quadratic part of the Hamiltonian, we can use the total occupation, a component of the total spin and the pattern of singly-occupied orbitals [115] as good quantum numbers.

For a d -shell, spherical symmetry, and assuming a fixed ratio between F^2 and F^4 , such as $F^4/F^2 = 5/8$ that we use as a good approximation for $3d$ orbitals [39, 264–267], the full spherical interaction can be specified in terms of two parameters U_S and J_S . With $U_S = F^0$ and $J_S = \frac{1}{14}(F^2 + F^4)$, cf. [39], the density-density and Kanamori forms of the interaction can be composed in terms of

$$U_0 = F^0 + \frac{8}{7} \frac{1}{14} (F^2 + F^4), \quad (4.16)$$

$$J_1 = \frac{1}{49} \left(3F^2 + \frac{20}{9} F^4 \right), \quad (4.17)$$

$$J_2 = -2 \frac{5}{7} \frac{1}{14} (F^2 + F^4) + 3J_1, \quad (4.18)$$

$$J_3 = 6 \frac{5}{7} \frac{1}{14} (F^2 + F^4) - 5J_1, \quad (4.19)$$

$$J_4 = 4 \frac{5}{7} \frac{1}{14} (F^2 + F^4) - 3J_1. \quad (4.20)$$

The matrices U_{ij} and J_{ij} used in the expression (2.3) and (2.4) for these forms of the interaction are then

$$J_{ij} = \begin{pmatrix} U_0 & J_1 & J_2 & J_1 & J_3 \\ J_1 & U_0 & J_4 & J_1 & J_1 \\ J_2 & J_4 & U_0 & J_4 & J_2 \\ J_1 & J_1 & J_4 & U_0 & J_1 \\ J_3 & J_1 & J_2 & J_1 & U_0 \end{pmatrix}, \quad (4.21)$$

$$U_{ij} = U_0 - (1 - \delta_{ij}) 2J_{ij}. \quad (4.22)$$

Using our values of $U_S = 4.0$ eV and $J_S = 0.9$ eV, we obtain Slater radial integrals of $F^0 = 4.0$ eV, $F^2 = 7.75$ eV, and $F^4 = 4.85$ eV, and as entries of the interaction matrices $U_0 = 5.02$ eV, $J_1 = 0.69$ eV, $J_2 = 0.80$ eV, $J_3 = 0.39$ eV, and $J_4 = 0.49$ eV. Compared with the interaction matrix elements calculated using first-principles cRPA in Ref. [244], we find that all of our values are slightly smaller to an extent that is unlikely to significantly

affect results and that the values calculated using cRPA partially break the spherical symmetry we assume for our interaction.

While the Kanamori interaction already restores the spin- $SU(2)$ symmetry of the interaction that is not present in the density-density form, the full interaction can contain further additional terms that are not included in the Kanamori interaction. Let us first consider matrix elements $U_{mm'm''}$ and $U_{m'm''mm}$ with three different orbital indices in the basis of spherical harmonics, with conservation of angular momentum allowing nonzero elements for $2m = m' + m''$. Either exactly the first two or exactly the last two indices must be the same to get matrix elements with three different indices. In the other cases, we could subtract the equal momenta from both sides of the conservation equation, which would imply that actually only two indices are different, and those elements are already included in the Kanamori interaction.

Matrix elements with three different indices belong to processes which fill an entirely empty or empty an entirely full orbital in the basis of spherical harmonics, which we could call the creation or annihilation of an (intraorbital) pair, shown in panels (h) and (i) in Fig. 4.10. Transformed into the basis of cubic harmonics, we additionally get three-orbital terms with the index combinations not allowed in the spherical harmonics due to angular momentum conservation, i.e. U_{jikj} and U_{jjjk} , which are associated with processes which involve one hopping and one resting electron that might e.g. be interpreted as a sort or generalization of the density-density interorbital repulsion, shown in panels (f) and (g).

If we instead require that none of the orbital indices be equal, we can also solve $m + m' = m'' + m'''$. These processes are simultaneous hopping processes of two electrons with all involved orbitals different and represented in panels (j) and (k) of Fig. 4.10. In CT-HYB the pattern of singly-occupied orbitals is not a good quantum number either any more with this interaction and we generally use automatic partitioning of the Hamiltonian on top of total occupation and a component of total spin to reduce superstate sizes further.

4.1.8 Conclusions

Our solution of an AIM at low temperatures reveals the importance of a realistic local interaction and inclusion of all five $3d$ -shell orbitals for an accurate description of the Kondo screening in the prototypical Co/Cu(001) system. The density-density approximation leads to a near-perfect realization of the $S = 1$ Kondo effect as explained by Nevidomskyy and Coleman [249] with an estimated Kondo temperature on the order of 1 K or below, no screening discernible even at half the experimental temperature, and only the two Kondo-active orbitals d_{z^2} and d_{xy} relevant as the others are always full. If

we switch to the full spherical Coulomb interaction instead, the filling of the $3d$ -shell is noticeably shifted from the full to the less full orbitals, leading to strong correlations between all of them in the process. The local moment has significant contributions from the entire $3d$ -shell then and the increase of charge fluctuations disrupts the $S = 1$ spin alignment tendency caused by Hund's coupling. The system exhibits considerable dynamical screening of still approximately the same instantaneous moment even at room temperature, and the Kondo temperature approaches the experimental value with resonances in the spectra of primarily the "Kondo-active" orbitals at the Fermi energy that are already clearly visible there. Although even in this realistic model it is thus these two orbitals that are the most significant, this demonstrates that due to the entanglement of the entire shell a separate treatment of the two orbitals or approximate treatment of the interaction cannot possibly be accurate and would likely lead us to characterize the Kondo screening process incorrectly. While our analysis of this Kondo impurity system is on a slightly more abstract level than many references that e.g. directly consider specific STM setups or other details that we could have included in our DFT step, our conclusions are a direct consequence of the local interaction on the impurity site and possibly relevant to even many other systems of cobalt and other transition metal impurities.

4.2 Kondo effect of a cobalt atom embedded into linear clusters of copper atoms on a Cu(111) surface

In this section, we report and try to interpret experimental results for the spectroscopy of one-dimensional atomic “wires” Cu_mCoCu_n made up of up to several non-magnetic copper atoms and one magnetic cobalt atom on a copper Cu(111) surface using a scanning tunneling microscope. From the line shapes of the Abrikosov-Suhl Kondo resonance, a significant dependence of the Kondo temperature on the amount of copper atoms can be inferred, including a total absence of the resonance at the experimental temperature of 5 K in two cases. We perform first-principles calculations combining the density-functional theory (DFT) with the continuous-time quantum Monte Carlo solution of a DFT-parameterized Anderson impurity model (AIM) in an attempt to explain the variance in Kondo temperatures, but only qualitative agreement with the nonzero Kondo temperatures is found with calculated quantitative differences between the clusters not following the experimentally determined ones and no quenching of the Kondo effect in any of the calculations.

This section is based on the following article, Ref. [286], which is also the source of the figures

*N. Néel, J. Kröger, M. Schüler, B. Shao, T. O. Wehling, A. Kowalski, and G. Sangiovanni,
“Single-Co Kondo effect in atomic Cu wires on Cu(111),”
Phys. Rev. Res. 2, 023309 (2020)*

4.2.1 Introduction

Since we revisit Kondo systems [28] similar to the one we have considered previously in Sec. 4.1, the context outlined in Sec. 4.1.1 applies. The experimental results¹ we report involve the spectroscopic detection of the Abrikosov-Suhl Kondo (ASK) resonance [222–224] due to the appearance of a low-energy many-body state at the Fermi surface. Photoemission and inverse photoemission experiments were able to demonstrate the existence of spectral features matching the expected ASK resonances before [287–293], but here the assembly and spectroscopy of the atomic wires was performed using a scanning tunneling microscope (STM). In the last three decades [231, 233, 234], STM spectroscopy (STS) has contributed considerably to the experimental investigation of magnetic impurities on metallic surfaces and the characterization of the Kondo effect in these systems reviewed e.g. in Refs. [294–296].

In STS, the ASK resonance is reflected in a feature near zero bias [231] in the differential conductance dI/dV with current I and sample bias voltage V . This is generally

¹by our collaborators Nicolas Néel and Jörg Kröger at TU Ilmenau

expected to appear as a Fano line shape [235, 236] that takes the interference between electrons tunneling directly into the conduction bands and indirectly through the ASK resonance state into account [231, 233, 297], which is however not a requirement for the line to take this shape [227, 237]. The resonance width at zero temperature is related to the Kondo temperature, and variations of the resonance line shape are used as experimental probes of the system properties, cf. e.g. Refs. [229, 247, 298–306] and many more. Of particular relevance for the present investigation is Ref. [307], in which the local electronic structure of the impurity was modified by embedding it in compact flat clusters of a varying number of additional Cu atoms and a nonmonotonic dependence of the Kondo temperature on the cluster size was found.

The experiment performed here deviates from that in Ref. [307] in the geometry of the surface Cu clusters in which the Co atom is embedded, which was a compact cluster of neighboring atoms there and is a linear wire here, with additional Cu atoms extending ever further away from the impurity the more are added. We apply the first-principles combination of density functional theory (DFT) with the solution of an Anderson impurity model derived for the impurity using numerically exact CT-HYB as previously discussed in Sec. 4.1.2 in an attempt to reproduce the results. This allows the incorporation of the DFT electronic structure that changes in response to the addition of atoms into the in principle unapproximated solution of the many-body problem of the correlated electrons in the impurity orbitals.

4.2.2 Experimental results

Single Co atoms were deposited on a cleaned Cu(111) surface with an electron beam evaporator and a STM in ultrahigh vacuum at a temperature of 5 K was used to transfer single Cu atoms onto the surface [308], assemble the linear Cu_mCoCu_n clusters [309, 310], record surface images at constant current, and measure differential conductance spectra as the current response to a sinusoidally varied bias voltage determined with a lock-in amplifier when the tip centers on the Co atom.

Recorded images of the linear clusters are shown as height profile heatmaps in the panels in the left half of Fig. 4.11. It is recognizable that the apparent height of the Co impurity increases as up to two Cu atoms are added to the atomic wire and that the Co atoms in a wire appear higher than any of the Cu atoms in the wire in all cases.

Differential conductance spectra are shown in the right panels of Fig. 4.11 and fitted using a linear background and a Fano line shape $f(V) = a(q + \varepsilon)^2 / (1 + \varepsilon^2)$ with amplitude a , Fano asymmetry parameter q , and energy difference from the resonance energy ε_0 relative to its width $\varepsilon = (eV - \varepsilon_0) / (k_B T_K)$ with electron charge e , bias voltage V , Boltzmann constant k_B and Kondo temperature T_K . Kondo temperatures determined from

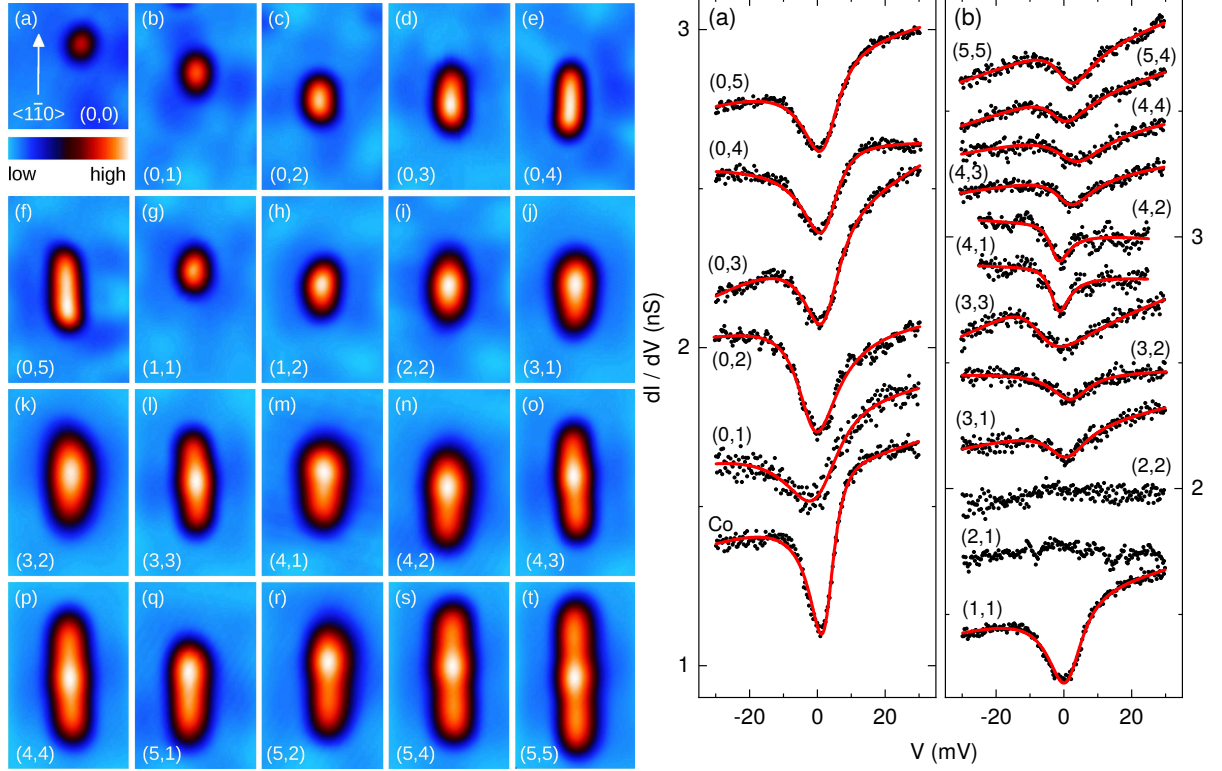


Figure 4.11: Left half: Height profiles of the Cu_mCoCu_n atomic clusters in top view onto the Cu(111) surface measured by STM as a heat map, with the cluster size (m, n) given in each panel. In the single atom image (a), a crystallographic $\langle 1\bar{1}0 \rangle$ direction is indicated, the field of view for the clusters shows an area of $2.6 \times 4 \text{ nm}^2$, and the scale goes from an apparent height of 0 pm to 120 pm. Right half: Differential conductance spectra dI/dV around zero bias voltage for a single atom and chains extended in only one direction in panel (a) and chains extended in both directions in panel (b). Spectra are shifted in vertical direction for clarity, labeled with (m, n) again, and fitted with Fano line shapes drawn as red solid lines in cases where an ASK resonance was recognizable, which are all except for $(2, 1)$ and $(2, 2)$

these fits are given in Tab. 4.2.

The Kondo temperature, determined as $T_K = (51 \pm 2) \text{ K}$ for a single Co atom, varies between $(38 \pm 3) \text{ K}$ and $(112 \pm 7) \text{ K}$ as a function of the cluster size, but no Kondo resonance at all is found at the experimental temperature of 5 K for Cu_2CoCu_1 and Cu_2CoCu_2 . The Kondo temperatures for a single Co atom agree with previously found values [228, 307]. Addition of Cu in only one direction almost doubles the Kondo temperature with the first atom, in qualitative agreement with Ref. [307], which drops back to roughly constant values about one and a half times the single-Co value with the addition of any further atoms in that direction. The rest of the results are mostly in about that same region as well, except for maxima in the Kondo temperatures for a symmetric amount

$m \backslash n$	0	1	2	3	4	5
0	51 ± 2	112 ± 7	82 ± 2	77 ± 2	77 ± 2	75 ± 2
1	112 ± 7	71 ± 2	no resonance	80 ± 7	38 ± 3	
2	82 ± 2	no resonance	no resonance	79 ± 7	39 ± 5	
3	77 ± 2	80 ± 7	79 ± 7	110 ± 8	74 ± 5	
4	77 ± 2	38 ± 3	39 ± 5	74 ± 5	96 ± 10	77 ± 6
5	75 ± 2				77 ± 6	76 ± 5

Table 4.2: Kondo temperature T_K [K] of Cu_mCoCu_n determined from the Fano line shape fit parameters of the differential conductance spectra shown in the right half of Fig. 4.11.

of atoms on both sides for $m = 3, 4$ but not $m = 5$ and unusually low ones for a long chain $m = 4$ on one side and a short chain $n = 1, 2$ on the other. The Kondo temperature for the linear CuCoCu cluster measured here is less than a third of that of the compact CoCu_2 cluster measured in Ref. [307], demonstrating an importance of geometry rather than just size.

4.2.3 Density functional theory

VASP [256, 257] with the projector-augmented plane wave (PAW) [257, 258] basis set and the PBE [311] generalized gradient approximation as exchange-correlation functional was used to perform DFT calculations for a supercell of $3 \times 13 \times 1$ unit cells with three surface layers of Cu atoms for structural relaxation and five surface layers for hybridization function calculations.

Both spin-polarized and non-spin-polarized calculations were performed and the spin-polarized solutions were found to be energetically favorable for each cluster independently of whether the relaxed adsorption distances of the Co atom per calculation or fixed equal adsorption distances in the range between the polarized and non-polarized solution were used. With spin polarization, a local magnetic moment of slightly less than $2 \mu_B$ in units of the Bohr magneton μ_B tends to form at the Co sites of all clusters and the relaxed adsorption distances of the Co atoms of about 185 pm are about 10 pm higher than without spin-polarization in all clusters. Local moments, adsorption distances, and total energy differences due to spin-polarization of the clusters without experimentally observed ASK resonance are not systematically lower or otherwise different from those of clusters with observed resonance.

As a consistency check of relaxed DFT geometries against experimental cluster geometries, the dependence of the resonance energy of an unoccupied p_z orbital significantly above the Fermi energy on the cluster size was calculated and found to agree

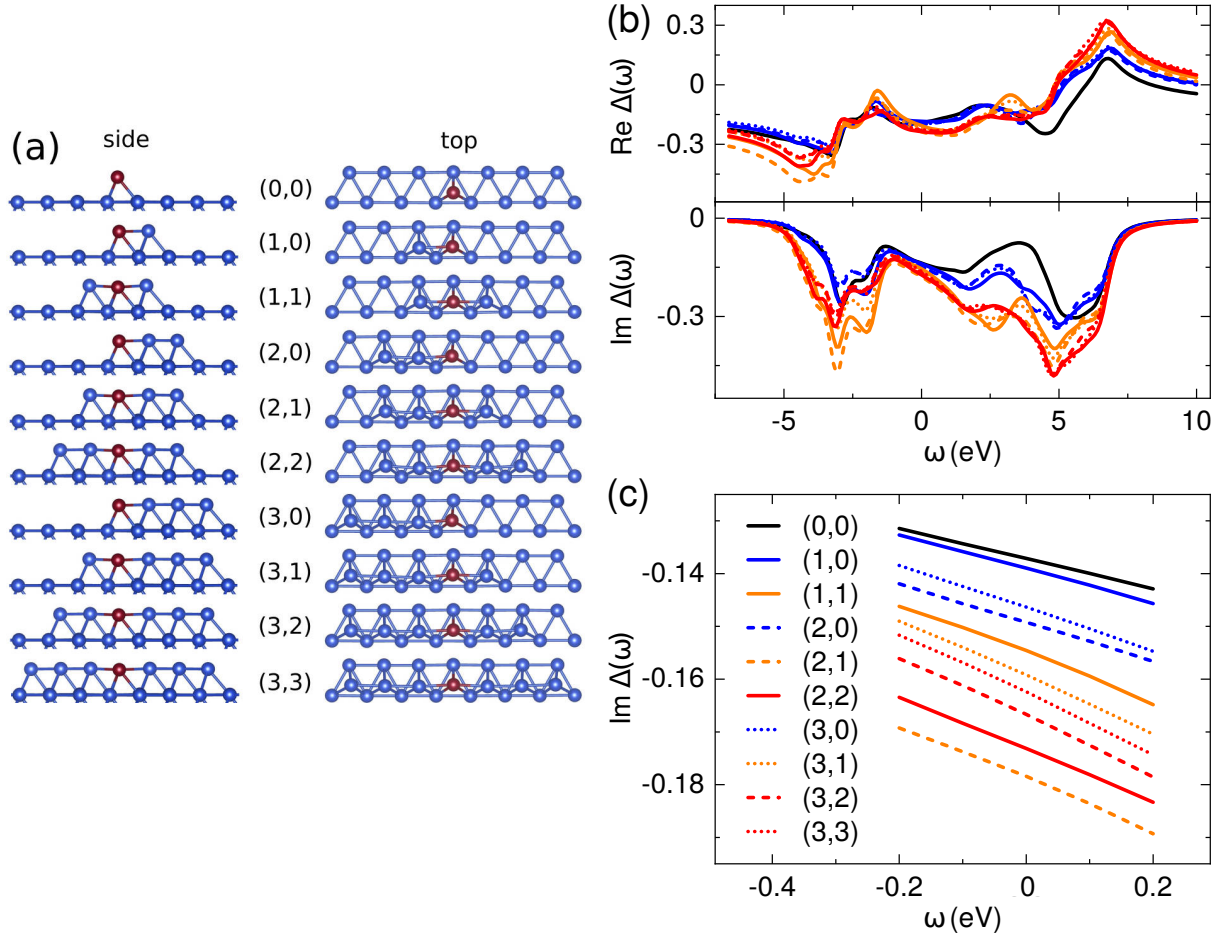


Figure 4.12: Panel (a): Relaxed structures from spin-polarized DFT calculations of linear Cu_mCoCu_n clusters on a Cu(111) surface shown in side view (left) and top view (right) with the Co atom in red and (m, n) per row given in the middle. Panel (b): Real and imaginary parts of the orbital-averaged hybridization functions on the real frequency axis for the AIMs modeling the Co impurity atoms in all clusters, with the legend in Panel (c) giving (m, n) . Panel (c): Zoom on the imaginary parts shown in panel (b) close to the Fermi energy.

with the dependence of the peak position in the STM spectrum. The relaxed structures of the linear Cu_mCoCu_n clusters on the surface are shown in panel (a) of Fig. 4.12.

Hybridization functions and local levels for the Anderson impurity models (AIMs) describing the Co impurity atoms in all clusters are extracted from the DFT calculations as described in Sec. 4.1.2 and Refs. [182, 260, 261]. Hybridization functions averaged over orbitals for all cases with a broadening of 0.31 eV are shown in panel (b) and a closer zoom of their imaginary parts around the Fermi energy in panel (c) of Fig. 4.12. The broadening was chosen high enough to smoothen peaks in the function and make it comparable between the different clusters. We find that the hybridization functions are overall rather similar in shape and magnitude for the different clusters and also

roughly agree with hybridization functions previously used for cobalt impurities on copper surfaces, cf. Refs. [244, 251]. As expected, the magnitude of the hybridization function of the cobalt impurity also roughly increases with the number of neighboring atoms, for which we can again consider panels (b) and (c) of Fig. 4.12. There black color indicates the single Co impurity, blue clusters with Cu atoms on one side of the cobalt atom only, yellow those with at least one Cu atom on each side, and red those with at least two Cu atoms on each side.

As a rough relation between Kondo temperature and the hybridization function at the Fermi energy E_F we can use

$$T_K \propto \exp\left(-\frac{\pi U}{M|\text{Im}(\Delta(E_F + i0^+))|}\right) \quad (4.23)$$

with local interaction U and a factor M depending on the number of orbitals following from a scaling analysis for the multi-orbital Kondo problem [225, 273]. We can read off the relevant values of the hybridization function from panel (c) of Fig. 4.12 and compare the experimental Kondo temperatures given in Tab. 4.2. While we would expect T_K to rise strongly for increasing $|\text{Im}(\Delta(E_F))|$, no such trend is recognizable. In fact, judging from the hybridization function only, we should expect the two systems without ASK resonance in experiment to have the largest Kondo temperatures. This formula is obviously a bit simplistic in its treatment of hybridization and interaction, for which we moreover use orbitally averaged values. Even just the form of the local interaction for otherwise unchanged magnitude can have a dramatic effect on local spin and charge fluctuations and the screening of the local moment [183, 252], so let us proceed to see whether the numerically exact treatment of correlations on the impurity can elucidate the situation.

4.2.4 Continuous-time quantum Monte Carlo simulations

We perform calculations using the continuous-time quantum Monte Carlo method in hybridization expansion (CT-HYB) as implemented in *w2dynamics* [40] to solve Anderson impurity models parameterized based on the DFT results of the previous section numerically exactly. The input quantities extracted from DFT results are the energies of the impurity levels and the diagonals of the hybridization function, while we ignore the offdiagonal elements of the hybridization function because they are of small magnitude but would increase the necessary numerical effort considerably. As double counting correction we set the chemical potential to the value that allows us to reach a total occupation of $n_d = 8.0$ of the cobalt $3d$ -shell [260].

For the local interaction, we choose the full spherically symmetric Coulomb interac-

tion because simplified forms of the local interaction can cause significant deviations in Kondo temperatures and spectra [183, 252]. Our interaction parameters are usually $U_S = 4.0$ eV and $J_S = 0.9$ eV, which were determined for cobalt atoms in the bulk in Ref. [38] and shown to be approximately equal to the parameters for cobalt atoms on a surface in Ref. [269]. These values of the parameters U_S and J_S , whose definitions can be found in Sec. 4.1.7, correspond to approximately $U_K = 5.0$ eV and $J_K = 0.64$ eV with alternative parameters U_K and J_K defined as orbital averages of the intraorbital repulsion and Hund's coupling, cf. Ref. [39, 268]. When we later consider the effect of changes of U and J on the Kondo temperature, we will give numerical values of these averages U_K and J_K rather than U_S and J_S . We neglect deviations from spherical symmetry since they were shown to have minor effects on $3d$ orbitals [312].

Our investigation of the Kondo effect in the Cu_mCoCu_n clusters is based on quantities evaluated from CT-HYB results for the Matsubara Green's function as we previously did in Sec. 4.1.6, without calculating spin-correlation functions, and we focus on trying to compare the clusters with and without experimentally observed ASK resonance. Distinguishing the clusters without observed ASK resonance by checking for the absence of a Fermi liquid state using the "first-Matsubara-rule" [164] for the low-temperature evolution of the low-frequency behavior of the imaginary part of the self-energy of a Fermi liquid on the Matsubara axis was unsuccessful.

Therefore we proceed with a quantitative analysis of the Kondo temperature scale, using the equation

$$T_{K,m} = -\frac{\pi}{4} Z_m \text{Im}(\Delta_m(0)) \quad (4.24)$$

for the Kondo temperature from renormalized perturbation theory [251, 313, 314], where Z_m is the quasiparticle weight of orbital m , a quantity that measures the amount of spectral weight contributing to the coherent quasiparticle peak compared to the total spectral weight, cf. Sec. 2.4, and Δ_m the hybridization function for orbital m . Since this directly gives us theoretical estimates for the Kondo temperature, it seems like an obvious choice for comparison with the experimental Kondo temperature. The latter is however one single temperature for the entire multi-orbital system determined experimentally from the ASK resonance width while our estimates are orbital-dependent and would rather correspond to the widths of the individual ASK resonances in orbital-resolved spectra.

We calculate estimates for the orbital-dependent quasiparticle weights as difference quotients of the imaginary part of the CT-HYB Matsubara Green's function,

$$Z_m = \frac{\text{Im}(\Sigma_m(i\omega_1)) - \text{Im}(\Sigma_m(i\omega_0))}{\omega_1 - \omega_0}, \quad \omega_n = \frac{(2n+1)\pi}{\beta}, \quad (4.25)$$

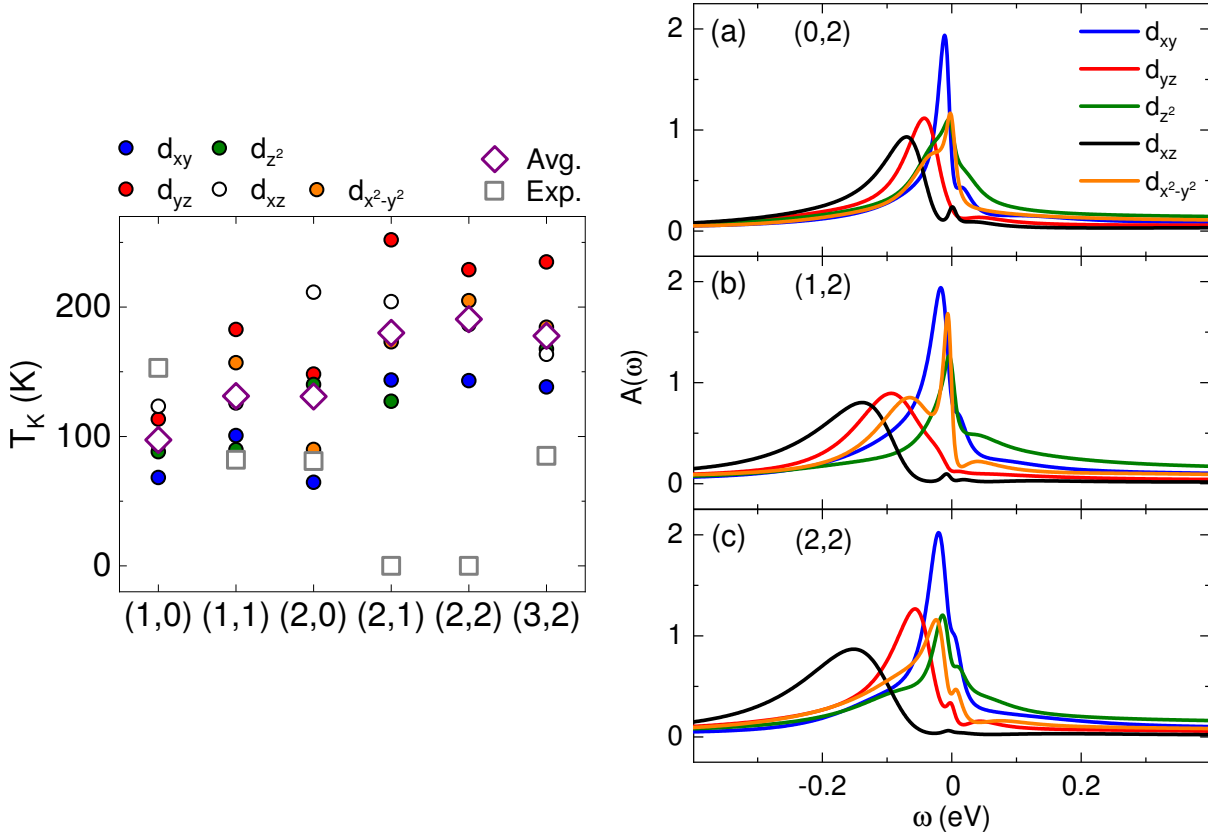


Figure 4.13: Left panel: Comparison of theoretical $T_{K,m}$ estimates from CT-HYB results for quasiparticle weights Z_m per orbital of the cobalt $3d$ -shell and orbital-averaged (Avg.) with experimentally determined Kondo temperature T_K of the system (Exp.) determined from the width of the ASK resonance or zero in the cases where no resonance was observed. Data is shown for all clusters with both experimental and theoretical results and the x-axis label (m, n) indicates cluster Cu_mCoCu_n . Right panel: Orbital-resolved spectral functions $A(\omega)$ obtained by maximum entropy analytic continuation of the Matsubara Green's function from CT-HYB calculated for a temperature of $T = 46$ K for the cluster Cu_0CoCu_2 with Kondo temperature $T_K = 82$ K (top panel) and the two clusters Cu_0CoCu_2 (middle panel) and Cu_0CoCu_2 (bottom panel) without experimentally observable ASK resonance.

for all clusters for which CT-HYB calculations were done and show the resulting temperatures per orbital as well as the orbital average and the experimental value determined from the ASK resonance width in the left panel of Fig. 4.13. In the cases where an experimental Kondo temperature could be determined, the average of the theoretical values does not quantitatively match, but gives the right idea qualitatively and is never off by more than a factor of two. In the cases where no ASK resonance could be observed in experiment, indicated in the figure with an experimental Kondo temperature of zero, the theoretical result is qualitatively incorrect. The theoretically estimated

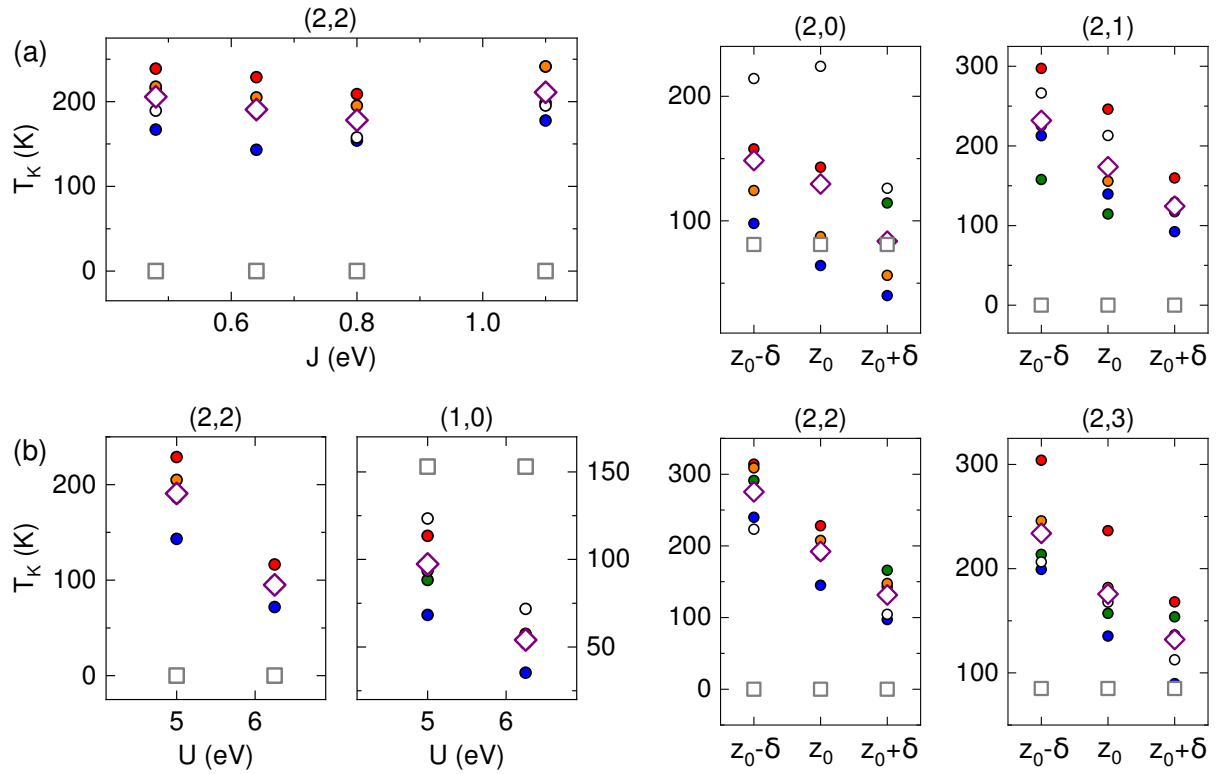


Figure 4.14: Theoretical $T_{K,m}$ estimates from CT-HYB results for quasiparticle weights Z_m per orbital of the cobalt $3d$ -shell (dots), orbital-averaged (diamonds), and experimentally determined Kondo temperatures T_K (squares) determined from the width of the ASK resonance or zero in the cases where no resonance was observed. The assignments of colors to orbitals can be found in the legend of the left panel of Fig. 4.13. Titles (m, n) above the panels indicate that the data of the panel applies to cluster Cu_mCoCu_n . In the three panels on the left the intraorbital repulsion U and the average Hund's coupling J are individually varied from their default values of $U = 5.0$ eV and $J = 0.64$ eV, based on first-principles calculations [38, 269], to investigate the dependence of the Kondo temperature on the strength of the interaction. In the four panels on the right, the adsorption height of the cobalt atom in the DFT calculations is changed by $\delta = 10$ pm from the value z_0 obtained by structural relaxation in DFT of around 185 pm (slightly dependent on the cluster) and CT-HYB calculations are repeated with the new local levels and hybridization functions to investigate the dependence of the Kondo temperature on the adsorption height.

Kondo temperatures for the two clusters without observed ASK resonance are qualitatively the same as for the other clusters with observed ASK resonance and in fact even the largest of all Kondo temperature estimates, in agreement with the observation that the hybridization functions of these two clusters calculated using DFT were those of the largest magnitude near the Fermi energy, cf. Fig. 4.12. Since we used the same local

interaction and same target filling for all clusters and they consequently differed in the local levels and hybridization functions from DFT only, this was to be expected because there were no significant qualitative differences of the DFT results depending on the cluster.

Let us further have a look at the corresponding spectral functions $A(\omega) = -\frac{\text{Im}(G_R(\omega))}{\pi}$ that tell us the single-particle excitations of the correlated many-body system, where we obtain the retarded Green's function $G_R(\omega)$ from the CT-HYB result for the interacting impurity Green's function $G(i\omega_n)$ on fermionic Matsubara frequencies ω_n . We analytically continue the Green's function from $i\omega_n$ to $\omega + i0^+$ using the maximum entropy method [168, 170, 173, 174], which is able to give qualitatively accurate results in a limited frequency range around the Fermi energy. We show the spectral functions of the two clusters (1, 2) and (2, 2) without experimentally observed ASK resonances and of the cluster (0, 2) with experimentally determined Kondo temperature $T_K = 82$ K in the right panels of Fig. 4.13, calculated at a temperature of $T = 46$ K. We find again that there are no systematic differences between the clusters, with peaks around the Fermi energy of similar size and similar orbital structure in all three cases consistent with the DFT input but not with experiment.

In order to explore possible reasons for this failure of the theoretical estimates to reproduce the absence of the ASK resonance in two of the clusters, we check the dependence of estimated Kondo temperatures on parameters of the interaction and structure. We start by individually increasing one of the local interaction parameters, i.e. the average intraorbital repulsion U or Hund's coupling J , by a quarter of their default values $U = 5.0$ eV and $J = 0.64$ eV and recomputing the Kondo temperature estimates, shown in Fig. 4.14. Since no considerable change due to this increase of J was recognizable in the Kondo temperature estimates for the cluster Cu_2CoCu_2 , we further checked whether increasing J by three quarters or decreasing it by one quarter cause a more pronounced effect, but the dependence of the Kondo temperature on Hund's coupling J is rather weak and not noticeably systematic in the entire range of values we considered, with the orbital-averaged Kondo temperature estimate varying between 178 K and 211 K. An increase of U from 5.0 eV to 6.25 eV instead significantly reduces the orbital-averaged Kondo temperature estimate to 95 K for the cluster Cu_2CoCu_2 , about half of its original value 191 K. We also verify the generalizability of the effect of U by performing the same test for the cluster Cu_1CoCu_0 , where we find a similar reduction in the Kondo temperature estimate from 97 K to 54 K.

Another possible cause of the discrepancy could be inaccuracies already on the level of the DFT structure. To examine the dependence of the results on the structure, we recompute results for the two clusters without observed resonance, Cu_2CoCu_1 and Cu_2CoCu_2 , as well as the clusters Cu_2CoCu_0 and Cu_2CoCu_3 with experimentally de-

terminated Kondo temperatures of $T_K = 82$ K and $T_K = 79$ K after changing the adsorption height of the cobalt atom from its value after structural relaxation z_0 by a distance of $\delta = 10$ pm. The results shown in the right half of Fig. 4.14 demonstrate a considerable increase of Kondo temperature estimates for lower distances and decrease of Kondo temperature estimates for higher distances, with about a factor of two between the lowest and highest adsorption heights differing by 20 pm. Different quantitative responses of the estimates per orbital also point to a dependence on the cluster of the variation of the orbital-resolved contributions to the spectra as the adsorption distance is changed, but the dependence of their average is similar for the considered clusters.

4.2.5 Conclusions

Surrounding a cobalt impurity atom on a Cu(111) surface by additional copper atoms to form a linear “atomic wire” cluster Cu_mCoCu_n was shown by scanning tunneling spectroscopy to cause significant changes to the line shape of the ASK resonance, leading to variations of the Kondo temperatures between about 40 K and 110 K for cluster sizes $m, n \leq 5$ and most interestingly the apparent suppression of the Kondo effect in the clusters Cu_2CoCu_1 and Cu_2CoCu_2 .

CT-HYB calculations for impurity models of the cobalt adatoms with full spherical Coulomb interaction based on parameters from first-principles calculations and with local levels and hybridization functions extracted from DFT-GGA calculations for relaxed structures of the clusters lead to estimates for Kondo temperatures between about 100 K and 200 K. Agreement with the theoretical estimates is thus at most qualitative, with the calculations failing to reproduce the experimental values by up to about factors of two, failing to reproduce the quantitative differences between clusters correctly, and describing the clusters without experimentally observable ASK resonances as systems with Kondo temperatures around 200 K similar to the other clusters and in contradiction to the spectroscopic results.

Variations of the system parameters with the intention of revealing possible causes of this discrepancy indicate only minor effects of even large changes of the average Hund’s coupling J on the Kondo temperature estimates, but a significant systematic dependence on the average intraorbital repulsion U and adsorption heights of the cobalt adatom. Slight tuning of these parameters was shown to be able to easily halve or double the resulting Kondo temperature for some exemplary clusters. While slight deviations of these parameters may be responsible for some of the quantitative differences between experimental results and theoretical estimates, unrealistically large changes would be needed to explain the complete absence of the ASK resonance in two of the clusters. Apart from changes in such parameters, there may be other inaccuracies in

the simulations responsible for the qualitative mismatch with experiments, such as insufficient momentum grids or supercell sizes in DFT, the transmission function or structural influence of the STM tip, an insufficient basis set of orbitals included in the impurity model, substantial deviations of the interaction parameters or symmetry in such linear clusters, assumption of an incorrect filling of the cobalt $3d$ -shell, and the disregard of spin-orbit interaction and other relativistic effects, particularly if e.g. the observed spectral anomaly at zero bias turns out to be caused by spin excitations rather than the Kondo effect as recently proposed [240–242].

The surprisingly strong dependence of the electronic structure of magnetic adatoms on the exact size of the linear cluster, where apparently even the existence of resonance at zero bias effectively depends on the presence or absence of an atom several sites down the atomic wire, shows a considerable complexity that poses a significant challenge to theoretical descriptions. While our state-of-the-art combination of DFT with CT-HYB for the accurate capture of the behavior of correlated electrons on an impurity was mostly able to describe the clusters qualitatively correctly, the fact that it failed for the two clusters without observed ASK resonance and quantitative deviations show a potential of the systems to serve as quantitative benchmarks for future improvements, although their exact modeling may depend on experimental details such as the STM tips [239, 315] that may be insufficiently precisely characterized here.

4.3 Dependence of spin screening on the adsorption site in iron impurities on partially oxygen-reconstructed niobium surfaces

In this section, we report the detection of Yu-Shiba-Rusinov bound states in iron adatom impurity systems on a superconducting Nb(110) surface by scanning tunneling spectroscopy and the characterization of their energies as strongly dependent on the specific adsorption site of the considered adatom on the partially oxygen-reconstructed (NbO_x) surface. We use the combination of density functional theory with continuous-time quantum Monte Carlo to model these systems in the normal state with their different adsorption sites leading most notably to different adsorption distances. The hybridization with the substrate and the magnetic moment in DFT are found to be influenced by the oxygen impurities as well. Results for the spin screening in the Anderson impurity model allow us to both identify considerably different Kondo scales depending on the site as found in experiment as well as to establish the reduced adsorption distance on NbO_x as the main cause of an increased Kondo scale.

This section is based on the following article, Ref. [316], which is also the source of the figures

*A. Odobesko, D. Di Sante, A. Kowalski, S. Wilfert,
F. Friedrich, R. Thomale, G. Sangiovanni, and M. Bode,
“Observation of tunable single-atom Yu-Shiba-Rusinov states,”
Phys. Rev. B **102**, 174504 (2020)*

4.3.1 Introduction

For our final investigation of the screening of impurity atom spins in this thesis we consider iron on niobium, a less conventional system than the cobalt adatoms on copper of the previous sections. The physical context outlined in their introductions in Sec. 4.1.1 and Sec. 4.2.1 is however highly relevant for this adatom system as well. With niobium as surface material instead of copper, superconductivity sets in around $T_c = 9.2$ K, a relatively high temperature for an elemental metallic surface. In a superconductor the spins of magnetic impurities lead to the formation of Yu-Shiba-Rusinov (YSR) bound states inside the superconducting energy gap [317–320], reminiscent of the Kondo resonance [28, 223, 224, 321] of a normal metal. Systems consisting of short atomic chains of such magnetic impurities have recently been proposed to host topologically protected Majorana fermion quasiparticle states localized at the wire edges [322–327], exemplary experimental realizations of which have also been reported soon thereafter [328–330]. These quasiparticle states have attracted considerable theoretical and experimental in-

terest due to their potential to serve as the base for “fault-tolerant” topological quantum computing [331, 332].

The resonances due to YSR bound states can manifest themselves in different ways. In the strong coupling limit of a Kondo scale $k_B T_K$ much larger than the superconducting gap Δ , Cooper pairs are broken to contribute to energetically preferable Kondo screening and singlet formation [333, 334]. In the opposite case of weak coupling, the impurity moment cannot be fully screened instead and can be described like a classical spin as the Kondo temperature becomes negligibly small [335, 336]. A quantum phase transition between zero and nonzero spin ground states is expected to occur for comparable values of $k_B T_K$ and Δ when the energies of the two YSR states cross [337–339]. Using scanning tunneling spectroscopy (STS), not only the regular Kondo effect but also the behavior of magnetic impurity systems in cases of superconducting host material has been investigated, which has provided experimental confirmation of the quantum phase transition and allowed the characterization and manipulation of YSR states including particularly their energy levels [330, 336, 340–343].

The presented experiments² measure the YSR state energies for various Fe adatoms deposited on the Nb(110) surface of niobium, partially oxygen-reconstructed due to impurities [344]. The positions of the YSR resonances vary depending on the individual adatom, with adatoms on the clean Nb(110) surface clearly belonging to the weakly coupled regime and adatoms on the oxygen-reconstructed NbO_x patches being closer to strong coupling. These two regimes are separated by a quantum phase transition. We perform calculations using first-principles density functional theory (DFT) to model the surface-adatom system and extract parameters for the construction of an Anderson impurity model (AIM) describing the many-body physics of the strongly correlated electrons of the iron *3d*-shell, solved using continuous-time quantum Monte Carlo in hybridization expansion (CT-HYB). This allows us to identify causes of the surface-dependent differences in Kondo temperatures measured in the experiment in the normal state, which is known as discussed above and here also explicitly experimentally shown to be correlated to the YSR state energies in the superconducting state.

4.3.2 Experimental results

Fe atoms were evaporated onto a cleaned [344] Nb(110) surface. Measurements with a scanning tunneling microscope were performed at a temperature of $T = 1.17$ K below the superconducting transition temperature, with a substrate-coated superconducting tip used for measurements of the YSR resonances for improved energy resolution [340].

²by our collaborators Artem Odobesko, Stefan Wilfert, Felix Friedrich, and Matthias Bode, also in Würzburg

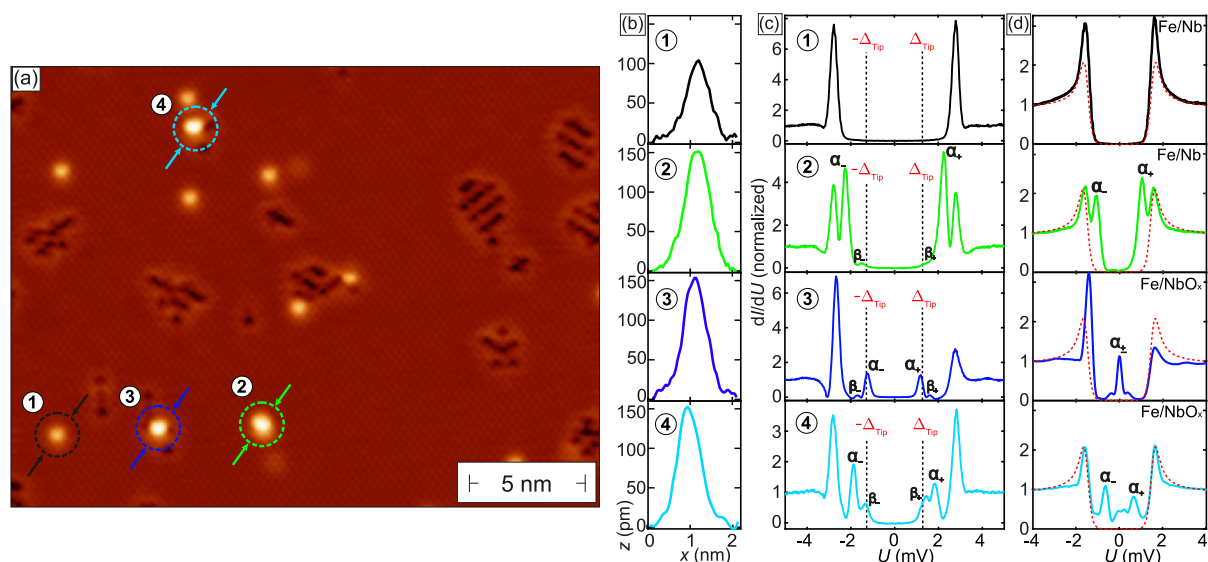


Figure 4.15: Panel (a): STM image of the Nb(110) surface with oxygen-reconstructed patches (dark patterns) and Fe impurities (bright spots) recognizable. Measurements shown in the other panels refer to the circled and labeled Fe adatoms, 1 and 2 on clean surface (Fe/Nb) and 3 and 4 on or near oxygen impurities (Fe/NbO_x). Panel (b): Apparent height profiles across the adatom positions along arrow directions. Panel (c): Differential conductances measured by the STM with superconducting tip (tip gap indicated by dashed lines) at the adatom positions. Panel (d): Spectra of the sample at the atom positions obtained by deconvolution of differential conductances with clean Nb(110) spectrum for comparison of gap position dashed in red.

This necessitates a deconvolution of obtained differential conductance spectra to obtain the pure spectra of the samples, see panels (c) and (d) of Fig. 4.15 for the difference, with details given in the supplemental material of Ref. [316], cf. Refs. [340, 345–347].

A STM image of the Nb(110) surface with oxygen-reconstructed patches recognizable by a darkened pattern and the deposited Fe adatoms visible as bright spots is shown in panel (a) of Fig. 4.15. Exemplary apparent height profiles (in STM constant current mode along arrow directions in panel (a)), measured differential conductance spectra, and sample energy spectra deconvolved from these measurements are shown in the remaining panels of Fig. 4.15 for four adatoms indicated by colored circles and labeled in panel (a). Atoms 1 and 2 (Fe/Nb) are adsorbed to clean Nb(110), 3 and 4 to or near the oxygen-reconstructed surface (Fe/NbO_x). While the bright Fe impurities inhibit experimental determination of the adsorption site, we will later compare the possible geometries using DFT. Apart from atom 1 with a maximum apparent height of only about 100 pm above the top niobium layer, the three other atoms appear at a height of about 150 pm.

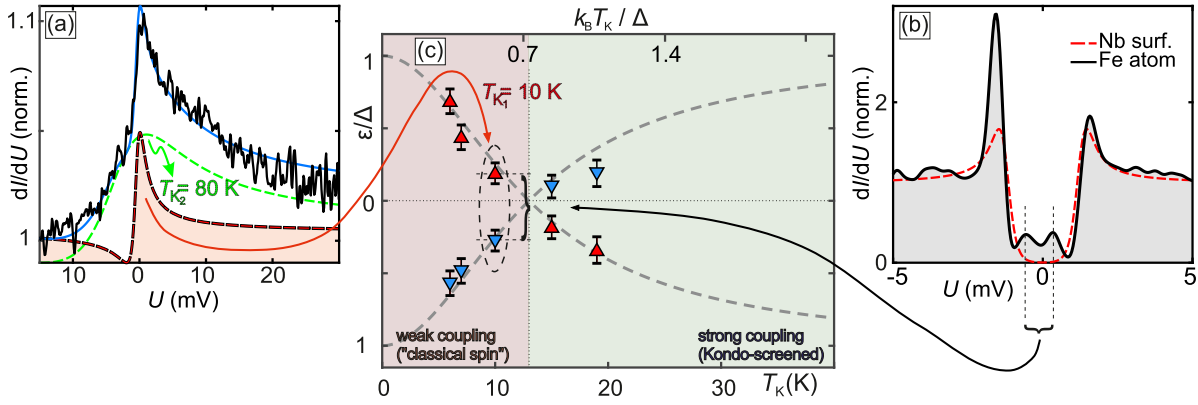


Figure 4.16: Panel (a): Differential conductance spectrum (black) of an Fe adatom at $T = 1.5$ K with superconductivity suppressed by an external magnetic field of $\mu_0 H = 0.6$ T showing a Kondo resonance. The sum of two Fano line shapes (blue) is fit to the curve, one with Kondo temperature $T_{K_1} = 10$ K (red dashed) and one with Kondo temperature $T_{K_2} = 80$ K (green dashed). Panel (b): Differential conductance spectrum (black) of the same Fe atom as in (a) at the same temperature without field suppressing superconductivity, showing peaks in the gap due to Yu-Shiba-Rusinov (YSR) bound states (vertical dashed black positions near zero U), with clean Nb(110) spectrum (red dashed) for comparison of gap position. Panel (c): YSR energies (triangles) for five different Fe adatoms as a function of their Kondo temperatures (when superconductivity suppressed), with evaluation for the example data of the adatom considered in (a) and (b) (two triangles in black dashed ellipse) indicated with arrows. The quantum phase transition where the two YSR states energies (fit with gray dashed curves) cross is indicated by a dashed line and different background coloring of the separated weak and strong coupling regimes.

All four examples are adsorbed on sufficiently different sites to result in qualitatively distinguishable spectra. Looking at the deconvolved spectra in panel (d) of Fig. 4.15 with the clean Nb(110) spectrum for comparison, we see that the YSR resonances for atom 1 are found so close to the gap edges as to be indistinguishable from them, while in-gap peaks are visible for the other atoms. According to the discussion in the introduction, partially visualized by the diagram in panel (c) of Fig. 4.16, this puts the atom apparently closest to the surface into the weakly coupled limit. Atom 2, a rarer case adsorbed to the clean surface, shows α_{\pm} peaks still quite close to the gap edge but clearly distinguishable from it. We should note that much smaller β_{\pm} peaks are visible in the spectra as well, but for the moment we do not include them in our analysis. Proceeding to the Fe/NbO_x examples corresponds to a much larger shift in the spectrum. In the spectrum of atom 3, the YSR states have both moved near the Fermi energy and sufficiently close to be hardly distinguishable. This situation is close to the

quantum phase transition between weak and strong coupling (as a function of ratio $k_B T_K/\Delta$ between Kondo temperature T_K and superconducting gap Δ) where a clear-cut distinction from zero modes (MZM) of Majorana bound states that could appear at the edges of chains of such atoms would be challenging. In the spectrum of atom 4, we actually find the strong coupling case as we can imagine the YSR states to have crossed and separated again, i.e. in our order of cases we figuratively move along $k_B T_K/\Delta$, cf. panel (c) of Fig. 4.16. The different height of the two peaks caused by the effect of the local crystal field on the Fe $3d$ -shell lets us clearly identify this case as opposed to the different order in a weak coupling case [335, 340, 348–350].

To quantify the shift from weak to strong coupling, the measurement of normal state Kondo temperatures T_K is necessary. This can be done with the same experimental setup by suppressing superconductivity with an applied external magnetic field. At the atom positions, differential conductance spectra like the example shown in panel (a) of Fig. 4.16 are measured, which in the case of our Fe impurities can be fit with two Fano line shapes [236] each to determine the Kondo temperatures from the optimal fit parameters, cf. Sec. 4.2.2. We shall see that the lower one is clearly the relevant one for our purposes, cf. also the values for both given in the supplemental material of Ref. [316] where the lower one also does vary with the Fe impurity in a similar manner as the YSR state energies as expected while the higher one is approximately independent of the specific impurity. Using the positions of the YSR resonances in spectra measured in the superconducting state like the ones we previously considered and the example in panel (b) of Fig. 4.16, we can determine the YSR state energies as shown in panels (b) and (c) of that figure and plot the energies of both states against the lower of the two Kondo temperatures per Fe impurity to create panel (c).

In this resulting panel (c) of Fig. 4.16, we can remarkably fit the two times five data points obtained from five different Fe impurities reasonably well using the weak coupling YSR state energy formula

$$\frac{\varepsilon_{\pm}}{\Delta} = \pm \frac{1 - a^2}{1 + a^2}, \quad (4.26)$$

derived under the assumption of a classical spin [318, 319]. Ordinarily, here $a = Jm\pi\rho_0$ with the exchange coupling J , impurity magnetic moment m and the density of states ρ_0 at the Fermi energy in the normal state. For the fit, $a = k_B T_K/(0.72\Delta)$ is used³, where the numerical factor 0.72 best approximates the data points and gives a position of the YSR state crossing and quantum phase transition between the weak and strong coupling regimes at $k_B T_K = 0.72\Delta$, only slightly below the value experimentally found

³Considering e.g. Wilson's NRG result for spin-1/2 [57], we actually have $T_K \propto \sqrt{J\rho_0} \exp(-1/(2J\rho_0))$, which is not proportional to $a \propto J\rho_0$. Apart from a temperature rescaling, which would be compensated anyway by a change in the fit parameter 0.72, solving Wilson's T_K for $J\rho_0$ and inserting that as a into (4.26) however results in a curve of almost the same shape as simply using $a \propto T_K$.

for the transition in Mn-phthalocyanine on Pb(111) [340, 351], and the general form of the dependence is in qualitative agreement with theoretical numerical results [337–339, 352, 353].

Since the largest effect on the peak positions seems to be caused by the vicinity of adatoms to oxygen-reconstructed patches, an experimental attempt to exclude other possible causes is done. An iron atom on the oxygen-reconstructed patch with YSR states significantly inside the gap is moved onto a clean spot on the Nb(110) surface using the STM tip [354], allowing both the confirmation of the presence of oxygen as well as YSR energies often barely distinguishable from the gap edges for atoms on the clean surface. Conversely, another atom at first on the clear surface with just such a spectrum is then moved next to the oxygen-reconstructed patch resulting in the appearance of YSR resonances in the gap and then brought to its center, which shifts the resonances closer to E_F .

In light of the YSR state energy formula (4.26) in the weak coupling limit [318, 319] the experimentally found connection between the presence of oxygen and YSR resonances deeper inside the gap seems contrary to expectation. Oxygen adsorption to the surface is known to have an influence that rather hampers the surface magnetization [355–357]. Further we would rather expect the interaction J to be lower as the Fe adsorption distance increases, which the higher apparent height of Fe/NbO_x measured with the STM would suggest. Both of these points should favor a smaller value of a and hence result in YSR resonances closer to the gap edge, contrary to the observed behavior. For a theoretical analysis beyond the classical spin result that clears up this apparent inconsistency, we turn to the first-principles calculations that combine DFT with the exact solution of the strongly correlated many-body system of the quantum impurity with local moment from the $3d$ electrons. We benefit from the established connection between YSR state energies and normal state Kondo temperatures, cf. Fig. 4.16, which allows us to perform calculations without explicit consideration of superconductivity.

4.3.3 Density functional theory

VASP [256, 257] with the projector-augmented plane wave (PAW) [257, 258] basis set and the PBE [311] generalized gradient approximation as exchange-correlation functional was used to perform DFT calculations for the unit cells shown viewed from the top in panel (a) and viewed from the side in panel (c) of Fig. 4.17, where the case of the pure surface Fe/Nb(110) is shown in the top panels and that of the oxygen-reconstructed one Fe/NbO_x in the bottom panels. The positions of the golden balls in the unit cell are the lowest energy equilibrium adsorption sites of Fe adatoms, with adsorption distances relative to the top surface layer of 170 pm for Fe/Nb(110) and

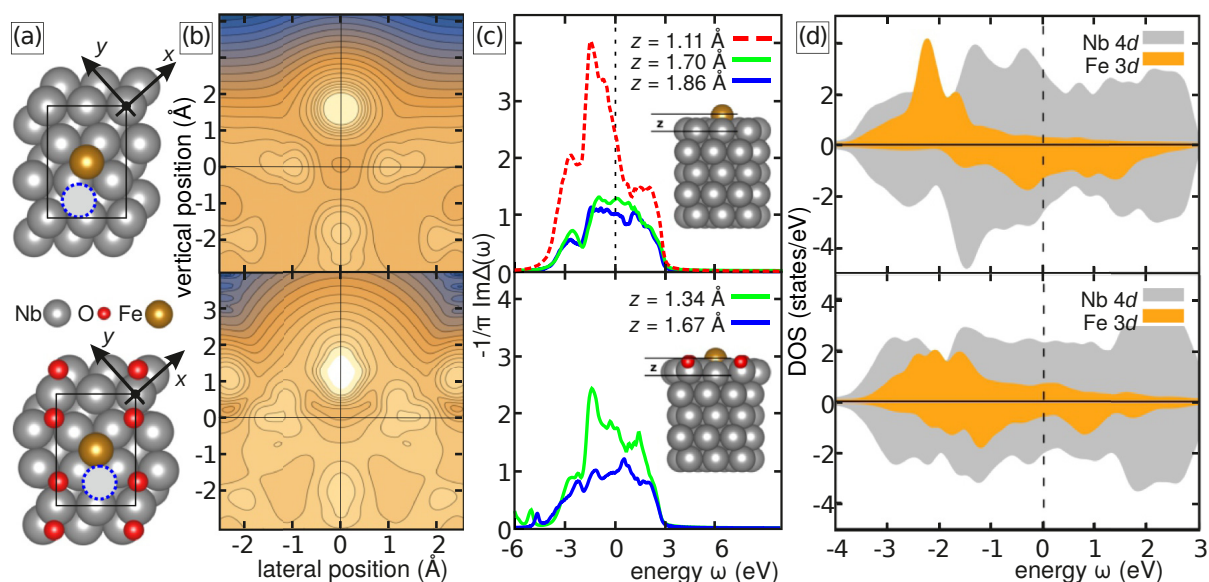


Figure 4.17: Panel (a): Unit cells used in DFT calculations for Fe (golden) adatoms on clean (top) and oxygen-reconstructed (bottom) Nb(110) surface viewed from the top. The corresponding side view is found in insets of Panel (c). Panel (b): Contour plot of the charge density profiles viewed from the side. The global maxima in the plots center on the Fe adatoms. In spite of the shorter adsorption distance (vertical position of the center of the density maximum relative to the top layer) in the oxygen-reconstructed case (bottom), the charge density above the adatom at equal surface distance is higher than in the case of a clean surface (top), leading to higher apparent heights in the STM images, cf. Fig. 4.15. Panel (c): Imaginary parts of the real-frequency hybridization functions for the impurity $3d$ -shell summed over orbitals, for energetically preferred equilibrium adsorption sites (green), secondary sites (blue, dashed sites in (a)), and sensitivity check (red dashed). Panel (d): Spin-polarized (majority spin positive, minority spin negative) DFT density of states resolving contributions by Fe adatom $3d$ -shell (golden) and Nb surface $4d$ -shell (gray) states.

134 pm for Fe/NbO_x. In both cases one of the less favorable other sites is shown as a blue dashed circle in panel (a). We assume that the difference between the two atoms adsorbed on clean Nb(110) that showed different spectroscopic results in experiment, atoms 1 and 2 in Fig. 4.15, is caused by atom 1 being adsorbed at the most favorable fourfold hollow site H_4 and atom 2 being adsorbed in a threefold hollow site H_{4d} instead.

The Fe atom on NbO_x is adsorbed closer to the surface than in the case of a Nb(110) surface, which suggests a larger charge density at the impurity on the oxygen-reconstructed surface than that of an impurity on the clean surface. The data shown in contour plots of a vertical section through the impurity of the DFT charge density in panel

(b) of Fig. 4.17 confirms this. Comparing the two cases, we find that although the center of the charge density is at a lower height for the impurity on the oxygen-reconstructed surface, the charge density at the same distance from the surface is actually greater above an impurity on NbO_x than above an impurity on $\text{Nb}(110)$ because of its greater value at the impurity in the former case. This means that an impurity at the favorable site on NbO_x appears higher in the constant current STM profiles than an impurity at the favorable site on $\text{Nb}(110)$ although its actual adsorption distance is lower, just as it was shown in panel (b) of Fig. 4.15.

The adatom distance to the surface has a considerable influence on the electronic structure including the Kondo scale of the impurity, which is e.g. reflected in the hybridization function. Using the procedure summarized in Sec. 4.1.2, cf. Refs. [182, 260, 261], the hybridization function can be calculated from DFT, and the imaginary part of the hybridization function summed over all Fe $3d$ -orbitals is shown in Fig. 4.17, where the functions for the favorable adsorption sites are shown in green. Around the Fermi level, its value is higher and also its shape generally different for the impurity on the oxygen-reconstructed surface with the lower surface distance than for the impurity on clean $\text{Nb}(110)$. This by itself suggests a higher Kondo temperature according to the crude estimate of T_K (4.23) from DFT quantities only we have considered previously in Sec. 4.2.3, although a many-body method for strongly correlated electrons like CT-HYB should be for a proper investigation of many-body effects like the Kondo effect since DFT is not able to capture strong correlation correctly. There, we represent the five orbitals of the strongly correlated $3d$ -shell of the Fe adatoms as Anderson impurity models including a orbitally uniform interaction of Kanamori form with screened interaction parameters, with the impurity single-particle energy levels and hybridization function taken from DFT. The hybridization function describes hopping processes of electrons from the impurity orbitals (the Fe $3d$ -shell) to a bath (the electronic environment of the impurity, i.e. the substrate bands). While the bath is non-interacting in the Anderson impurity model, this refers to just the sort of interaction that we use for the strongly correlated impurity orbitals, as the interaction treated by DFT is still included via its effect on the bands.

On the other hand, when we consider the spin-resolved DOS of the iron $3d$ -shell, shown in panel (d) of Fig. 4.17, we find a much smaller imbalance below the Fermi energy in the case of the oxygen-reconstructed surface than for the clean surface. This results in a much smaller magnetic moment $m = 0.9\mu_B$ for Fe/NbO_x than for $\text{Fe}/\text{Nb}(110)$, $m = 2.2\mu_B$. Considering the previously found connection between Kondo temperatures and YSR state energies and the energy formula (4.26), we would expect a reduction of the Kondo temperature for a decreased moment.

Compared to the clean surface, we have in total an increase of the hybridization

function due to the closer adsorption distance but a reduced magnetic moment on the oxygen-reconstructed surface. These changes have an opposite effect on the Kondo screening scale; considering (4.26) as proxy, the magnitude of the hybridization function is directly correlated to the exchange coupling J between conduction bands and impurity, which is multiplied with the moment m . In order to determine the resulting effect of these opposite influences, we proceed by performing the exact solution of the strongly correlated problem for the impurity orbitals using the DFT local levels and hybridization function as input.

4.3.4 Continuous-time quantum Monte Carlo simulation

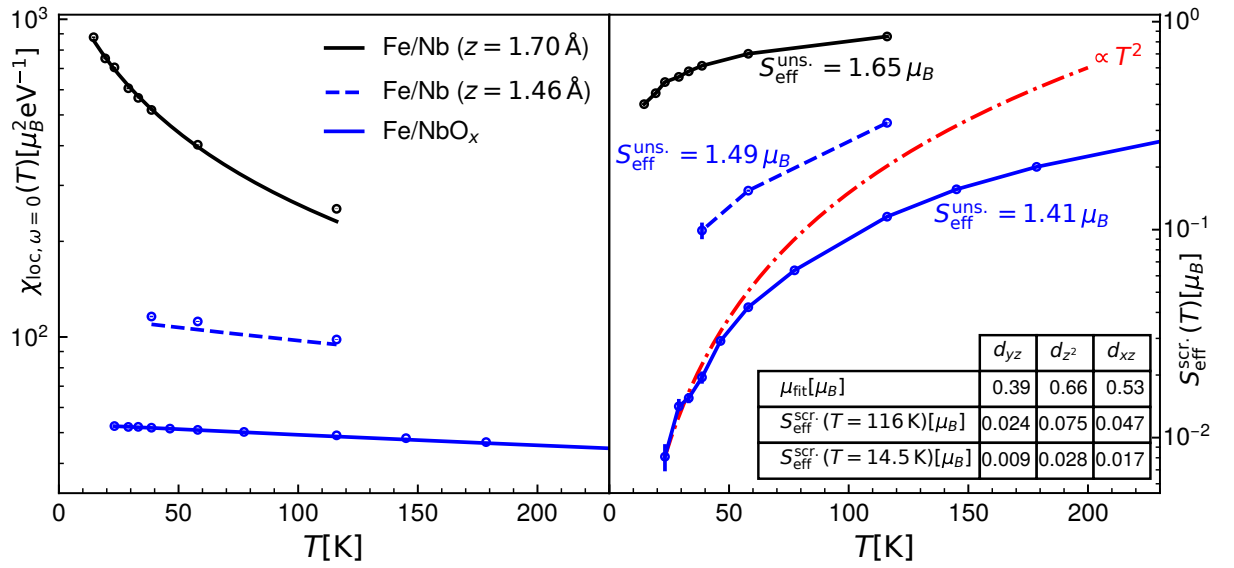


Figure 4.18: Left panel: Total static ($\omega = 0$) local spin susceptibility $\chi_{\text{loc}, \omega=0}(T)$ as a function of temperature of the impurity $3d$ -shell of Fe adatoms adsorbed in equilibrium positions with relaxed distances $z = 1.70 \text{ \AA}$ on a clean (solid black) and $z = 1.34 \text{ \AA}$ on an oxygen-reconstructed (solid blue) Nb(110) surface, and additionally for an “intermediate case” of adsorption on a clean surface with fictitiously reduced adsorption distance of $z = 1.34 \text{ \AA}$ (dashed blue). Curves are fits to the Curie-Weiss behavior of Wilson’s intermediate temperature NRG fit function $\mu_{\text{fit}}^2/3(T + 2T_K)$ with moment μ_{fit} and Kondo temperature T_K . Right panel: Effective spin of the impurity dynamically screened at long imaginary times, with total instantaneous (unscreened) moments given next to the curves and a dashed red T^2 curve for comparison (fit to lowest temperatures of oxygen-reconstructed case). For the more relevant out-of-plane orbitals d_{yz} , d_{z^2} , and d_{xz} , the numerical values of moment fit parameters and effective spin contributions in the equilibrium bare surface case at two different temperatures are given in the inset table (all values in units of the Bohr magneton μ_B).

We use the CT-HYB implementation of *w2dynamics* [40] to solve the impurity problem for the iron $3d$ -shell, with its local single-particle energy levels and the orbital diagonals of the hybridization function as input from DFT, neglecting the offdiagonal elements of small magnitude. Additionally, parameters for the orbitally uniform interaction of Kanamori form $U_K = 3.85$ eV and $J_K = 0.72$ eV, are taken from Ref. [268] where they were calculated for bulk iron using cRPA [37, 38, 269]. As double-counting correction, we fix the chemical potential such that the resulting total occupation of the $3d$ -shell is the same as in DFT [260].

In order to determine the total effect of the different adsorption surfaces on the Kondo screening of the impurity spin, we calculate the imaginary-time spin-spin correlation function $\chi_{ij}(\tau) = g^2 \langle S_{z,i}(\tau) S_{z,j}(0) \rangle$ between impurity orbitals i and j in CT-HYB calculations for several temperatures and perform an evaluation like in Sec. 4.1.4. To summarize, we compute the static impurity spin susceptibility $\chi_{\text{loc},\omega=0}(T) = \sum_{ij} \int_0^\beta \chi_{ij}(\tau)$ and dynamically screened and unscreened effective spins $S_{\text{eff}}^{\text{scr}} = S_{\text{eff}}(\tau = \beta/2)$ and $S_{\text{eff}}^{\text{uns}} = S_{\text{eff}}(\tau = 0)$, for which we solve $m^2(\tau) = 3 \sum_{ij} \chi_{ij}(\tau) = g^2 S_{\text{eff}}(\tau) (S_{\text{eff}}(\tau) + 1)$ for the positive solution of $S_{\text{eff}}(\tau)$, cf. equation (4.6) and the paragraph around it for a more detailed explanation.

The static local spin susceptibility and screened effective spin as functions of temperature are shown in Fig. 4.18. We show values for the Fe impurity on a clean Nb(110) surface (Fe/Nb) at equilibrium adsorption distance $z = 1.70$ Å, the impurity Fe/NbO_x on the oxygen-reconstructed surface at its equilibrium adsorption distance ($z = 1.34$ Å), and a Fe impurity on a clean Nb(110) surface at the adsorption distance $z = 1.34$ Å that is intended to separate out the change between the other two that originates purely from the adsorption distance difference. Comparing the susceptibilities, we find a weak low-temperature dependence approaching the constant Pauli susceptibility for Fe/NbO_x and Fe/Nb at $z = 1.34$ Å, which indicates that screening of the impurity moments sets in inside of the temperature range where we performed calculations for these systems. For the Fe/Nb impurity at its equilibrium distance a clear Curie-Weiss behavior ($\propto T^{-1}$) indicating an unscreened moment can instead be recognized over the entire temperature range of our calculations, which go down to $T = 14.5$ K in that case. This is confirmed by the screened effective spin, which has an inflection point⁴ around 40 K that can serve as a proxy for the Kondo temperature and reaches Fermi-liquid-like behavior [35] proportional to T^2 at lower temperatures in the case of Fe/NbO_x. For Fe/Nb, no inflection point is recognizable and at 14.5 K a screened effective spin of more than a fifth of the instantaneous spin still remains, while it is only less than 1% for Fe/NbO_x. Qualitatively, Fe/Nb with reduced adsorption distance behaves more like Fe/NbO_x, which identifies the distance as an important part of the mechanism leading

⁴Note that the change in curvature is not visible in Fig. 4.18 due to its logarithmic scale.

to different Kondo scales, but we can also recognize from the differences in spin susceptibilities and effective spins plotted logarithmically in Fig. 4.18 that it quantitatively accounts only for about half the difference in magnitudes. We also find an unscreened moment of $1.42\mu_B$ for Fe/NbO_x, slightly smaller than the moment $1.49\mu_B$ of Fe/Nb at the same distance, which together with the quantitative differences in magnitudes points out the expected reduction of the moment because of the oxygen impurities.

Using Wilson’s formula [57] for the susceptibility at intermediate temperatures in the Kondo problem, $\mu_{\text{fit}}^2/3(T + 2T_K)$, we fit both the total static local susceptibility of Fe/Nb at its equilibrium distance resulting in the black fit curve shown in Fig. 4.18 and the diagonal susceptibility components of that impurity for the out-of-plane orbitals d_{yz} , d_{z^2} , and d_{xz} that are most relevant for tunneling from the STM tip in order to determine the fit parameters. The fitted moments for these diagonal susceptibility components as well as the orbital-resolved diagonal contributions to the screened effective spin for the same orbitals of the Fe/Nb ($z = 1.70 \text{ \AA}$) impurity at two different temperatures are given in the inset table of Fig. 4.18. The higher values of the fitted moment and higher contributions to the screened effective spin of the Fe d_{z^2} orbital compared to the other out-of-plane orbitals indicate that the d_{z^2} is in a sense the “most correlated” with most contribution to the moment, which is also confirmed by its occupation that is closer to half-filling than that of the other two, cf. our discussion in 4.1.5.

From the fit of Wilson’s formula, we obtain a Kondo temperature estimate of roughly 10 K for Fe/Nb ($z = 1.70 \text{ \AA}$), compared to the four times higher estimate for Fe/NbO_x from the inflection point of the screened effective spin. This qualitatively confirms the experimental observation of higher Kondo temperatures for iron impurities on the oxygen-reconstructed surface, cf. Fig. 4.16 and identifies the adsorption distance, which is actually smaller in the case of Fe/NbO_x in spite of the greater apparent height in constant current STM profiles as seen in Fig. 4.15, and the increase of hybridization with the substrate caused by it as the driving mechanism behind this difference.

While the strong correlations of the iron $3d$ -shell lead to many-body entanglement and forbid a simple interpretation of the Kondo effect (or YSR resonances) separately for individual orbitals in realistic situations, cf. Sec. 4.1, we may expect that the d_{z^2} orbital that we identified as the largest contributor to the moment and that also points straight in the direction of substrate and STM tip is most responsible for the change of YSR peak positions with the change in adsorption height between Fe/Nb(110) and Fe/NbO_x and that therefore the large α_{\pm} resonances (cf. Fig. 4.15) are related to it. This is reminiscent of the typically high sensitivity of strongly correlated electron systems to small changes of system parameters [23, 358, 359]. The smaller β_{\pm} resonances, whose positions also do not systematically depend on the surface and thus the adsorption height, may be related to tunneling processes involving other orbitals, most likely the

$d_{xz,yz}$ ones that are not in-plane either, and are likely also connected to the second Fano line shape with considerably higher Kondo temperature necessary to fit the normal state differential conductance spectra, cf. Fig. 4.16. Multiple Kondo screening channels with different Kondo scales are consistent with previous results for Fe impurities [341].

4.3.5 Conclusions

In systems of iron impurities on a niobium Nb(110) surface a strong dependence of the positions of the YSR resonances in the superconducting state and Kondo temperatures in the normal state on the concrete adsorption site is found in STM spectroscopy. Adsorption on clean Nb(110) leads to a small Kondo temperature and YSR resonances overlapping with the gap edges, corresponding to the weakly coupled regime where the impurity moment can be described as a classical spin, while adsorption near and ideally on oxygen-reconstructed patches of the surface leads to an increased Kondo temperature and YSR resonances in the middle of the gap, corresponding to the strong coupling regime. This characterization may contribute to the directing of efforts to assemble nanostructures hosting Majorana bound states that are candidates for topological quantum computation [322, 328], where the comparatively high critical temperature of niobium for an s -wave superconductor could be an advantage.

The observation that Fe/NbO_x impurities are in the strong coupling regime while Fe/Nb(110) impurities are not is contrary to the normally expected influence of oxygen impurities. Calculations with DFT followed by CT-HYB solutions of the strongly correlated behavior of the iron $3d$ -shell are performed to elucidate this. DFT results indicate that the actual equilibrium adsorption distance on the oxygen-reconstructed surface is significantly smaller than on the clean surface, leading to stronger hybridization with the substrate. The magnetic moment on the oxygen-reconstructed surface resulting from spin-polarized DFT is however reduced considerably compared to that on the clean surface.

In total, it is found that the reduced adsorption distance contributes considerably to a higher Kondo temperature in CT-HYB results, both in results for the actual Fe/NbO_x impurity as well as for a comparison system consisting of an impurity on the clean surface with the adsorption distance of Fe/NbO_x rather than the energetically preferred one. The unscreened spin moments of the $3d$ -shell in CT-HYB only differ slightly, but the moment of the impurity on the oxygen-reconstructed surface is screened at qualitatively higher temperatures of around 40 K in comparison to a much lower Kondo temperature for the clean surface of around 10 K, which confirms the experimental results and allows us to attribute this effect primarily to the reduced adsorption distance that increases hybridization with the substrate.

5 DMFT analysis of the doped two-orbital Hubbard model with Hund's coupling

5.1 Mott quantum critical point at finite doping

In this section, we investigate the phase diagram of a two-orbital Hubbard model with Hund's coupling by application of dynamical mean-field theory (DMFT), a numerical method that allows access to the non-perturbative behavior of lattice models. The first-order interaction-driven Mott transition and its phase separation zone present at all sufficiently low temperatures are found to extend into the finite doping region, where the transition turns into one between a weakly and a strongly correlated metal. At constant temperature, the multi-valued solution with meta- and unstable branches that describes the system in the coexistence region unfolds with increasing chemical potential and becomes single-valued at finite doping. Due to continuity, the first order of the transition at half-filling implies the existence of a line of critical points ending in a quantum critical point at zero temperature. Splitting of the on-site ground state multiplet by a small term is identified as the cause of the transition being of first order at half filling through the physical interpretation of our results with the aid of a perturbative expansion. This suggests a generalization of the results to cases with a small parameter other than Hund's coupling.

This section covers mostly results previously published in the following article and its supplemental material, Ref. [193], which are also the source of some of the figures, and also discussed in Ref. [360]

*M. Chatzieftheriou, A. Kowalski, M. Berović, A. Amaricci, M. Capone, L. De Leo, G. Sangiovanni, and L. de' Medici, "Mott Quantum Critical Points at Finite Doping," Phys. Rev. Lett. **130**, 066401 (2023)*

5.1.1 Mott transition in the Hubbard model: background and methods

The Hubbard model that we consider in this chapter is one of the prototypical models in the physics of strongly correlated systems. First introduced and approximately solved by Hubbard [31, 66, 119], it consists of a lattice of sites with one orbital each that in addition to the usual inter-site hopping term also incorporates a local on-site interaction term. The kinetic energy of the electrons is lowered by their delocalization thanks to the hopping term, which gives rise to energy bands describing the behavior of weakly correlated electrons. However, the additional on-site repulsion penalizes this delocalization with an increase of potential energy for doubly-occupied sites. At half-filling, the competition between these two terms taken together is already sufficient to obtain a transition between a conducting and an insulating state as the ratio of their coefficients is varied, while a partially filled band should always be conducting according to band theory. Materials with partially filled bands that still fail to conduct due to strong correlations are called Mott insulators, named after Nevill Mott who had previously proposed that mechanism [361] as well as considered the possibility of a so-called Mott transition between this insulating state and a metallic state due to changes in material parameters [21].

In spite of its relative simplicity, the Hubbard model whose Hamiltonian consists of only two terms that are easily solvable individually is in general not analytically tractable. Great progress was achieved through the mapping to an impurity model with self-consistently determined bath [33, 70, 135], which is exact in the limit of infinite coordination and serves as a “dynamical mean-field theory” (DMFT, see Sec.2.3) approximation for finite dimensions. In contrast to standard mean-field theory [47], DMFT includes temporal fluctuations and allowed for the first time numerical treatment of the Hubbard model in a non-perturbative way that captures both quasiparticle as well as incoherent excitations.

When we consider the Hubbard model on a bipartite lattice it is possible for antiferromagnetic order to arise as well. This requires a description with a magnetic unit cell of doubled dimensions and correspondingly a Brillouin zone of half the size. In the case of a half-filled band, this can cause an insulating state due to the creation of a gap in the middle of the original bands at the new Brillouin zone edges. This alternative mechanism, which does not identify local on-site repulsion as the cause in contrast to the one proposed by Mott, was proposed by Slater as the cause of insulating behavior at half-filling [364]. Solving the Hubbard model in the case of a bipartite lattice using DMFT reproduces such a transition to an antiferromagnetic insulator [134] with a transition temperature usually well above the critical temperature of the Mott transi-

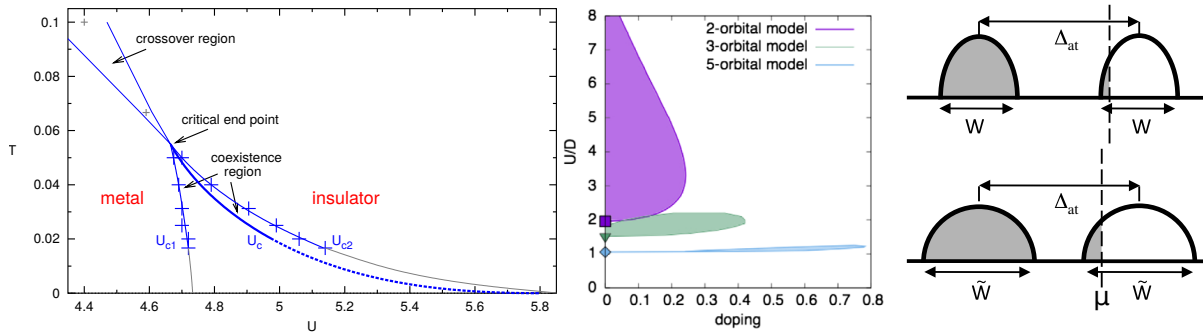


Figure 5.1: Left panel: DMFT phase diagram of the half-filled single-band paramagnetic Hubbard model with semicircular density of states in the plane of temperature T and interaction strength parameter U using a quantum Monte Carlo impurity solver. The critical point with a second order transition at non-zero temperature is marked as “critical end point” and the thinner blue lines going down toward zero temperature from the critical end point and their gray extrapolations delimit the coexistence region, where solutions for both phases can be found but one is only metastable rather than stable. The line of the first-order transition between the metal and insulator (thickest blue line, partially dashed) runs through the coexistence region relatively close to its upper end U_{c2} with which it coincides at the critical end point and at zero temperature, where the transition is of second order again as well. Taken from Fig. 3.50 of Ref. [362]. Middle panel: Zones of instability against phase separation in the phase diagram of multiorbital Hubbard models with Hund’s coupling in the plane of interaction strength U and doping from half-filling calculated using the not numerically exact slave-spin mean field theory. Right panels: Sketch of the spectral functions as schematic explanation of the instability. The doping is increased going from the upper panel to the lower panel, but an increase in the doping also increases orbital fluctuations that are quenched at half-filling by Hund’s coupling, which widens the Hubbard bands. This counteracts the effect of the increased occupation sufficiently to give a lower chemical potential in total contrary to the typical case. Middle and right panel taken from Fig. 2 of Ref. [363]¹.

tion that would take place in case of a paramagnetic or magnetically frustrated model [136, 365]. In the case of an unfrustrated bipartite lattice, the low-temperature region is thus entirely “covered” by the antiferromagnetic phase with no Mott metal-insulator transition but only a smooth crossover in dependence of the interaction strength.

When we perform a (dynamical) mean-field solution of the Hubbard model, however, nothing forces us to allow the solution to become spin-dependent and thus e.g. antiferromagnetic. We are free to ignore the energetically favorable magnetic order and

¹Reprinted figure with permission from L. de’Medici, “Hund’s Induced Fermi-Liquid Instabilities and Enhanced Quasiparticle Interactions,” *Phys. Rev. Lett.* **118**, 167003 (2017). Copyright 2017 by the American Physical Society.

use the self-consistency equations for the paramagnetic case anyway, which allows us to investigate the Mott metal-insulator transition that happens in this case down to zero temperature [135]. In this way, at half-filling a phase diagram as shown in Fig. 5.1 can be obtained, with a metallic phase at small interaction strength U turning into a Mott insulating phase for large U , which happens as a continuous crossover above the critical temperature and as a first-order phase transition across the bold line for non-zero temperatures below it [136, 365]. At the phase transition line, the phase with the lowest free energy changes, but around it there is a coexistence region (with dotted lines as boundaries) where both phases are at least metastable. With DMFT, both solutions can be calculated by starting with the right initial conditions, analogous to the hysteretic behavior known e.g. from ferromagnetism [366]. Critical points with second-order transitions are found at both the non-zero (filled square) and the zero temperature end of the first-order transition line [367–369].

Let us now consider a simple multiorbital extension with degenerate orbitals. If we do not include Hund’s coupling, i.e. the reduction of the Coulomb repulsion between electrons with parallel spin [42], the continuous transition at zero temperature persists [370]. If Hund’s coupling is included in the multiorbital case however, this “bandwidth-” or “interaction-controlled” transition due to a change in U relative to the bandwidth at constant half-filling can become discontinuous at $T = 0$ [271, 371, 372]. As a consequence, one can expect that the doping-controlled transition turns into a first-order transition as well, and a phase separation region extends off half-filling to finite doping [373]. Such charge instabilities have been studied before in the context of models for cuprate superconductivity [374–378], which usually occurs in compounds that can be characterized as doped Mott insulators of the charge-transfer type [23]. For these systems, it is one single d -orbital that is primarily relevant for the low-energy description [23] and so an effective single-orbital description [379, 380] is often considered enough, but even in a one-orbital Hubbard model finite-doping charge instabilities can appear due to the inclusion of next-nearest neighbor hopping [381].

Contrary to the cuprate superconductors, in the so-called “Hund’s metals” [20, 382, 383], which include other transition metal oxides [20, 384] and among them in particular the iron-based superconductors [27, 382], multiple bands derived from transition metal d -orbitals are relevant to the low-energy electronic structure around the Fermi level [20]. In their metallic states, strong electronic correlations are induced by Hund’s coupling (occasionally termed “Hundness”) even far away from the Mott-insulating state [187], while in the cuprates for example it is specifically the proximity to the Mott insulator (“Mottness”) that is regarded as the only source of correlations. Metallic states with strong correlations due to Hund’s coupling are characterized by a number of unusual properties, such as large effective masses indicating a low quasiparticle

weight in the low-temperature Fermi-liquid state [184, 186, 188] and particularly also a strongly decreased quasiparticle coherence temperature which limits the applicability of the Fermi-liquid description [35, 184, 186, 188]. Above this temperature, this manifests itself in features like the broadening of spectral quasiparticle peaks [186] and strong deviations from the typical Fermi-liquid temperature scaling of quantities such as the self-energy or scattering rate [35, 186], resistivity [184, 188] and susceptibility or spin-spin correlation function [35, 184, 186, 188]. Further, the behavior of the spin-spin correlation function and magnetic susceptibility implies the presence of unscreened local moments down to the coherence temperature [35, 184, 385, 386]. This behavior of the spin degree of freedom stands in contrast to the concurrent quenching of orbital fluctuations and increase of orbitally differentiated correlations [284, 285, 387–389], such as orbital-selective Mott phases, provided that the orbital degeneracy is lifted; these dramatically different energy scales for spin and orbital screening due to Hundness and their effects are also termed “spin-orbital separation (SOS)” [190–192].

This strongly correlated bad metallic behavior is particularly prominent around integer fillings that are neither half- nor single-filling (by a single electron *or* hole), as there Hund’s coupling can both increase correlations with its spin-aligning effect while disfavoring the Mott transition at the same time [187, 390]. Minimal models therefore tend to have at least three orbitals, which is also the size of the t_{2g} shell relevant for the transition metal oxides with cubic symmetry [20]. However, the strong multiorbital correlations due to Hund’s coupling were also discovered to cause a region of instability towards phase separation with a divergence of the compressibility, surrounded by a zone with enhanced compressibility in the stable phases [363, 391, 392]. The phase separation region is situated at finite doping adjacent to the Mott transition at half-filling, illustrated using the results of slave-spin mean-field theory [363] in the middle panel of Fig. 5.1, roughly where the crossover between the strongly correlated Hund’s metal phase and a weakly correlated (“good”) metallic phase coming from higher doping would otherwise continue toward half-filling [35, 285, 385]. Schematically, one can explain the possibility for a charge instability due to the resurgence of charge fluctuations away from half-filling, which can widen the Hubbard bands sufficiently quickly to bring down the niveau of the highest filled level even as the filling itself is increased [363], see the right panels of Fig. 5.1. Qualitatively, these features do not even require the three orbitals originally considered in this context, but can already be investigated in two-orbital models, which we will consider here. There are indications of such behavior in iron-based superconductors [393] and in particular also that trends in the superconductivity might be related to their vicinity to the zone of compressibility enhancement and divergence in the parameter space of the Hubbard model [394, 395]. The connection to superconductivity is speculated [363] to be explained by the relation

of the same Landau parameter in Fermi-liquid theory to both compressibility enhancement and effectively attractive interactions between quasiparticles.

Previous investigations of this instability [363, 391, 392, 394, 395] were primarily based on the use of slave-spin mean field theory (SSMF) [396, 397], a computationally much less demanding technique than DMFT which, however, is only capable of describing the interacting metallic states as Fermi liquid states [398]. As we have already noted, the literature points to an unusually low coherence temperature in the Hund's metal phase [35, 184, 186, 188], and while in fact a Fermi liquid description may be sufficient for the parameter region most relevant for iron-based superconductivity [20, 399–402], we can obviously not expect this mean-field technique to be numerically exact either. Here, we perform DMFT calculations in the relevant parameter regions at zero and non-zero temperatures to confirm the presence of the instability and further demonstrate the presence of a quantum critical point at the boundary of the zero temperature phase separation region at finite doping.

A quantum critical point (QCP) as we find here is definition-wise a transition point of a continuous phase transition at zero temperature [403]. There, the system passes from one phase to another as one of its control parameters other than the temperature is tuned through its critical value [403, 404]. Since the temperature thus remains at zero, the states on either side of the QCP, whose properties are strikingly different, are still both ground states. Therefore, quantum fluctuations rather than thermal fluctuations are responsible for the critical behavior, unlike at a classical critical point [403]. As the behavior at the critical value of the control parameter up to relatively high temperatures is dictated by the thermal excitations of the quantum critical ground state [403], which cannot be described in terms of quasiparticles, the presence of a QCP can however cause unusual behavior in a relatively large part of the phase diagram [403, 404], which is a feature that makes their presence particularly interesting. Quantum critical behavior, e.g. critical scaling of observables, is known to be relevant for the Mott metal-insulator transition [197, 405–410] and has also received considerable interest in the particular context of cuprate superconductors and models for them [23, 411–425].

We consider the paramagnetic degenerate two-orbital Hubbard model described by the Hamiltonian

$$H = \sum_{\langle i,j \rangle, m, \sigma} t_{ij} c_{im\sigma}^\dagger c_{jm\sigma} \quad (5.1)$$

$$+ U \sum_{im} n_{im\uparrow} n_{im\downarrow} + (U - 2J) \sum_{im, m' \neq m} n_{im\uparrow} n_{im'\downarrow} + (U - 3J) \sum_{i, m < m', \sigma} n_{im\sigma} n_{im'\sigma} \quad (5.2)$$

$$- J \sum_{i, m' \neq m} c_{im\uparrow}^\dagger c_{im\downarrow} c_{im'\downarrow}^\dagger c_{im'\uparrow} + J \sum_{i, m' \neq m} c_{im\uparrow}^\dagger c_{im\downarrow}^\dagger c_{im'\downarrow} c_{im'\uparrow} \quad (5.3)$$

with creation and annihilation operators $c_{im\sigma}^\dagger$ and $c_{im\sigma}$ for electrons on lattice site i with orbital $m \in \{1, 2\}$ and spin σ , density operators $n_{im\sigma} = c_{im\sigma}^\dagger c_{im\sigma}$, hopping amplitudes t_{ij} and as interaction parameters the on-site intra-orbital repulsion U and Hund exchange coupling J . For most calculations, we use only the density-density parts (5.2) of the interaction and neglect the spin-flip and pair-hopping terms (5.3). With any change in U , we perform a proportional change in J to keep the ratio U/J fixed to 0.25 for calculations with density-density interaction. We choose a semi-circular density of states (DOS) $D(\epsilon) = \frac{2}{\pi D} \sqrt{1 - (\frac{\epsilon}{D})^2}$ with half-bandwidth $D = 1$ unless explicitly specified otherwise. This DOS corresponds to a Bethe lattice in the limit of infinite coordination number, but the choice of lattice plays only a minor role as our phenomena of interest are caused by the electronic many-body interaction.

For the numerical solution of this lattice model, we perform DMFT calculations using a numerical renormalization group (NRG) [58, 211, 426] implementation based on *NRG Ljubljana* [427] and the exact diagonalization (ED) [4] implementation *EDIPack* [428] as impurity solvers at zero temperature² and the continuous-time quantum Monte Carlo in hybridization expansion (CT-HYB) [34, 36] (see Sec. 2.2) implementation of *w2dynamics* [40] at other temperatures.

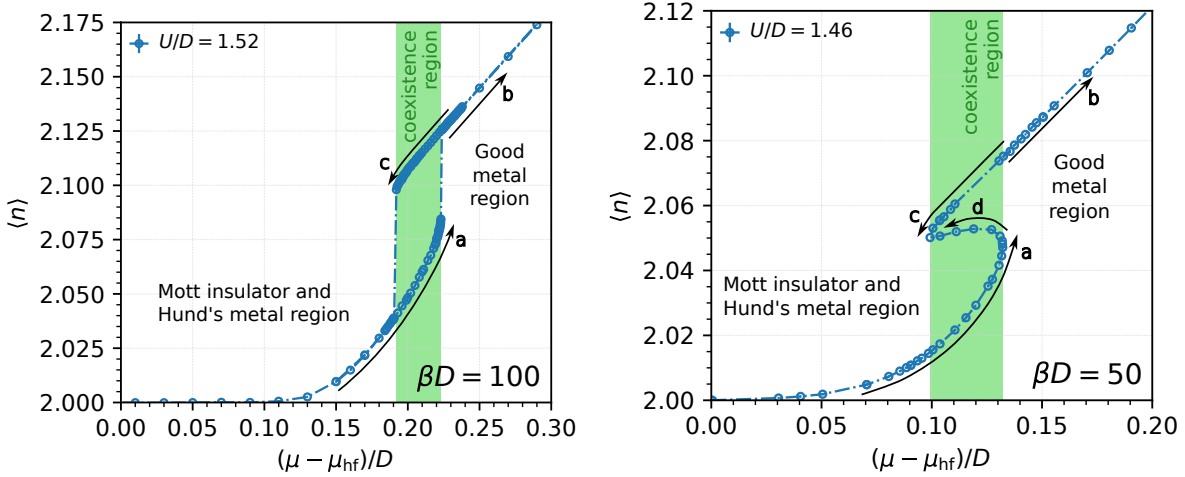


Figure 5.2: Order in which points on the $\langle n \rangle(\mu)$ -curves are calculated, indicated by arrows labeled alphabetically in order of calculated sections, with chemical potential relative to the chemical potential μ_{hf} at half-filling $\langle n \rangle = 2.0$. Left panel: Curve at $\beta D = 100$ without calculation of unstable branch. Right panel: Curve at $\beta D = 50$ with calculation of unstable branch.

This way, we can e.g. trace the $\langle n \rangle(\mu)$ -curves we are particularly interested in by performing DMFT calculations for all the sets of system parameters, i.e. μ , U and the

²NRG and ED calculations were performed by our collaborators Maria Chatzieftheriou and Luca de' Medici

temperature $T =: 1/\beta$, in our region of interest. Outside of the coexistence region, the specification of the model and one of these parameter sets maps to one unique correct result, but in the coexistence region and its vicinity, we can obtain multiple results due to the coexistence of phases [366], see Fig. 5.2. Even though only one of the phases in the coexistence region is stable in the thermodynamic sense [429], given appropriate initial conditions, i.e. starting from the self-energy of the previous point along the arrows in Fig. 5.2, the DMFT iteration converges to the metastable continuation of the other stable branch just as easily. Metastable sections are situated close to the tips of the arrows labeled a and c in Fig. 5.2. The equilibrium solution would instead follow a curve that is single-valued everywhere except at one chemical potential in the coexistence region, where the two stable branches are connected by a vertical line segment, the Maxwell construction [430] (see e.g. the red segment in the upper right panel of Fig. 5.13), along which phase separated solutions exist.

Our procedure per β and U is therefore the following, where we refer to the Fig. 5.2 illustrating the procedure in the text. We begin calculations with $\mu = \mu_{\text{hf}}$ to obtain the point at half-filling $\langle n \rangle = 2.0$. The starting self-energy is taken from a half-filling solution at smaller interaction strength U in order to favor the metallic solution if it exists, such that recognize early when we are in or below the coexistence region at half-filling, which is likely at lower interaction strength than the critical point we are interested in, cf. the right panel of Fig. 5.11. We then obtain additional data points at the same U and β following the branch of the phase at half-filling by repeatedly increasing μ and starting each subsequent calculation from a reasonably well converged self-energy for the previous μ as initial guess, i.e. we calculate the points along the arrows labeled a using the self-energy of the previous point as input. If U is small enough that the solution at half-filling is metallic or larger than that of the critical point at the current temperature, i.e. if we do not enter a coexistence region at $\mu > \mu_{\text{hf}}$, this already traces out the entire $\langle n \rangle(\mu)$ -curve. These cases e.g. occur at temperature $\beta = 50$ for $U \lesssim 1.44$ and $U \gtrsim 1.4920$, cf. the left panel of Fig. 5.12.

Otherwise, we get the unique section of the curve to the left of the coexistence region and the insulating, i.e. lowest, branch inside of it, whose end at the right end of the coexistence region we recognize by a discontinuous jump in $\langle n \rangle(\mu)$. From the point right after the jump, we can just continue increasing the chemical potential to trace out the unique section to the right of the coexistence region by following the arrow labeled b. Additionally, we can also trace out the stable metallic branch inside of the coexistence region from there by following arrow c instead, where we instead decrease μ until we find the jump at the left end of the coexistence region. This is enough to give us all points on sections corresponding to stable and metastable phases, which results in a “hysteresis curve” in the cases with coexistence regions displayed in the left panel

of Fig. 5.2, where the dash-dotted line that serves as a guide to the eye connects points across the jumps.

We may finally choose to also calculate the points on the unstable metallic middle branch in the coexistence region, which are solutions that are unstable both thermodynamically and as fixed points of DMFT. It is therefore necessary to take care to use a fixed-point solution algorithm (also called “mixing” as it computes new trial inputs from previous results) that converges for unstable fixed points as well as a phase-space extension that allows us to force converge to the solution that is not on one of the other two branches, as described in Ref. [146]. Here we use a modified version of Broyden’s method described in Refs. [145] and [431] as fixed-point solver and consider the quantity $\frac{\text{Im}\{\Sigma(i\omega_0)\}}{\omega_0}$ for the phase-space extension, which can be considered as an estimate of the quasiparticle weight Z using only the first Matsubara frequency (cf. Sec. 2.4). This quantity changes monotonically along the complete continuous multi-valued curve in all cases where we have calculated unstable fixed points and it therefore suitable for targeting unique points. Having followed the sections along the arrows a and c to their ends before, we can take the values of Z at those ends as lower and upper bounds for the values on the unstable branch, which allows us to set well-spaced target values and follow the unstable branch along the arrow labeled d, with an example shown in the right panel of Fig. 5.2.

In the next section, which first revisits the half-filling case and therefore fixes the chemical potential to μ_{hf} , we perform an analogous procedure varying U instead of μ . The description of the procedure assumes filling greater than half-filling, but could be performed analogously for fillings less than half-filling. Except for the examples mentioned in the outlook section, we only consider filling greater than half-filling and additionally the results for the simple degenerate two-orbital Bethe lattice system we consider are symmetric around μ_{hf} .

5.1.2 Half-filling case

Let us first revisit the case of half-filling and its properties known from the literature since we shall later demonstrate the connection between the order of the Mott transition at half-filling and the presence of a quantum critical point at finite doping. To do that, we perform DMFT calculations at various temperatures T for increasing values of the interaction parameter U with concomitant adjustment of the chemical potential to keep the resulting occupation per site fixed to half-filling. For symmetric densities of state such as the semicircular one and an interaction of density-density or Kanamori form, we can rewrite the Hamiltonian in a particle-hole symmetric form to find the appropriate value of the chemical potential for half-filling $\mu_{\text{HF}} = (2N_{\text{orb}} - 1)\frac{U}{2} - (N_{\text{orb}} - 1)\frac{5J}{2}$

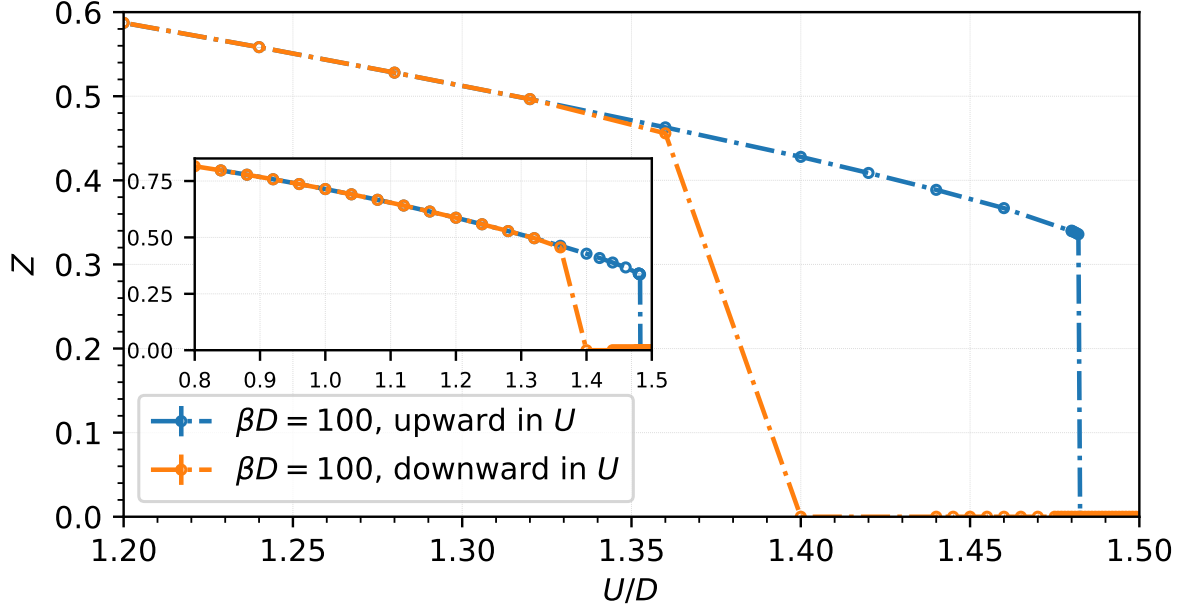


Figure 5.3: Quasiparticle weight Z as a function of the relative interaction parameter U/D for the model with density-density interaction at $\beta D = 100$. Solutions were calculated both by using self-energies from lower U results as initial guess (“up” in U) as well as by using self-energies from higher U results (“down” in U), with a wider range shown in the inset.

as a function of the interaction parameters U and J and the number of orbitals N_{orb} , which is explicitly shown in Sec. 5.1.4 for the density-density case.

As primary indicator of the system state we use the quasiparticle weight Z introduced in Sec. 2.4, a measure of the correlation strength going from 1 for uncorrelated electrons to 0 in the Mott insulating state, estimated from a linear fit of the Matsubara axis self-energy $\Sigma_m(i\omega)$ for orbital m at the two lowest positive Matsubara frequencies

$$Z_m = \frac{\text{Im}(\Sigma_m(i\omega_1)) - \text{Im}(\Sigma_m(i\omega_0))}{\omega_1 - \omega_0}, \quad \omega_n = \frac{(2n+1)\pi}{\beta}. \quad (5.4)$$

Due to the orbital symmetry of our system, we obtain only one unique value of Z . At temperature $\beta D = 100$ for the case with density-density interaction, we perform calculations both using converged self-energies from both lower and higher interaction strength results as initial guesses, i.e. we go both upward and downward in U -direction in order to obtain both of the two different branches of $Z(U)$ shown in Fig. 5.3. This confirms that there is a coexistence region with lower and upper bounds U_{c1} and U_{c2} , as already in the one-band case [33], in which both a metallic and an insulating solution can be stabilized. The quasiparticle weight in the metallic state decreases monotonically with increasing interaction strength, and as Z does not vanish continuously

but abruptly jumps to zero at the end of the coexistence region, we conclude that the interaction-driven Mott transition is of first order.

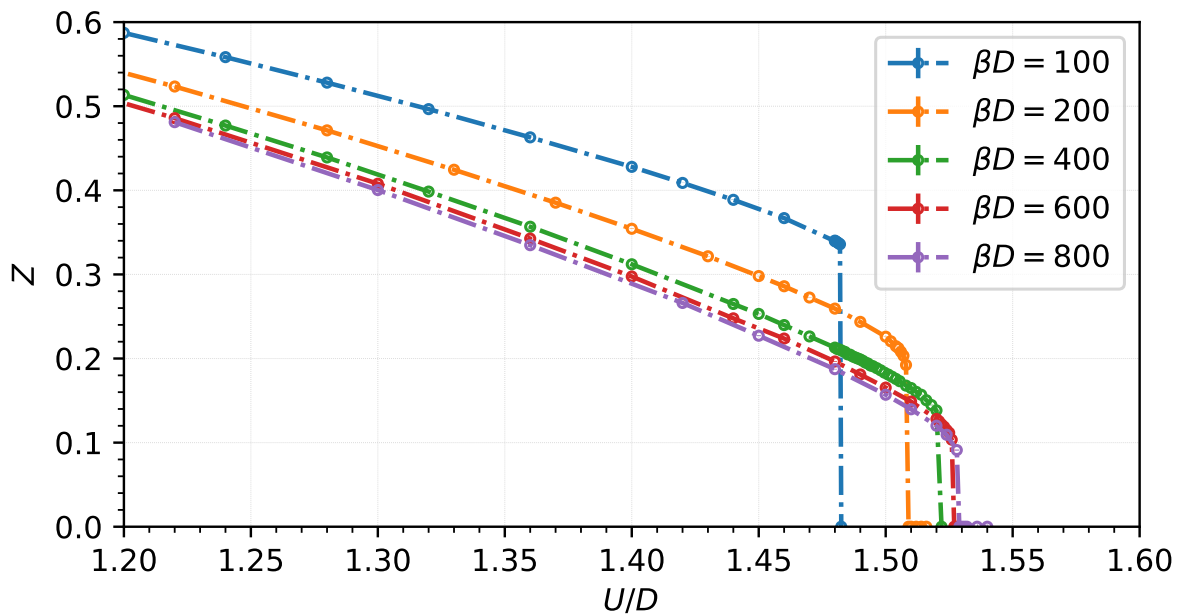


Figure 5.4: Quasiparticle weight Z as a function of the relative interaction parameter U/D for the model with density-density interaction at various temperatures.

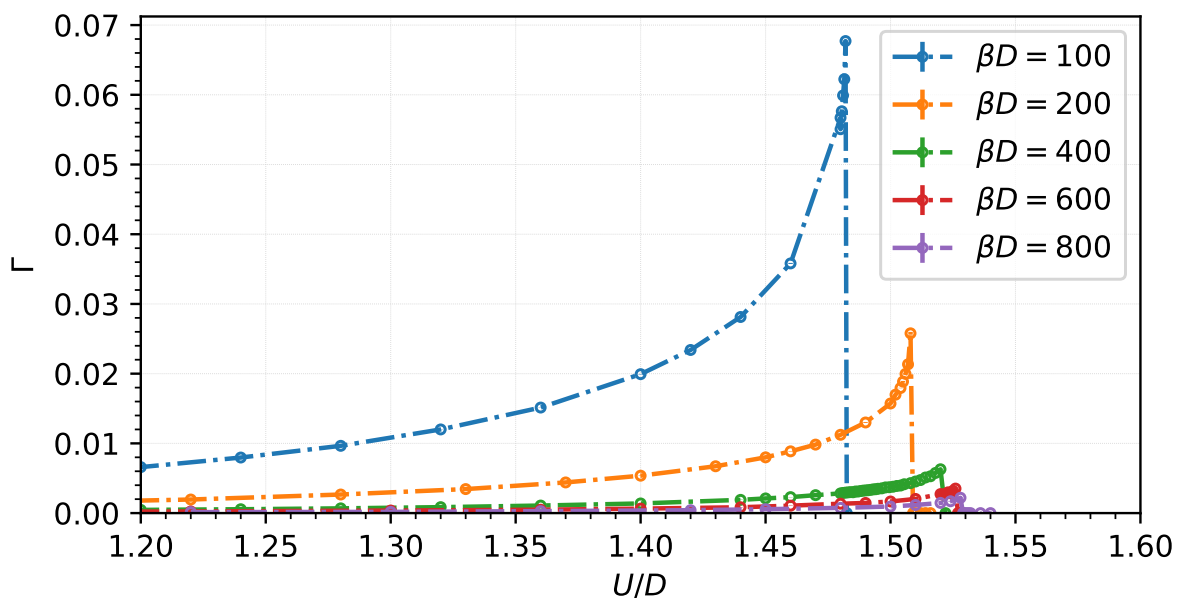


Figure 5.5: Quasiparticle scattering rate Γ as a function of the relative interaction parameter U/D for the model with density-density interaction at various temperatures.

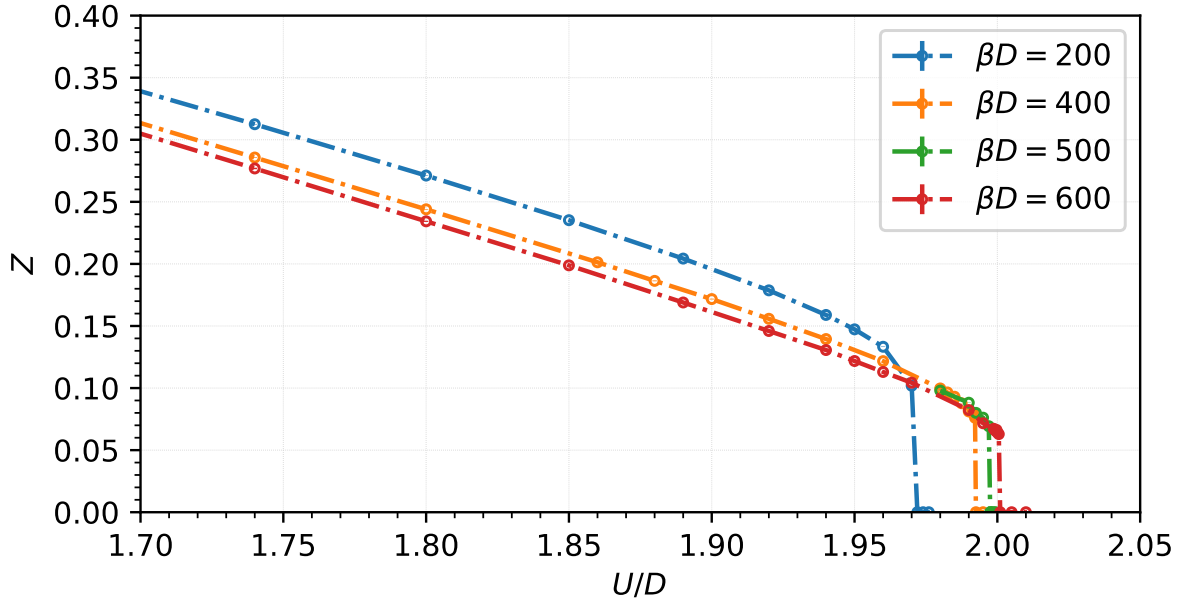


Figure 5.6: Quasiparticle weight Z as a function of the relative interaction parameter U/D for the model with Kanamori interaction at various temperatures.

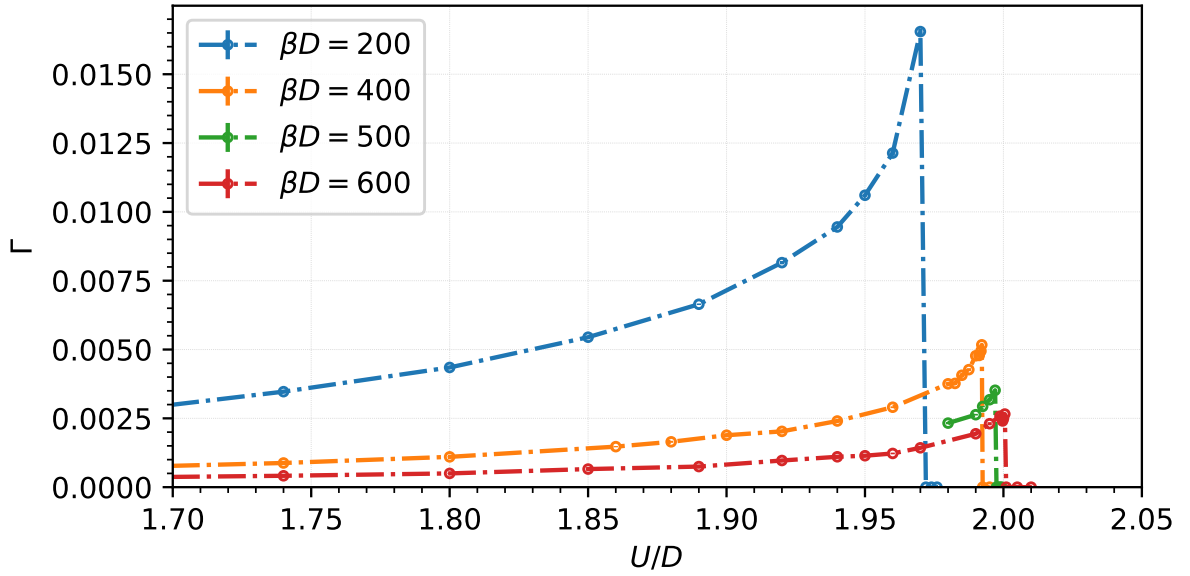


Figure 5.7: Quasiparticle scattering rate Γ as a function of the relative interaction parameter U/D for the model with Kanamori interaction at various temperatures.

Results for other temperatures and Kanamori interaction, shown in Figs. 5.4 and 5.6, are similar: $Z(U)$ decreases monotonically with U up to an abrupt jump to zero at U_{c2} , which gets more pronounced with decreasing temperature. The difference in U_{c2} between density-density and Kanamori interaction originates at least partially from

the difference in the used Hund's couplings $J/U = 1/4$ and $J/U = 0.15$, as a higher Hund's coupling is known to decrease U_c at half-filling independently of the form of the interaction [187, 433]. We can further consider the quasiparticle scattering rate $\Gamma_m \propto -Z_m \text{Im}(\Sigma_m(i\omega \rightarrow 0))$ [47], whose due to orbital symmetry also single unique value is shown in Figs. 5.5 and 5.7 for the same cases. It monotonically increases with U up to a comparatively sharper peak just before the Mott transition in spite of the opposite change of Z , and also indicates a strengthening of correlations. Reducing the temperature at constant U on the other hand, Z and Γ both decrease indicating a less metallic state in spite of lower scattering rate, which seems to roughly follow its expected low-temperature scaling in a Fermi liquid.

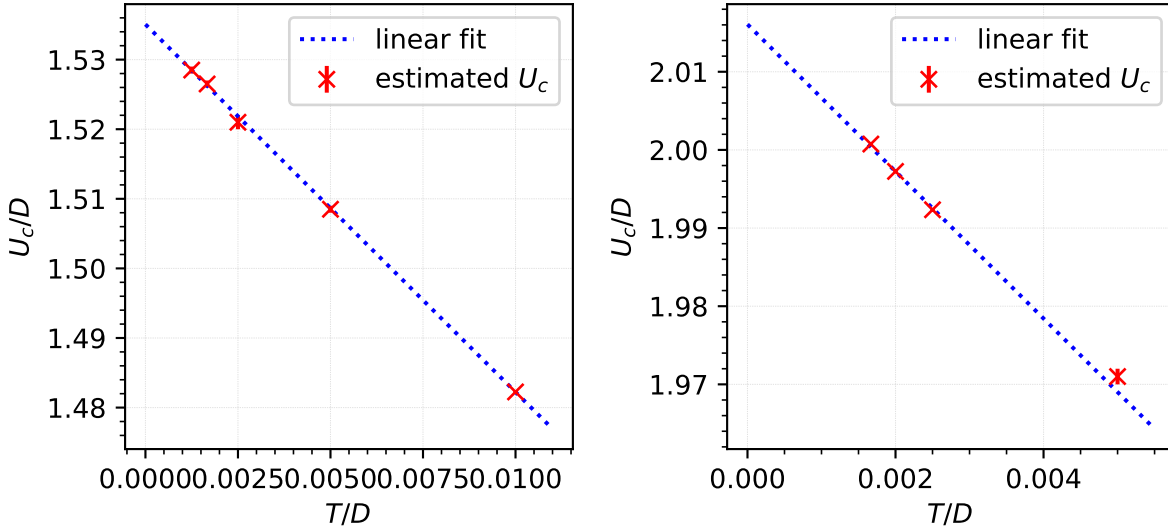


Figure 5.8: Estimation of the relative upper interaction strength bound of the phase coexistence region at half-filling U_{c2}/D as function of relative temperature, fitted linearly. Left panel: density-density interaction, right panel: Kanamori interaction.

While the abruptness of the jump of Z to zero at all non-zero temperatures suggests that the metal-insulator transition is of first order below its critical temperature as usual, at zero temperature the transition has been shown to remain a first-order transition within DMFT in models with non-zero Hund's coupling only [271, 372]. In the one-orbital model and degenerate multiorbital models without Hund's coupling it becomes a second-order transition instead [33, 370]. Zero temperature is not directly accessible to DMFT calculations using a CTQMC solver, but we can extrapolate low-temperature data to try to access the zero-temperature properties. In Figs. 5.8 and 5.9, we show the extrapolations of both the upper bound of the coexistence region $U_{c2}(T)$ and the quasiparticle weight $Z(T)$ as functions of temperature to $T = \beta^{-1} = 0$ for both forms of the interaction term. For the upper bound, we obtain values of ap-

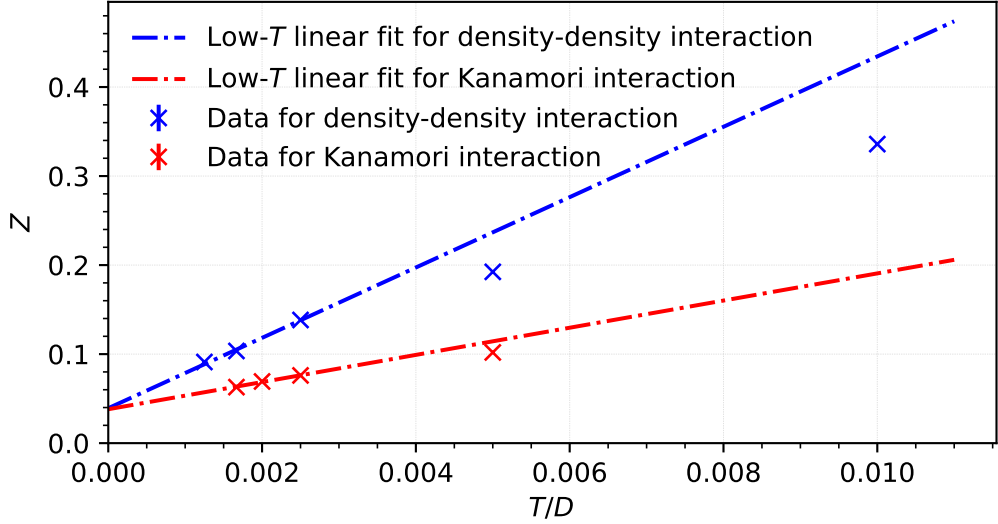


Figure 5.9: Quasiparticle weights at the highest relative interaction strength $U/D \approx U_{c2}/D$ resulting in a metallic solution as function of temperature, for both density-density as well as Kanamori interaction, fitted linearly through the three data points at lowest relative temperature T/D each.

proximately $U_{c2}(T=0)/D = 1.535$ for density-density interaction (with $J/U = 1/4$) and $U_{c2}(T=0)/D = 2.016$ for Kanamori interaction (with $J/U = 0.15$), and for the quasiparticle weight at the transition extrapolated to zero temperature $Z_{T=0}(U_{c2})$ almost equal values of approximately $Z_{T=0}(U_{c2}) = 0.039$ for density-density and $Z_{T=0}(U_{c2}) = 0.038$ for Kanamori interaction. These are in particular different from zero, i.e. we confirm the first-order nature of the transition even at zero temperature for non-zero Hund's coupling.

For this analysis, the middle point between the highest U with nonzero Z and the lowest U with zero Z was used as U_{c2} estimate and the range as uncertainty interval. An error for Z at fixed U can be calculated from its variation over DMFT iterations or the QMC error giving an estimate slightly below the difference of subsequent Z values, but it should be noted that any $Z(U) > 0$ must tend to slightly overestimate $Z(U_{c2})$ because the precision with which we can determine U_{c2} is limited, and even though the uncertainties for U_{c2} are approximately equal for the low temperature points, the size of the overestimation could still vary slightly depending on the actual value of U_{c2} . Therefore we did not take uncertainties into account in the extrapolation, and in order to prevent a possible systematic overestimation due to the high-temperature points that appear not to follow the low-temperature linear relationship well, cf. Fig. 5.9, we linearly fitted only the three points at the lowest temperatures for each type of interaction. Based on QMC or even DMFT errors for $Z(U_{c2})$, the temperature dependence of Z is still clearly not linear at the lowest temperatures we were able to reach, but even if we

assume errors on $Z(U_{c2})$ scaled up sufficiently to make a linear fit appropriate, a value of zero for $Z_{T=0}(U_{c2})$ remains far outside of the error range of the intercept of then about 0.005 for Kanamori interaction. Given this rather high robustness of the extrapolation result and the small variation of the points around the line of best fit we assume that the qualitative characterization of the zero temperature transition as of first order is reasonably reliable.

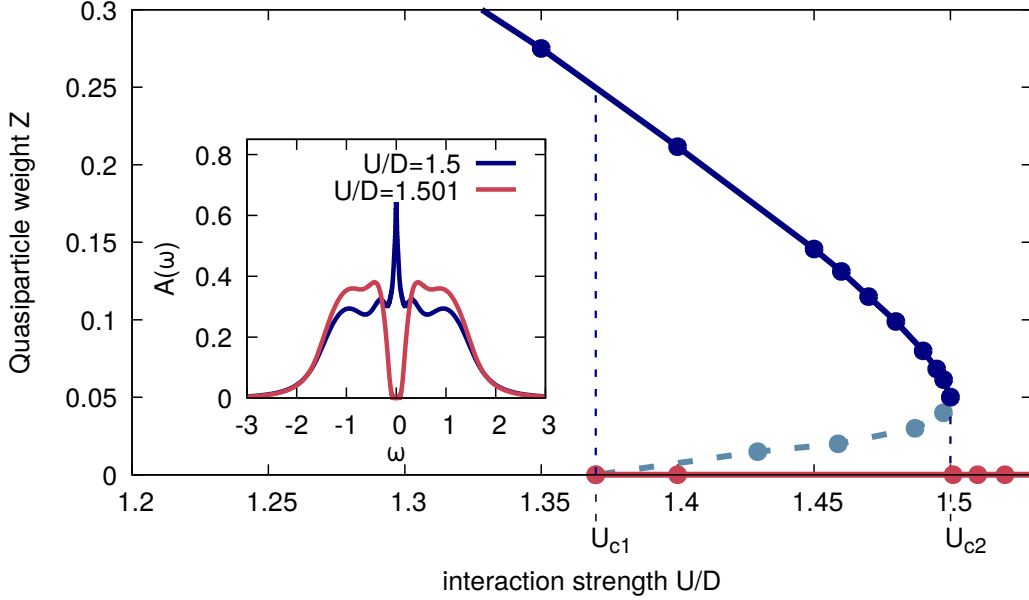


Figure 5.10: Quasiparticle weight Z as a function of the interaction parameter U for the model with density-density interaction at zero temperature calculated using NRG as impurity solver. The stable metallic solution is the upper dark blue part of the curve and the stable insulating solution the lower red part. An unstable metallic solution (dashed part in the middle) connects their ends across the coexistence zone. Spectral functions from the stable metallic branch just below its end U_{c2} and the insulating point just after it shown in the inset still differ drastically showing a clear zero temperature peak and gap respectively.

The first-order nature of this transition for density-density interaction is also confirmed by data obtained using NRG and ED impurity solvers to perform DMFT directly at zero temperature. The zero temperature $Z(U)$ curve resulting from calculations using NRG is shown in Fig. 5.10 together with the change of the spectral function as the metallic branch is followed upward across U_{c2} . Just below the transition, we find a strong quasiparticle peak at the Fermi energy ($\omega = 0$) as expected for a metallic density of states, but the entire spectral weight of the peak is abruptly moved to the Hubbard bands as the transition is crossed, leaving a gap at the Fermi energy. Being the prefactor of the coherent particle-like part of the Green's and thus spectral function, the quasiparticle weight Z accordingly abruptly jumps from $Z \approx 0.05$ to $Z = 0$

too as $U_{c2}/D = 1.5$ is crossed coming from the metallic solution. Due to the inaccuracies affecting the necessary extrapolation of the CTQMC results, but also inaccuracies affecting the NRG results, a perfect quantitative agreement can not be expected. However, our results for both Z and U_{c2} are close enough to assume agreement between CTQMC and NRG.

In the curve resulting from NRG DMFT calculations shown in Fig. 5.10, a third branch of $Z(U)$ only present in the coexistence region between U_{c1} and U_{c2} can be seen. As we already mentioned in our method discussion, this branch can ordinarily not be reached by simply following one of the solutions from outside of the coexistence region, it is however continuously connected to both of the other branches at their end points such that all three branches together form one continuous curve or “multi-valued function” $Z(U)$. This branch is also metallic as Z is non-zero, but it consists of solutions that are thermodynamically unstable and also unstable fixed points of DMFT, which are connected properties [434]. Unstable branches in the coexistence region of the Mott transition for single-orbital models have already been found using DMFT previously [146, 371, 429]. When the Mott metal-insulator transition is considered by analogy to a liquid-gas transition [435, 436], with the interaction strength U playing the role of the pressure p and the double occupancy $d = \langle n_{\uparrow}n_{\downarrow} \rangle$ playing the role of the volume V in the one-band case, the unstable metallic branch recalls e.g. the unstable branch of the van der Waals gas [429]. The conjugate variable of U playing the role of the volume is in general $\langle H_{\text{int}} \rangle / U$, which is a linear combination of multiple double occupancies in the multiorbital case..

5.1.3 Doped case

Our central result follows from the presence of a first-order transition at half-filling: At half-filling we find a coexistence region, i.e. a multi-valued S-shaped solution curve for the equation of state if non-stable (meta- and unstable) parts are included, even at zero temperature, schematically depicted in the zero chemical potential plane of the upper left panel of Fig. 5.11. Since we also know that for sufficiently high doping (cf. maximum chemical potential plane in the same figure) there is at most a smooth crossover as a function of the interaction strength U rather than a phase transition in this system, the solution curve of the equation of state has to unfold as the chemical potential μ is moved away from half-filling. We can alternatively consider the equation of state as a function of the chemical potential, i.e. in terms of the schematic depiction in the left panel of Fig. 5.11 cuts of the surface representing the solutions at constant U rather than at constant μ . For small U below the half-filling value of U_{c1} marked on the axis, there are only metallic solutions, for intermediate U up to that of the red solution curve,

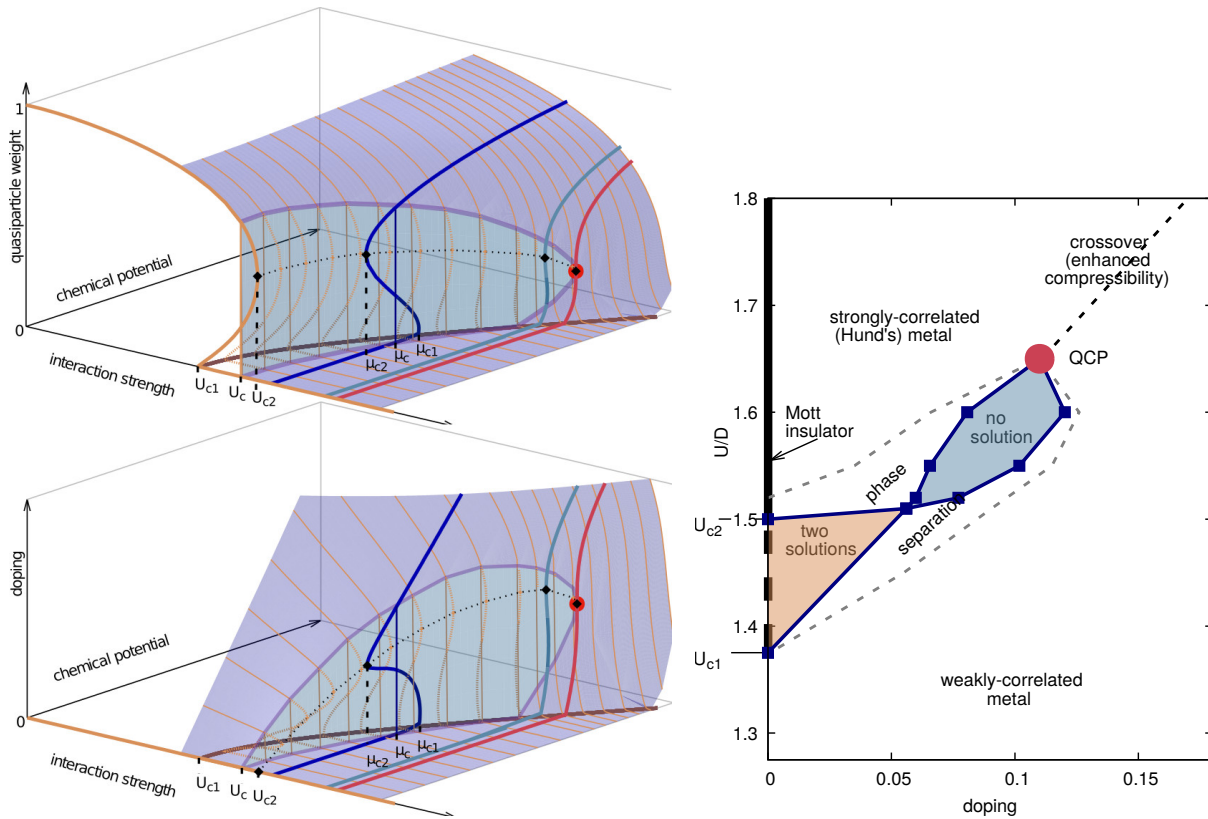


Figure 5.11: Left panel: Schematic solution surfaces of the equation of state for the quasiparticle weight Z (top) or doping (bottom) as functions of interaction strength U and chemical potential $\mu - \mu_{hf}$ with stable single-phase solutions (purple) and a Maxwell construction in case of phase separation (light greenish blue). Orange lines are constant μ solutions, with non-stable sections dotted, while lines of other colors are constant U solutions (corr. to equally colored NRG-DMFT results in Fig. 5.12). Right panel: Zero temperature phase diagram from NRG-DMFT results in the doping- U plane, indicating both metallic phases and the phase separation region (dotted boundary) or crossover line (dotted line) between them. Where the crossover line meets the phase separation boundary, a quantum critical point (QCP, red dot) is found at zero temperature. In the phase separation region, areas where multiple or no μ giving a (meta-)stable solution with given doping exist are marked in color. Phase diagrams for temperatures above zero but below the critical one would only differ quantitatively.

there is a phase transition with coexistence region between the Mott insulator / Hund's metal at low chemical potential and the weakly correlated metal at high chemical potential, and for high U above that of the red solution curve, there is only a crossover instead of the phase transition. In total, considering the two-dimensional solution surface of the equation of state as a function of U and μ , we have a reasonably smooth sheet at high μ that folds back up on itself as the Mott insulator transition at half-filling

is approached, i.e. as we go from the back right to the front left of the figure. The solutions stable without phase separation are shown as a darker purple surface, while a lighter greenish blue surface, extending straight in doping or quasiparticle weight direction, represents the stable solutions in thermodynamic equilibrium with phase separation obtained in the manner of the Maxwell construction. A series of orange lines, intersections of the surface representing the solution with surfaces of constant chemical potential, however, follows the non-stable solutions instead and can be used to visualize the aforementioned folding of the solution.

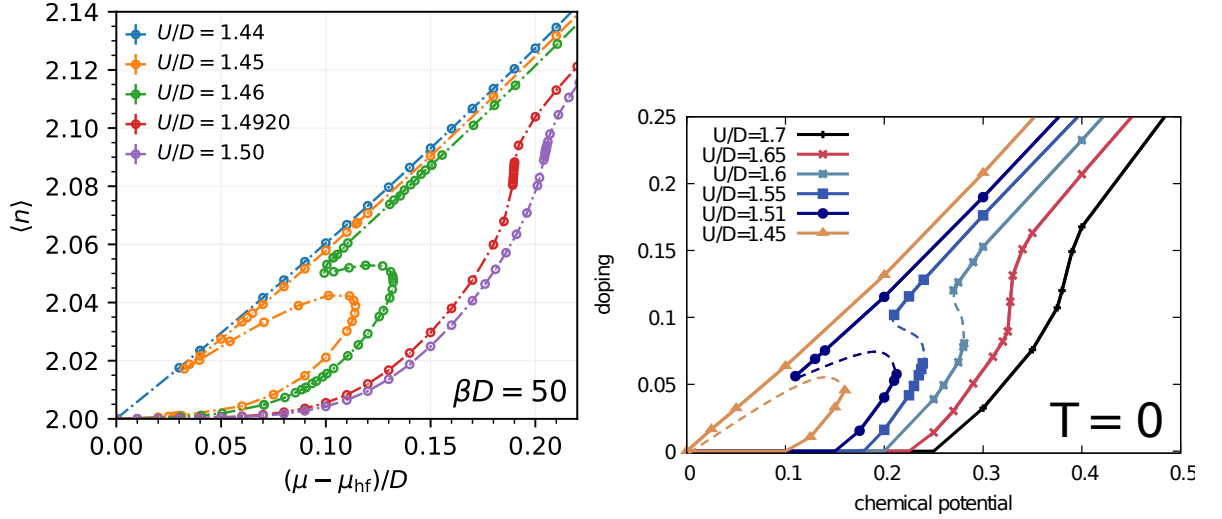


Figure 5.12: Dependence of the total occupation $\langle n \rangle$ or doping ($\langle n \rangle - 2$) on the chemical potential relative to half-filling $\mu - \mu_{\text{hf}}$ for various values of the interaction strength U . Left panel: QMC-DMFT results for temperature $\beta D = 50$. Right panel: NRG-DMFT results for zero temperature (unstable branches sketched following ED results).

We examine the continuous folding of the solution surface of the equation of state more closely by considering cuts along one of the two input dimensions. In Fig. 5.12, we show the partially multi-valued dependence of the total occupation $\langle n \rangle$ on the chemical potential relative to half-filling $\mu - \mu_{\text{hf}}$, both using zero temperature NRG data as well as QMC data, which looks very similar at sufficiently low temperature. As we can see, for fixed U the coexistence interval must actually be considered as a chemical potential interval $[\mu_{c1}(U, T), \mu_{c2}(U, T)]$ whose boundaries depend on the other parameters. For $U < U_{c1}(\mu_{\text{hf}})$, only the weakly correlated (“good”) metallic solution would exist, with an almost linear dependence of the filling on μ . As long as $U_{c1}(\mu_{\text{hf}}) < U < U_{c2}(\mu_{\text{hf}})$, the good metallic solution also exists at half-filling but might be metastable, as for $U/D = 1.45$ in the NRG data (part of yellow curve) or $U/D = 1.44$ in the QMC data (blue curve, insulating solution not shown). For $U > U_{c2}(\mu_{\text{hf}})$ on the other hand, the weakly correlated metallic solution, represented by points on the nearly linear parts of

the curves in Fig. 5.12, only begins existing at sufficiently high μ . Below that μ , only the other stable solution exists. This solution starts out as the Mott insulator pinned to half-filling for a finite interval of μ , visible in form of the zero-doping Mott plateaus particularly at $T = 0$, but then lifts off and continues at finite doping as strongly correlated metallic solution (“Hund’s metal”), represented by the points on the upward curving parts in Fig. 5.12. In the cases where the weakly correlated metallic branch only starts at higher chemical potential (e.g. the green curve corresponding to $U/D = 1.46$ for $\beta D = 50$ and the lighter blue curve corresponding to $U/D = 1.55$ for $T = 0$) we can clearly recognize that a Hund’s metal solution, represented by the points on the lower branches at non-zero doping, can also be the single stable solution of the system for the right choice of parameters and must not necessarily be metastable.

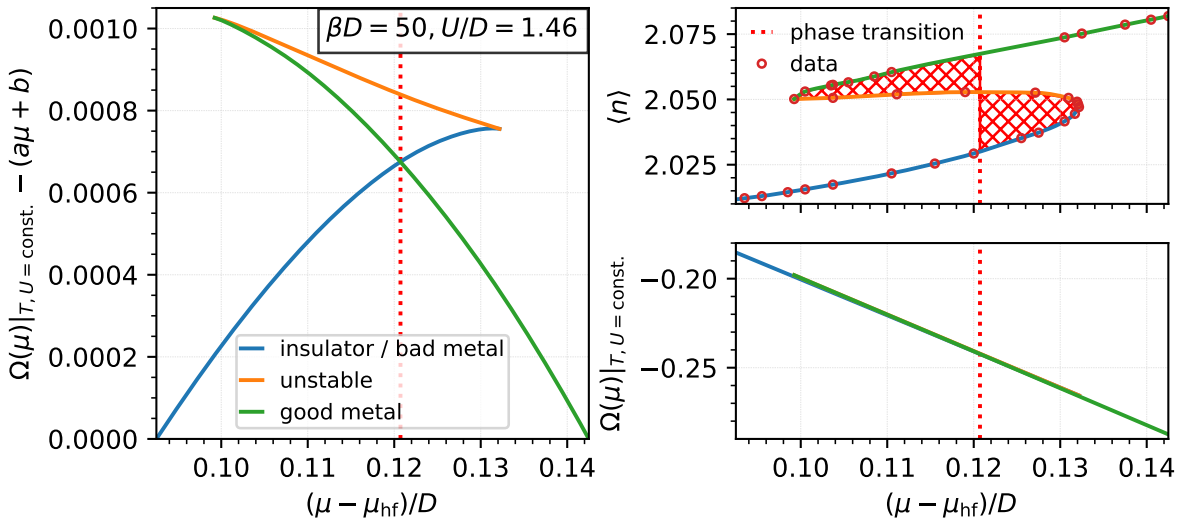


Figure 5.13: Left panel: Grand potential $\Omega(T, \mu, U)$ as a function of μ calculated by integration of an interpolating polynomial of $\langle n \rangle(\mu)$ from QMC for constant $\beta = 50$ and $U = 1.46$, with a linear function of μ subtracted that allows for easier visual interpretation without changing the curvature or differences between phases at fixed μ . The chemical potential at which the phase transition happens, i.e. where the grand potentials of the two stable phases cross, is marked using a red dotted vertical line. The grand potential for the stable phases is always concave, while that for the unstable phase is convex, although only partially in this case. Upper right panel: $\langle n \rangle(\mu)$ data from QMC connected using the piecewise cubic monotonicity-preserving Hermite interpolating polynomial fit that was integrated to obtain the grand potential. The two cross-hatched areas are those enclosed by the full interpolating polynomial fit and the phase transition line, which should be chosen such that the areas are equal according to the Maxwell construction. Lower right panel: Grand potential $\Omega(T, \mu, U)$ without subtraction of a linear function of μ for reference.

In the coexistence region $[\mu_{c1}(U, T), \mu_{c2}(U, T)]$, both the weakly correlated and the strongly correlated phase exist, and as we can see in Fig. 5.12, an unstable metallic phase connects their ends across the coexistence region (middle branches in the figure, dashed in the right panel), leading to the S-shape or folding of the total solution curves. Unlike the stable phases, this unstable phase does not necessarily always have positive electronic compressibility $1/n^2 \partial n / \partial \mu$. If we only want to consider stable equilibrium states of the system, we would instead have to connect both stable phases using the Maxwell construction at one $\mu_{\text{transition}}(U, T)$, where phase separation into a mixture of both stable phases according to the actually realized doping would occur. For this construction, the constant μ at which the connecting vertical line segment is placed must be chosen such that the two areas enclosed by the line and the full solution curve including meta- and unstable states are equal, cf. the red line given as example in the upper right panel of Fig. 5.13.

This condition is equivalent to choosing the μ where the relevant thermodynamic potentials as a function of μ for the two stable phases cross. In Fig. 5.13, we show both the grand potential $\Omega(T, \mu, U)$, calculated by integrating a piecewise cubic monotonicity-preserving interpolating Hermite polynomial fit [437, 438] of the QMC-DMFT $\langle n \rangle(\mu)$ curve for $\beta = 50$ and $U = 1.46$ and the corresponding Maxwell construction. The formulation of the potential Ω as integral follows from its differential as function of the differentials of its natural variables

$$d\Omega = -S dT - n d\mu + \frac{\langle H_{\text{int}} \rangle}{U} dU, \quad \Omega(\mu) = \Omega(\mu_0) - \int_{\mu_0}^{\mu} n(\mu') d\mu', \quad (5.5)$$

and if we integrate along the total solution curve properly taking account of all signs due to directions, we can see that the potential crossing condition is exactly equal to the Maxwell construction. In the figure we can further see that while the potential for the stable phases is always concave, as a thermodynamic potential for a stable phase as a function of an intensive variable should be [439], the potential for the unstable phase changes its curvature just as its compressibility changes its sign. While the local curvature of the grand potential as function of μ does therefore not indicate the instability of the unstable phase at these points with positive compressibility, we checked for one of them that the analogous derivative of potential energy $\langle H_{\text{int}} \rangle / U$ with respect to U does.

As indicated by the progression from the dark blue to the green and then red curve in Fig. 5.11, which qualitatively represent the zero temperature results of Fig. 5.12 with the same colors, the coexistence region and equivalently the extent of the phase separated solutions in doping continuously shrinks with increasing interaction strength U as successive solution curves are folded less tightly. Just where it vanishes, which

the red curves in Fig. 5.12 try to approximate, we reach the zero temperature quantum critical point. Here the two stable phases are connected via a continuous second-order phase transition, where the compressibility at a single point diverges to infinity coming from the crossover (unlike the formally also infinite but discontinuous compressibility along a vertical line segment corresponding to the Maxwell construction in the phase separation region). Due to the continuity of the solution as a function of U and μ , the existence of a first-order transition at half-filling and zero temperature necessarily implies that the continuous transition at the quantum critical point must occur at the end of the phase separation zone, which extends to finite doping in such a case. If we continue to even higher values of the interaction strength, no phase transition occurs any more, but a crossover with enhanced though not diverging compressibility between the weakly correlated and a more strongly correlated or Hund's metal state remains.

The zero-temperature DMFT calculations performed using NRG as impurity solver result in the phase diagram in the right panel of Fig. 5.11, shown in the plane of interaction strength U and doping $(\langle n \rangle - 2)$ now, which qualitatively also holds at higher temperatures. As we have seen previously, the region where a phase transition occurs extends out from the Mott transition at half-filling not only in chemical potential, but also significantly to non-zero doping, where it is a transition between a weakly correlated metal and a strongly correlated metal instead. In the phase-separation region, shown with a dotted boundary, the chemical potential is constant and colored highlighting further indicates what the solution curve $\langle n \rangle(\mu)$ for constant U looks like assuming only (possibly meta-stable) single-phase states instead of phase separation: there is not necessarily exactly one μ on the solution curve for a given U and $\langle n \rangle$, one may also find two or none at all instead, if the line representing the requested doping intersects both stable branches or only the unstable branch of the solution curve (cf. $U/D = 1.45, 1.51$ below and resp. slightly above a doping of 0.05 for the first case and $U/D = 1.55, 1.6$ at doping slightly below and resp. around 0.1 in the zero-temperature data shown in Fig. 5.12).

As far as the transition between two metals is concerned, a comparison of spectra (Fig. 5.14) produced using maximum entropy analytic continuation [168, 174] of QMC results for one metastable point per phase at $\beta D = 100$ shows us that these phases are indeed quite different even when their doping is similar: the spectrum in the good metallic phase has a strong peak at the Fermi energy ($\omega = 0$), while the spectrum for the strongly correlated metallic phase features a kind of pseudogap instead.

Let us also quickly note the changes with temperature. For this, we use the zero-temperature NRG- and $\beta D = 50$ QMC-DMFT results shown in Fig. 5.12 and QMC-DMFT results for some more temperatures shown in Fig. 5.15. By comparing the data for all temperatures except $\beta D = 25$, we can note some general trends below the critical

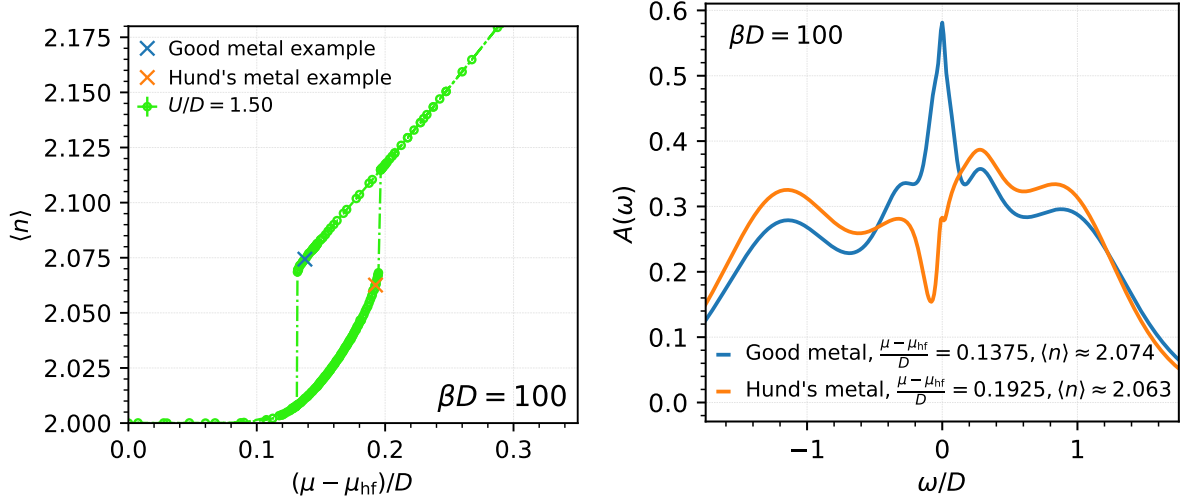


Figure 5.14: Left panel: Solution curve $\langle n \rangle (\mu - \mu_{\text{hf}})$ for the total occupation as function of the chemical potential relative to half-filling for interaction strength $U/D = 1.50$ at temperature $\beta D = 100$ using QMC-DMFT with only points that correspond to phases that are at least metastable. The two points for which spectra are shown in the right panel are highlighted. Right panel: Comparison of the spectra calculated using the maximum entropy method from QMC results for the weakly and strongly correlated phases at similar doping using two meta-stable points close to the ends of the two solution branches shown in the left panel.

temperature: the lower coexistence region boundary at half-filling $U_{c1}(\mu_{\text{hf}})$ increases with decreasing temperature at least down to $\beta D = 200$, but is lower again for $T = 0$, while the upper boundary $U_{c2}(\mu_{\text{hf}})$ increases with decreasing temperature down to $T = 0$. In total, the extent of the coexistence region in U at half-filling grows with decreasing temperature, even for the higher temperatures $\beta D < 200$. With decreasing temperature, the Mott plateaus of $\langle n \rangle (\mu) = 2$ around μ_{hf} become much more pronounced, starting out with no visible plateau at $\beta = 35$ and reaching an extent of occupations not visibly different from half-filling at $\beta = 200$ that is about as wide in μ as for the zero temperature results. Further, the ranges in doping for which the equilibrium solution is phase separated grows and the doping and chemical potential of the critical point increase as temperature decreases, with the critical point reaching about the same position in the $n(\mu - \mu_{\text{hf}})$ graph, and for about the same value of U , for $\beta = 200$ as the quantum critical point at zero temperature.

At our highest temperature $\beta D = 25$, the compressibility $\partial \langle n \rangle / \partial \mu$ for small $\mu - \mu_{\text{hf}}$ still decreases with increasing interaction strength U , but we can not observe any sign of a phase transition or compressibility maximum for the available data. Given that we should have expected to see them even earlier than at $\beta D = 35$ if they were present

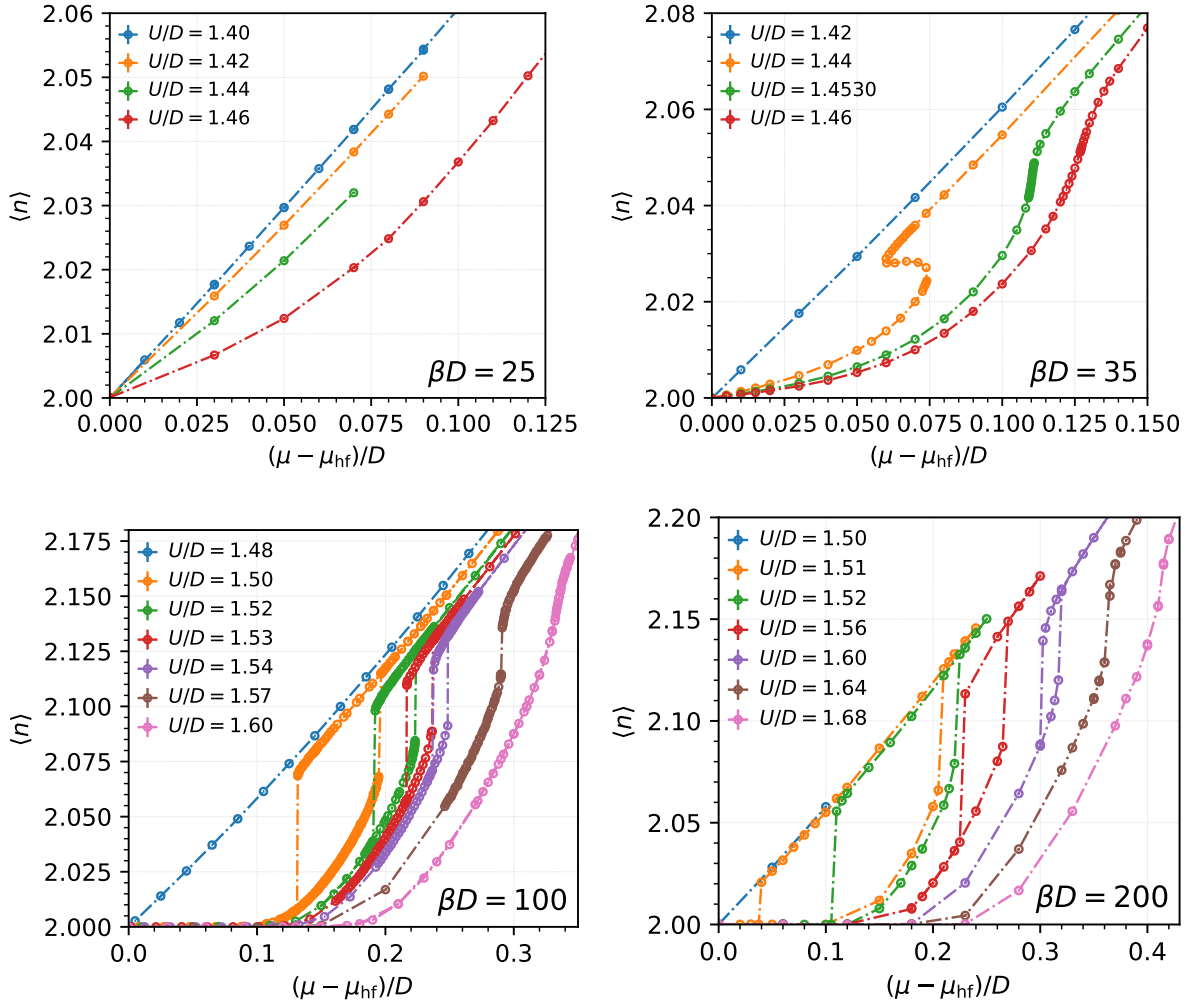


Figure 5.15: Total occupation $\langle n \rangle$ for the model with density-density interaction at various interaction strengths U and temperatures as a function of the chemical potential $\mu - \mu_{\text{hf}}$. For the temperatures lower than $\beta D = 25$, a doping-driven transition can be observed for sufficient U that eventually turns into a crossover. For $\beta D = 35$ and $\beta D = 50$, unstable branches were calculated with CT-HYB DMFT by employing a phase-space extension. At other temperatures, only (meta)stable branches are shown.

based on the temperature trends, we determine the critical temperature of the Mott transition for this model to lie between $\beta D = 25$ and $\beta D = 35$. Insofar as we have used equivalent parameters and interaction type and the differing bandwidths are taken into account, this as well as all of our other results agrees with the data presented in Ref. [386] to the extent that our parameter ranges overlap.

Just as we can consider the solution at constant U , we can consider the solution at constant μ . In Fig. 5.16, the graphs of both $\langle n \rangle(U)$ and $\frac{\langle H_{\text{int}} \rangle}{U}(U)$ obtained from QMC-DMFT at temperature $\beta D = 50$, are shown at two fixed values of μ , once deep in the co-

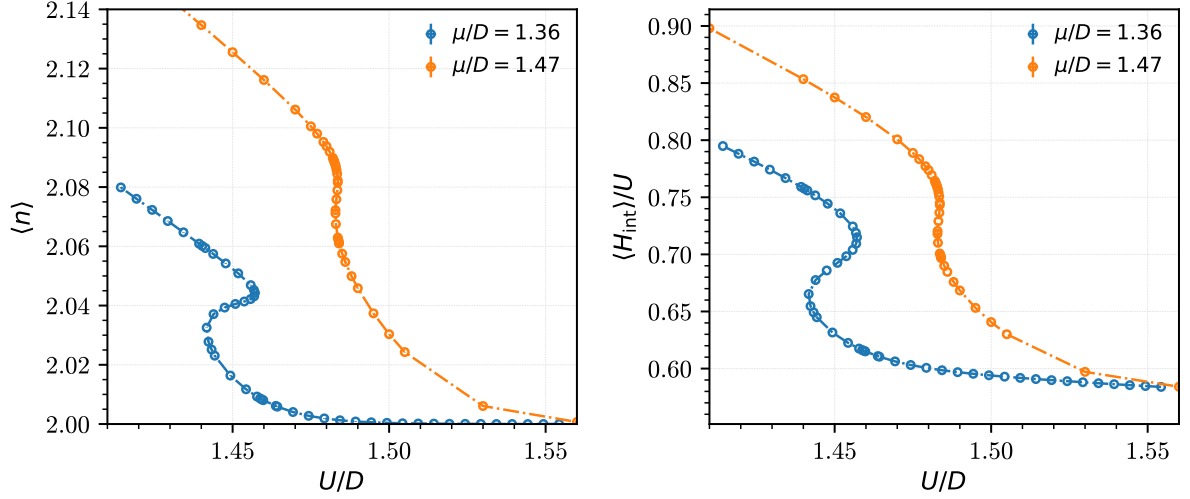


Figure 5.16: Dependence of the total occupation $\langle n \rangle$ (left panel) or potential energy divided by U , $\langle H_{\text{int}} \rangle / U$, (right panel) on the interaction strength U for different values of the chemical potential μ , calculated using QMC-DMFT at temperature $\beta D = 50$.

existence region and once close to the critical point. The latter quantity is more closely analogous to $\langle n \rangle(\mu)$ as it can be considered the conjugate variable of U in the thermodynamic sense, just as μ and $\langle n \rangle$ are, i.e. its product with U is a contribution to the internal energy. As we already recalled in our discussion of the half-filling case, the role of interaction strength U and double occupancy $d = \langle n_{\uparrow} n_{\downarrow} \rangle$ for the Mott transition in the single-orbital Hubbard model has previously been considered in analogy to pressure and volume in the liquid-gas transition of a van der Waals gas [435, 436], but in the multiorbital case the general equivalent of volume is $\langle H_{\text{int}} \rangle / U$. This is not just one single double occupancy but a linear combination of all possible ones with coefficients dependent on the relative Hund's coupling J/U . This graph lets us confirm the continuous folding of the solution surface of the equation of state by following the solution in the other direction of the parameter space, approximately that indicated by the orange lines in Fig. 5.11 (where the chemical potential μ is taken relative to μ_{hf} however, which is not constant but a linear function of U).

We can further observe that the critical point scenario of a continuous transition with a single point of infinite derivative, here with respect to U , is approached by both $\langle n \rangle(U)$ and $\frac{\langle H_{\text{int}} \rangle}{U}(U)$ at the same point in parameter space, and that the middle sections of both curves with positive derivative also have the same boundaries in U . The coexistence region between the weakly correlated metallic solution at lower U , the strongly correlated metallic or Mott insulating solution at higher U and the unstable metallic solution in between is thus reflected in the same way in the multivaluedness of both of

these relations as expected. However, we also find that the derivatives of the unstable branches of both relations have constant sign opposite to that of their stable branches (or in other words, their inverse is single-valued) judging by the limited amount of data we have for constant μ , while all three of the unstable branches of $\langle n \rangle (\mu)$ at constant U we have calculated have derivatives which change sign and therefore partially have the same sign as the derivatives of their stable branches (cf. Figs. 5.12 and 5.15).

To conclude, the various properties we have analyzed here using DMFT at zero and nonzero temperatures indicate enhanced compressibilities and the presence of a region of phase separation ending in a quantum critical point at low doping between a weakly correlated metallic phase at low interaction strength and a strongly correlated “Hund’s metal” phase continuously connected to the Mott insulator at higher strength. We have thus extended and confirmed the previous results for the two-orbital Hubbard model with Hund’s coupling around half-filling [363, 386, 391, 392, 394, 395].

5.1.4 Physical origin of the first-order transition at half-filling

In the previous subsections we have seen numerical DMFT results that show the first-order character of the Mott transition even at zero temperature in the multiorbital Hubbard model with Hund’s coupling and how this feature is directly connected to the presence of a quantum critical point at finite doping. In order to get some physical insight into the relation between Hund’s coupling and the order of the transition beyond numerics, let us now instead of DMFT consider an approximation that is simple enough to be amenable to a perturbative analytical treatment around the Mott transition that can be interpreted in the framework of Landau’s theory of phase transitions [440].

We will use the slave-spin mean-field theory (SSMF) for this analysis [396, 397] and start with a short introduction closely following that in Ref. [398], but focus on the specific case of a half-filled model with two degenerate orbitals and density-density interaction leaving aside complications that would only be necessary for the general case. Conceptually, the SSMF is based on the introduction of auxiliary particles whose states live in a Hilbert space that embeds a description of the original system, but which also contains states that do not correspond to any of the original physical system. As long as the necessary constraints restricting the system to physical states are satisfied, this is just an exact reformulation that does not simplify the problem, so the productive application of this method to strongly correlated electron systems involves a mean-field treatment of the constraint, which is then only satisfied on average instead of exactly. In SSMF, one spin-1/2 per fermionic single-particle state of the original model are introduced as auxiliary particles, but as there is considerable freedom in the choice of

auxiliary particles [441], other methods based on the same idea are also in use, such as the more popular older slave boson [442, 443] and the slave rotor [444] mean-field theories. SSMF introduces comparatively few auxiliary particles while still being able to describe a general multiorbital system, and it has previously been used to numerically investigate models similar to ours with the same resulting physics of a phase-separation region and enhanced compressibilities [363, 392].

We begin by rewriting our Hubbard model Hamiltonian with density-density interaction

$$H = \sum_{\langle i,j \rangle, m, \sigma} t_{ij}^m c_{im\sigma}^\dagger c_{jm\sigma} \quad (5.6)$$

$$+ U \sum_{im} n_{im\uparrow} n_{im\downarrow} + (U - 2J) \sum_{im, m' \neq m} n_{im\uparrow} n_{im'\downarrow} + (U - 3J) \sum_{i, m < m', \sigma} n_{im\sigma} n_{im'\sigma} \quad (5.7)$$

in a form manifestly invariant under a particle-hole transformation, as it should be at half-filling considering the symmetries of our system. It can be shown that the hopping term (5.6) is invariant apart from a gauge transformation for a bipartite lattice [398], which a Bethe lattice of any coordination number obviously is due to its tree-like structure with hopping from a node at even depth only to one at odd depth and vice versa. The interaction term (5.7) is clearly not invariant under the transformation $n_\alpha \rightarrow (1 - n_\alpha)$. We therefore replace all occupation operators with a ‘‘symmetrized’’ form, $n_\alpha \rightarrow \bar{n}_\alpha = n_\alpha - \frac{1}{2}$ which is exactly negated under a particle-hole transformation so that the interaction term, which contains only terms quadratic in occupation operators, remains invariant. In this way, we obtain a symmetrized Hamiltonian H_s invariant under particle-hole transformation from the original Hamiltonian $H =: H_a$. However, by doing the replacement of occupation operators we have also changed H_s compared to H_a by terms at most linear in the original occupations, as we could see by multiplying out the symmetrized operators. This is not problematic as the linear terms only correspond to a shift in the chemical potential and the constant terms to a total energy shift. A chemical potential term $-\mu N$ is not invariant, so to get half-filling we must not add any additional non-zero chemical potential term to H_s . By demanding that $H_a - \mu_{\text{HF}} N$ be equal to H_s up to constant terms, we can additionally determine the value of the chemical potential μ_{HF} needed for half-filling when we use the asymmetric form of the Hamiltonian as we did in our QMC-DMFT calculations. The coefficient of the total occupation N that we get by multiplying out the interaction term is $\mu_{\text{HF}} = (2N_{\text{orb}} - 1)\frac{U}{2} - (N_{\text{orb}} - 1)\frac{5J}{2}$, and this also remains the correct value if the pair hopping and spin-flip terms of Kanamori interaction are included [398].

Starting from the symmetrized Hamiltonian, we first just introduce one auxiliary $S_{im\sigma}$ per fermionic single-particle state $n_{im\sigma}$, demand that the relationship $S_{im\sigma}^z = n_{im\sigma} -$

$\frac{1}{2}$ be fulfilled exactly and rewrite our Hamiltonian exactly in terms of operators for this enlarged system. Labeling the operators and quantum numbers related to the original fermions with c and those related to the fermions for use in SSMF with f , this corresponds to a mapping

$$|\dots, n_{im\sigma}^c = 0, \dots\rangle \rightarrow |\dots, n_{im\sigma}^f = 0, S_{im\sigma}^z = -\frac{1}{2} \dots\rangle \quad (5.8)$$

$$|\dots, n_{im\sigma}^c = 1, \dots\rangle \rightarrow |\dots, n_{im\sigma}^f = 1, S_{im\sigma}^z = \frac{1}{2} \dots\rangle \quad (5.9)$$

from original occupation number basis states to new states in mixed occupation number and auxiliary spin z-component basis. The operators for the combined basis must act on the basis states on the right-hand side as the c -fermion operators act on those on the left-hand side, but the additional “unphysical” states in the new basis that do not fulfill the condition and do not correspond to any states of the original system, like the ones with $n_{im\sigma}^f = 0$ but the corresponding spin $S_{im\sigma}^z = \frac{1}{2}$, do not further restrict the choice of the new operators. Since a change in the occupation number requires a corresponding spin change in the new description, we need a combination of an f -fermion creation or annihilation operator and a spin operator $O_{im\sigma}$ to replace one single c -fermion operator: $c_{im\sigma} \rightarrow f_{im\sigma} O_{im\sigma}$. When $O_{im\sigma}$ or its adjoint are applied to a physical basis state, the spin state must change to the orthogonal basis state just as the occupation number changes on the application of a fermionic creator or annihilator that does not result in zero. The diagonals of $O_{im\sigma}$ are therefore zero and, with $|S_{im\sigma}^z = +\frac{1}{2}\rangle$ as first basis state, $(O_{im\sigma})_{21} = (O_{im\sigma}^\dagger)_{12}^* = 1$ preserves unit length for transitions between non-zero state vectors. The other off-diagonal value, which corresponds to raising the spin on annihilation or lowering it on creation, must be fixed in another way because applied to physical states, the fermionic anticommutation relations of the f -fermion operators already ensure a zero result. As we consider a system with particle-hole symmetry, invariance of the kinetic term under an exchange of creators and annihilators requires the $O_{im\sigma}$ operators to be Hermitian and so the other diagonal to be one as well, giving in total $O_{im\sigma} = S_{im\sigma}^+ + S_{im\sigma}^- = 2S_{im\sigma}^x$. In general, the value of the element would be fixed by demanding that the resulting quasiparticle weight Z without interaction be exactly one, which would give the same result in our case [398].

In the kinetic term of the Hubbard Hamiltonian, we perform this replacement of the original creators and annihilators, but for the interaction term we choose another way: comparing the condition connecting occupation numbers and spins, we see that $S_{im\sigma}^z$ can directly be substituted for the symmetrized occupation number operators $\bar{n}_{im\sigma}$. This gives us an interaction purely in terms of spin operators not involving any f -

fermion operators at all. The Hubbard Hamiltonian then takes the form

$$H = \sum_{\langle i,j \rangle, m, \sigma} t_{ij}^m 4S_{im\sigma}^x S_{jm\sigma}^x f_{im\sigma}^\dagger f_{jm\sigma} \quad (5.10)$$

$$+ U \sum_{im} S_{im\uparrow}^z S_{im\downarrow}^z + (U - 2J) \sum_{im, m' \neq m} S_{im\uparrow}^z S_{im'\downarrow}^z + (U - 3J) \sum_{i, m < m', \sigma} S_{im\sigma}^z S_{im'\sigma}^z \quad (5.11)$$

and the condition $S_{im\sigma}^z = n_{im\sigma}^f - \frac{1}{2}$ must be enforced exactly for the f -fermions to be an exact description of the original fermions.

A standard mean-field approximation (cf. e.g. Ref. [47])

$$\begin{aligned} & \sum_{\langle i,j \rangle, m, \sigma} t_{ij}^m 4S_{im\sigma}^x S_{jm\sigma}^x f_{im\sigma}^\dagger f_{jm\sigma} \quad (5.12) \\ \rightarrow & \sum_{\langle i,j \rangle, m, \sigma} t_{ij}^m 4 \left(\left\langle S_{im\sigma}^x S_{jm\sigma}^x \right\rangle f_{im\sigma}^\dagger f_{jm\sigma} + S_{im\sigma}^x S_{jm\sigma}^x \left\langle f_{im\sigma}^\dagger f_{jm\sigma} \right\rangle - \left\langle S_{im\sigma}^x S_{jm\sigma}^x \right\rangle \left\langle f_{im\sigma}^\dagger f_{jm\sigma} \right\rangle \right) \end{aligned} \quad (5.13)$$

can be performed for the four-operator kinetic term in order to split the Hamiltonian into separate purely fermionic and purely spin parts, with the last term being just a number, i.e. an absolute shift of the entire energy scale that can be ignored. In the particle-hole symmetric case, the first term constitutes the entire fermionic Hamiltonian, an interaction-free tight-binding Hamiltonian where a static renormalization of the hopping is the only influence of the auxiliary spins, and the second term is the kinetic part of the spin Hamiltonian which includes the influence of the fermions in the same way. For a direct solution of such a mean-field approximated system, self-consistent values of $\left\langle S_{im\sigma}^x S_{jm\sigma}^x \right\rangle$ and $\left\langle f_{im\sigma}^\dagger f_{jm\sigma} \right\rangle$ would have to be found.

We proceed with further approximation by relaxing the condition $S_{im\sigma}^z = \bar{n}_{im\sigma}$ to be only fulfilled on average using a method similar to Lagrange multipliers. If we add chemical potential-like terms $-\lambda_{im\sigma} f_{im\sigma}^\dagger f_{im\sigma}$ to the fermionic Hamiltonian and $\lambda_{im\sigma} (S_{im\sigma}^z + 1/2)$ to the spin Hamiltonian, the average fulfillment of the condition is now ensured by finding $\lambda_{im\sigma}$ for which the thermodynamic potential $\Omega = -\beta^{-1} \log Z$ has an extremum:

$$\begin{aligned} \frac{\partial \Omega}{\partial \lambda_{jn\sigma'}} &= -\partial_{\lambda_{jn\sigma'}} \beta^{-1} \log Z = -\beta^{-1} Z^{-1} \partial_{\lambda_{jn\sigma'}} \text{Tr} \left(e^{(-\beta H - \beta \sum_{im\sigma} \lambda_{im\sigma} (S_{im\sigma}^z + \frac{1}{2} - f_{im\sigma}^\dagger f_{im\sigma}))} \right) \quad (5.14) \\ &= Z^{-1} \text{Tr} \left(e^{(-\beta H - \beta \sum_{im\sigma} \lambda_{im\sigma} (S_{im\sigma}^z + \frac{1}{2} - f_{im\sigma}^\dagger f_{im\sigma}))} (S_{jn\sigma'}^z + \frac{1}{2} - f_{jn\sigma'}^\dagger f_{jn\sigma'}) \right) \\ &= \left\langle S_{jn\sigma'}^z + \frac{1}{2} - f_{jn\sigma'}^\dagger f_{jn\sigma'} \right\rangle \stackrel{!}{=} 0. \end{aligned}$$

Since we consider only the particle-hole symmetric situation at half-filling here, we can

demand that quantities like H , Ω and Z be invariant under a particle-hole transformation. The terms with the multiplier variables λ are not invariant, so the solution in this case is $\lambda = 0$. In general, the solutions of all λ variables remaining after taking into account all symmetries that are present or imposed as approximations must be determined numerically during the self-consistent solution of this model.

Finally, we treat the spin part of the model itself in single-site mean-field approximation as well, i.e. we perform an additional decoupling and also impose translational invariance:

$$S_{im\sigma}^x S_{jm\sigma}^x \rightarrow \langle S_{im\sigma}^x \rangle S_{jm\sigma}^x + S_{im\sigma}^x \langle S_{jm\sigma}^x \rangle \quad (5.15)$$

$$\rightarrow \langle S_{m\sigma}^x \rangle S_{m\sigma}^x + S_{m\sigma}^x \langle S_{m\sigma}^x \rangle - \langle S_{m\sigma}^x \rangle \langle S_{m\sigma}^x \rangle. \quad (5.16)$$

We can apply this to both the expectation value in the fermionic Hamiltonian and the operator product in the kinetic part of the spin Hamiltonian, but in the former all terms multiply the fermionic operators and must so be retained to get effectively $\langle S_{im\sigma}^x S_{jm\sigma}^x \rangle \rightarrow \langle S_{m\sigma}^x \rangle^2$. In the latter, however, the last term results again in a pure number that can be ignored, and we proceed by simplifying it with a Fourier transform to get

$$H_{\text{spin, kin.}} = \sum_{\langle i,j \rangle, m, \sigma} t_{ij}^m 8 \langle S_{m\sigma}^x \rangle S_{m\sigma}^x \langle f_{im\sigma}^\dagger f_{jm\sigma} \rangle \quad (5.17)$$

$$= 8 \sum_{m\sigma} \langle S_{m\sigma}^x \rangle S_{m\sigma}^x \sum_{\langle i,j \rangle} t_{ij}^m \langle f_{im\sigma}^\dagger f_{jm\sigma} \rangle \quad (5.18)$$

$$= 8 \sum_{m\sigma} \langle S_{m\sigma}^x \rangle S_{m\sigma}^x \sum_k \epsilon_k^m \langle n_{km\sigma} \rangle \quad (5.19)$$

$$= 8\bar{\epsilon} \sum_{m\sigma} \langle S_{m\sigma}^x \rangle S_{m\sigma}^x \quad (5.20)$$

where $\bar{\epsilon}$ is the average energy per free f -fermion. This energy can be calculated as

$$\bar{\epsilon} = \int_{-\infty}^{\mu} E D(E) dE \quad (5.21)$$

in terms of the fermionic single-particle density of states $D(E)$, which is the same for f - and d -fermions and so semicircular in our case.

After all these approximations, the fermionic and spin parts of the Hamiltonian, which together make up that of the entire system, take the form

$$H_{\text{ferm.}} = 4 \sum_{m\sigma} \langle S_{m\sigma}^x \rangle^2 \sum_k \epsilon_k^m n_{km\sigma} \quad (5.22)$$

$$\begin{aligned}
H_{\text{spin}} = & 8\bar{\epsilon} \sum_{m\sigma} \langle S_{m\sigma}^x \rangle S_{m\sigma}^x & (5.23) \\
& + U \sum_m S_{m\uparrow}^z S_{m\downarrow}^z + (U - 2J) \sum_{m,m' \neq m} S_{m\uparrow}^z S_{m'\downarrow}^z + (U - 3J) \sum_{m < m', \sigma} S_{m\sigma}^z S_{m'\sigma}^z, \\
& \underbrace{\hspace{15em}}_{H_{\text{spin, int.}}}
\end{aligned}$$

where we may further define the auxiliary spin magnetization $m_x = 2N_{\text{orb}} \langle S_{m\sigma}^x \rangle = 4 \langle S_{m\sigma}^x \rangle$ and can also identify the fermionic quasiparticle weight $Z_m = 4 \langle S_{m\sigma}^x \rangle^2$, which can e.g. be shown using its definition in terms of the coherent part of the spectral weight [398].

Since the quasiparticle weight Z can be considered as an order parameter for the Mott transition and its square root is proportional to the auxiliary spin magnetization m_x , getting the self-consistent solution for m_x is enough for our purposes, and since the constant non-interacting kinetic energy $\bar{\epsilon}$ is the only information about the fermionic system entering into the spin Hamiltonian, the fermionic part (5.22) is no longer relevant from here on. The Mott transition corresponds to the ferromagnetic transition of the auxiliary spin system, and at zero temperature the ground state energy of the spin Hamiltonian (5.23) is the only ingredient we need to consider for the thermodynamic potential.

Using Landau's theory of phase transitions [440] we can determine which of the phases is stable in the vicinity of the critical point and whether the transition is continuous. Considering the Landau function, which is similar to a thermodynamic potential, as a function of the order parameter, the global minimum corresponds to the stable phase of the system. In addition to the self-consistent field $h_{\text{sc}} := 8\bar{\epsilon} \langle S_{m\sigma}^x \rangle$, we additionally introduce a hypothetical external field h_{ext} , such that the energy and thus zero-temperature free energy of the spin system is $E(h_{\text{ext}}) = \langle H_{\text{spin}} + h_{\text{ext}} \sum_{m\sigma} S_{m\sigma}^x \rangle$ and we obtain its Gibbs free energy as Legendre transform $\Gamma(m_x) = E(h_{\text{ext}}(m_x)) - h_{\text{ext}}(m_x) m_x$. Because this thermodynamic potential is based on a mean-field approximated Hamiltonian and so cannot include influence from states in which the system as a whole has a different magnetization, it is directly suitable for use as Landau function [43, 445].

Our model is entirely symmetric under a sign change of the magnetization m_x in x -direction and we naturally care about the case of zero "external field" only, so the series expansion of the Landau function contains only even powers of m_x . In order to show the discontinuity of the Mott transition in our case, we need to explicitly include at least the second and fourth order terms in our expansion: a discontinuous transition happens when the value of Γ at the central ($m_x = 0$) local minimum, caused by a positive second order term, equals its value at the local minimum at non-zero m_x , caused by a negative fourth order term. The two phases differ in which of the local minima is

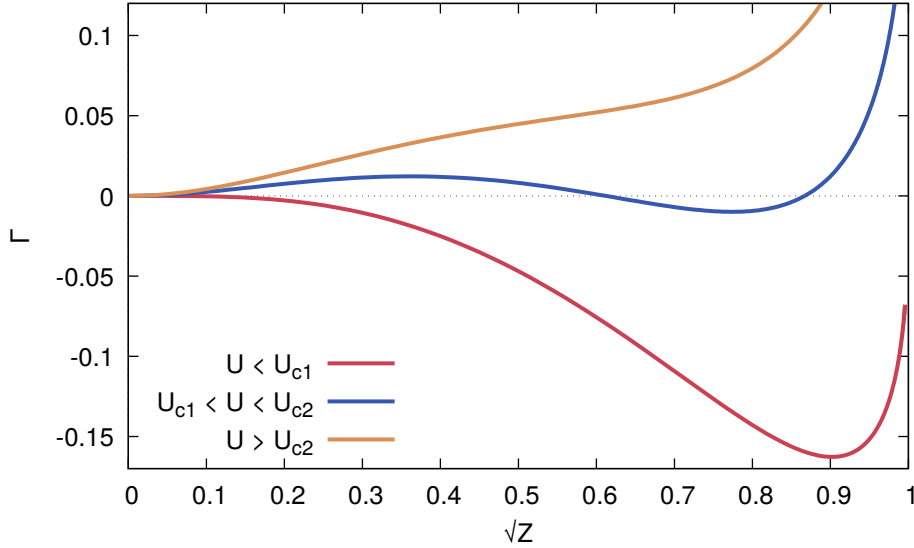


Figure 5.17: Gibbs free energy $\Gamma(m_x)$ calculated numerically using SSMF as function of the auxiliary spin magnetization m_x , equal to the square root of the quasi-particle weight \sqrt{Z} . This function serves as Landau function and is symmetric around $m_x = 0$. For interaction strengths $U < U_{c1}$ or $U > U_{c2}$ outside of the coexistence region, the global and only minimum is the stable metallic ($Z > 0$) or insulating ($Z = 0$) solution. In the coexistence region ($U_{c1} < U < U_{c2}$), both solutions are local minima and so at least metastable, with an additional unstable solution at the local maximum in between. At the phase transition, the global minimum changes between the two local minima while their positions remain well separated throughout, indicating a transition of first order. This form of the Landau function with three local extrema (at nonnegative m_x) around the transition is realized for a positive second order and negative fourth order coefficient.

the global minimum. Before we show how to determine the coefficients using a perturbative expansion of the ground state energy, we can already use the numerical results from full SSMF to visualize the expected behavior. In Fig. 5.17, the blue curve for U in the coexistence region is a Landau function with three local minima (at $m_x = 0$ and $m_x \approx \pm 0.8$) as it is realized at the transition if the fourth order coefficient is negative while those of the second and all higher orders are positive: For m close enough to zero, the second order always dominates and causes a local minimum if its coefficient is positive, and having at least one negative coefficient is a necessary condition to have any further local minima. Whether there actually are more depends on the coefficient ratios, but this must be necessarily the case at the phase transition as there would not be another phase otherwise.

Our Ansatz for the expansion of Γ around the Mott transition at $\sqrt{Z} \propto m_x = 0$ is therefore

$$\Gamma(m_x) = \gamma_2 m_x^2 + \gamma_4 m_x^4 + O(m_x^6), \quad (5.24)$$

which gives us the field in terms of the magnetization as

$$h_{\text{ext}}(m_x) = -\frac{\partial \Gamma}{\partial m_x} = -2\gamma_2 m_x - 4\gamma_4 m_x^3 + O(m_x^5). \quad (5.25)$$

With the spin Hamiltonian (5.23) and the external field term, we can explicitly express the total ground state energy as

$$E = \left\langle \underbrace{(h_{\text{sc}} + h_{\text{ext}})}_h \underbrace{\sum_{m\sigma} S_{m\sigma}^x}_{m_x} + H_{\text{spin,int.}} \right\rangle, \quad (5.26)$$

for which a perturbative series expansion of the form

$$E(h) = e_2 h^2 + e_4 h^4 + O(h^6) \quad (5.27)$$

can be done. In terms of these coefficients the magnetization in terms of the total field can now be calculated as well,

$$m_x(h) = \frac{\partial E}{\partial h} = 2e_2 h + 4e_4 h^3 + O(h^5), \quad (5.28)$$

which can be inverted up to fourth order to get

$$h(m_x) = \frac{1}{2e_2} m_x - \frac{4e_4}{(2e_2)^4} m_x^3 + O(m_x^5). \quad (5.29)$$

After subtracting the self-consistent field we have another expression for the expansion of the external field,

$$h_{\text{ext}}(m_x) = \left(\frac{1}{2e_2} - \frac{4\bar{e}}{M} \right) m_x - \frac{4e_4}{(2e_2)^4} m_x^3 + O(m_x^5), \quad (5.30)$$

which can be compared term by term with (5.25) to get the relations between the coefficients of the perturbative series for the ground state energy and those of the Landau function,

$$\gamma_2 = -\frac{1}{4e_2} + \frac{2\bar{e}}{M}, \quad \gamma_4 = \frac{e_4}{(2e_2)^4}. \quad (5.31)$$

We can therefore determine the coefficients of the Landau function and so gain insight into the stability of the competing solutions and the order of the transition by calculating the perturbative corrections to the ground state energy of $H_{\text{spin,int.}}$. Because this spin interaction Hamiltonian is equivalent to the interacting part of our original

$E \backslash N$	0	1	2	3	4
$2U - 2J$	$ 0, 0\rangle$				$ \uparrow\downarrow, \uparrow\downarrow\rangle$
$3J$			$ \uparrow\downarrow, 0\rangle, 0, \uparrow\downarrow\rangle$		
$U/2 + J/2$		$ \uparrow, 0\rangle, \downarrow, 0\rangle,$ $ 0, \uparrow\rangle, 0, \downarrow\rangle$		$ \uparrow\downarrow, \uparrow\rangle, \uparrow\downarrow, \downarrow\rangle,$ $ \uparrow, \uparrow\downarrow\rangle, \downarrow, \uparrow\downarrow\rangle$	
J			$ \uparrow, \downarrow\rangle, \downarrow, \uparrow\rangle$		
0			$ \uparrow, \uparrow\rangle, \downarrow, \downarrow\rangle$		

Table 5.1: Many-body states of a single-site Hubbard model arranged horizontally with respect to occupation number N and vertically with respect to eigenenergies E relative to the ground state energy (ordered assuming $J = U/4$). The energy of the many-body states includes both interaction as well as the chemical potential for half-filling.

Hubbard model Hamiltonian, which corresponds to the entirety of a single site Hubbard model or “Hubbard atom”, we will denote the states in terms of the equivalent single-site many-body states (see Tab. 5.1) rather than the auxiliary spin basis states, e.g. the ground states as $|\uparrow, \uparrow\rangle$ and $|\downarrow, \downarrow\rangle$ rather than $|\uparrow\downarrow\uparrow\downarrow\rangle$ and $|\downarrow\uparrow\downarrow\uparrow\rangle$ for clarity. The full operator of the perturbation is the kinetic term $V = (h_{sc} + h_{ext})(\sum_{m\sigma} S_{m\sigma}^x)$, where we may set the hypothetical external field to zero again and the remaining coefficient $h_{sc} \propto m_x \propto \sqrt{Z}$ is indeed small around the Mott transition, where $Z = 0$ on the insulating side.

Due to the double degeneracy of the ground state, the spin-aligned half-filled states $|\uparrow, \uparrow\rangle$ and $|\downarrow, \downarrow\rangle$ favored by Hund’s coupling in absence of the perturbation, we need to proceed with degenerate perturbation theory [446]. This procedure deals with the formally diverging terms that the version for non-degenerate cases would produce due to contributions from the same degenerate subspace the considered state belongs to and requires the diagonalization of the perturbation in that subspace to find the appropriate basis.

Ordinarily, it is directly V that must be diagonalized, but in our case the odd powers of V are zero in the ground state subspace because the application of V changes the occupation by exactly one, so they are diagonal in any basis. Additionally, in the case $J \neq 0$ two allowed hopping processes in sequence connect each of the occupation basis ground states just to itself with the exactly same coefficient due to spin symmetry, so V^2 is proportional to a unit matrix and also has equal eigenvalues and no preferred basis. The terms proportional to V^4 are the first ones not diagonal in the degenerate

subspace, and those that revisit the ground state subspace already after the second application of V do not need to be considered for the diagonalization as they correspond to $(V^2)^2$, proportional to a unit matrix, which shifts both eigenvalues equally. All the other terms reach intermediate states at energies $J, 3J$ or $2U - 2J$, which are all equally connected to either of the two ground states by the perturbation, and so we have to diagonalize a matrix proportional to $\begin{pmatrix} 1 & 1 \\ 1 & 1 \end{pmatrix}$. Its eigenvalues are 0 and 2, with the latter belonging to the ground state $(|\uparrow, \uparrow\rangle + |\downarrow, \downarrow\rangle)/\sqrt{2}$ due to the overall negative sign of the fourth order terms. Therefore the total effect of the degeneracy compared to non-degenerate perturbation theory to fourth order is an additional factor of 2 for fourth-order processes which do not have the ground state as intermediate state.

In total, the non-zero corrections to the unperturbed ground state energy $E_n^{(0)}$ in second and fourth order of perturbation theory are

$$E_n^{(2)} = \sum_m \frac{|V_{nm}|^2}{E_{nm}}, \quad (5.32)$$

$$E_n^{(4)} = \sum_{mpq} \frac{V_{nm}V_{mp}V_{pq}V_{qn}}{E_{nm}E_{np}E_{nq}} - E_n^{(2)} \sum_m \frac{|V_{nm}|^2}{E_{nm}^2}, \quad (5.33)$$

where V_{nm} are the matrix elements of the perturbation operator, $E_{nm} := E_n^{(0)} - E_m^{(0)}$ is used as abbreviation in the denominators and with all summations over all states not in the degenerate ground state subspace. It is clear that the odd order terms must vanish because the operator V flips one auxiliary spin per application: recall that $S^x \propto S^+ + S^-$, and in each term of the sum $\sum_{m\sigma} S_{m\sigma}^x$ identity operators implicitly act on the three other auxiliary spins. This corresponds to a change of the occupation of the single-site Hubbard model by exactly one, and so the matrix elements of all odd powers of V are exactly 0 between two states with the same occupation number.

The total ground state energy correction is

$$E(h) = \underbrace{-\frac{2}{U(1+j)}}_{e_2} h^2 - \underbrace{\frac{2(7j^2 - 9j + 8)}{U^3(1+j)^3(1-j)3j}}_{e_4} h^4, \quad (5.34)$$

where $j = J/U$. For $0 < J < U$, which includes the realistic values of J/U , the denominator of e_4 is positive and so e_4 itself as well as γ_4 are negative, as it is required to have a first-order transition.

We can additionally analyze which hopping processes favor a first-order transition by looking at their individual contributions to e_4 . They can be categorized by the sub-

space to which their intermediate states after the second hop belong, which is either that of the ground state for the, diagrammatically speaking, disconnected process described by the second term in (5.33) or the ones with energies J , $3J$ or $2U - 2J$ for the first term. In this order, their numerator contributions are $24j^2 - 24j$, $-12j^2 + 12$, $-4j^2 + 4$, and $6j^2 + 6j$ respectively. In the range $0 < J < U$, only the first contribution due to the disconnected process composed from two separate two-stage hopping processes is negative and so disfavors the first-order transition, particularly at relatively high values of J around $J = U/2$, while all the contributions by connected processes are positive and so favor the first-order transition, with those visiting the J and after it the $3J$ levels being the larger contributions for low J .

This qualitatively explains why no first-order transition is observed for $J = 0$, as the J and $3J$ levels belong to the ground state subspace in that case and must be treated during the diagonalization step of degenerate perturbation theory instead, and why the range of J with a first-order transition is smaller for Kanamori interaction, because the levels there are $2J$ and $4J$ instead. Data for the latter as well as a detailed treatment of both of these other cases can be found in Ref. [360], and similar behavior has previously been described in Ref. [447] using the rotationally invariant slave-boson method (RISB), where the empirical rule of thumb is suggested that a first-order transition should be expected if the lowest-lying excitations of the single-site Hamiltonian have the same occupation as its ground state. This reasoning is in principle not limited to a splitting of the ground state multiplet by Hund's coupling either: as long as we get excited states with the same occupation number, ideally lying as low as possible, we can expect the same effect on the order of the transition. e.g. also due to a Jahn-Teller distortion [448] or crystal field [360, 392].

Regarding our DMFT calculations, we can employ the perturbative expansion for one more important observation: as long as the ground state of the single-site model is degenerate, including also the $J = 0$ case with six-fold degeneracy, the transition at sufficiently low but non-zero temperature will be of first order independent of its behavior at zero temperature [449], and therefore results demonstrating a first-order transition at one single arbitrarily low but non-zero temperature, e.g. from DMFT using a QMC solver, would not directly by itself allow us to draw a conclusion about the nature of the transition at zero temperature or distinguish the cases with and without Hund's coupling.

This can be shown by considering the internal energy around the Mott transition at a temperature slightly above zero [449], at which we have to include all the states from the original ground state subspace of dimension N_{deg} rather than just the lowest lying after perturbation, as all their energies $E_i = e_0 + e_{i,2}h^2 + e_{i,4}h^4 + O(h^6)$ differ from the ground state energy only by powers of the small quantity h . For a low enough

temperature, we can still assume that contributions from any of the other state with a distance of about J or more from the ground state are negligible. After setting the unperturbed ground state energy e_0 to zero for simplification, we can expand the total internal energy

$$\langle E \rangle = \frac{\sum_i E_i \exp(-\beta E_i)}{\sum_i \exp(-\beta E_i)} = \frac{\sum_i E_i (1 - \beta E_i)}{\sum_i (1 - \beta E_i)} + O(h^6) \quad (5.35)$$

$$= \left(\sum_i E_i (1 - \beta E_i) \right) N_{\text{deg}}^{-1} \left(1 + \frac{\beta}{N_{\text{deg}}} \sum_i E_i \right) + O(h^6) \quad (5.36)$$

by first expanding the exponential functions for $E_i \rightarrow 0$ and, after factoring out the degeneracy, the inverse as binomial series to just two terms, as this suffices for all the decisive terms of fourth order in h in total. With the average energy $\bar{E} = N_{\text{deg}}^{-1} \sum_i E_i$ of the original ground states after perturbation, we can rearrange this after multiplying out to get

$$\langle E \rangle = \bar{E} - \beta \left(\sum_i \frac{E_i^2}{N_{\text{deg}}} - \bar{E}^2 \right) = \bar{E} - \overline{\beta(E - \bar{E})^2} + O(h^6), \quad (5.37)$$

where $\overline{\beta(E - \bar{E})^2}$ contains a strictly positive fourth-order contribution that ensures due to its coefficient β that the total fourth order terms of the energy and the Landau function are negative for sufficiently low temperature, indicating a first-order transition. For exactly zero temperature on the other hand, only the energy contribution of the ground state after perturbation is relevant, and so the transition order not generally determined.

5.1.5 Conclusion, contextualization and outlook

Our results show that a zero temperature Mott transition of first order at half-filling, which is present in the two-orbital Hubbard model with Hund's coupling, implies a quantum critical point (QCP) at finite doping. Using a perturbative analysis, we are able to attribute the order of the phase transition at half-filling and thus the underlying cause of the finite-doping QCP to the splitting of the ground state multiplet by a term small relative to U , which is the Hund's coupling J in this case. This feature is neither unique to models with two orbitals nor does it depend on our use of the semicircular (Bethe lattice) density of states and it is reasonable to assume that at least other models differing in only these aspects show similar behavior.

Other models for which we have performed similar analysis (using QMC-DMFT calculations only) are e.g. a two-dimensional two-orbital model with a simple Hamiltonian designed to reproduce the LDA Fermi surface of iron-pnictide superconductors

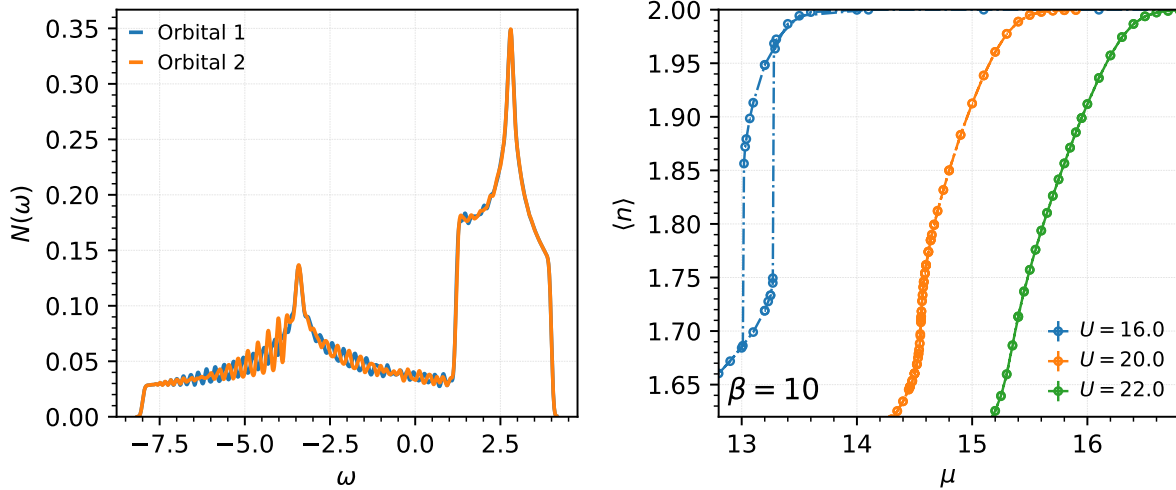


Figure 5.18: Left panel: Single-particle density of states $N(\omega)$ of the Hamiltonian of a two-dimensional model for iron-pnictide superconductors with two degenerate orbitals [450] used as DMFT input with a resolution of 107×109 k -points. Right panel: Total occupation $\langle n \rangle$ for this model with density-density interaction at three different interaction strengths U . Depending on U , we observe either a doping-driven phase transition (lowest U) or a crossover.

[450]. The effective single-particle density of states for the resolution of the Hamiltonian in k -space used as input for the DMFT calculations is shown in the left panel of Fig. 5.18 with the resulting $\langle n \rangle (\mu)$ curve (still for density-density interaction) next to it. The shape of this density of states, which consists of two clearly distinguishable contributions with different spreads, inversely proportional weights, and one typically two-dimensional van Hove singularity each, slightly impacts the quantitative comparability with our two-orbital Bethe lattice calculations. For this model, the total bandwidth is $12t_1$ with t_1 the nearest-neighbor hopping between the orbitals extended in the direction of the neighbor, which places the shown graph for $\beta t_1 = 10$ in approximately the region of the $\beta D = 50$ graph (Fig. 5.12) for the Bethe lattice model. We can recognize a coexistence region for $U/t_1 = 16.0$ for this model, which has an extent comparatively smaller in the chemical potential μ (after rescaling) but larger in the doping or occupation $\langle n \rangle$, even comparing with data for the next lower temperature of $\beta D = 100$ (Fig. 5.15) in the Bethe lattice model.

In addition to this comparison with another two-orbital model with only a more realistic density of states, we have also compared models with more and non-degenerate orbitals and more complicated forms of the interaction Hamiltonian. In the left panel of Fig. 5.19, we show the $\langle n \rangle (\mu)$ curve for a Bethe lattice model with three degenerate orbitals and Kanamori interaction, and beside it that for a DFT-derived five-orbital

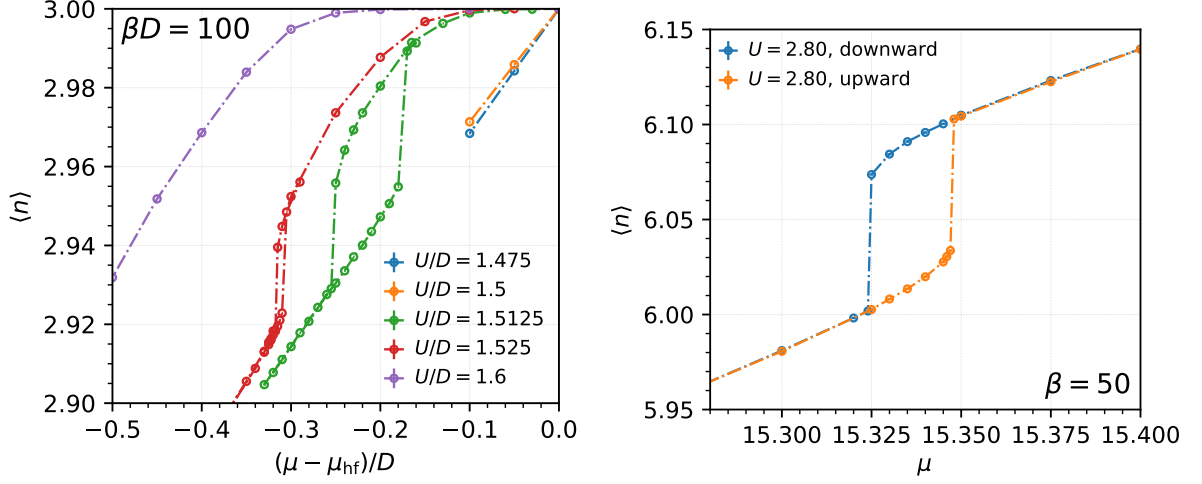


Figure 5.19: Left panel: Total occupation $\langle n \rangle(\mu - \mu_{\text{HF}})$ as a function of chemical potential relative to half-filling for a Bethe lattice model with three degenerate orbitals and Kanamori interaction at several different interaction strengths U , with a doping-driven phase transition recognizable for intermediate U . Right panel: Total occupation $\langle n \rangle(\mu)$ for a five-orbital model using a DFT-derived Hamiltonian for BaFe_2As_2 with density-density interaction using realistic interaction strength parameters $U = 2.8$ eV, $J = 0.43$ eV [451].

BaFe_2As_2 Hamiltonian with density-density interaction. For a suitably chosen value of the interaction strength, we can see coexistence regions of multiple phases near integer filling in both of these systems as well. In BaFe_2As_2 calculations with Kanamori or Coulomb interaction (not shown), we have so far only been able to identify a region of increased compressibility, but no phase separation. This is in agreement with the observation from SSMF [392], which we also confirmed for the two-orbital model at non-zero temperature using QMC-DMFT (not shown), that coexistence regions with Kanamori interaction tend to be smaller than with density-density interaction given otherwise comparable systems. As we mentioned in the previous chapter, Hund’s coupling is however not the only way to induce a splitting of the ground state multiplet, so with the inclusion of other neglected effects such as spin-orbit coupling it may be possible to find phase separation in BaFe_2As_2 as well.

However, our analysis is not only relevant for systems that require a multiorbital description due to intrinsically multiorbital physics “per site” like Hund’s metals, but can also be connected with other systems in the context of which our orbital degree of freedom would represent something more abstract than simple atomic orbitals. Due to the need of momentum-space dependence for an accurate description of the cuprates’ d -wave superconductivity for example [33, 452], the two-dimensional single-orbital Hubbard model is typically not solved using plain single-site DMFT any more in this con-

text, but rather using cluster extensions of DMFT [453–455], which allow the resulting self-energy functions to capture the effects of short-ranged spatial correlations through their momentum dependence. As little as two orbitals, assigned to different patches of momentum space in the DCA approach, can already give a qualitative agreement of calculated ARPES spectra with cuprate phenomenology [456].

In this way, our results of compressibility enhancement, phase separation with co-existence of two metals and quantum criticality at finite doping lend themselves easily to a comparison with the similar picture that already started to form in earlier studies of cuprate models [374–376] and is substantially confirmed and enhanced by cluster DMFT calculations for the two-dimensional Hubbard model [421, 422, 457–465], which indicate the influence of a (possibly quantum) critical point in the region of the pseudogap and superconducting phases.

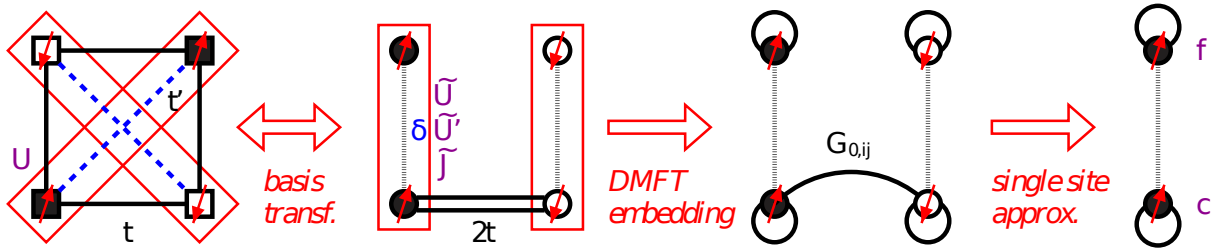


Figure 5.20: Illustration of the approximate mapping from CDMFT using a 2×2 -plaquette cluster for the single-orbital Hubbard model, used as cuprate superconductor model in cluster DMFT calculations, to single-site DMFT using a two-orbital model. By performing the change of basis (5.38) from single orbitals (squares) to bonding (c) and antibonding (f) combinations across the plaquette diagonals (red rectangles), we effectively end up with two equal sites with Kanamori-interacting two orbitals each connected by hopping only. This is an exact transformation of the plaquette cluster up to the step where we neglect the depicted off-diagonal component of the Weiss function G_0 that connects the two sites in order to perform single-site rather than two site DMFT as an approximation. Taken from Fig. 1 of Ref. [466]³.

The relevance of the phenomenology of Hund’s metals including iron pnictide superconductors to the description of cuprates as another prominent class of high-temperature superconductor has been speculated on before [383, 466]. Following this argumentation, the physics of “spin-freezing” [35] that leads to non-Fermi-liquid states and orbitally decoupled physics down to comparatively low temperature could be considered as the underlying shared mechanism between both of them. An explicit mapping

³Reprinted figure with permission from P. Werner, S. Hoshino, and H. Shinaoka, “Spin-freezing perspective on cuprates,” *Phys. Rev. B* **94**, 245134 (2016). Copyright 2016 by the American Physical Society.

from a 2×2 -plaquette with one orbital per site as it could be used in cluster DMFT for a cuprate-inspired model to a two-site two-orbital model with was performed in Ref. [466] in order to interpret the cuprate model behavior in terms of the spin-freezing behavior typical for multiorbital models: By going into the basis of bonding (c_i) and antibonding (f_i) orbitals between the two pairs ($i \in \{1, 2\}$) of diagonally opposite corners of the plaquette (red rectangles in Fig. 5.20),

$$c_1 = \frac{d_1 + d_3}{\sqrt{2}}, \quad f_1 = \frac{d_1 - d_3}{\sqrt{2}}, \quad c_2 = \frac{d_2 + d_4}{\sqrt{2}}, \quad f_2 = \frac{d_2 - d_4}{\sqrt{2}}, \quad (5.38)$$

$$d_1 = \frac{c_1 + f_1}{\sqrt{2}}, \quad d_2 = \frac{c_2 + f_2}{\sqrt{2}}, \quad d_3 = \frac{c_1 - f_1}{\sqrt{2}}, \quad d_4 = \frac{c_2 - f_2}{\sqrt{2}}, \quad (5.39)$$

where d_i is the local orbital on each site ($i \in \{1, 2, 3, 4\}$) of the plaquette enumerated in anticlockwise order (see Fig. 5.20), the single-orbital on-site repulsive interaction is transformed into an interaction of Kanamori form between the two orbitals that belong to the same pair of sites each with all interaction parameters equal, i.e. $U^{c/f} = U^{c'/f} = J^{c/f} = U^d/2$ with the original on-site repulsion U^d and the new intraorbital repulsion $U^{c/f}$, interorbital repulsion $U^{c'/f}$ and Hund's coupling $J^{c/f}$. Aside from the local interaction, the chemical potential term for d electrons turns into the same chemical potential term for c and f electrons, the nearest neighbor t hopping term for d electrons turns into a nearest neighbor hopping term with double coefficient $2t$ for c electrons only and the next nearest (diagonal) t' hopping term turns into a crystal field splitting of size $2t'$ between the c - and f -orbital on a site.

Obtaining the Weiss Green's function in the new basis by transforming that of the plaquette, we see that we have two equal sites with diagonal elements of \mathcal{G}_0 for each orbital and additionally off-diagonals only between the two c -orbitals. As seen in the last step of Fig. 5.20, it is then proposed in Ref. [466] further approximate the model by now dropping one of the two sites and only performing single-site DMFT, such that all the hoppings between orbitals of the same type including the site-offdiagonal ones are at most treated through DMFT. This leads to a solution that is structurally the same as that of our two-orbital model if we choose the Kanamori form for the interaction, but the unusual values interaction parameters, which make the Hund's coupling J not at all a small scale compared to U , mean that no direct quantitative conclusions can be drawn for this model.

5.2 Detection of thermodynamic instabilities from quantities on the two-particle level

In this section, we investigate the transition and crossover between weakly and strongly correlated metal emerging from the Mott transition at half-filling at non-zero temperature and doping using two-particle response functions calculated by continuous-time quantum Monte Carlo for DMFT solutions of the two-orbital Hubbard model. These local quantities allow us to reproduce values for electronic compressibilities estimated from numerical derivatives, including its enhancement and divergence in the vicinity of the critical point. We find that reformulations in terms of the local generalized susceptibilities are also possible for the other derivatives of thermodynamic potentials and can be used to express thermodynamic stability conditions. Using the spectral representation of the generalized susceptibility, an eigenvalue condition for the compressibility divergence can be established and is found to serve as a threshold for the distinction between stable and unstable phases as well, even if the compressibility of an unstable solution is positive and would thus not suffice to establish instability by itself.

This section covers mostly results published in the following preprint, Ref. [194], which is also the source of some of the figures

*A. Kowalski, M. Reitner, L. Del Re, M. Chatzieftheriou, A. Amaricci, A. Toschi,
L. de' Medici, G. Sangiovanni, and T. Schäfer,
"Thermodynamic Stability at the Two-Particle Level",
arXiv:2309.11108 [cond-mat]*

5.2.1 The physics of response functions and vertex divergences

In the previous section, we examined the Mott metal-insulator transition as well as the metal-metal transition and crossover that are its continuation at non-zero doping by solving the Hubbard model using DMFT. The quantities we considered primarily were e.g. the occupation or doping, double occupancies, quasiparticle weight, and spectrum as functions of the interaction strength U and chemical potential μ as parameters. Apart from the double occupancies, all of them are one-particle quantities that we obtain by processing the local Green's function and self-energy of the DMFT solution. The compressibility enhancement and divergence associated with the phase transitions [363, 369] manifest themselves in increased slopes of the $n(\mu)$ curves, see e.g. Fig. 5.15. The physical information that we can extract from these slopes, i.e. from values of the one-particle quantity n from *multiple* DMFT solutions with different μ , tells

us about the response of the occupation of the system to a change in its chemical potential, which effectively changes that occupation. At first glance this seems a little cyclical, but CT-HYB allows us access to arbitrary correlation functions of the auxiliary AIM, and we can e.g. consider the correlation $\langle n(\tau)n(0) \rangle$ of the occupation with its value at some *different* imaginary time. This charge-charge susceptibility or response function is a two-particle correlation function made of four creators and annihilators and tells us how the auxiliary impurity itself responds to a change of its μ parameter. Within the DMFT embedding the direct change of the impurity μ , though it is the same as the lattice μ , is not the only term that contributes to the compressibility $\partial n/\partial\mu$ of the lattice model. Still, it is possible in DMFT to use other more general two-particle quantities we obtain for the impurity from CT-HYB to calculate also the response functions for the lattice. With their informational content that essentially includes the lattice $\partial n/\partial\mu$, this allows us to roughly locate ourselves in the lattice phase diagram (a divergence of the susceptibility would e.g. put us at the critical point) even though we only calculate properties of one single DMFT solution. In this section, we will see how derivatives of thermodynamic potentials and the thermodynamic stability conditions for the lattice model can be rewritten in DMFT in terms of correlation functions of the auxiliary AIM that can be calculated “locally” in parameter space. By analyzing the two-particle response functions in their eigenbasis, we will further identify a remarkable connection between the lowest eigenvalue, one single number, and thermodynamic stability.

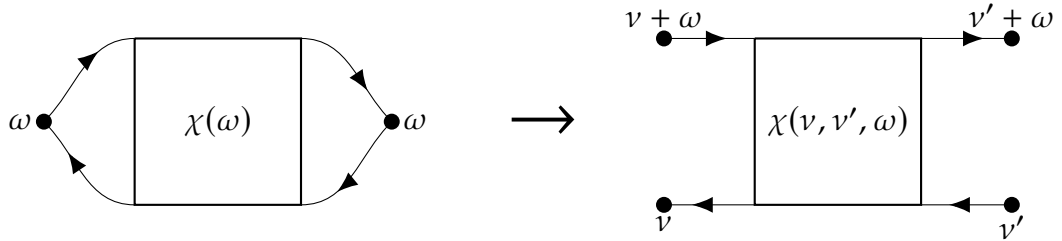


Figure 5.21: Comparison between the representations of a physical response function $\chi(\omega)$ (left) and a generalized susceptibility $\chi(v, v', \omega)$ (right) as Feynman diagrams [212]. The physical response function has only one frequency argument, just as a correlation function like $\langle T_\tau n(\tau)n(0) \rangle$ only needs one time argument assuming time-translational invariance. With reference to this function, we could describe the generalization (arrow) leading to the generalized susceptibility as splitting the densities into creators and annihilators and relaxing the restrictions on all their time differences, which pictorially “unties” the contracted legs and results in a different frequency for each of them (of which only three are independent due to energy conservation).

The concrete quantity we are interested in is the uniform ($\mathbf{q} = \mathbf{0}$) two-particle charge-charge correlation function $\chi_{d,\mathbf{q}=0}$ of the lattice in DMFT, which tells us how the occu-

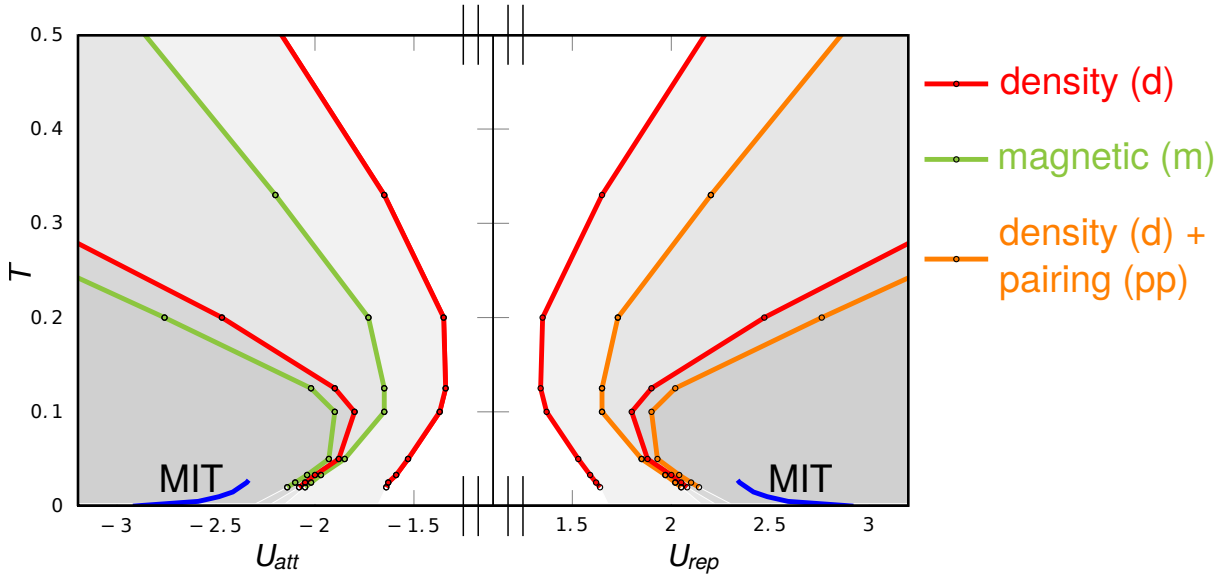


Figure 5.22: Divergence lines of irreducible vertices in different channels in the repulsive and attractive one-band Hubbard model at half-filling with the Mott metal-insulator transition (blue, cf. Fig. 5.1) for reference. As the interaction is moved from zero, the first vertex divergences are encountered significantly before reaching the Mott transition and are accompanied by sign changes of the eigenvalues of the response function associated with the channel. Taken from Fig. 1 of Ref. [467]⁴.

pation of the entire lattice responds. Its vertex part, i.e. the unit in its diagrammatic representation that can not be split into disconnected parts by cutting two separate one-particle Green's function lines, is the two-particle irreducible vertex function $\Gamma_{d, \mathbf{k}\mathbf{k}'\mathbf{q}}$. In DMFT, a local vertex function calculated in the auxiliary AIM can be used for the calculation of susceptibilities of the lattice problem [468]. The irreducible vertex function is thus the link between two-particle impurity and lattice quantities, similar to the self-energy in the one-particle case. The equation analogous to the Dyson equation, which allows us to first extract the vertex function from the CT-HYB impurity results and then to use it to calculate the lattice quantity is the Bethe-Salpeter equation $\chi_d = \chi_{0,d} - \beta^{-2} \chi_{0,d} \Gamma_d \chi_d$ [33]. The quantity χ_d here is a *generalized susceptibility* [214], differing from a physical susceptibility in having four uncontracted outer legs as shown in Fig. 5.21 that can be linked together with other two-particle quantities to make up longer diagrammatic contributions as in the second term of the Bethe-Salpeter equation. It consists of two- and one-particle Green's functions, which we can calculate for the auxiliary AIM to invert the Bethe-Salpeter equation and obtain the impurity vertex function $\Gamma_{\text{imp},d}$. Inserted in the lattice Bethe-Salpeter equation, we can get the general-

⁴Reprinted figure with permission from D. Springer, P. Chalupa, S. Ciuchi, G. Sangiovanni, and A. Toschi, "Interplay between local response and vertex divergences in many-fermion systems with on-site attraction," Phys. Rev. B **101**, 155148 (2020). Copyright 2020 by the American Physical Society.

ized susceptibility of the lattice and sum over the fermionic Matsubara frequencies to get physical susceptibilities.

While we consider the Hubbard model in the vicinity of its critical point where the susceptibility $\chi_{d,q=0}$ diverges, the divergences of the vertex function Γ_d itself that we insert into the Bethe-Salpeter equation have been of some interest recently. Solving the equation for Γ_d , we get $\Gamma_d = \beta^2(\chi_d^{-1} - \chi_{0,d}^{-1})$ which tells us that a zero eigenvalue of the generalized susceptibility will cause a divergence [469]. At $U = 0$, all eigenvalues are positive, but we know that in the Hubbard model, electrons start forming fluctuating local moments as we approach the Mott transition, accompanied by the gradual increase of spin fluctuations and suppression of charge fluctuations. In the eigenbasis of the generalized susceptibility, this decrease of the charge susceptibility does not happen uniformly. Instead, more and more eigenvalues in the charge channel move from positive to negative to bring down the value of the charge susceptibility, and this is associated with a divergence of the vertex for each of the eigenvalues [215, 469]. Fig. 5.22 shows the curves in the parameter space of the Hubbard model along which the divergences of the irreducible vertices in the different channels occur, marking different channels separately. These correspond to different components of the generalized susceptibility for which the Bethe-Salpeter equations decouple. Consequently, with each channel a different irreducible vertex *irreducible in that particular channel* is associated. For repulsive interaction the diagram shows that the first divergence does indeed happen in the charge channel, and that it in fact already occurs at interaction strengths significantly below the coexistence region of the Mott transition as a sort of precursor effect [470] and persists at temperature considerably above the critical temperature of the Mott transition.

The area in phase space at high interaction strength that is separated from the weakly correlated metal by the divergence line, which includes the coexistence region, is interpreted to be the region where a perturbative description is no longer adequate as it cannot capture the vertex divergence [471]. This breakdown of dressed perturbation theory is rooted in the multivaluedness of the Luttinger-Ward functional in the Hubbard and other interacting models [469, 472–477]. With increasing interaction, physical and unphysical solutions for the non-interacting Green's function $G_0[G]$ and consequently the self-energy $\Sigma[G]$ as functionals of the full Green's function G cross [469], leading to the failure of convergence of “skeleton” (or “bold”) diagrammatic series in terms of full (“dressed”) G , which are resummations of the still converging series in terms of G_0 [472]. As the irreducible vertex Γ_c can be expressed as functional derivative of $\Sigma[G]$ in the Luttinger-Ward formalism, this is naturally related to its divergence [467, 470, 478–481]. Diagrammatic approaches to physical interpretation [215] as well as diagrammatic and perturbative calculation schemes [472, 474] as well as non-local

extensions of DMFT [216, 482] may be affected. Depending on the specific method this may only have an effect very close to the divergence line and just require extra care, but can necessitate the use of alternative methods or workarounds in other cases [483–488]. Divergences of the irreducible two-particle vertices are however not only important for technical considerations, but are linked to prominent physical features of the systems. They arise due to the formation of local moments and suppression of fluctuations as interactions increase [215, 467, 469–471, 479, 481, 488, 489], and are thus necessary precursors of the compressibility divergence related to the Mott transition [470]. Further, they may contribute to other features of strongly correlated systems such as high-temperature superconductivity, which could be promoted by vertex divergences turning a repulsive interaction effectively attractive [490, 491].

We focus our attention on the connection between divergences of the charge susceptibility and the physics of the Mott metal-insulator and the associated metal-metal transition and crossover in the two-orbital Hubbard model with Hund’s coupling that we previously considered in Sec. 5.1 and Ref. [193]. In the vicinity of the critical points of the Mott transition in the one-band model, Ref. [491] found a peak of the electronic compressibility associated with the lowest eigenvalue of the two-particle charge response function. We therefore consider particularly the area in parameter space around the critical point at the end of the phase separation region at non-zero temperature and doping in the two-orbital Hubbard model as well. For orientation, the zero temperature phase diagram in Fig. 5.11 can be used, which is also indicative of the situation at finite low temperature. As that figure also shows, the area where we observe the compressibility enhancement and divergence is at relatively high doping compared to the one necessary for the one-band Hubbard model [482, 491]. We use the QMC-DMFT results for one-particle quantities previously calculated using *w2dynamics* [40] for that model, as described by the Hamiltonian given in (5.1) with only the density-density terms (5.2) as interaction on a Bethe lattice with half-bandwidth $D = 1$. Let us note the importance of the implementation of phase-space extension [146] and non-linear mixing [145, 431] for the convergence of solutions in the unstable phase again and refer to Sec. 5.1.1 for more details concerning the model and its DMFT solution. In order to obtain two-particle vertices, we calculate the two-particle impurity Green’s function using component-wise worm sampling [74, 492–494] as implemented in the CT-HYB impurity solver of *w2dynamics* with self-energies taken from our converged DMFT solutions as input.

5.2.2 Background on two-particle quantities

Introduction and definitions

As we have seen in Sec. 5.1, one of the characteristic features occurring at the phase transition between the strongly correlated metal and the weakly correlated metal is a pronounced enhancement of the electronic compressibility $\kappa = \frac{1}{n^2} \frac{\partial n}{\partial \mu}$, a quantity proportional to the slope of the $n(\mu)$ curves we have studied in detail. The simplest way to calculate it from such data is the difference quotient of chemical potential input μ and total occupation output n of two points from calculations with a small difference in μ only. In principle, this requires only the one-particle quantities which we already have access to in our study by virtue of using DMFT. The total occupation is related to the sum of the diagonals of the one-particle Green's function (5.41) at zero imaginary time difference $\langle n \rangle = \sum_{\alpha} \langle n_{\alpha} \rangle = \sum_{\alpha} \langle c_{\alpha}^{\dagger} c_{\alpha} \rangle = \sum_{\alpha} (G_{\alpha}(\tau \rightarrow 0^+))$, where the Greek index α combines spin and orbital.

While this is a simple procedure, some disadvantages of the difference quotient are that the results are only interval-averaged values of the true compressibility, which in particular means that local maxima tend to be underestimated, and that the occupation, as a difference of Monte Carlo results which we would like to get as close to zero as possible to reduce that underestimation, suffers from a rather high propagated uncertainty. By getting the compressibility directly from a calculation for one single point in parameter space, we could avoid such problems. Since we can obtain response functions like susceptibilities from two-particle Green's functions just as we can get values for one-particle observables from the one-particle Green's function [47, 214], all we need to do is calculate the two-particle Green's function using CT-HYB and use it to get the DMFT lattice susceptibilities [33].

Let us start with a short introduction to two-particle quantities following Refs. [47, 214, 495] and for simplicity consider only impurity quantities until we get to the Bethe-Salpeter equation. The basic two-particle impurity quantity that we directly have access to using CT-HYB is the already mentioned impurity two-particle Green's function in imaginary time [214]

$$G_{\alpha\beta\gamma\delta}(\tau_1, \tau_2, \tau_3, \tau_4) = \langle T_{\tau} c_{\alpha}^{\dagger}(\tau_1) c_{\beta}(\tau_2) c_{\gamma}^{\dagger}(\tau_3) c_{\delta}(\tau_4) \rangle, \quad (5.40)$$

with different argument order in this section compared to (3.7) and for consistency we choose to define the one-particle Green's function in this section as [214]

$$G_{\alpha\beta}(\tau_1, \tau_2) = \langle T_{\tau} c_{\alpha}^{\dagger}(\tau_1) c_{\beta}(\tau_2) \rangle, \quad (5.41)$$

also with opposite argument order compared to (2.12). The Lehmann representation

[149] of the two-particle Green's function,

$$G_{\alpha\beta\gamma\delta}(\tau_1, \tau_2, \tau_3, \tau_4) = \sum_n \langle n | \frac{e^{-\beta H}}{Z} e^{\tau_1 H} c_\alpha^\dagger e^{-(\tau_1 - \tau_2)H} c_\beta e^{-(\tau_2 - \tau_3)H} c_\gamma^\dagger e^{-(\tau_3 - \tau_4)H} c_\delta e^{-\tau_4 H} | n \rangle \quad (5.42)$$

$$= \sum_n \frac{e^{(-\beta - (\tau_4 - \tau_1))E_n}}{Z} \langle n | c_\alpha^\dagger e^{-(\tau_1 - \tau_2)H} c_\beta e^{-(\tau_2 - \tau_3)H} c_\gamma^\dagger e^{-(\tau_3 - \tau_4)H} c_\delta | n \rangle, \quad (5.43)$$

where we assume $\tau_1 > \tau_2 > \tau_3 > \tau_4$ without loss of generality, allows us to consider some of its properties. Due to cyclic invariance of the trace and time-independence of the Hamiltonian, the two-particle Green's function depends only on three time differences rather than all times, and so we may fix one time to zero by subtracting it from all of them. As the energy eigenvalues of an unbounded system would not necessarily have an upper bound, when we evaluate the Green's function using its definition we must require that the term $\tau_1 - \tau_4$ in the exponent is less than β in order to obtain a finite value, i.e. all imaginary times are contained in one single interval of size β . We will choose to define it everywhere else as the antiperiodic continuation from this domain with period β in all arguments, consistent with the final property we show: the Green's function changes sign if the largest time is reduced by β or the smallest increased by it. Due to the previous requirement, such a change necessarily moves the first operator to the back or the last one to the front, which picks up a minus sign from the time ordering due to three exchanges of fermionic operators. Looking at one of the resulting values,

$$G_{\alpha\beta\gamma\delta}(\tau_1 - \beta, \tau_2, \tau_3, \tau_4) = - \sum_n \langle n | \frac{e^{-\beta H}}{Z} e^{\tau_2 H} c_\beta e^{-(\tau_2 - \tau_3)H} c_\gamma^\dagger e^{-(\tau_3 - \tau_4)H} c_\delta e^{-\tau_4 H} e^{(\tau_1 - \beta)H} c_\alpha^\dagger e^{-(\tau_1 - \beta)H} | n \rangle$$

explicitly, we can see that by cyclically moving the last three factors to the front, we get exactly minus the original expression after rearranging the exponents.

Such a two-particle Green's function by itself also contains contributions from simple products of two one-particle Green's functions representing disconnected processes. Therefore, we will later consider mainly the *generalized susceptibilities* [214]

$$\chi_{\alpha\beta\gamma\delta}(\tau_1, \tau_2, \tau_3, \tau_4) = G_{\alpha\beta\gamma\delta}(\tau_1, \tau_2, \tau_3, \tau_4) - G_{\alpha\beta}(\tau_1, \tau_2)G_{\gamma\delta}(\tau_3, \tau_4), \quad (5.44)$$

combinations of the two- and one-particle Green's functions such that the disconnected process in the transverse channel that we later identify as "uncorrelated part" is removed, represented diagrammatically in Fig. 5.23. For convenience, we usually work

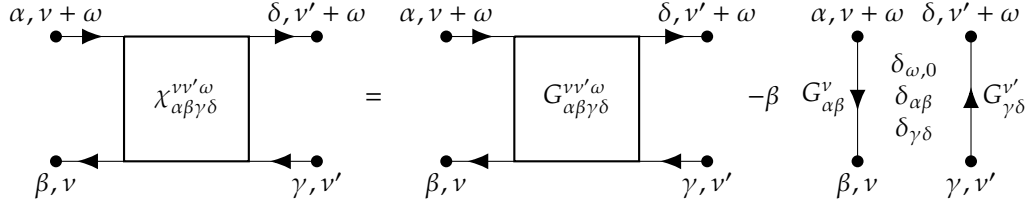


Figure 5.23: Diagrammatic representation of the definition (5.46) of the generalized susceptibility $\chi_{\alpha\beta\gamma\delta}^{vv'\omega}$ in Matsubara frequency space with the three independent frequencies chosen according to the particle-hole frequency convention (5.45) such that ω can be interpreted as energy transfer in a scattering process of an incoming electron (upper left vertex, drawn as thick dot) and incoming hole (upper right vertex). $\chi_{\alpha\beta\gamma\delta}^{vv'\omega}$ consists of a two-particle Green's function $G_{\alpha\beta\gamma\delta}$ function with the transverse disconnected part $\beta G_{\alpha\beta}^v G_{\gamma\delta}^{v'}$ subtracted. When physical response functions are calculated, this corresponds to the subtraction of the “uncorrelated part” as discussed later. For visual clarity, this is the definition in the impurity context. In the lattice context, momentum indices must be added, cf. Fig. 5.24.

with such quantities in Matsubara frequency space. Since all the Green's functions depend on time differences only, the transform to Matsubara space is a function of only three frequencies, two fermionic ones ν, ν' and a bosonic one ω . This may be interpreted as energy conservation: the last frequency is fixed by the other three. We choose a “particle-hole” convention for the frequencies, specifically

$$\nu_1 = \nu + \omega, \quad \nu_2 = \nu, \quad \nu_3 = \nu', \quad \nu_4 = \nu' + \omega \quad (5.45)$$

where each ν_i goes with τ_i in the transform. Using frequency-dependent Green's functions, we can express our generalized susceptibility in Matsubara frequency space as

$$\chi_{\alpha\beta\gamma\delta}(\nu, \nu', \omega) = G_{\alpha\beta\gamma\delta}(\nu, \nu', \omega) - \beta \delta_{\omega,0} G_{\alpha\beta}(\nu) G_{\gamma\delta}(\nu'), \quad (5.46)$$

where the fact that two time variables rather than just one are redundant in the disconnected term and that the two single-particle Green's functions do not share any time variables causes the additional relative factor of β as well as a non-zero contribution only if the bosonic frequency ω is zero. This can also be interpreted as no energy transfer between the two independently propagating particles, cf. its representation in Fig. 5.23 where it simply follows from energy conservation along single-particle propagations which manifests itself in the Green's function being diagonal in frequency. In Appendix A we show how to perform the integrations for the Fourier transform to Matsubara frequencies explicitly.

Relation between electronic compressibility and generalized susceptibility

With this definition of the generalized susceptibility at hand, let us make the connection back to the electronic compressibility and show how it can be calculated from two-particle quantities. While we are more interested in the lattice compressibility κ , for simplicity we will perform this derivation for the connection between the electronic compressibility κ_{imp} of the AIM and the impurity generalized susceptibility χ_{imp} . Their values are of course different from those of the lattice quantities, in particular the compressibility κ_{imp} of the auxiliary AIM does not diverge at the critical point of the DMFT lattice problem [491], but the relation between κ_{imp} and χ_{imp} that we derive is the same as that between the DMFT lattice compressibility κ and the static uniform DMFT generalized susceptibility of the lattice $\chi_{\mathbf{q}=0}^{\omega=0}$ since DMFT is thermodynamically consistent at this level, cf. Ref. [496].

Starting from the resulting formula

$$\kappa_{\text{imp}} = \frac{1}{n^2\beta^2} \sum_{vv'\alpha\beta} \chi_{\text{imp},\alpha\alpha\beta\beta}(v, v', \omega = 0), \quad (5.47)$$

cf. the single-orbital version of χ_{loc} given in Ref. [491], we begin by inserting the definition of the impurity generalized susceptibility in terms of impurity Green's functions,

$$\kappa_{\text{imp}} = \frac{1}{n^2\beta^2} \sum_{vv'\alpha\beta} \left(G_{\alpha\alpha\beta\beta}(v, v', \omega = 0) - \beta G_{\alpha\alpha}(v) G_{\beta\beta}(v') \right) \quad (5.48)$$

$$= \frac{1}{n^2\beta^3} \sum_{vv'\alpha\beta} \left(\int_0^\beta d\tau_i e^{i(v(\tau_1-\tau_2)+v'(\tau_3-\tau_4))} \left\langle T_\tau c_\alpha^\dagger(\tau_1) c_\alpha(\tau_2) c_\beta^\dagger(\tau_3) c_\beta(\tau_4) \right\rangle \right. \\ \left. - \int_0^\beta d\tau_i e^{iv(\tau_1-\tau_2)} \left\langle T_\tau c_\alpha^\dagger(\tau_1) c_\alpha(\tau_2) \right\rangle \int_0^\beta d\tau_i e^{iv'(\tau_3-\tau_4)} \left\langle T_\tau c_\beta^\dagger(\tau_3) c_\beta(\tau_4) \right\rangle \right). \quad (5.49)$$

By pulling the Matsubara frequency summations into the integrals and identifying expressions $\beta^{-1} \sum_\nu e^{i\nu\tau} = \delta(\tau)$ for the delta distribution, two tau integrals can be performed explicitly to set two time variables each equal in the next step,

$$\kappa_{\text{imp}} = \frac{1}{n^2\beta} \sum_{\alpha\beta} \left(\int_0^\beta d\tau_i \left\langle T_\tau (c_\alpha^\dagger(\tau_1) c_\alpha(\tau_1) c_\beta^\dagger(\tau_3) c_\beta(\tau_3)) \right\rangle \right) \quad (5.50)$$

$$- \int_0^\beta d\tau_1 \left\langle T_\tau (c_\alpha^\dagger(\tau_1) c_\alpha(\tau_1)) \right\rangle \int_0^\beta d\tau_3 \left\langle T_\tau (c_\beta^\dagger(\tau_3) c_\beta(\tau_3)) \right\rangle \\ = \frac{1}{n^2\beta} \sum_{\alpha\beta} \left(\int_0^\beta d\tau_i \left\langle T_\tau (n_\alpha(\tau_1) n_\beta(\tau_3)) \right\rangle \right) \quad (5.51)$$

$$- \int_0^\beta d\tau_1 \langle n_\alpha(\tau_1) \rangle \int_0^\beta d\tau_3 \langle n_\beta(\tau_3) \rangle \Big).$$

The density correlation function in the first term depends only on the time difference because it corresponds to a two-particle Green's function with the first two and last two time arguments equal. We can therefore set the time argument of the second operator to zero and shift integral bounds of the first time integral over τ_1 to $-\tau_3$ and $\beta - \tau_3$. For the same reason, minus signs from antiperiodicity would cancel and the function is thus β -periodic in its remaining argument like a bosonic correlation function, so the bounds of the first time integral over τ_1 can be reset to 0 and β , allowing us to perform the integral over τ_3 yielding β . The steps of a similar calculation are explicitly demonstrated at the end of Appendix A, with the difference that antiperiodic functions are involved there and the exponential factor from the Matsubara transform is necessary to cancel the minus sign. By taking into account that expectation values of static observables like single occupations do not depend on their imaginary time argument at all, we can simplify the second term as well and get the final result

$$\kappa_{\text{imp}} = \frac{1}{n^2} \sum_{\alpha\beta} \left(\int_0^\beta d\tau \langle T_\tau(n_\alpha(\tau)n_\beta(0)) \rangle - \beta \langle n_\alpha \rangle \langle n_\beta \rangle \right). \quad (5.52)$$

To verify this result for the impurity compressibility κ_{imp} , we need to compute the derivative $\partial n / \partial \mu$ for the AIM in terms of correlation functions as well. We usually consider such a derivative in the context of DMFT, but the two derivatives differ even though $\langle n \rangle$ and μ are equal for the lattice and its auxiliary AIM. However, in the case of an independent AIM all other impurity parameters are kept fixed for the derivative $\partial n / \partial \mu$, while the change of DMFT results with μ requires an adjustment of the self-consistent hybridization function as well. We shall write $(\partial n / \partial \mu)|_{\Delta=\text{const.}}$ to make it very explicit that we consider the derivative in the context of an independent AIM for the moment rather than the DMFT one.

We perform the derivative for the AIM in the path integral formalism, using the partition function (2.5) of the AIM with action (2.9). The total occupation is

$$\langle n \rangle = Z^{-1} \int \mathcal{D}(\bar{c}, c) \sum_\alpha n_\alpha(0) \exp(-S), \quad (5.53)$$

the expectation value of the sum of individual occupations per spin and orbital, where n in the path integral is shorthand for $\bar{c}c$ and we have chosen to set its arbitrary imaginary time argument to 0. μ only appears in the action term $S_\mu = -\mu \int_0^\beta d\tau \sum_\alpha n_\alpha$, i.e. once in the numerator and once in the denominator, so the derivative of $\langle n \rangle$ can be

calculated using the product rule resulting in

$$\left. \frac{\partial \langle n \rangle}{\partial \mu} \right|_{\Delta=\text{const.}} = Z^{-1} \int_0^\beta d\tau \int \mathcal{D}(\bar{c}, c) \sum_{\alpha\beta} n_\alpha(\tau) n_\beta(0) \exp(-S) \quad (5.54)$$

$$\begin{aligned} & - Z^{-2} \left(\int \mathcal{D}(\bar{c}, c) \sum_\alpha n_\alpha(0) \exp(-S) \right) \left(\int_0^\beta d\tau \int \mathcal{D}(\bar{c}, c) \sum_\alpha n_\alpha(\tau) \exp(-S) \right) \\ & = \int_0^\beta d\tau \sum_{\alpha\beta} \langle T_\tau (n_\alpha(\tau) n_\beta(0)) \rangle - \beta \sum_{\alpha\beta} \langle n_\alpha \rangle \langle n_\beta \rangle. \end{aligned} \quad (5.55)$$

Divided by n^2 , this is identical to the final expression we obtained for the compressibility κ_{imp} from the summation of the impurity generalized susceptibility in (5.52), proving that we can indeed sum the generalized susceptibility of the impurity calculated from its two- and one-particle Green's functions according to (5.47) to get the impurity compressibility $n^{-2} (\partial n / \partial \mu)|_{\Delta=\text{const.}}$.

Bethe-Salpeter equation

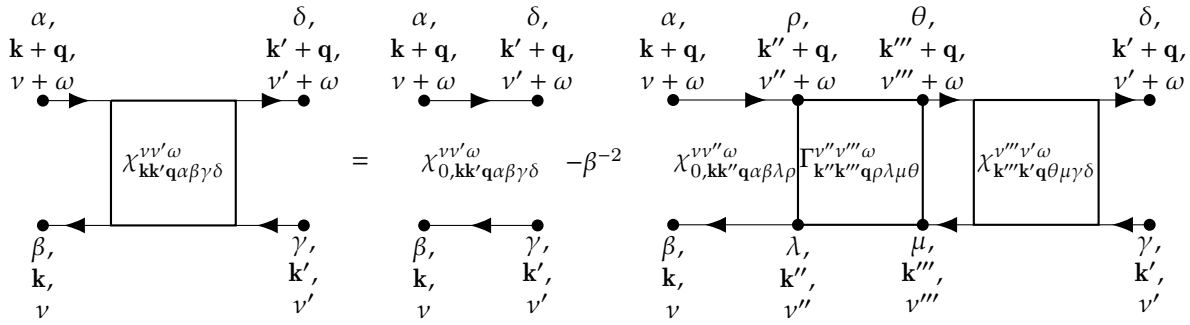


Figure 5.24: Bethe-Salpeter equation (5.56) for the generalized susceptibility χ , bubble part χ_0 and irreducible vertex Γ in the longitudinal particle-hole channel in its most general form for electrons in a lattice expressed in terms of Feynman diagrams. All these quantities are two-particle quantities with four legs, which are marked by dots. Where a quantity shares its right dots with the left dots of another, the corresponding legs are connected, i.e. corresponding indices associated to each of the legs are set equal and the quantities' product summed over all values they can attain. The indices associated with the legs are here combinations of momentum vectors in bold font, combinations of frequencies ν , partially primed, and ω , and other Greek indices for the combinations of remaining quantum numbers, in particular orbitals and spins.

Two-particle Green's functions and with them generalized susceptibilities of the AIM can be calculated using CT-HYB, allowing us to compute the compressibility κ_{imp} of

an independent impurity from two-particle quantities as shown above. We are however actually interested in calculating the lattice compressibility κ , which requires the DMFT result for the uniform generalized susceptibility $\chi_{\mathbf{q}=0}$ of the lattice that describes the charge response of the entire lattice. Similarly to how the self-energy is the quantity establishing the connection between the one-particle Green's function of the lattice and that of the self-consistent impurity in DMFT, the irreducible vertex function is the quantity connecting the two-particle response functions of the lattice and those of the self-consistent impurity [33]. To extract it from the impurity problem and use it in the lattice problem, we need the Bethe-Salpeter equation. Since we need the equations in this section in both contexts, we will for completeness occasionally explicitly write lattice momentum indices like \mathbf{k} and \mathbf{q} . For clarity, we will however often suppress all indices that are not relevant at the considered stage of the derivation, and vectorial momentum indices like \mathbf{k} , \mathbf{k}' , and \mathbf{q} may be restored in any relation by placing them at the same diagrammatic positions as the frequencies ν , ν' , and ω respectively.

The Bethe-Salpeter equation is an equation relating two-particle quantities in a way analogous to how the Dyson equation $G_{\mathbf{k}\alpha\beta}(\nu) = G_{0,\mathbf{k}\alpha\beta}(\nu) + G_{0,\mathbf{k}\alpha\gamma}(\nu)\Sigma_{\mathbf{k}\gamma\delta}(\nu)G_{\mathbf{k}\delta\beta}(\nu)$ relates the full one-particle Green's function G , the non-interacting one-particle Green's function G_0 , and the one-particle irreducible self-energy Σ that represents the essential correction due to interaction without any non-interacting propagation mixed in. When we consider the propagation of two particles, the simplest identifiable contribution at the two-particle level consists of any arbitrary propagation of the individual particles without any interaction between them. The full generalized susceptibility χ contains such *two-particle reducible* contributions, which are diagrams whose parts can be disconnected by removing two single-particle propagators G . The Bethe-Salpeter equation [33, 214]

$$\chi_{\mathbf{k}\mathbf{k}'\mathbf{q}\alpha\beta\gamma\delta}^{\nu\nu'\omega} = \chi_{0,\mathbf{k}\mathbf{k}'\mathbf{q}\alpha\beta\gamma\delta} - \beta^{-2} \sum_{\mathbf{k}''\mathbf{k}'''\nu''\nu'''\lambda\rho\mu\theta} \chi_{0,\mathbf{k}\mathbf{k}''\mathbf{q}\alpha\beta\lambda\rho}^{\nu\nu''\omega} \Gamma_{\mathbf{k}''\mathbf{k}'''\mathbf{q},\rho\lambda\mu\theta}^{\nu''\nu'''\omega} \chi_{\mathbf{k}'''\mathbf{k}'\mathbf{q}\theta\mu\gamma\delta'}^{\nu'''\nu'\omega} \quad (5.56)$$

diagrammatically represented in Fig. 5.24, describes how the full generalizable χ is related to the basic reducible two-particle "bubble" $\chi_{0,\mathbf{k}\mathbf{k}'\mathbf{q}\alpha\beta\gamma\delta}^{\nu\nu'\omega} = -\beta G_{\mathbf{k},\gamma\beta}^{\nu} G_{\mathbf{k}+\mathbf{q},\alpha\delta}^{\nu+\omega} \delta_{\nu\nu'} \delta_{\mathbf{k}\mathbf{k}'}$, named after the circular form of the diagram when its outer legs are contracted, and the two-particle irreducible vertex function $\Gamma_{\mathbf{k}\mathbf{k}'\mathbf{q},\rho\lambda\mu\theta}^{\nu''\nu'''\omega}$, the two-particle analogon of the self-energy. In this expression for the Bethe-Salpeter equation, all quantities take all arguments and indices that are necessary in the context of a lattice, but as previously mentioned we shall suppress all those that are not directly relevant to the considered step in the following and possibly make implicit use of simplifications due to e.g. our

diagonal one-particle Green's functions and spin and orbital degeneracy.

Unlike in the case of the Dyson equation and the self-energy, there are actually multiple Bethe-Salpeter equations and irreducible vertex functions. What we consider here is the Bethe-Salpeter equation in the longitudinal particle-hole channel for the vertex function irreducible in the longitudinal particle-hole channel, which are the most suitable ones for our purposes [33]. Reducibility in different channels distinguishes between the different ways a diagram involving two incoming and two outgoing lines can fall apart when two Green's function lines are cut [214].

Let us interpret the terms of the Bethe-Salpeter equation in the longitudinal particle hole channel as depicted in Fig. 5.24, starting with the full generalized susceptibility $\chi^{vv'\omega}$. In our diagram, its two free right legs correspond to the first two operators and its two left legs correspond to the last two operators of the two-particle Green's function (5.40) it is made of. We can contract the two right legs and two left legs into one vertex each, summing over all internal indices and arguments at the vertices to receive a physical susceptibility as shown in Fig. 5.21. In that case, we have to imagine often not explicitly depicted momentum \mathbf{q} and energy ω flowing into the diagram from the left and leaving to the right [47], otherwise momentum and energy conservation at the vertices would force them to zero.

Considering the explicit form of the Fourier transform of our generalized susceptibility (5.44) into Matsubara frequencies with particle-hole frequency convention (5.45), which is given by (A.8), we see that the summation over the internal indices $\nu, \nu', \mathbf{k}, \mathbf{k}', \alpha = \beta$, and $\delta = \gamma$ will result in several Dirac delta distributions and Kronecker deltas. These in particular send $\tau_1 - \tau_2$ and $\tau_3 - \tau_4$ to zero and thus, in combination with the equality of the other indices, turn the two-particle Green's function contained in χ into a density correlation function of the form $\langle T_\tau n_\alpha(\tau_1, \mathbf{r}_1) n_\delta(\tau_4, \mathbf{r}_4) \rangle$ with the distance $\tau_1 - \tau_4$ in time associated with the free bosonic Matsubara frequency ω and the distance $\mathbf{r}_1 - \mathbf{r}_4$ in space with the free momentum \mathbf{q} . The choice $\omega = 0$ corresponds to the static function integrated over imaginary time difference, which we have already seen to be the right choice for the compressibility before in the derivation of (5.47), and $\mathbf{q} = 0$ to the uniform lattice function summed over all lattice sites. A similar consideration allows us to recognize the reason for the explicit subtraction of the transverse contribution in the definition (5.44) of χ . When its legs are contracted, it turns into an uncorrelated product $G_{\mathbf{k}\alpha\alpha}^\nu G_{\mathbf{k}'\alpha\alpha}^{\nu'} \rightarrow \langle n_\alpha(\tau_1, \mathbf{r}_1) \rangle \langle n_\alpha(\tau_4, \mathbf{r}_4) \rangle$ that is subtracted from the function $\langle T_\tau n_\alpha(\tau_1, \mathbf{r}_1) n_\delta(\tau_4, \mathbf{r}_4) \rangle$ to extract its "correlated part", which is e.g. zero if the correlation function itself can already be decomposed into such a product.

The first term on the right-hand side of the Bethe-Salpeter equation shown in Fig. 5.24 is the bubble contribution $\chi_0^{vv'\omega} = -\beta G_{\mathbf{k},\gamma\beta}^\nu G_{\mathbf{k}+\mathbf{q},\alpha\delta}^{\nu+\omega} \delta_{\nu\nu'} \delta_{\mathbf{k}\mathbf{k}'}$, which is reducible in the particle-hole channel and turns into a product of the form $\langle T_\tau c_\alpha^\dagger(\tau_1, \mathbf{r}_1) c_\alpha(\tau_4, \mathbf{r}_4) \rangle^2$ on

contraction. The other contribution is a χ_0 -like product of two Green's functions attached to the left vertices of the irreducible vertex $\Gamma^{v''v'''\omega}$ that includes all propagation processes irreducible in the particle-hole channel connected to the full generalized susceptibility $\chi^{vv'\omega}$ itself to its left. Like in the case of the Dyson equation, the repeated insertion of the Bethe-Salpeter expression for $\chi^{vv'\omega}$ into the second term of its right-hand side leads to a "ladder" decomposition (where the χ_0 and parallel edges of Γ in the diagram look like the rails and the orthogonal edges of Γ like the rungs of a ladder) containing all contributions from chains containing any number of irreducible $\Gamma^{v''v'''\omega}$ blocks linked by and surrounded by insertions of the reducible χ_0 [33].

Due to the separate summations over internal indices at each vertex where multiple legs are contracted, it is clear that the Bethe-Salpeter equations for different elements of χ are in general coupled. By taking symmetries into account [214], we can decompose the Bethe-Salpeter equation for the full matrix quantities χ and Γ into several equations for the actually coupled blocks.

We begin by considering the spin indices. Due to $SU(2)$ -symmetry and the implied spin conservation, only the three spin index combinations $\uparrow\uparrow = \uparrow\uparrow\uparrow\uparrow$, $\uparrow\downarrow = \uparrow\uparrow\downarrow\downarrow$, $\overline{\uparrow\downarrow} = \uparrow\downarrow\downarrow\uparrow$ are non-zero and independent [214, 495], and crossing symmetry could additionally provide a relation between the latter two. In case we use the density-density form of the interaction, which is the only one we consider in the following, our system is not actually symmetric under arbitrary $SU(2)$ transformations. The preceding properties follow from S_z being a good quantum number and from the consideration of a simultaneous flip of all spin indices, which do however still apply. Since we are interested in the charge compressibility and phases related to paramagnetic Mott metal-insulator and metal-metal transitions and do not want to consider any magnetic phenomena, we only need to consider their density combination $x_d = x_{\uparrow\uparrow} + x_{\uparrow\downarrow}$. Because $\Gamma_{\uparrow\uparrow} = \Gamma_{\downarrow\downarrow}$, $\Gamma_{\uparrow\downarrow} = \Gamma_{\downarrow\uparrow}$ and the same relations hold for the elements of χ as well, the Bethe-Salpeter equation for the "density channel" quantities reduces to

$$\begin{aligned}
\chi_d(v, v', \omega) &= \chi_{\uparrow\uparrow}^{vv'\omega} + \chi_{\uparrow\downarrow}^{vv'\omega} && (\Gamma\chi)_{\uparrow\uparrow}^{vv'\omega} && (5.57) \\
&= \chi_{0,\uparrow\uparrow}^{vv'\omega} - \beta^{-2} \chi_{0,\uparrow\uparrow}^{vv\omega} \left(\sum_{v''} \Gamma_{\uparrow\uparrow}^{vv''\omega} \chi_{\uparrow\uparrow}^{v''v'\omega} + \sum_{v''} \Gamma_{\uparrow\downarrow}^{vv''\omega} \chi_{\downarrow\uparrow}^{v''v'\omega} \right) \\
&\quad + \chi_{0,\uparrow\downarrow}^{vv'\omega} - \beta^{-2} \chi_{0,\uparrow\uparrow}^{vv\omega} \left(\sum_{v''} \Gamma_{\uparrow\uparrow}^{vv''\omega} \chi_{\uparrow\downarrow}^{v''v'\omega} + \sum_{v''} \Gamma_{\uparrow\downarrow}^{vv''\omega} \chi_{\downarrow\downarrow}^{v''v'\omega} \right) \\
&= \chi_{0,d}(v, v', \omega) && (\Gamma\chi)_{\uparrow\downarrow}^{vv'\omega} \\
&\quad - \beta^{-2} \sum_{v''} \chi_{0,d}(v, v, \omega) \Gamma_d(v, v'', \omega) \chi_d(v'', v', \omega),
\end{aligned}$$

which is decoupled from the equations for the other spin index combinations and where some zero terms in the intermediate steps were left out for clarity. For the density channel of the generalized susceptibility of the impurity, we calculate $\chi_{\text{imp},d} = (\chi_{\text{imp},\uparrow\uparrow} + \chi_{\text{imp},\uparrow\downarrow} + \chi_{\text{imp},\downarrow\uparrow} + \chi_{\text{imp},\downarrow\downarrow})/2$ in practice to make efficient use of the available QMC results, which are not exactly symmetric due to the stochastic nature of the method. From here on, we shall assume that density channel combinations are handled if the spin indices of a two-particle quantity are not given explicitly, and where they do not appear in the expression for a one-particle quantity a spin-diagonal element is implied (as the diagonal elements are equal due to symmetry and the off-diagonals zero).

For the orbital indices, we can proceed analogously [497]. Since we give indices of four-legged objects in anticlockwise order starting from top left, matrices of the structure

$$\mathbf{\Gamma} = \begin{pmatrix} \Gamma_{1111} & \Gamma_{1122} & \Gamma_{1121} & \Gamma_{1112} \\ \Gamma_{2211} & \Gamma_{2222} & \Gamma_{2221} & \Gamma_{2212} \\ \Gamma_{1211} & \Gamma_{1222} & \Gamma_{1221} & \Gamma_{1212} \\ \Gamma_{2111} & \Gamma_{2122} & \Gamma_{2121} & \Gamma_{2112} \end{pmatrix}, \quad (5.58)$$

allow us to write expressions corresponding to ladder diagrams in the longitudinal particle-hole channel [214] extending in left-right direction as matrix products. The first two orbital indices change with the row and the last two with the column. However, the order of index combinations for rows and columns is chosen differently. Specifically, the two individual indices for row i must be swapped compared to those for column i , which is exemplified by elements such as Γ_{1221} in the third row and third column. In this way, the summation for the matrix product causes the indices of the right legs of the first factor and the left legs of the second factor to match as demanded by the diagram. This peculiar ordering is necessary because we assign indices in anticlockwise order to the legs of both factors. This means that we give the index of the lower leg first on the right side (mapped to column) of a two-particle quantity, but that of the upper leg first on its left side (mapped to row).

Using such matrices for the irreducible vertex $\mathbf{\Gamma}$, the generalized susceptibility χ and its bubble part χ_0 , the Bethe-Salpeter equation with orbital indices can explicitly be written as the matrix equation

$$\chi = \chi_0 - \beta^{-2} \chi_0 \mathbf{\Gamma} \chi. \quad (5.59)$$

Due to the structure of our interaction, all elements with an orbital index that occurs an odd number of times are zero. The matrix equation thus decouples into separate equations for the upper left diagonal 2×2 -block, which we shall call the “orbital-

longitudinal" channel, and the lower right diagonal 2×2 -block, which we shall call the "orbital-transverse" channel [497]. For the case of density-density interaction that we exclusively consider in the following, the non-zero index patterns are in fact exactly the same as for the spin dimensions, i.e. of the transverse block only the \overline{ab} -elements remain using the usual index abbreviations $ab = aabb$ and $\overline{ab} = abba$. The explicit expressions for the longitudinal blocks are then

$$\Gamma_{\parallel} = \begin{pmatrix} \Gamma_{11} & \Gamma_{12} \\ \Gamma_{21} & \Gamma_{22} \end{pmatrix}, \quad \chi_{\parallel} = \begin{pmatrix} \chi_{11} & \chi_{12} \\ \chi_{21} & \chi_{22} \end{pmatrix}, \quad \chi_{0,\parallel} = -\beta \begin{pmatrix} G_{11}G_{11} & 0 \\ 0 & G_{22}G_{22} \end{pmatrix}, \quad (5.60)$$

and those for the transverse blocks

$$\Gamma_{\perp} = \begin{pmatrix} \Gamma_{\overline{12}} & 0 \\ 0 & \Gamma_{\overline{21}} \end{pmatrix}, \quad \chi_{\perp} = \begin{pmatrix} \chi_{\overline{12}} & 0 \\ 0 & \chi_{\overline{21}} \end{pmatrix}, \quad \chi_{0,\perp} = -\beta \begin{pmatrix} G_{11}G_{22} & 0 \\ 0 & G_{22}G_{11} \end{pmatrix}. \quad (5.61)$$

Two-particle lattice quantities in DMFT

The equations of DMFT establish relations between quantities of the lattice of interest and quantities of the auxiliary AIM. On the one-particle level, the self-consistent solution is characterized by the equality of the impurity Green's function $G_{\text{imp}}(i\omega_n)$ and the local Green's function $G_{\text{loc}}(i\omega_n) = \int \frac{D(E)}{i\omega_n + \mu - \Sigma_{\text{imp}}(i\omega_n) - E} dE$ of the lattice, where $D(E)$ is the density of states of the lattice and $\Sigma_{\text{imp}}(i\omega_n)$ the purely local self-energy of the impurity model. CT-HYB allows us only to calculate the correlation functions of the auxiliary AIM directly, which can be used to compute the impurity self-energy Σ_{imp} and impurity generalized susceptibility χ_{imp} according to the definitions (2.13) and (5.46). Let us consider how we can use this data to get access to the uniform susceptibility $\chi_{q=0}$ of the *lattice* that is actually relevant to the extremal behavior of the lattice compressibility of interest to us. We follow the discussion of response functions in DMFT given in Ref. [33].

Power counting in the limit of infinite coordination number in the contributions to the irreducible vertex function $\Gamma_{\mathbf{k}\mathbf{k}'\mathbf{q}\alpha\beta\gamma\delta}^{vv'\omega}$ of the lattice proves that when all its vertices are summed over and may thus be considered internal, such as in the ladder sums of two-particle quantities in the Bethe-Salpeter equation, it can be replaced by the purely local vertex function $\Gamma_{\text{imp},\alpha\beta\gamma\delta}^{vv'\omega}$ of the impurity [33, 468]. Apart from the restriction to summations, this is the two-particle analogon of the self-energy [123]. Note that while the self-consistency equations directly ensure the equality of the impurity and local lattice Green's functions $G_{\text{imp}} = G_{\text{loc}}$ even when DMFT is used as an approximation for finite dimensions, this is in general not the case for χ_{loc} . The susceptibility of the impurity $\chi_{\text{imp},\alpha\beta\gamma\delta}$ is e.g. not equal to the local susceptibility of the lattice $\chi_{\text{loc},\alpha\beta\gamma\delta} =$

$\sum_{\mathbf{q}} \chi_{\mathbf{q}\alpha\beta\gamma\delta}$ in finite dimensions, and replacing the irreducible vertex function of the lattice $\Gamma_{\mathbf{k}\mathbf{k}'\mathbf{q}\alpha\beta\gamma\delta}^{vv'\omega}$ by a local quantity constitutes an *additional* approximation in the finite-dimensional case [33]. In infinite dimensions however, DMFT is *exact*, so the equality between impurity and local lattice quantity holds.

In order to get to the irreducible vertex function of the impurity, it is first necessary to calculate the full generalized susceptibility of the impurity according to (5.46) and the bubble $\chi_{\text{imp},0\alpha\beta\gamma\delta}^{vv'\omega} = -\beta G_{\text{imp},\gamma\beta}^v G_{\text{imp},\alpha\delta}^{v+\omega} \delta_{vv'}$ from the Green's functions calculated by CT-HYB as input for the Bethe-Salpeter equation for the impurity

$$\begin{aligned}\chi &= \chi_0 - \beta^{-2} \chi_0 \Gamma \chi \\ \Gamma &= \beta^2 (\chi^{-1} - \chi_0^{-1}),\end{aligned}\tag{5.62}$$

which we solve for the irreducible vertex function of the impurity. Since we can use this purely local quantity as vertex function in the Bethe-Salpeter equation for the lattice, where we specifically care about the uniform case $\mathbf{q} = 0$, we can skip intermediate steps by directly equating the differences of inverted susceptibilities and obtaining

$$\chi_{\mathbf{q}=0}^{-1} = \chi_{\text{imp}}^{-1} - \chi_{0,\text{imp}}^{-1} + \chi_{0,\mathbf{q}=0}^{-1}.\tag{5.63}$$

This is an expression for the uniform generalized susceptibility of the lattice that can be computed using quantities of the impurity model only [33].

It is possible to further evaluate the bubble terms in a way that leads to a very simple result for DMFT on the Bethe lattice in particular [33], which is the case we consider. To do so, we express them in terms of the Hilbert transform $\tilde{D}(x) := \int \frac{D(E)}{x-E} dE$ of the density of states first, which for the impurity bubble as product of two local Green's functions trivially yields [33]

$$\chi_{0,\text{imp},abba}^{vv'\omega} = -\beta \delta_{vv'} \tilde{D}(\zeta_{aa,v+\omega}) \tilde{D}(\zeta_{bb,v})\tag{5.64}$$

using the DMFT self-consistency condition with $\zeta_{ab,v} := iv + \mu - \Sigma_{\text{imp},ab}(v)$. For the lattice bubble, due to the summation $\sum_{\mathbf{k}\mathbf{k}'} \chi_{0,\mathbf{k}\mathbf{k}'\mathbf{q},abba}^{vv'\omega} = -\beta \sum_{\mathbf{k}} G_{\mathbf{k}+\mathbf{q},aa}^{v+\omega} G_{\mathbf{k},bb}^v$ over the Green's functions' momentum indices or the equivalent integral

$$\chi_{0,\mathbf{q}=0,abba}^{vv'\omega} = -\beta \delta_{vv'} \int \frac{D(E)}{(\zeta_{aa,v+\omega} - E)(\zeta_{bb,v} - E)} dE,\tag{5.65}$$

which can not directly be written as a product of Hilbert transformations, we additionally need to perform a partial fraction decomposition of the integrand. In this way, we

obtain [33]

$$\begin{aligned}\chi_{0,\mathbf{q}=0,abba}^{vv'\omega} &= \beta\delta_{vv'} \int \frac{D(E)}{\zeta_{aa,v+\omega} - \zeta_{bb,v}} \left(\frac{1}{\zeta_{aa,v+\omega} - E} - \frac{1}{\zeta_{bb,v} - E} \right) dE \\ &= \beta\delta_{vv'} \frac{\tilde{D}(\zeta_{aa,v+\omega}) - \tilde{D}(\zeta_{bb,v})}{\zeta_{aa,v+\omega} - \zeta_{bb,v}},\end{aligned}\quad (5.66)$$

a difference of two Hilbert transforms, which further gives the expression $\chi_{0,\mathbf{q}=0,aaaa}^{vv'\omega=0} = \beta\delta_{vv'} \tilde{D}'(\zeta_{aa,v})$ for the special case of four equal orbital indices and a static quantity, which we concretely interpret as the limit $\omega \rightarrow 0$ here, by identifying the limit as an expression for the derivative.

Since only the static uniform $\omega = 0, \mathbf{q} = 0$ case is relevant for the lattice compressibility, the latter case directly applies to the orbital-longitudinal part (5.60), for which the relation between impurity and lattice susceptibility (5.63) takes the form

$$\begin{aligned}(\chi_{\parallel,\mathbf{q}=0}^{-1})^{vv'\omega=0} &= (\chi_{\parallel,\text{imp}}^{-1})^{vv'\omega=0} + \beta^{-1}\delta_{vv'}\delta_{ab} \left(\frac{1}{\tilde{D}^2(\zeta_{aa,v})} + \frac{1}{\tilde{D}'(\zeta_{aa,v})} \right) \\ &= (\chi_{\parallel,\text{imp}}^{-1})^{vv'\omega=0} + t^2\beta^{-1}\delta_{vv'}\delta_{ab},\end{aligned}\quad (5.67)$$

where we used the analytical form $R(\tilde{D}(\zeta)) = t^2\tilde{D}(\zeta) + (\tilde{D}(\zeta))^{-1} = \zeta$ of the inverse Hilbert transform for the Bethe lattice [33] and the rule for differentiation of inverse functions, $\tilde{D}'(\zeta) = (R'(\tilde{D}(\zeta)))^{-1} = (t^2 - \tilde{D}^{-2}(\zeta))^{-1}$, with the hopping t on the Bethe lattice equal to one quarter of its bandwidth [33].

For the diagonal orbital-transverse part (5.60), we have the same result

$$\begin{aligned}(\chi_{\perp,\mathbf{q}=0}^{-1})^{vv'\omega=0} &= (\chi_{\perp,\text{imp}}^{-1})^{vv'\omega=0} + \beta^{-1}\delta_{vv'} \left(\frac{1}{\tilde{D}(\zeta_{aa,v})\tilde{D}(\zeta_{bb,v})} + \frac{\zeta_{aa,v} - \zeta_{bb,v}}{\tilde{D}(\zeta_{aa,v}) - \tilde{D}(\zeta_{bb,v})} \right) \\ &= (\chi_{\perp,\text{imp}}^{-1})^{vv'\omega=0} + t^2\beta^{-1}\delta_{vv'},\end{aligned}\quad (5.68)$$

for the diagonals, where however $a \neq b$ in this case, using the analytical form $\tilde{D}(\zeta) = \frac{\zeta - \sqrt{\zeta^2 - 4t^2}}{2t^2}$ of the Hilbert transform for the Bethe lattice with hopping t equal to one quarter of its bandwidth [33]. One can verify this identity by converting both fractions to a common denominator and multiplying out all expressions in the numerator and denominator, which in particular also includes the squares of the square roots in the latter case.

Spectral representation of generalized susceptibilities

A zero eigenvalue of a generalized susceptibility is associated with a divergence of the associated vertex function [470, 479] and a divergent eigenvalue with a divergence of the susceptibility itself [491]. Both are of course connected to the behavior of physical susceptibilities [215, 467, 469, 491], so for our analysis in the vicinity of the critical point of the lattice problem where the lattice compressibility diverges, we would like to consider the behavior of the eigenvalues of the uniform generalized susceptibility of the lattice. Usually this would mean bringing it into its spectral representation by diagonalizing it and rewriting it as sum of contributions in its eigenbasis, or in general by performing a singular vector decomposition if it is not symmetric enough to guarantee diagonalizability [479]. We will however see that using the relations (5.67) and (5.68) between the uniform generalized susceptibility of the Bethe lattice and the impurity generalized susceptibility, we can derive a simple relation between their eigenvalues. For our purposes it is thus never necessary to explicitly diagonalize or even calculate a generalized susceptibility of the lattice. Numerically we only handle generalized susceptibilities of the auxiliary impurity model and their eigenvalues, and our conclusions about lattice quantities and their eigenvalues only follow from the impurity quantities through the relations we derive.

For a model with only one orbital, we can consider a static generalized susceptibility as matrix with respect to its two fermionic Matsubara frequency as dimensions [491]. In our case of a two- or generally multi-orbital model, even the static generalized susceptibility still has orbital dimensions in addition to the Matsubara frequencies. In this case, two of the four orbital dimensions can be combined with each of the two Matsubara frequency dimensions to obtain a two-dimensional object for diagonalization. Exploiting the decoupling of the susceptibility with orbital dimensions into orbital-longitudinal and orbital-transverse parts reduces the size of the matrix blocks that need to be numerically diagonalized enabling considerable reduction of computing time due to the scaling of diagonalization with the third power of the matrix dimension [498].

Given a matrix \mathbf{S} with the eigenvectors $\{\mathbf{v}_1, \dots, \mathbf{v}_n\}$ of $\chi^{\nu\nu'}$ as its columns, where ν and ν' may be combined indices for one fermionic Matsubara and two orbital dimensions each, the diagonal matrix λ with the eigenvalues $\{\lambda_1, \dots, \lambda_n\}$ of $\chi^{\nu\nu'}$ on its diagonal can be expressed as the product $\lambda = \mathbf{S}^{-1}\chi\mathbf{S}$. Conversely, the generalized susceptibility can then be expressed as $\chi = \mathbf{S}\lambda\mathbf{S}^{-1}$. The relation between the compressibility κ of the lattice and the static uniform generalized susceptibility of the lattice the uniform lattice generalized susceptibility $\chi_{\mathbf{q}=0}^{\omega=0}$, analogous to the equation (5.47) for the

corresponding impurity quantities, can thus be rewritten as

$$\begin{aligned}\kappa &= \frac{1}{n^2\beta^2} \sum_{vv'\alpha\beta} \chi_{\mathbf{q}=0,\alpha\alpha\beta\beta}^{vv'\omega=0} = \frac{2}{n^2\beta^2} \sum_{vv'ab} \chi_{\mathbf{q}=0,d,aabb}^{vv'\omega=0} \\ &= \frac{2}{n^2\beta^2} \sum_{abcd} S_{ab} \lambda_{\mathbf{q}=0,b} \delta_{bc} (S^{-1})_{cd} = \frac{2}{n^2\beta^2} \sum_{abd} (\mathbf{v}_b)_a \lambda_{\mathbf{q}=0,b} (\mathbf{v}_b^{-1})_d = \frac{2}{n^2\beta^2} \sum_b \lambda_{\mathbf{q}=0,b} w_b,\end{aligned}\quad (5.69)$$

where the vectors $\{\mathbf{v}_1^{-1}, \dots, \mathbf{v}_n^{-1}\}$ are the rows of the inverse \mathbf{S}^{-1} of the eigenvector matrix \mathbf{S} and we identify the weight w_b of the contribution to the electronic compressibility associated with a particular eigenvalue $\lambda_{\mathbf{q}=0,b}$ of the static uniform generalized susceptibility as $w_b = \left(\sum_a (\mathbf{v}_b)_a\right) \left(\sum_a (\mathbf{v}_b^{-1})_a\right)$. Due to the pairing of orbital indices in the summation for the compressibility, it is only the orbital-longitudinal part (5.60) of the static uniform generalized susceptibility of the lattice that contributes here, and due to the spin summation over all rather than just the density channel combinations a factor of 2 enters. According to (5.67), the inverse generalized susceptibility of the impurity becomes the inverse generalized susceptibility of the Bethe lattice by addition of a term proportional to a unit matrix in Matsubara frequencies. We therefore only need to perform the diagonalization of the generalized susceptibility of the impurity, which we get relatively directly from CT-HYB results, and can obtain the eigenvalues of the static uniform lattice quantity using

$$\lambda_{\mathbf{q}=0,b} = \left(\lambda_{\text{imp},b}^{-1} + \frac{t^2}{\beta} \right)^{-1}. \quad (5.70)$$

The eigenvectors remain the same, and from this formula we can derive the condition that the static uniform lattice susceptibility diverges when an eigenvalue of the impurity susceptibility reaches the value $-\beta/t^2$. In the following text and figures all explicit numerical results for eigenvalues will be for eigenvalues $\lambda_{\text{imp},b}$ of generalized susceptibilities of the impurity, and any properties of eigenvalues of generalized susceptibilities of the lattice that we discuss or interpret follow exclusively from the impurity eigenvalues through the relation (5.70).

5.2.3 Compressibility enhancement and divergence in the two-orbital Hubbard model

Using the DMFT results for the degenerate two-orbital Hubbard model on a Bethe lattice calculated as described in Sec. 5.1.1, we can estimate the lattice compressibility $\kappa(\mu) = \frac{1}{n^2} \frac{\partial n}{\partial \mu}(\mu)$ using finite difference quotients for a non-uniform grid of accuracy order two as implemented in Ref. [499]. In this way, the derivative at a given chemical

potential μ is approximated using the data point for that chemical potential and the two points around it where possible, or, at the boundaries of the range, two points toward the interior of the range. In cases with only a crossover, we simply apply this procedure to the entire data range at once. In cases with a phase transition however, we apply this procedure separately to each of the two stable and the one unstable branches, such that the curve is divided into individually handled segments where $n(\mu)$ is a proper single-valued function.

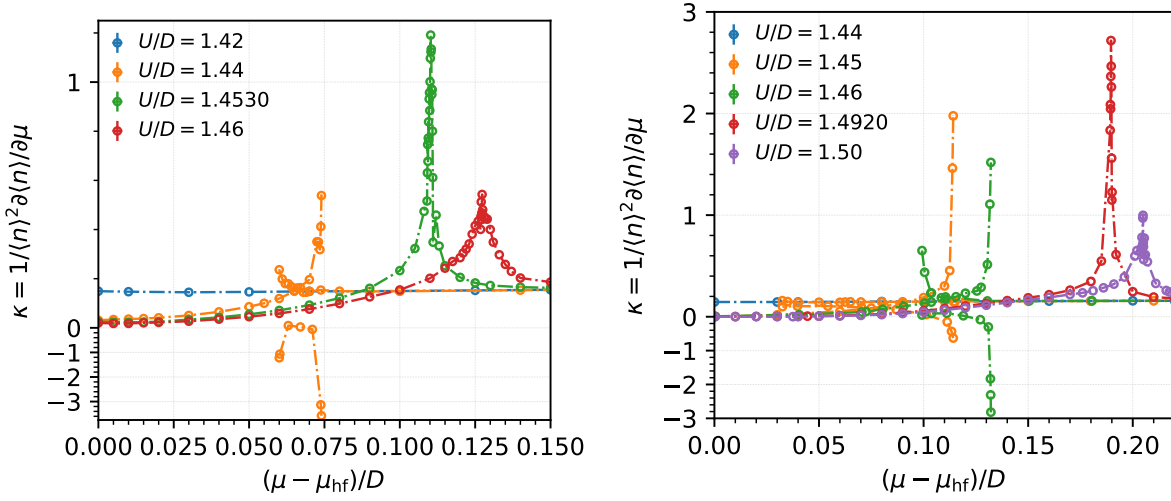


Figure 5.25: Calculation of difference quotients as estimates of the electronic compressibility $\kappa(\mu) = \frac{1}{n^2} \frac{\partial n}{\partial \mu}(\mu)$ of the two-orbital Hubbard model with density-density interaction on the Bethe lattice solved with DMFT. We show curves for various interaction strengths U at two temperatures (left: $\beta D = 35$, right: $\beta D = 50$) as a function of the chemical potential μ relative to its value at half-filling μ_{hf} .

The estimated compressibilities for temperatures $\beta D = 35$ and $\beta D = 50$ are shown in Fig. 5.25 and the corresponding $n(\mu)$ curves were shown in Figs. 5.15 and 5.12. In the case of the metallic branches starting from half-filling at the smallest interaction strengths U , the compressibilities are visually constant at this scale and the numerical data indicates a slight but systematic increase with μ . At the two largest interaction strengths shown for each temperature, we are in the crossover region with clearly visible peaks of the compressibility with a height that increases as we approach the critical point by reducing the interaction strength.

In the phase transition cases, which are the remaining ones at intermediate interaction strengths, strong single-sided enhancements are visible at the ends of each of the metastable solutions, where a further in- or decrease of μ would cause a jump to the other stable solution. In some of the cases, such as the lower μ phase boundary at $\beta = 50, U = 1.45$, the enhancements are comparably small, which stems from the fact

that both the weakly correlated metastable and the unstable branch approach the actual turning point of the curve, where the two branches meet, almost linearly for a comparatively long stretch. This makes the section of the curve around the turning point, where we find the divergence and around it the largest enhancements, much sharper and an enhancement more difficult to resolve with numerical QMC-DMFT data points than in the other cases. For the phase transition cases, the plots show not only the compressibility on the stable branches, which are those two curves per interaction strength U that are always positive, go up to one of the shown ends of the domain each and overlap for a part around the middle, but also the compressibility on the unstable branch, which is one additional curve per interaction strength whose domain is that segment of chemical potential in the middle where the other two compressibility curves overlap. Towards the ends of its domain, it takes on particularly small negative values, i.e. such of particularly large magnitude, mirroring the enhancements visible at the end of the stable branches, while it attains a maximum somewhere in the middle of its domain. In all the cases we show and calculated, that maximum has a positive value of κ , i.e. the compressibility by itself is not even a sufficient criterion for the instability there, but at interaction strength values closer to the upper end of the phase separation region the $n(\mu)$ curves should be less stretched with compressibilities of the unstable branches negative on their entire domain, as seen in two of the NRG-DMFT curves in Fig. 5.12.

From the general shape of the $n(\mu)$ curves shown in Figs. 5.15 and 5.12, this behavior of the compressibility is exactly what we should expect. For an interaction strength low enough to start with a weakly correlated solution at half-filling, the occupation is almost linearly dependent on the chemical potential, reflected in the nearly constant compressibility. In the cases with a crossover, the compressibility is nearly zero at the Mott plateau around half-filling and then increases rapidly with increasing μ up to its maximum at the inflection point after which it drops again as the $n(\mu)$ curve approaches the nearly linear behavior that it has in the weakly correlated metallic phase further away from half-filling. In the cases with a phase transition, when we follow the curve starting from half-filling we first have a strongly interacting branch, but rather than smoothly crossing over into a stable weakly interacting branch, it becomes metastable at some μ (where phase separation happens and the system in stable equilibrium follows the Maxwell construction, cf. Fig. 5.13) and ceases to exist at even higher μ . Assuming that we are taking the necessary measures to follow unstable branches in DMFT described previously, the metastable branches at their ends continuously transition into the unstable branch. However, this branch connects the ends of both metastable branches and the end of the high- μ weakly correlated branch is at lower μ than that of the low- μ strongly correlated one, so as we follow the curve from a metastable branch onto the unstable one, its direction along the μ -axis changes. If the curve is continuously differen-

tiable in that point, the compressibility diverges, which we can deduce by considering derivatives along the curve length variable s : the change of direction in μ corresponds to $d\mu/ds = 0$, such that $dn/d\mu = (dn/ds)(ds/d\mu) \rightarrow \infty$. Considering the formula (5.69) we found for the compressibility in terms of the eigenvalues of the (static) uniform generalized susceptibility $\chi_{\mathbf{q}=0}^{\omega=0}$ of the lattice, this quantity diverges when one of its eigenvalues with non-zero associated weight diverges, which according to (5.70) is exactly then the case when an eigenvalue of the (static) generalized susceptibility of the impurity $\chi_{\text{imp}}^{\omega=0}$ reaches the value $-\beta/t^2$.

In order to check for this condition, we perform CT-HYB using worm sampling [74, 492–494] to calculate the impurity two-particle Green’s function as implemented in *w2dynamics* [40]. As input data we use the converged DMFT self-energies from the points closest to the compressibility peaks in the crossover cases and in cases with a phase transition, for lack of a clear distinguishing criterion, from some points close to the transition region, preferably multiple ones on multiple branches for comparison. Using the newly calculated impurity two-particle Green’s functions and the local Green’s functions from the converged DMFT solutions, we calculate the impurity generalized susceptibility using (5.46) and diagonalize its orbital-longitudinal and transverse blocks, cf. (5.60) and (5.61), of the density combination of spins (5.57) to obtain eigenvectors and eigenvalues. According to (5.70), which follows from (5.67) and (5.68), the eigenvalues of the generalized susceptibility of the impurity we get in this way are related to the eigenvalues of the uniform generalized susceptibility of the lattice by inversion, addition of t^2/β to the inverse, and inversion of the result of the addition.

We plot the lowest eigenvalues λ_I of the generalized susceptibility χ_{imp} of the impurity together with linear fits, difference quotient estimations of the lattice compressibility κ with inverse function fits, and the $n(\mu)$ curve plots with markers indicating some of the position where two-particle calculations were performed in Fig. 5.26 for temperature $\beta D = 35$ and in Fig. 5.27 for $\beta D = 50$. The numerical results confirms that the scenario of a diverging eigenvalue of the uniform lattice compressibility $\chi_{\mathbf{q}=0}$ applies here, corresponding to an eigenvalue $\lambda_I = -\beta/t^2$ of χ_{imp} . As we go toward the critical point along the crossover line (cf. Fig. 5.11), for which our compressibility peak positions can be used as one possible proxy, the lowest eigenvalue of the generalized susceptibility χ_{imp} of the impurity gets closer to $-\beta/t^2$ approximately linearly with $U - U_{\text{CP}}$. At the same time, the compressibility κ estimated via difference quotient (to establish an independent reference value) even approximately follows the form of an inverse function with a single first-order pole at the interaction strength value of the critical point for the given temperature, which is just what we would expect if only the contribution of the lowest eigenvalue λ_I is relevant and its weight constant.

Let us consider the contributions to the electronic compressibility κ of the lattice per

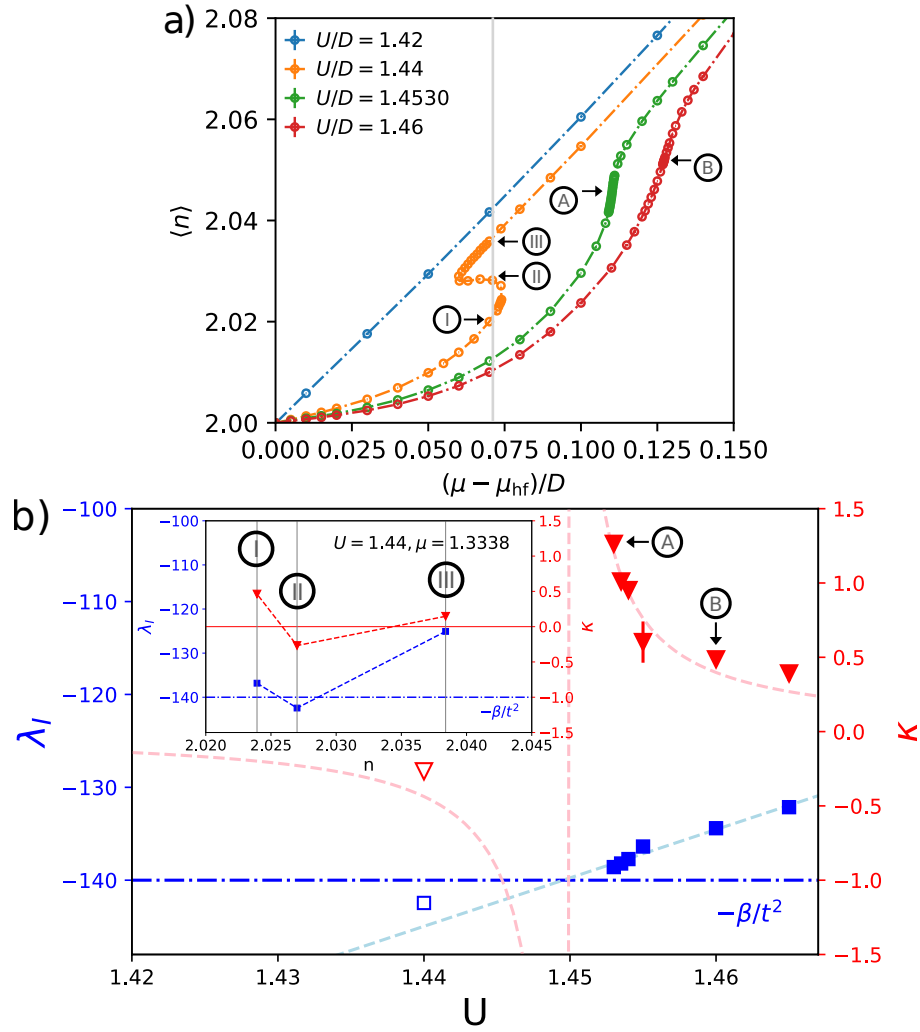


Figure 5.26: Analysis of eigenvalues of χ_{imp} along the crossover line for the two-orbital Hubbard model at $\beta D = 35$. Panel a: $n(\mu)$ curve with points used for two-particle calculations marked (when full curves shown) Panel b: Lowest eigenvalues λ_I of the generalized impurity susceptibility χ_{imp} (blue squares) with linear fit and compressibilities κ estimated via difference quotient (red triangles) with inverse fit. The condition $\lambda_I = -\beta/t^2$ for a divergence of the corresponding eigenvalue of the uniform lattice susceptibility $\chi_{q=0}$ is marked by a horizontal line, the compressibility pole is where the impurity eigenvalue λ_I reaches it. Inset: eigenvalues and compressibilities in a phase transition case of $U/D = 1.44$ for fixed arbitrary $\mu = 1.3338$ on all three branches, with eigenvalue below divergence condition only on the unstable branch. Unstable branch values in main plot for comparison as unfilled points.

eigenvalue of χ_{imp} as shown in Fig. 5.28 for points along the crossover. The contribution associated to an eigenvalue λ_{imp} of χ_{imp} is to be understood as the term in (5.69) associated with the corresponding eigenvalue $\lambda_{q=0}$ of $\chi_{q=0}$ computed via (5.70). We find

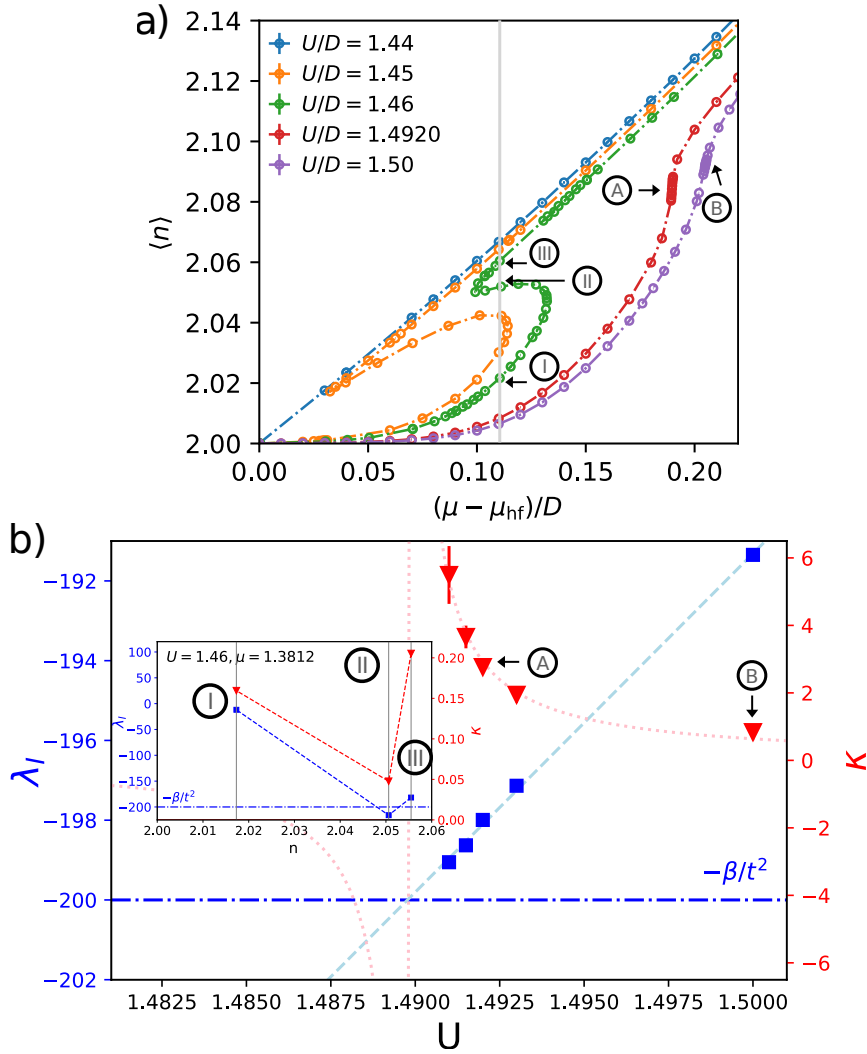


Figure 5.27: Analysis of eigenvalues of χ_{imp} along the crossover line for the two-orbital Hubbard model at $\beta D = 50$. Panel a: $n(\mu)$ curve with points used for two-particle calculations marked (when full curves shown) Panel b: Lowest eigenvalues λ_I of the generalized impurity susceptibility χ_{imp} (blue squares) with linear fit and compressibilities κ estimated via difference quotient (red triangles) with inverse fit. The condition $\lambda_I = -\beta/t^2$ for a divergence of the corresponding eigenvalue of the uniform lattice susceptibility $\chi_{q=0}$ is marked by a horizontal line, the compressibility pole is where the impurity eigenvalue λ_I reaches it. Inset: impurity eigenvalues and compressibilities in a phase transition case of $U/D = 1.46$ for fixed arbitrary $\mu = 1.3812$ on all three branches, with eigenvalue below divergence condition only on the unstable branch.

that in the entire region of interaction values shown for the fits of κ in Figs. 5.26 and 5.27, the by far largest contribution is indeed that of the lowest eigenvalue, and that the total sum matches the values previously estimated by difference quotients well. Since our generalized susceptibility matrices are not real bisymmetric as in the case

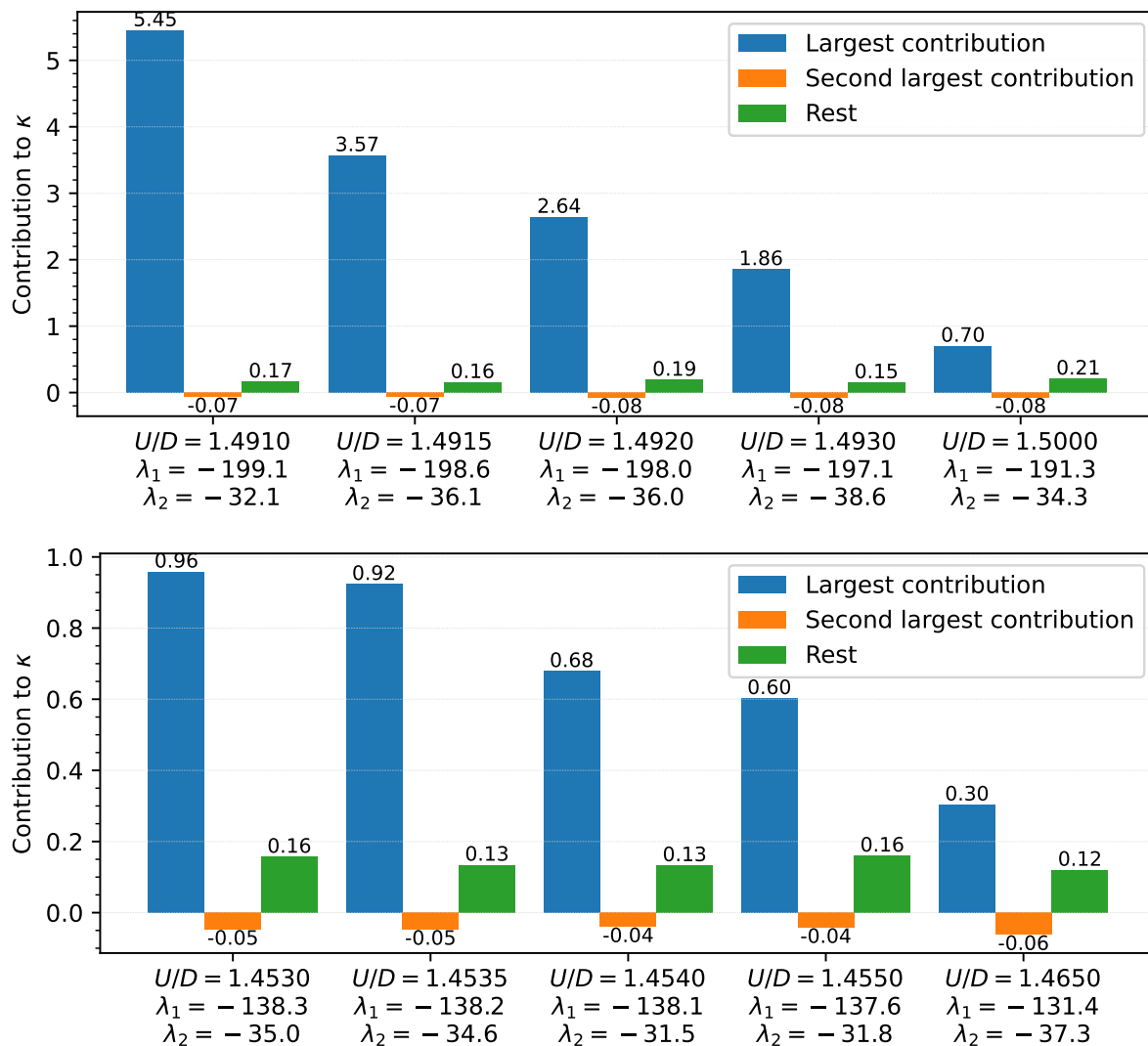


Figure 5.28: Contributions to lattice compressibility κ per eigenvalue of χ_{imp} for points along the crossover line for (top panel) $\beta D = 50$, cf. Fig. 5.27 and (bottom panel) $\beta D = 35$, cf. Fig. 5.26. The two largest contributions in these cases also belong to the two smallest eigenvalues λ_1 and λ_2 , whose values are given in the tick labels.

with particle-hole symmetry [467, 491], but only centrohermitian [491], the eigenvalue-associated weights are just real but not necessarily positive [491, 500]. The remaining contributions could therefore partially cancel each other, so we also separately consider the second largest contribution for comparison to verify that the remaining contributions are indeed individually smaller than the largest one. In all these cases, the second largest contribution is also that of the second-lowest eigenvalue, always negative and has a magnitude of at most one fifth down to about one eightieth of that of the largest eigenvalue. Further, we can observe that apart from the contribution of the lowest

eigenvalue that strongly increases as we go to the critical point, the second largest contribution as well as the sum of remaining contributions remain approximately constant as we move along the crossover line. This further confirms that the divergence of the compressibility is caused by the divergence of the contribution associated to the lowest eigenvalue of the generalized susceptibility of the impurity, as it was previously found in a one-orbital model in Ref. [491].

So far, we have only approached the critical point from the crossover region and thus considered the lattice compressibility contributions for stable phases only, finding the largest contribution associated with the lowest eigenvalue of χ_{imp} positive and diverging as the eigenvalue approaches $-\beta/t^2$. Let us now observe how the contribution structure changes for solutions at an interaction strength with a phase transition as function of μ , particularly on the unstable branch. In Fig. 5.29, we examine contributions per eigenvalue again, but consider multiple solutions for the same temperature $\beta D = 50$ and interaction $U/D = 1.46$, a case in which a first-order phase transition happens. The solutions are the three points at equal chemical potential on the three different branches of the solution marked with roman numerals in Fig. 5.27, and additionally one more unstable solution at larger chemical potential that has negative compressibility unlike the other unstable one. For the Hund's metal solution and the unstable solution at the same chemical potential, the eigenvalues of χ_{imp} themselves are additionally plotted in the complex plane in the lower panels of Fig. 5.29.

As previously discussed, we can see that the eigenvalues λ_{imp} are not purely real as they would be for a bisymmetric matrix, which the generalized susceptibility is only in case of particle-hole symmetry, but those that are not real come in complex conjugated pairs [467, 491]. We can observe that the unstable solution has one real eigenvalue λ_{imp} less than $-\beta/t^2$, which is -200 in this case, which also applies to the other unstable solution as well as further not shown unstable solutions at the same temperature and both unstable solutions at temperature $\beta D = 35$ for which we calculated two-particle quantities, but is not the case for the shown stable solution or any other stable or metastable solution for which we calculated two-particle quantities. The smallest real eigenvalues of the stable Hund's metal solution, which is significantly farther away from the end of its branch than the metastable good metal solution, is only slightly negative but far away from $-\beta/t^2$, in particular much farther than that of the good metal solution. The smallest real eigenvalues of χ_{imp} are of particular interest here since, if they stay real, they cause a divergence of the lattice compressibility when they cross the value $-\beta/t^2$ according to (5.70), while a complex eigenvalue with non-zero imaginary part does not cause a divergence regardless of its real part. We observe that in the case of the stable solution here, several conjugated pairs of complex eigenvalues of χ_{imp} have significantly more negative real parts than its smallest real eigenvalue. The imaginary

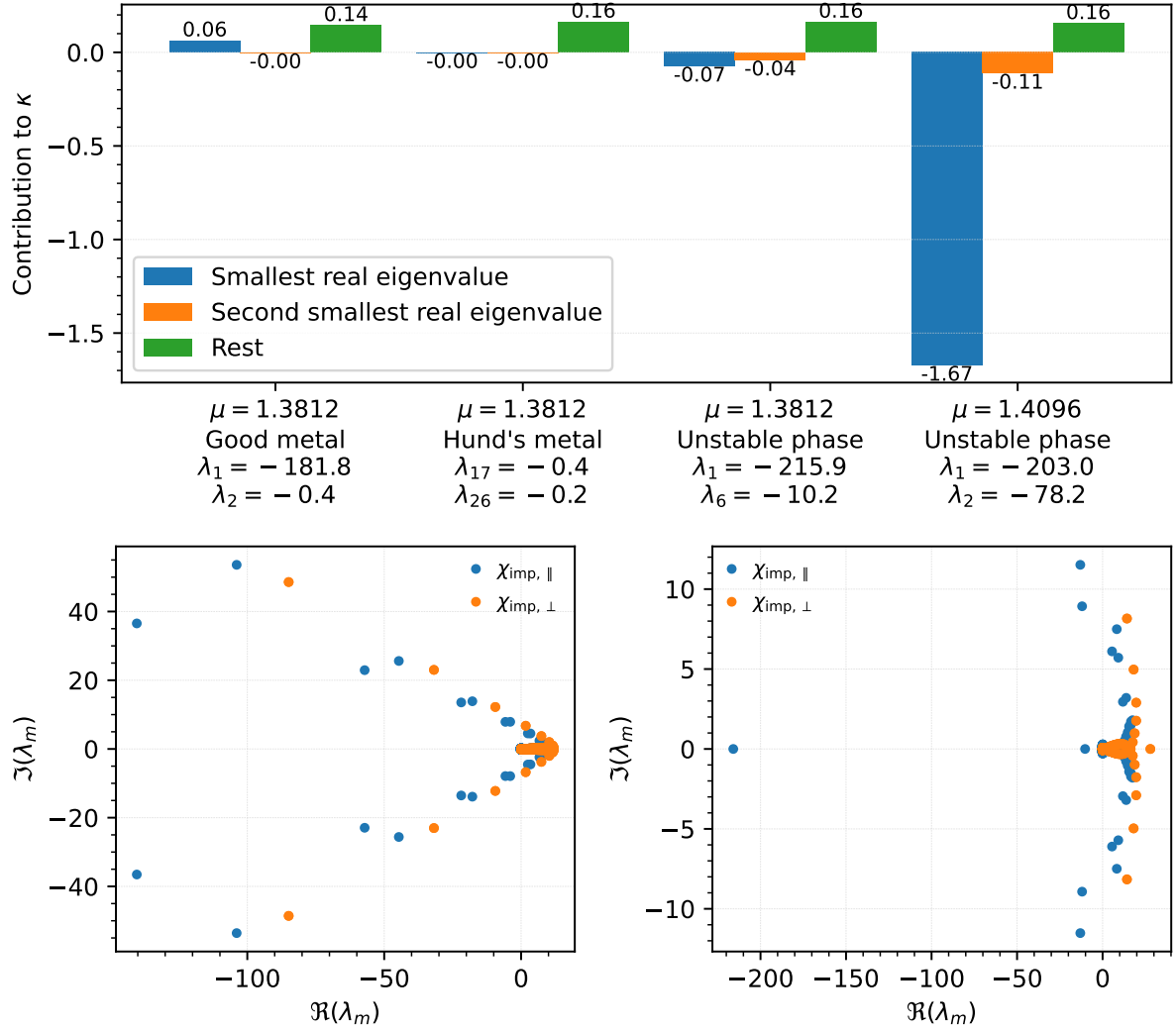


Figure 5.29: Top panel: Contributions to lattice compressibility per eigenvalue of χ_{imp} for points corresponding to solutions in different phases at $\beta D = 50, U/D = 1.46$, three of which are the points labeled with roman numerals in Fig. 5.27. The contributions associated with the two smallest real eigenvalues are shown, whose values are given in the tick labels, where the index of λ indicates their position in the eigenvalue list including complex eigenvalues sorted by ascending real part. Bottom panels: Eigenvalues of the orbital-longitudinal ($\chi_{\text{imp}, \parallel}$) and orbital-transverse ($\chi_{\text{imp}, \perp}$) generalized susceptibility of the impurity plotted in the complex plane for the (left) Hund's metal and (right) unstable solution at $\beta D = 50, U/D = 1.46, \mu = 1.3812$.

parts of the eigenvalues of χ_{imp} are not the primary reason why the corresponding eigenvalue of $\chi_{q=0}$ does not diverge, as the real parts are still not close to $-\beta/t^2$, but the situation is slightly reminiscent of the disappearance of vertex divergences due to eigenvalues acquiring imaginary parts [482].

We can further see that in the unstable cases, the contribution of the lowest eigenvalue always has a negative sign, while it has a positive sign in all other cases where it is significantly different from zero. This is exactly what should be expected assuming that the weight associated to the lowest eigenvalue does not change its sign when λ_{imp} is close to $-\beta/t^2$, as the according to (5.70) corresponding eigenvalue $\lambda_{q=0}$ has a pole of first order as a function of λ_{imp} at $\lambda_{\text{imp}} = -\beta/t^2$, so $\lambda_{q=0}$ changes its sign across the divergence. In total, the empirical picture we get from the data we have suggests that the smallest real impurity eigenvalue of χ_{imp} is above $-\beta/t^2$ on the stable branches, crosses that value at the ends of the metastable branches inside the phase separation region or at the critical point, which causes the divergence of the generalized susceptibility $\chi_{q=0}$ of the lattice and the lattice compressibility κ , and is actually below $-\beta/t^2$ on the entirety of the unstable branch found between the ends of the metastable branches. The resolution of contributions per eigenvalue of χ_{imp} shown in Fig. 5.29 also allows us to understand how the positive compressibility on the unstable branch arises: While the negative contribution associated with the smallest real eigenvalue has a large magnitude close to the divergence at the end of the unstable phase such that it dominates the other contributions and causes a negative compressibility in total, further from the ends of the unstable phase the smallest real eigenvalue may be sufficiently far below $-\beta/t^2$ that its contribution is of comparable magnitude to those associated with other eigenvalues and thus the compressibility in total positive again.

Let us finally note that the eigenvalue structures as shown in the bottom panels of Fig. 5.29 do not sensitively depend on the number of Matsubara frequencies included in the generalized susceptibility. In the cases included in the figure as well as two other cases, the diagonalization was repeated using data for only approximately one tenth of the Matsubara frequencies originally calculated using QMC with the only visible difference being the size of the cluster of eigenvalues around zero. Numerically, differences in the eigenvalues not belonging to that cluster were usually not found in the first few decimal digits, the same is however not true for the associated weights and contributions. Slightly related to that, the components of the eigenvector associated with the smallest real eigenvalue and thus the susceptibility divergence were in all our calculations actually found to be strongly peaked around zero frequency. We may however speculate that as we go to lower temperature along the line of critical points, we would find a broadening analogous to that in the case of the first vertex divergence line of the irreducible vertex at half-filling [479, 481]. This would be supported by the slightly more pronounced peak at $\beta D = 35$ than at $\beta D = 50$ (not shown), and we might try to interpret the relatively sharp peaks of the eigenvector components merely as indicators that we are only slightly below the critical temperature of the MIT in our calculations in a manner similar to the interpretation of the structure of the full susceptibility in

Ref. [471].

5.2.4 Connection between generalized susceptibility eigenvalues and thermodynamic quantities

In the preceding section we have observed that all eigenvalues of the generalized susceptibility χ_{imp} of the impurity on stable branches are greater than $-\beta/t^2$, the value at which the lattice compressibility diverges according to (5.70), see e.g. the lowest eigenvalues shown in the right panels and insets of Fig. 5.26 and 5.27. The divergence condition $\lambda_{\text{imp}} = -\beta/t^2$ is shown in the plots as blue dash-dotted line. On the unstable branches on the other hand, for which we included one data point labeled II in each figure, and looking at numerical values of further two-particle calculations, we find that the lowest eigenvalue is below the divergence condition in all cases we calculated. Let us therefore consider the link between the eigenvalues of the generalized susceptibility and thermodynamic properties of the system in more detail.

The basic condition for local thermodynamic stability of a phase is concavity of the entropy in its natural variables, or, equivalently, concavity in intensive variables and convexity in extensive variables of the internal energy or another thermodynamic potential [439]. We shall consider the grand potential and its differential [459],

$$\Omega = E - TS - \mu n + UD, \quad d\Omega = -S dT - n d\mu + D dU, \quad (5.71)$$

where E is the internal energy, T the temperature, S the entropy, and $D := \langle H_{\text{int}} \rangle / U$ proportional to the potential or interaction energy. This variable would be exactly the only double occupancy in the single-orbital case and is in general a linear combination of double occupancies, which we shall call the normalized potential energy in the following since it is the potential energy divided by its interaction strength prefactor, where we assume fixed ratios between U and Hund's coupling J as previously. The stability condition at fixed temperature can be expressed as the condition that the Hessian matrix

$$\begin{pmatrix} \frac{\partial^2 \Omega}{\partial \mu^2} & \frac{\partial^2 \Omega}{\partial U \partial \mu} \\ \frac{\partial^2 \Omega}{\partial U \partial \mu} & \frac{\partial^2 \Omega}{\partial U^2} \end{pmatrix} \quad (5.72)$$

of Ω is negative definite, which in particular requires both of its diagonal elements to be negative as well. For the first diagonal element, this results in the well-known condition that the lattice compressibility should be positive,

$$-\frac{\partial^2 \Omega}{\partial \mu^2} = -\frac{\partial}{\partial \mu}(-n) = n^2 \kappa > 0, \quad (5.73)$$

and for the second diagonal element in the condition that the normalized potential energy D should decrease with increasing interaction strength parameter U ,

$$\frac{\partial^2 \Omega}{\partial U^2} = \frac{\partial}{\partial U} D < 0. \quad (5.74)$$

According to Sylvester's criterion, either of these conditions together with the condition that the determinant be positive,

$$\frac{\partial^2 \Omega}{\partial \mu^2} \frac{\partial^2 \Omega}{\partial U^2} - \frac{\partial^2 \Omega}{\partial U \partial \mu} \frac{\partial^2 \Omega}{\partial U \partial \mu} = -\frac{\partial n}{\partial \mu} \frac{\partial D}{\partial U} - \left(\frac{\partial n}{\partial U} \right)^2 > 0, \quad (5.75)$$

is sufficient for negative definiteness and thus local stability, and since all of them are necessary, instability directly follows from e.g. the negativity of the lattice compressibility. We should note that the local stability conditions expressed in terms of derivatives do not necessarily imply "global" stability, for which we may consider the metastable phases as an example. As seen in Fig. 5.13, the metastable continuations of the stable branches of the grand potential across the thermodynamic phase transition fulfill local stability conditions as recognizable from the curvature, but they are not the actual minima of the grand potential Ω for a given choice of the system parameter μ .

As we have previously shown, the compressibility and thus one of these conditions can be expressed in terms of eigenvalues of the uniform generalized susceptibility $\chi_{\mathbf{q}=0}$ of the lattice and associated weights calculated from the eigenvectors using (5.69), and consequently also in terms of the eigenvalues of the generalized susceptibility χ_{imp} of the impurity using (5.70). We now continue with the connection of the derivative of the normalized potential energy D with respect to the interaction strength parameter U [501]. Using the formula of Galitskii and Migdal [148] for the potential energy $\langle H_{\text{int}} \rangle$, whose derivation can be found in Appendix B, we can express the derivative

$$\frac{dD}{dU} = \frac{d}{dU} \left(\frac{\langle H_{\text{int}} \rangle}{U} \right) = -\frac{D}{U} + \frac{1}{U} \frac{d\langle H_{\text{int}} \rangle}{dU} \quad (5.76)$$

in terms of a derivative of one-particle quantities

$$\frac{dD}{dU} = -\frac{D}{U} + \frac{1}{U\beta} \frac{d}{dU} \sum_{\nu, a} \Sigma_a(i\nu) G_a(i\nu), \quad (5.77)$$

where we can use the Dyson equation and the known relation [33] for DMFT on the

Bethe lattice $\Delta_a(iv) = t^2 G_a(iv)$ to get the expression

$$\frac{dD}{dU} = -\frac{D}{U} + \frac{1}{U\beta} \sum_{v,a} (iv + \mu) \frac{dG_a}{dU}(iv) - 2t^2 G_a(iv) \frac{dG_a}{dU}(iv) \quad (5.78)$$

in terms of the one-particle Green's function and its derivative only.

Although the self-consistent DMFT local lattice Green's function is equal to the impurity Green's function of the auxiliary AIM, its derivative with respect to the lattice parameter U is not the same as that of the impurity Green's function with respect to the same parameter of the AIM. The derivative of the self-consistent Green's function in DMFT consists of two separate contributions, one due to the change of the impurity Green's function as a reaction to the change of the interaction U in the impurity model and an additional one due to the change of the impurity Green's function as a reaction to the change of the hybridization function of the impurity model, which depends on the impurity Green's function due to the DMFT self-consistency condition. We therefore denote the former as $\left. \frac{\partial G}{\partial U}(iv) \right|_{\Delta=\text{const.}}$, which could only be further evaluated in terms of three-particle correlation functions and we so leave as it is, and focus our attention on further evaluation of the latter, which can be written as functional derivative of the impurity model partition sum (2.5) with action (2.9). By applying the product rule and identifying the one- and two-particle Green's functions in the evaluated derivatives, we can therefore evaluate the total derivative of the local Green's function as

$$\begin{aligned} \frac{dG_a}{dU}(iv) &= \sum_{v',b} \frac{\delta G_a(iv)}{\delta \Delta_b(iv')} \frac{\partial \Delta_b(iv')}{\partial U} + \left. \frac{\partial G_a}{\partial U}(iv) \right|_{\Delta=\text{const.}} \\ &= \sum_{v',b} \frac{\delta \frac{-\delta Z_{\text{imp}}}{2Z_{\text{imp}} \delta \Delta_a(iv)}}{\delta \Delta_b(iv')} \frac{\partial \Delta_b(iv')}{\partial U} + \left. \frac{\partial G_a}{\partial U}(iv) \right|_{\Delta=\text{const.}} \\ &= \sum_{v',b} \left(\frac{1}{2Z_{\text{imp}}^2} \frac{\delta Z_{\text{imp}}}{\delta \Delta_a(iv)} \frac{\delta Z_{\text{imp}}}{\delta \Delta_b(iv')} - \frac{\delta Z_{\text{imp}}}{2Z_{\text{imp}} \delta \Delta_a(iv) \delta \Delta_b(iv')} \right) \frac{\partial \Delta_b(iv')}{\partial U} + \left. \frac{\partial G_a}{\partial U}(iv) \right|_{\Delta=\text{const.}} \\ &= \sum_{v',b} \left(2G_a(iv)G_b(iv') - \frac{1}{2} \sum_{\sigma,\sigma'} \langle c_{va\sigma}^\dagger c_{va\sigma} c_{v'b\sigma'}^\dagger c_{v'b\sigma'} \rangle \right) \frac{\partial \Delta_b(iv')}{\partial U} + \left. \frac{\partial G_a}{\partial U}(iv) \right|_{\Delta=\text{const.}} \\ &= -\beta^{-1} \sum_{v',b} \chi_{\text{imp},\parallel,ab}(v, v', \omega = 0) \frac{\partial \Delta_b(iv')}{\partial U} + \left. \frac{\partial G_a}{\partial U}(iv) \right|_{\Delta=\text{const.}}, \quad (5.79) \end{aligned}$$

where the inserted factors of two are necessary due to the continued use of our implicit convention that without spin indices, one-particle quantities refer to diagonals and two-particle quantities to the density channel combination. Using vector-valued Green's and hybridization functions and a matrix-valued generalized susceptibility,

where components would be referred to by combined orbital and Matsubara frequency indices, the derivative can be expressed as

$$\frac{d\mathbf{G}}{dU} = -\beta^{-1}\chi_{\text{imp},\parallel}^{\omega=0} \frac{\partial\Delta}{\partial U} + \left. \frac{\partial\mathbf{G}}{\partial U} \right|_{\Delta=\text{const.}}. \quad (5.80)$$

If we insert the Bethe lattice hybridization function $\Delta = t^2G$, it is then possible to solve for the total derivative of the Green's function in terms of only the generalized susceptibility of the impurity and the fixed-hybridization partial derivative, yielding

$$\frac{d\mathbf{G}}{dU} = \left(\mathbf{1} + \frac{t^2}{\beta}\chi_{\text{imp},\parallel}^{\omega=0} \right)^{-1} \left. \frac{\partial\mathbf{G}}{\partial U} \right|_{\Delta=\text{const.}}, \quad (5.81)$$

and further by insertion into (5.78) the derivative of the thermodynamic quantity D

$$\frac{dD}{dU} = -\frac{D}{U} + \frac{1}{U\beta} \sum_{v,a} (iv + \mu - 2t^2G_a(iv)) \left[\left(\mathbf{1} + \frac{t^2}{\beta}\chi_{\text{imp},\parallel}^{\omega=0} \right)^{-1} \left. \frac{\partial G}{\partial U} \right|_{\Delta=\text{const.}} \right]_{av}. \quad (5.82)$$

Here, we can again employ the spectral representation of the generalized susceptibility and write $\chi_{\text{imp}} = \mathbf{S}\lambda_{\text{imp}}\mathbf{S}^{-1}$ to obtain a form of the derivative with the dependence on the eigenvalues clearly recognizable similar to (5.69),

$$\frac{dD}{dU} = -\frac{D}{U} + \frac{1}{U\beta} \sum_{abc} (iv + \mu - 2t^2G)_a S_{ab} \frac{1}{1 + \frac{t^2}{\beta}\lambda_{\text{imp},\parallel,b}} (S^{-1})_{bc} \left. \frac{\partial G_c}{\partial U} \right|_{\Delta=\text{const.}}, \quad (5.83)$$

where \mathbf{S} is again the matrix with the eigenvectors of $\chi_{\text{imp},\parallel}^{\omega=0}$ as columns, all indices are combined indices of one Matsubara frequency and one orbital index, and standard simplification rules were used to bring the matrices \mathbf{S} and \mathbf{S}^{-1} as far outside as possible. We can identify the divergence condition $1 + t^2\lambda_{\text{imp},\parallel,b}/\beta = 0$ here, giving again the result $\lambda_{\text{imp},\parallel,b} = -\beta/t^2$ equal to the one that follows from (5.70). Note that the divergence condition did not follow from explicitly replacing a lattice susceptibility $\chi_{q=0}$ by an impurity susceptibility χ_{imp} this time. Instead, we directly got a correlation function of four impurity operators during the derivation from the term representing the change of the self-consistent Green's function due to the change of the self-consistent hybridization function in DMFT, and after applying the relation between hybridization and Green's function on the Bethe lattice we were able to separate out a factor that diverges under the same condition. Due to (5.67) we derived earlier, we could however identify the factor in parentheses in (5.81) as a sort of ratio between impurity and lattice

susceptibility,

$$\left(\mathbf{1} + \frac{t^2}{\beta} \chi_{\text{imp},\parallel}^{\omega=0} \right)^{-1} = \left(\chi_{\text{imp},\parallel}^{\omega=0} \right)^{-1} \chi_{\mathbf{q}=0,\parallel}^{\omega=0}, \quad (5.84)$$

and equivalently write the derivative (5.81) as

$$\frac{d\mathbf{G}}{dU} = \left(\chi_{\text{imp},\parallel}^{\omega=0} \right)^{-1} \chi_{\mathbf{q}=0,\parallel}^{\omega=0} \left. \frac{\partial \mathbf{G}}{\partial U} \right|_{\Delta=\text{const.}}. \quad (5.85)$$

Coming back to (5.83) after this slight detour, let us wrap up the compared to the compressibility somewhat larger amount of other factors as weight as well to obtain

$$\frac{dD}{dU} = -\frac{D}{U} + \frac{1}{U\beta} \sum_b \frac{1}{1 + \frac{t^2}{\beta} \lambda_{\text{imp},\parallel,b}} w_b \quad (5.86)$$

with a weight $w_b = (\sum_a (iv + \mu - 2t^2 G)_a (\mathbf{v}_b)_a) \left(\sum_a \left. \frac{\partial G_a}{\partial U} \right|_{\Delta=\text{const.}} (\mathbf{v}_b^{-1})_a \right)$. Apart from just being more factors, the factors do not just depend on the eigenvectors this time but on the Green's function and even the derivative of the impurity Green's function with respect to the impurity U , corresponding to a three-particle correlation function of the impurity.

Nevertheless, with this expression at hand we may note that dD/dU and κ diverge under the exact same conditions. Also, at least close to the divergence, i.e. sufficiently close to the ends of the unstable and metastable phases, the eigenvalue closest to the divergence (which has so far always been the smallest real one) will be associated to the dominating contribution to both quantities, such that both change sign across the divergence and thus are sufficient for instability at the edges of the unstable branch. As we have seen in the previous subsection, the lowest eigenvalue may drop sufficiently far below the divergence threshold in the interior of the unstable branch that its contribution no longer dominates and these quantities change sign again, so this alone is still not sufficient to show instability on the entire unstable branch.

We can finally also express all terms of the determinant condition (5.75) using the spectral representation of the generalized susceptibility. Apart from the derivatives of lattice quantities dD/dU and κ that we already have, this additionally requires the derivative $\partial n/\partial U$ of the lattice filling n with respect to the lattice interaction strength U , which is partial in the sense that the other parameter μ is kept fixed. Given that the sum over all components of the Green's function at fixed time or equivalently summed over all Matsubara frequencies using $\frac{1}{\beta} \sum_\nu e^{i\nu\tau} = \delta(\tau)$ corresponds to the total occupation, we can reuse the expression (5.81) for the total derivative of the self-consistent DMFT local lattice Green's function with respect to the lattice interaction parameter U . We

thus obtain

$$\begin{aligned}
\frac{\partial n}{\partial U} &= \frac{1}{\beta} \sum_{\alpha,\nu} \frac{dG_\alpha}{dU}(i\nu) \\
&= \frac{2}{\beta} \sum_{ab} \left[\left(\mathbf{1} + \frac{t^2}{\beta} \chi_{\text{imp},\parallel}^{\omega=0} \right)^{-1} \right]_{ab} \frac{\partial G_b}{\partial U} \Big|_{\Delta=\text{const.}} \\
&= \frac{2}{\beta} \sum_b \frac{1}{1 + \frac{t^2}{\beta} \lambda_{\text{imp},\parallel,b}} \left(\sum_a (\mathbf{v}_b)_a \right) \left(\sum_a \frac{\partial G_a}{\partial U} \Big|_{\Delta=\text{const.}} (\mathbf{v}_b^{-1})_a \right) \quad (5.87)
\end{aligned}$$

in the same way as we transform the expression for dD/dU from (5.82) to (5.86), with the sum over spins included in Greek indices turning into a factor of two, Latin indices as combined orbital and Matsubara frequency indices and the last two expressions in parentheses identifiable as weight.

Using all our expressions in spectral representation, i.e. (5.69), (5.86), and (5.87), we can write the entire determinant condition (5.75) in spectral representation. Note that the eigenvalues $\lambda_{\mathbf{q}=0,b}$ in the expression (5.69) were eigenvalues for the (exclusively relevant) orbital-longitudinal part of the generalized susceptibility $\chi_{\mathbf{q}=0,\parallel}$ of the lattice that we replaced with the actually calculated eigenvalues $\lambda_{\text{imp},\parallel,b}$ of the impurity susceptibility $\chi_{\text{imp},\parallel}$ using (5.70), while the eigenvalues $\lambda_{\text{imp},\parallel,b}$ in the other expressions were eigenvalues of the impurity quantity $\chi_{\text{imp},\parallel}$ already. For our final expression, we therefore finally explicitly replace the lattice eigenvalues $\lambda_{\mathbf{q}=0,b}$ in (5.69) with impurity eigenvalues $\lambda_{\text{imp},\parallel,b}$ using $\lambda_{\mathbf{q}=0,\parallel,b} = \lambda_{\text{imp},\parallel,b}/(1 + t^2 \lambda_{\text{imp},\parallel,b}/\beta)$, which is (5.70) expanded by another factor of impurity quantity $\lambda_{\text{imp},\parallel,b}$, to make it look more similar to the other expressions. This results in

$$\begin{aligned}
0 &< - \frac{\partial n}{\partial \mu} \frac{\partial D}{\partial U} - \left(\frac{\partial n}{\partial U} \right)^2 \\
&= - \frac{2}{U \beta^3} \sum_{b_1, b_2} \frac{\lambda_{\text{imp},\parallel,b_1} \left(\sum_a (\mathbf{v}_{b_1})_a \right) \left(\sum_a (\mathbf{v}_{b_1}^{-1})_a \right) \left(\sum_a (i\nu + \mu - 2t^2 G)_a (\mathbf{v}_{b_2})_a \right) \left(\sum_a \frac{\partial G_a}{\partial U} \Big|_{\Delta=\text{const.}} (\mathbf{v}_{b_2}^{-1})_a \right)}{(1 + \frac{t^2}{\beta} \lambda_{\text{imp},\parallel,b_1})(1 + \frac{t^2}{\beta} \lambda_{\text{imp},\parallel,b_2})} \\
&\quad - \frac{4}{\beta^2} \sum_{b_1, b_2} \frac{\left(\sum_a (\mathbf{v}_{b_1})_a \right) \left(\sum_a \frac{\partial G_a}{\partial U} \Big|_{\Delta=\text{const.}} (\mathbf{v}_{b_1}^{-1})_a \right) \left(\sum_a (\mathbf{v}_{b_2})_a \right) \left(\sum_a \frac{\partial G_a}{\partial U} \Big|_{\Delta=\text{const.}} (\mathbf{v}_{b_2}^{-1})_a \right)}{(1 + \frac{t^2}{\beta} \lambda_{\text{imp},\parallel,b_1})(1 + \frac{t^2}{\beta} \lambda_{\text{imp},\parallel,b_2})} \\
&\quad + \frac{2D}{U \beta^2} \sum_b \frac{\lambda_{\text{imp},\parallel,b} \left(\sum_a (\mathbf{v}_b)_a \right) \left(\sum_a (\mathbf{v}_b^{-1})_a \right)}{1 + \frac{t^2}{\beta} \lambda_{\text{imp},\parallel,b}}, \quad (5.88)
\end{aligned}$$

which does not change sign as the lowest eigenvalue of the impurity susceptibility $\chi_{\text{imp},\parallel}$ crosses $\lambda_{\text{imp},\parallel} = -\beta/t^2$ because the terms with two denominator factors crossing zero dominate in a region sufficiently close to that point. Since the determinant is equal to the product of the eigenvalues and both eigenvalues must be negative in a stable phase, this is consistent with both eigenvalues changing their signs at once. Considering that we have previously found that both diagonal elements dD/dU and $-n^2\kappa$ change their signs and the trace is the sum of the eigenvalues, this is also the only possibility.

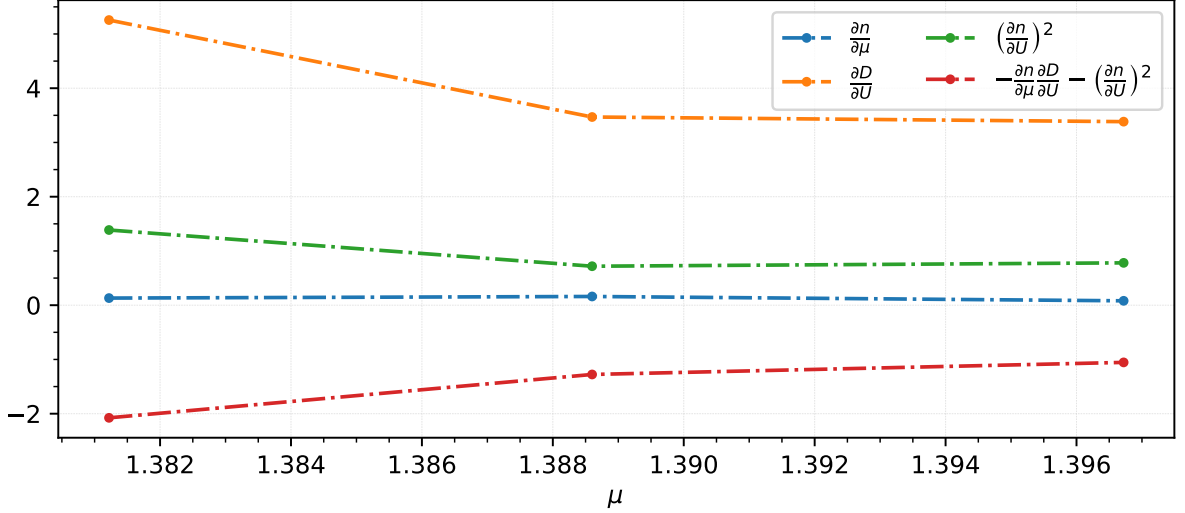


Figure 5.30: Evaluation of all expressions occurring in thermodynamic stability conditions for three points on the unstable branch $\beta D = 50$, $U/D = 1.46$, cf. Fig. 5.27. While the compressibility is positive, the derivative $\partial D/\partial U > 0$ and the determinant condition $-(\partial n/\partial \mu)(\partial D/\partial U) - (\partial n/\partial U)^2 < 0$ indicate instability.

In conclusion, all thermodynamic stability conditions admit formulations showing a clear dependence on the eigenvalues and eigenvectors of the generalized susceptibility. In particular, the expressions show that all derivatives of the thermodynamic potential diverge when an eigenvalue $\lambda_{\text{imp},\parallel}$ of the orbital-longitudinal part of the generalized susceptibility $\chi_{\text{imp},\parallel}$ of the impurity reaches $-\beta/t^2$, as it happens at the critical point and the ends of metastable branches, unless the associated weight is zero. Empirically, we also found that an eigenvalue $\lambda_{\text{imp},\parallel} < -\beta/t^2$ below the divergence threshold always indicated the thermodynamic instability of a DMFT solution, as we found such eigenvalues exactly for all the solutions we calculated on unstable branches. While we can reliably say that the expressions for the instability conditions change their signs as an eigenvalue passes $-\beta/t^2$ unless the weight changes its sign too, we have not proven that any of them keep that new sign when the contribution associated with that eigen-

value is no longer dominant. It is even precisely not the case for the condition related to the compressibility at the points on the unstable branch where the compressibility is positive, but numerical evaluation of the other two conditions shows that they are still sufficient to demonstrate instability of all such points we checked, see Fig. 5.30. A short survey of our total available data indicates also that we are mostly able to demonstrate that the numerically evaluated stability conditions are fulfilled on stable branches including in particular the region close to half-filling where the compressibility is strongly suppressed, and this in spite of the relative sparsity with which we collected data points away from the transition and crossover.

5.2.5 Conclusion and outlook

We have been able to identify the origin of the enhanced and diverging compressibility along the Hund’s metal crossover at small doping in the two-orbital Hubbard model [363] in the charge response contribution associated with the smallest eigenvalue of the generalized susceptibility of the impurity. This contribution drives the system towards a divergence of the charge-charge response function at the critical point of the Mott transition while all other contributions in eigenbasis remain almost constant. Apart from confirming the one-band results [491] systematically along the crossover line up to the critical point at finite doping in a more complex two-band system with Hund’s coupling, we further went beyond that analysis by calculating the generalized susceptibilities at DMFT fixed points in the unstable phase. There, we discovered that the lowest eigenvalue of the generalized susceptibility of the impurity also serves as a potential criterion indicating the thermodynamic instability of a solution, namely then when it has crossed *below* the threshold value that would indicate the divergence of its associated compressibility contribution.

Unlike the evaluation of thermodynamic stability conditions using difference quotients, which becomes difficult near critical points due to the small distances in parameter space that are needed to resolve sharp features but worsen the relative error of the result, the calculation of the generalized susceptibility can be performed for a single point, i.e. “locally” in parameter space. In DMFT, the generalized susceptibility of the lattice can be determined in a lattice-dependent way from the calculated impurity vertex with an error that in principle does not deteriorate near the critical point except possibly due to critical slowing down. However, this also affects the difference quotients in addition to their other problems and can be ameliorated by using sophisticated fixed-point solvers instead of simple iteration [145].

If the observation that the eigenvalue of the generalized susceptibility indicates thermodynamic instability is generalizable, one single calculation of two-particle quanti-

ties would suffice to demonstrate thermodynamic instability of a solution. In a general case, this might be considerably less effort than the additional DMFT calculations necessary to evaluate the difference quotients. For each parameter of the system, in our case μ and U , one additional calculation is necessary that also must be close enough in parameter space to be relevant and at the same time precise enough to reliably evaluate the stability conditions. Particularly close to the critical point, this might be more difficult to achieve than one single calculation of two-particle quantities.

With a multi-orbital model as considered here, we also come closer to direct physical applicability, given that minimal models for the iron-pnictide superconductors with just two orbitals have actually been proposed [450] as we have commented on before in Sec. 5.1.5 and the same analysis is in principle also extensible to more models, although that will not only require higher resource usage for the impurity solver but also increase the number of non-zero components of the two-particle Green's function that need to be calculated. As it was done in Ref. [491], that would allow the calculation of the momentum-dependent structure of the susceptibility and identification of potential effectively attractive interactions.

6 Conclusion

We found the CT-HYB algorithm to be a powerful state-of-the-art method for the solution of multi-orbital Anderson impurity models of the complexity necessary for the realistic description of strongly correlated materials. The state and superstate sampling algorithms we introduced enhanced its efficiency particularly in the case of more realistic interaction parameterizations of higher accuracy, and symmetric improved estimators make the calculation of self-energies and vertex functions with constant error possible, allowing us to get more accurate intermediate-frequency behavior that could be advantageous for analytic continuation.

We were able to show that an accurate parameterization of the local interaction is necessary to get qualitatively right results for the prototypical Kondo system of a cobalt impurity on a copper surface, demonstrating how the density-density form of the interaction, which disproportionately freezes out orbital fluctuations, would incorrectly lead us to believe in a picture with only two relevant $3d$ -shell orbitals and a Nevidomskyy-Coleman spin-1 scenario with a Kondo temperature suppressed by orders of magnitude compared to the experimental one. This result should help to inform future first-principles investigations of Kondo impurities of the dangers of simplified approximations of the interaction and consideration of insufficient orbital subsets.

The quantitative dependence of the Kondo effect of cobalt adatoms on a copper surface embedded in “atomic wire” clusters of additional copper atoms of varying length found in experiment could not be reproduced, in particular also not the qualitative total absence of a resonance in the spectra of two clusters. Given no significant distinctions between the hybridization functions and local impurity levels, the failure is not entirely surprising. While effects of the environment on the local interaction are expected to be minor, the considerable dependence of numerical results on at least the Hubbard- U repulsion, the adsorption distance, and likely the filling suggests that more accurate model parameters may be necessary for quantitative statements. Recent challenges to the identification of the zero-bias spectral feature as Kondo resonance also point to the importance of spin-orbit coupling that we neglected, which could however be included in future CT-HYB studies at additional computational cost.

Our results computed using the first-principles combination of DFT and CT-HYB were able to reproduce the experimentally found variation of the Kondo temperature of

iron impurities on niobium with respect to the absorption site, connected to Yu-Shiba-Rusinov resonance positions in the superconducting state. We identified the reduced actual adsorption height of the iron adatoms on the oxygen-reconstructed surface as primary cause that moves it into the strong-coupling regime, while those on the clean surface are in the weak-coupling regime that admits a description as a classical spin. The characterization of the surface dependence should guide potential attempts to assemble atomic iron wires hosting Majorana zero modes.

In our DMFT investigation of the two-orbital Hubbard model with Hund's coupling, we were able to identify the first-order interaction-driven Mott transition at half-filling as a clear signature indicating the presence of a phase separation zone extending off half-filling and terminating in a quantum critical point at finite doping. A perturbative expansion around the phase transition point corroborates the connection between Hund's coupling and the first-order nature of the transition and demonstrates that any small term splitting the ground-state multiplet could have a similar effect. We evoke tentative investigations of a minimal two-orbital model for iron-pnictides and even a full five-orbital DFT-parameterized model of an iron-pnictide superconductor along similar lines, where we also found a phase separation region or at least a zone of compressibility enhancement, which may be connected to an electronic pairing mechanism.

Finally, we trace the origin of the compressibility divergence at the critical points of this model at finite temperature and doping in the eigenbasis of the two-particle generalized susceptibility of the DMFT lattice solution. We identify a threshold for the eigenvalues of the generalized impurity susceptibility as divergence condition and show how the approach of the lowest eigenvalue to this threshold is responsible for the compressibility enhancement along the crossover line and its divergence at the critical point away from half-filling. We further follow the eigenvalue structure into the phase separation zone, where we calculate it for all phases including the unstable one. We derive expressions for the thermodynamic derivatives that show their dependence on the eigenvalues of the generalized susceptibility and demonstrate empirically that our threshold value distinguishes between thermodynamic stability and instability of DMFT solutions.

A Fourier transforms between imaginary time and Matsubara frequencies

In accordance with Ref. [47], we may define our Fourier transforms between imaginary time and Matsubara frequencies for one-particle Green's functions (5.41) as

$$G(iv_n) = \int_0^\beta \exp(iv_n \tau) G(\tau) d\tau \quad (\text{A.1})$$

$$G(\tau) = \beta^{-1} \sum_{\nu_n} \exp(-i\nu_n \tau) G(iv_n) \quad (\text{A.2})$$

with fermionic Matsubara frequencies $\nu_n = (2n+1)\pi\beta^{-1}$ (as for the one-particle Green's function in our case) or bosonic Matsubara frequencies $\nu_n = 2n\pi\beta^{-1}$, where $n \in \mathbb{Z}$. This expansion in terms of Matsubara frequencies is essentially just a Fourier series for periodic functions on $[-\beta, \beta]$, exploiting additionally the fact that our correlation functions are either fermionic and β -antiperiodic or bosonic and β -periodic.

In this definition, we took advantage of time-translational invariance to fix one time argument to zero and write the one-particle Green's function as a function of the time difference of its constituting operators only, cf. Sec. 5.2.2. In general, we can use

$$G(iv_1, \dots, iv_{2n}) = \int_0^\beta e^{i(\nu_1 \tau_1 - \nu_2 \tau_2 + \dots + \nu_{2n-1} \tau_{2n-1} - \nu_{2n} \tau_{2n})} G(\tau_1, \dots, \tau_{2n}) d\tau_1 \dots d\tau_{2n} \quad (\text{A.3})$$

$$G(\tau_1, \dots, \tau_{2n}) = \beta^{-2n} \sum_{\nu_1, \dots, \nu_{2n}} e^{-i(\nu_1 \tau_1 - \nu_2 \tau_2 + \dots + \nu_{2n-1} \tau_{2n-1} - \nu_{2n} \tau_{2n})} G(iv_1, \dots, iv_{2n}) \quad (\text{A.4})$$

to transform n -particle Green's functions like (5.40) [214], i.e. correlation functions with $2n$ times. If we impose the Matsubara frequency transform

$$c(iv_n) = \int_0^\beta \exp(-i\nu_n \tau) c(\tau) d\tau, \quad (\text{A.5})$$

$$c^\dagger(iv_n) = \int_0^\beta \exp(i\nu_n \tau) c^\dagger(\tau) d\tau. \quad (\text{A.6})$$

on creation and annihilation operators, we can get (A.3) simply by transforming all involved operators.

By choosing $n = 1$, we can apply (A.3) to the one-particle Green's function, and for comparison with our earlier expression (A.1) we can introduce time-translational invariance into this general expression in the form of the energy conservation $\nu_1 = \nu_2$ that it implies [502]. We can then identify $\tau = \tau_1 - \tau_2$, but are still left with two time integrals rather than one. As we shall soon see, this gives us an additional factor of β compared to our earlier expression. While the functions as arguments of time are simply related by $G(\tau_1, \tau_2) = G(\tau_1 - \tau_2)$ in the case of time-translational invariance, the function of $2n - 1$ frequency arguments is related to the one with an additional redundant argument by $G(\nu_1, \nu_2) = \delta_{\nu_1, \nu_2} \beta G(\nu_1)$, i.e. it differs by a factor of β [214].

Let's work out the form of the generalized susceptibility (5.44) in Matsubara frequencies in terms of n -particle Green's functions with $2n - 1$ frequency arguments as an example. Since the sum of ingoing frequencies must equal that of outgoing frequencies, $\nu_1 + \nu_3 = \nu_2 + \nu_4$, our final expressions will involve three frequencies only. We may e.g. choose a particle-hole frequency convention (5.45) [214], $\nu_1 = \nu + \omega, \nu_2 = \nu, \nu_3 = \nu', \nu_4 = \nu' + \omega$, where we choose to decompose the first ingoing fermionic frequency into a sum of a fermionic frequency variable and a difference, which must be a bosonic frequency variable. That bosonic frequency can be interpreted as the energy transfer in a scattering process from an (ingoing) electron with initial energy $\nu + \omega$ to an ingoing hole (corresponding to an outgoing electron) with initial energy $-(\nu' + \omega)$. Using this frequency convention and (A.3), we want to compute

$$\chi_{\alpha\beta\gamma\delta}^{\nu\nu'\omega} = \beta^{-1} \int_0^\beta d\tau_{1,\dots,4} e^{i((\nu+\omega)\tau_1 - \nu\tau_2 + \nu'\tau_3 - (\nu'+\omega)\tau_4)} \chi_{\alpha\beta\gamma\delta}^{\tau_1, \tau_2, \tau_3, \tau_4} \quad (\text{A.7})$$

$$= \beta^{-1} \int_0^\beta d\tau_{1,\dots,4} e^{i((\nu+\omega)\tau_1 - \nu\tau_2 + \nu'\tau_3 - (\nu'+\omega)\tau_4)} (G_{\alpha\beta\gamma\delta}^{\tau_1, \tau_2, \tau_3, \tau_4} - G_{\alpha\beta}^{\tau_1, \tau_2} G_{\gamma\delta}^{\tau_3, \tau_4}), \quad (\text{A.8})$$

where the factor of β is the conversion factor between the four-argument function resulting from the Fourier transform and the three-argument function we want, with energy conservation already enforced by our parametrization of the four frequencies.

Assuming time-translational invariance, we can use differences with respect to τ_4 in the first term, differences with respect to τ_2 for the first Green's function and associated exponential of the second term, and differences with respect to τ_4 for the rest of the second term. After the changes of variables $\tau'_{1,\dots,3} = \tau_{1,\dots,3} - \tau_4, \tau'_4 = \tau_4, \tilde{\tau}_1 = \tau_1 - \tau_2, \tilde{\tau}_2 = \tau_2, \tilde{\tau}_3 = \tau_3 - \tau_4, \tilde{\tau}_4 = \tau_4$, the integral in (A.8) turns into

$$\begin{aligned}
& \int_0^\beta d\tau'_4 \int_{-\tau'_4}^{\beta-\tau'_4} d\tau'_{1,\dots,3} e^{i((\nu+\omega)(\tau'_1+\tau'_4)-\nu(\tau'_2+\tau'_4)+\nu'(\tau'_3+\tau'_4)-(\nu'+\omega)\tau'_4)} G_{\alpha\beta\gamma\delta}^{\tau'_1\tau'_2\tau'_3} \\
& - \int_0^\beta d\tilde{\tau}_2 \int_{-\tilde{\tau}_2}^{\beta-\tilde{\tau}_2} d\tilde{\tau}_1 e^{i((\nu+\omega)(\tilde{\tau}_1+\tilde{\tau}_2)-\nu\tilde{\tau}_2)} G_{\alpha\beta}^{\tilde{\tau}_1} \int_0^\beta d\tilde{\tau}_4 \int_{-\tilde{\tau}_4}^{\beta-\tilde{\tau}_4} d\tilde{\tau}_3 e^{i(\nu'(\tilde{\tau}_3+\tilde{\tau}_4)-(\nu'+\omega)\tilde{\tau}_4)} G_{\gamma\delta}^{\tilde{\tau}_3}.
\end{aligned} \tag{A.9}$$

Using the antiperiodicity of Green's functions in all their time variables, cf. Sec. 5.2.2, we can show that the bounds of the integrals over the time differences can all be set back to 0 and β without changing their values. With $f(\tau)$ a β -antiperiodic function

$$\int_{-x}^{\beta-x} d\tau e^{i\nu\tau} f(\tau) = \int_{-x}^0 d\tau e^{i\nu\tau} f(\tau) + \int_0^{\beta-x} d\tau e^{i\nu\tau} f(\tau) \tag{A.10}$$

$$= \int_{\beta-x}^\beta d\tau' e^{i\nu\tau'-i\nu\beta} f(\tau' - \beta) + \int_0^{\beta-x} d\tau e^{i\nu\tau} f(\tau) \tag{A.11}$$

$$= \int_{\beta-x}^\beta d\tau' e^{i\nu\tau'} f(\tau') + \int_0^{\beta-x} d\tau e^{i\nu\tau} f(\tau) \tag{A.12}$$

$$= \int_0^\beta d\tau e^{i\nu\tau} f(\tau), \tag{A.13}$$

where we can use β -antiperiodicity of f and explicitly evaluate $e^{-i\nu\beta}$ for a fermionic Matsubara frequency ν from (A.11) to (A.12) resulting in two factors of minus one that cancel each other.

Therefore the inner integrals in (A.9) do not actually depend on τ'_4 , $\tilde{\tau}_2$, or $\tilde{\tau}_4$ and we can perform the integrals over these variables first. Since the Green's functions do not depend on the variables, the integrals are simple integrals over either an exponential function if a nonzero frequency ν'_4 multiplies the variable or a constant otherwise. Integrating the complex exponential over a multiple of its period results in zero, so they evaluate to $\beta\delta_{0,\nu'_4}$ in total. For the two-particle Green's function, this just ensures energy conservation and is redundant with our parametrization in terms of three frequencies, but for the product of two one-particle Green's functions, we are left with both $\delta_{\omega,0}$ and a total factor of β after taking the conversion factor into account. Identifying the remaining integrals as the Fourier transforms of the Green's functions, the expression for the generalized susceptibility as a function of three frequencies in terms of Green's functions as functions of three or one frequencies is

$$\chi_{\alpha\beta\gamma\delta}^{\nu\nu'\omega} = G_{\alpha\beta\gamma\delta}^{\nu\nu'\omega} - \beta\delta_{\omega,0} G_{\alpha\beta}^\nu G_{\gamma\delta}^{\nu'} \tag{A.14}$$

as given in (5.46).

B Equation of motion for the AIM Green's function

In this appendix, we show how to calculate the equation of motion for the one-particle Green's function of the Anderson impurity model by differentiating it with respect to its time arguments. In this way, we derive the improved estimator [200] and symmetric improved estimator equations (3.10) and (3.14) for the one-particle Green's function of the AIM and the Galitskii-Migdal formula for the potential energy [148] that we use to express the derivative of the potential energy of the AIM in (5.76) as a derivative of the one-particle Green's function of the AIM instead. The derivation closely follows the one found in Appendix A of Ref. [198].

Let us first note some definitions and properties that will be useful for the derivation, all of which can e.g. be found in a textbook such as Ref. [47]. An operator A can be written in the Heisenberg picture for imaginary time τ as

$$A(\tau) = \exp(H\tau)A \exp(-H\tau), \quad (\text{B.1})$$

where H is the Hamiltonian. If the operator has no explicit time dependence, i.e. $\partial_\tau A = 0$ in the Schrödinger picture, and the Hamiltonian is time-independent as well, the derivative of the operator $A(\tau)$ in the Heisenberg picture is therefore

$$\partial_\tau A(\tau) = [H, A](\tau), \quad (\text{B.2})$$

where $[H, A] := HA - AH$ is the commutator. We define the time-ordering symbol T_τ in imaginary time for fermionic, i.e. anticommuting, operators $A(\tau_1)$ and $B(\tau_2)$ as

$$T_\tau A(\tau_1)B(\tau_2) = \theta(\tau_1 - \tau_2)A(\tau_1)B(\tau_2) - \theta(\tau_2 - \tau_1)B(\tau_2)A(\tau_1), \quad (\text{B.3})$$

where θ is the Heaviside step function, which is one for positive argument, zero for negative argument, and turns into the Dirac delta distribution when differentiated with respect to its argument. The anticommutation relations for fermionic creation and an-

annihilation operators c^\dagger and c are

$$\{c_\alpha(\tau_1), c_\beta(\tau_2)\} = 0, \quad (\text{B.4})$$

$$\{c_\alpha^\dagger(\tau_1), c_\beta^\dagger(\tau_2)\} = 0, \quad (\text{B.5})$$

$$\{c_\alpha(\tau_1), c_\beta^\dagger(\tau_2)\} = \delta_{\alpha\beta} \delta(\tau_1 - \tau_2), \quad (\text{B.6})$$

where $\{A, B\} := AB + BA$ is the anticommutator. Simple rules for the evaluation of commutators and anticommutators of products are

$$[AB, C] = A\{B, C\} - \{A, C\}B = A[B, C] + [A, C]B, \quad (\text{B.7a})$$

$$[A, BC] = \{A, B\}C - B\{A, C\} = B[A, C] + [A, B]C, \quad (\text{B.7b})$$

$$\{AB, C\} = A[B, C] + \{A, C\}B = A\{B, C\} - [A, C]B, \quad (\text{B.7c})$$

$$\{A, BC\} = B\{A, C\} + [A, B]C = \{A, B\}C - B[A, C], \quad (\text{B.7d})$$

which can be verified by using the definitions and elementary manipulations.

With the help of these basic relations we find that the time derivative of the one-particle Green's function with two time arguments (3.6) of the AIM, whose Hamiltonian is given in (2.1), is

$$\partial_{\tau_1} G_{\alpha\beta}(\tau_1, \tau_2) = -\partial_{\tau_1} \left\langle T_\tau c_\alpha(\tau_1) c_\beta^\dagger(\tau_2) \right\rangle \quad (\text{B.8})$$

$$= -\partial_{\tau_1} \left(\theta(\tau_1 - \tau_2) \left\langle c_\alpha(\tau_1) c_\beta^\dagger(\tau_2) \right\rangle - \theta(\tau_2 - \tau_1) \left\langle c_\beta^\dagger(\tau_2) c_\alpha(\tau_1) \right\rangle \right) \quad (\text{B.9})$$

$$= -\delta(\tau_1 - \tau_2) \delta_{\alpha\beta} - \left\langle T_\tau [H_{\text{AIM}}, c_\alpha](\tau_1) c_\beta^\dagger(\tau_2) \right\rangle, \quad (\text{B.10})$$

where we inserted the definition of time-ordering, and have the derivative of the step functions in the first term with the fermionic anticommutation relation for $\{c_\alpha, c_\beta^\dagger\}$ giving us $\delta_{\alpha\beta}$ and the derivative of the annihilation operator in Heisenberg picture in the second term.

We proceed by evaluating the commutator

$$[H_{\text{AIM}}, c_\alpha] = \sum_{\mu, \beta} E_{\mu\beta} [c_\mu^\dagger c_\beta, c_\alpha] + \sum_{\mu, \beta, \gamma, \delta} \frac{U_{\mu\beta\gamma\delta}}{2} [c_\mu^\dagger c_\beta^\dagger c_\delta c_\gamma, c_\alpha] \quad (\text{B.11})$$

$$+ \sum_{\mathbf{k}, \rho} \varepsilon_{\mathbf{k}\rho} [a_{\mathbf{k}\rho}^\dagger a_{\mathbf{k}\rho}, c_\alpha] + \sum_{\mathbf{k}, \mu, \rho} V_{\mathbf{k}\rho, \mu} [a_{\mathbf{k}\rho}^\dagger c_\mu, c_\alpha] + V_{\mathbf{k}\rho, \mu}^* [c_\mu^\dagger a_{\mathbf{k}\rho}, c_\alpha] \\ = - \sum_{\beta} E_{\alpha\beta} c_\beta - \sum_{\beta\gamma\delta} U_{[\alpha\beta]\gamma\delta} c_\beta^\dagger c_\delta c_\gamma - \sum_{\mathbf{k}, \rho} V_{\mathbf{k}\rho, \alpha}^* a_{\mathbf{k}\rho}, \quad (\text{B.12})$$

where we used the rules for products in (B.7) and fermionic anticommutation relations

once for most terms and several times for the interaction term, there also followed by renaming a summation index to collect terms and using the antisymmetrized interaction matrix $U_{[\alpha\beta]\gamma\delta} := \frac{1}{2}(U_{\alpha\beta\gamma\delta} - U_{\beta\alpha\gamma\delta})$ introduced in (3.13). We will further replace $q_\alpha := \sum_{\beta\gamma\delta} U_{[\alpha\beta]\gamma\delta} c_\beta^\dagger c_\delta c_\gamma$ as defined in (3.12) to reach the expression

$$\begin{aligned} \partial_{\tau_1} G_{\alpha\beta}(\tau_1, \tau_2) = & -\delta(\tau_1 - \tau_2)\delta_{\alpha\beta} + \sum_{\gamma} E_{\alpha\gamma} \left\langle T_{\tau} c_{\gamma}(\tau_1) c_{\beta}^{\dagger}(\tau_2) \right\rangle + \left\langle T_{\tau} q_{\alpha}(\tau_1) c_{\beta}^{\dagger}(\tau_2) \right\rangle \\ & + \sum_{\mathbf{k}, \rho} V_{\mathbf{k}\rho, \alpha}^* \left\langle T_{\tau} a_{\mathbf{k}\rho}(\tau_1) c_{\beta}^{\dagger}(\tau_2) \right\rangle \end{aligned} \quad (\text{B.13})$$

for the time derivative of the impurity Green's function.

Similarly to (B.8), but with no delta term because a and c^\dagger always anticommute, we can compute the time derivative of the mixed Green's function in the last term as

$$\partial_{\tau_1} \left\langle T_{\tau} a_{\mathbf{k}\rho}(\tau_1) c_{\beta}^{\dagger}(\tau_2) \right\rangle = \left\langle T_{\tau} [H_{\text{AIM}}, a_{\mathbf{k}\rho}](\tau_1) c_{\beta}^{\dagger}(\tau_2) \right\rangle. \quad (\text{B.14})$$

Using the rules for products, the commutator can be evaluated even more easily this time to yield

$$\begin{aligned} [H_{\text{AIM}}, a_{\mathbf{k}\rho}] = & \sum_{\alpha, \beta} E_{\alpha\beta} [c_{\alpha}^{\dagger} c_{\beta}, a_{\mathbf{k}\rho}] + \sum_{\alpha, \beta, \gamma, \delta} \frac{U_{\alpha\beta\gamma\delta}}{2} [c_{\alpha}^{\dagger} c_{\beta}^{\dagger} c_{\delta} c_{\gamma}, a_{\mathbf{k}\rho}] \\ & + \sum_{\mathbf{q}, \mu} \varepsilon_{\mathbf{q}\mu} [a_{\mathbf{q}\mu}^{\dagger} a_{\mathbf{q}\mu}, a_{\mathbf{k}\rho}] + \sum_{\mathbf{q}, \alpha, \mu} V_{\mathbf{q}\mu, \alpha} [a_{\mathbf{q}\mu}^{\dagger} c_{\alpha}, a_{\mathbf{k}\rho}] + V_{\mathbf{q}\mu, \alpha}^* [c_{\alpha}^{\dagger} a_{\mathbf{q}\mu}, a_{\mathbf{k}\rho}] \\ = & -\varepsilon_{\mathbf{k}\rho} a_{\mathbf{k}\rho} - \sum_{\alpha} V_{\mathbf{k}\rho, \alpha} c_{\alpha}. \end{aligned} \quad (\text{B.15})$$

$$= -\varepsilon_{\mathbf{k}\rho} a_{\mathbf{k}\rho} - \sum_{\alpha} V_{\mathbf{k}\rho, \alpha} c_{\alpha}. \quad (\text{B.16})$$

Inserting this into (B.14), we get the expression

$$\partial_{\tau_1} \left\langle T_{\tau} a_{\mathbf{k}\rho}(\tau_1) c_{\beta}^{\dagger}(\tau_2) \right\rangle = -\varepsilon_{\mathbf{k}\rho} \left\langle T_{\tau} a_{\mathbf{k}\rho}(\tau_1) c_{\beta}^{\dagger}(\tau_2) \right\rangle - \sum_{\alpha} V_{\mathbf{k}\rho, \alpha} \left\langle T_{\tau} c_{\alpha}(\tau_1) c_{\beta}^{\dagger}(\tau_2) \right\rangle \quad (\text{B.17})$$

for the time derivative of the mixed Green's function.

We get rid of the time derivative in this equation by first applying the Fourier transform $\int_0^{\beta} d\tau_1 \exp(i\nu_1 \tau_1)$ from τ_1 to fermionic Matsubara frequency ν_1

$$\begin{aligned} \int_0^{\beta} d\tau_1 e^{i\nu_1 \tau_1} \partial_{\tau_1} \left\langle T_{\tau} a_{\mathbf{k}\rho}(\tau_1) c_{\beta}^{\dagger}(\tau_2) \right\rangle = & -\varepsilon_{\mathbf{k}\rho} \int_0^{\beta} d\tau_1 e^{i\nu_1 \tau_1} \left\langle T_{\tau} a_{\mathbf{k}\rho}(\tau_1) c_{\beta}^{\dagger}(\tau_2) \right\rangle \\ & - \sum_{\alpha} V_{\mathbf{k}\rho, \alpha} \int_0^{\beta} d\tau_1 e^{i\nu_1 \tau_1} \left\langle T_{\tau} c_{\alpha}(\tau_1) c_{\beta}^{\dagger}(\tau_2) \right\rangle \end{aligned} \quad (\text{B.18})$$

and then integrating the integral containing the time derivative by parts to obtain

$$\int_0^\beta d\tau_1 e^{i\nu_1\tau_1} \left\langle T_\tau a_{\mathbf{k}\rho}(\tau_1) c_\beta^\dagger(\tau_2) \right\rangle = \sum_\alpha \frac{V_{\mathbf{k}\rho,\alpha}}{i\nu_1 - \varepsilon_{\mathbf{k}\rho}} \int_0^\beta d\tau_1 e^{i\nu_1\tau_1} \left\langle T_\tau c_\alpha(\tau_1) c_\beta^\dagger(\tau_2) \right\rangle, \quad (\text{B.19})$$

where boundary terms vanished as $e^{i\nu_1\beta} = -1$ for a fermionic Matsubara frequency ν_1 and the value of the two-time Green's function for $\tau_1 = 0$ differs from that for $\tau_1 = \beta$ by a minus sign only due to β -antiperiodicity, cf. Sec. 5.2.2. From the term with the derivative of the exponential we got an extra factor of $-i\nu_1$, and bringing all the coefficients together we get a coefficient that is almost the hybridization function (2.10).

After applying the same Fourier transform and integration by parts to our last expression so far for the equation of motion of the impurity Green's function (B.13), we can insert the equation of motion (B.19) for the mixed Green's function to get an equation purely in terms of correlation functions of impurity operators,

$$\begin{aligned} -i\nu_1 \int_0^\beta d\tau_1 e^{i\nu_1\tau_1} G_{\alpha\beta}(\tau_1, \tau_2) &= - \int_0^\beta d\tau_1 e^{i\nu_1\tau_1} \delta(\tau_1 - \tau_2) \delta_{\alpha\beta} \\ &+ \sum_\gamma E_{\alpha\gamma} \int_0^\beta d\tau_1 e^{i\nu_1\tau_1} \left\langle T_\tau c_\gamma(\tau_1) c_\beta^\dagger(\tau_2) \right\rangle \\ &+ \int_0^\beta d\tau_1 e^{i\nu_1\tau_1} \left\langle T_\tau q_\alpha(\tau_1) c_\beta^\dagger(\tau_2) \right\rangle \\ &+ \sum_{\mathbf{k},\rho,\mu} \frac{V_{\mathbf{k}\rho,\alpha}^* V_{\mathbf{k}\rho,\mu}}{i\nu_1 - \varepsilon_{\mathbf{k}\rho}} \int_0^\beta d\tau_1 e^{i\nu_1\tau_1} \left\langle T_\tau c_\mu(\tau_1) c_\beta^\dagger(\tau_2) \right\rangle, \end{aligned} \quad (\text{B.20})$$

where we can actually identify the second and fourth term on the right-hand side as matrix products with impurity Green's functions, and the matrix in the fourth term is now exactly the hybridization function $\Delta_{\alpha\mu}(i\nu_1)$ defined in (2.10). Bringing all these terms to one side and adjusting all index names, we have

$$\begin{aligned} \sum_\mu (i\nu_1 \delta_{\alpha\mu} - E_{\alpha\mu} - \Delta_{\alpha\mu}(i\nu_1)) \int_0^\beta d\tau_1 e^{i\nu_1\tau_1} G_{\mu\beta}(\tau_1, \tau_2) \\ = e^{i\nu_1\tau_2} \delta_{\alpha\beta} - \int_0^\beta d\tau_1 e^{i\nu_1\tau_1} \left\langle T_\tau q_\alpha(\tau_1) c_\beta^\dagger(\tau_2) \right\rangle, \end{aligned} \quad (\text{B.21})$$

where we can further identify $\mathcal{G}_{0,\alpha\mu}^{-1}(i\nu_1) = (i\nu_1 \delta_{\alpha\mu} - E_{\alpha\mu} - \Delta_{\alpha\mu}(i\nu_1))$ to get

$$\sum_\mu \mathcal{G}_{0,\alpha\mu}^{-1}(i\nu_1) \int_0^\beta d\tau_1 e^{i\nu_1\tau_1} G_{\mu\beta}(\tau_1, \tau_2) = e^{i\nu_1\tau_2} \delta_{\alpha\beta} - \int_0^\beta d\tau_1 e^{i\nu_1\tau_1} \left\langle T_\tau q_\alpha(\tau_1) c_\beta^\dagger(\tau_2) \right\rangle. \quad (\text{B.22})$$

By Fourier transforming this equation from time τ_2 to Matsubara frequency ν_2 with $\int_0^\beta d\tau_2 \exp(-i\nu_2\tau_2)$, canceling the appearing factor of β (cf. Appendix A), multiplying the matrix \mathcal{G}_0 from the left to bring \mathcal{G}_0 to the other side, renaming some indices, and identifying the last term as the correlation function ξ defined in (3.11), we can get the improved estimator equation (3.10).

If we want to proceed to the symmetric improved estimator equation, we instead continue by computing the equation of motion for the correlation function in the last term by differentiating with respect to τ_2 analogously to (B.10),

$$\partial_{\tau_2} \left\langle T_\tau q_\alpha(\tau_1) c_\beta^\dagger(\tau_2) \right\rangle = -\delta(\tau_1 - \tau_2) \left\langle \{q_\alpha, c_\beta^\dagger\}(\tau_1) \right\rangle + \left\langle T_\tau q_\alpha(\tau_1) [H_{\text{AIM}}, c_\beta^\dagger](\tau_2) \right\rangle. \quad (\text{B.23})$$

We calculate the anticommutator using the definition (3.12) of q and rule (B.7c) followed by rule (B.7a) as

$$\{q_\alpha, c_\beta^\dagger\} = \sum_{\mu\gamma\delta} U_{[\alpha\mu]\gamma\delta} \{c_\mu^\dagger c_\delta c_\gamma, c_\beta^\dagger\} = \sum_{\mu\gamma\delta} U_{[\alpha\mu]\gamma\delta} (c_\mu^\dagger c_\delta \delta_{\gamma\beta} - c_\mu^\dagger \delta_{\delta\beta} c_\gamma) = 2 \sum_{\mu\gamma} U_{[\alpha\mu][\beta\gamma]} c_\mu^\dagger c_\gamma \quad (\text{B.24})$$

using definition (3.13) again, and for the commutator with the Hamiltonian we can just reuse (B.12) by applying $[A, B]^\dagger = -[A^\dagger, B^\dagger]$, which gives us

$$[H_{\text{AIM}}, c_\beta^\dagger] = \sum_{\delta} E_{\beta\delta}^* c_\delta^\dagger + q_\beta^\dagger + \sum_{\mathbf{k},\rho} V_{\mathbf{k}\rho,\beta} a_{\mathbf{k}\rho}^\dagger \quad (\text{B.25})$$

using definition (3.12) and keeping in mind that $U_{\alpha\beta\gamma\delta} = U_{\gamma\delta\alpha\beta}^*$ due to hermiticity of the Hamiltonian.

Using these to evaluate the terms of the equation of motion (B.23) for ξ , we obtain

$$\begin{aligned} \partial_{\tau_2} \left\langle T_\tau q_\alpha(\tau_1) c_\beta^\dagger(\tau_2) \right\rangle &= -2\delta(\tau_1 - \tau_2) \sum_{\mu\gamma} U_{[\alpha\mu][\beta\gamma]} \left\langle c_\mu^\dagger c_\gamma \right\rangle + \sum_{\delta} E_{\beta\delta}^* \left\langle T_\tau q_\alpha(\tau_1) c_\delta^\dagger(\tau_2) \right\rangle \\ &\quad + \left\langle T_\tau q_\alpha(\tau_1) q_\beta^\dagger(\tau_2) \right\rangle + \sum_{\mathbf{k},\rho} V_{\mathbf{k}\rho,\beta} \left\langle T_\tau q_\alpha(\tau_1) a_{\mathbf{k}\rho}^\dagger(\tau_2) \right\rangle \end{aligned} \quad (\text{B.26})$$

and proceed again by computing the equation of motion for the mixed correlation function including the bath operator by differentiating it with respect to τ_2 .

With no delta term again as q and a^\dagger anticommute, we have

$$\partial_{\tau_2} \left\langle T_\tau q_\alpha(\tau_1) a_{\mathbf{k}\rho}^\dagger(\tau_2) \right\rangle = \left\langle T_\tau q_\alpha(\tau_1) [H_{\text{AIM}}, a_{\mathbf{k}\rho}^\dagger](\tau_2) \right\rangle \quad (\text{B.27})$$

where a previously calculated commutator, (B.16), can again be reused

$$[H_{\text{AIM}}, a_{\mathbf{k}\rho}^\dagger] = \varepsilon_{\mathbf{k}\rho} a_{\mathbf{k}\rho}^\dagger + \sum_{\mu} V_{\mathbf{k}\rho, \mu}^* c_{\mu}^\dagger. \quad (\text{B.28})$$

We perform the Fourier transform $\int_0^\beta d\tau_2 \exp(-i\nu_2\tau_2)$ of (B.27) from time τ_2 to Matsubara frequency ν_2

$$\begin{aligned} \int_0^\beta d\tau_2 e^{-i\nu_2\tau_2} \partial_{\tau_2} \left\langle T_{\tau} q_{\alpha}(\tau_1) a_{\mathbf{k}\rho}^\dagger(\tau_2) \right\rangle &= \varepsilon_{\mathbf{k}\rho} \int_0^\beta d\tau_2 e^{-i\nu_2\tau_2} \left\langle T_{\tau} q_{\alpha}(\tau_1) a_{\mathbf{k}\rho}^\dagger(\tau_2) \right\rangle \\ &+ \sum_{\mu} V_{\mathbf{k}\rho, \mu}^* \int_0^\beta d\tau_2 e^{-i\nu_2\tau_2} \left\langle T_{\tau} q_{\alpha}(\tau_1) c_{\mu}^\dagger(\tau_2) \right\rangle \end{aligned} \quad (\text{B.29})$$

and integrate by parts like before from (B.18) to (B.19) yielding

$$\int_0^\beta d\tau_2 e^{-i\nu_2\tau_2} \left\langle T_{\tau} q_{\alpha}(\tau_1) a_{\mathbf{k}\rho}^\dagger(\tau_2) \right\rangle = \sum_{\mu} \frac{V_{\mathbf{k}\rho, \mu}^*}{i\nu_2 - \varepsilon_{\mathbf{k}\rho}} \int_0^\beta d\tau_2 e^{-i\nu_2\tau_2} \left\langle T_{\tau} q_{\alpha}(\tau_1) c_{\mu}^\dagger(\tau_2) \right\rangle. \quad (\text{B.30})$$

Inserting into (B.26) after first Fourier transforming it we obtain an equation in terms of impurity correlation functions only

$$\begin{aligned} i\nu_2 \int_0^\beta d\tau_2 e^{-i\nu_2\tau_2} \left\langle T_{\tau} q_{\alpha}(\tau_1) c_{\beta}^\dagger(\tau_2) \right\rangle &= -2e^{-i\nu_2\tau_1} \sum_{\mu\gamma} U_{[\alpha\mu][\beta\gamma]} \left\langle c_{\mu}^\dagger c_{\gamma} \right\rangle \\ &+ \sum_{\delta} E_{\beta\delta}^* \int_0^\beta d\tau_2 e^{-i\nu_2\tau_2} \left\langle T_{\tau} q_{\alpha}(\tau_1) c_{\delta}^\dagger(\tau_2) \right\rangle \\ &+ \int_0^\beta d\tau_2 e^{-i\nu_2\tau_2} \left\langle T_{\tau} q_{\alpha}(\tau_1) q_{\beta}^\dagger(\tau_2) \right\rangle \\ &+ \sum_{\mu} \Delta_{\mu\beta}(i\nu_2) \left\langle T_{\tau} q_{\alpha}(\tau_1) c_{\mu}^\dagger(\tau_2) \right\rangle \end{aligned}$$

that can be rearranged to

$$\begin{aligned} \sum_{\mu} (i\nu_2 \delta_{\mu\beta} - E_{\mu\beta} - \Delta_{\mu\beta}(i\nu_2)) \int_0^\beta d\tau_2 e^{-i\nu_2\tau_2} \left\langle T_{\tau} q_{\alpha}(\tau_1) c_{\mu}^\dagger(\tau_2) \right\rangle & \quad (\text{B.31}) \\ = -2e^{-i\nu_2\tau_1} \sum_{\mu\gamma} U_{[\alpha\mu][\beta\gamma]} \left\langle c_{\mu}^\dagger c_{\gamma} \right\rangle + \int_0^\beta d\tau_2 e^{-i\nu_2\tau_2} \left\langle T_{\tau} q_{\alpha}(\tau_1) q_{\beta}^\dagger(\tau_2) \right\rangle, \end{aligned}$$

where we can identify $\mathcal{G}_{0, \mu\beta}^{-1}(i\nu_2) = (i\nu_2 \delta_{\mu\beta} - E_{\mu\beta} - \Delta_{\mu\beta}(i\nu_2))$, but this time the sum over its indices is equivalent to the matrix product of $\mathcal{G}_0^{-1}(i\nu_2)$ and the correlation function

with $\mathcal{G}_0^{-1}(iv_2)$ as the *right* factor.

Fourier transforming this equation from time τ_1 to Matsubara frequency ν_1 with $\int_0^\beta d\tau_1 \exp(iv_1\tau_1)$, bringing \mathcal{G}_0 to the other side and using the definitions (3.11) of ξ and (3.15) of \mathfrak{D} results in

$$\xi_{\alpha\delta}^{\nu_2} = 2 \sum_{\mu\gamma\beta} U_{[\alpha\mu][\beta\gamma]} \langle c_\mu^\dagger c_\gamma \rangle \mathcal{G}_{0,\beta\delta}^{\nu_2} + \mathfrak{D}_{\alpha\beta}^{\nu_2} \mathcal{G}_{0,\beta\delta}^{\nu_2}, \quad (\text{B.32})$$

which can be inserted into the improved estimator equation (3.10) to obtain the symmetric improved estimator equation (3.14).

Let us finally show how to derive the Galitskii-Migdal expression for the potential energy, for which we return to equation (B.22). We explicitly perform the Fourier transform from τ_2 to fermionic Matsubara frequency ν_2 to obtain

$$\sum_{\mu} \mathcal{G}_{0,\alpha\mu}^{-1}(iv) G_{\mu\beta}(iv) = \delta_{\alpha\beta} - \int_0^\beta d\tau_1 d\tau_2 e^{iv(\tau_1-\tau_2)} \langle T_\tau q_\alpha(\tau_1) c_\beta^\dagger(\tau_2) \rangle, \quad (\text{B.33})$$

where we may retain only one fermionic Matsubara frequency on the left-hand side for reasons discussed in Appendix A. Multiplying the Dyson equation $G_{\mu\beta}(iv) = \mathcal{G}_{0,\mu\beta}(iv) + \sum_{\gamma,\rho} \mathcal{G}_{0,\mu\gamma}(iv) \Sigma_{\gamma\rho}(iv) G_{\rho\beta}(iv)$ with \mathcal{G}_0^{-1} from the left, we can insert it into (B.33) and are left with

$$\sum_{\mu} \Sigma_{\alpha\mu}(iv) G_{\mu\beta}(iv) = - \int_0^\beta d\tau_1 d\tau_2 e^{iv(\tau_1-\tau_2)} \langle T_\tau q_\alpha(\tau_1) c_\beta^\dagger(\tau_2) \rangle. \quad (\text{B.34})$$

Considering the definition (3.12) of q , to get something resembling the potential energy $\langle H_{\text{loc,int}} \rangle$ (cf. (2.1)) we want to evaluate the correlation function on the right-hand side at $\tau_1 - \tau_2 \rightarrow 0^-$, which gives us exactly the right operator product, and further take the trace to sum over the free outer indices in just the same way as in $\langle H_{\text{loc,int}} \rangle$. For the evaluation, we can just apply the transform back from Matsubara frequencies $\beta^{-1} \sum_{\nu_n} \exp(-i\nu_n\beta^-) = -\beta^{-1} \sum_{\nu_n}$, where we use the value $\tau \rightarrow \beta^-$ in $[0, \beta]$ instead keeping in mind that fermionic correlation functions are β -antiperiodic. This already takes care of the sign we would get from performing time order, so we have

$$\beta^{-1} \sum_{\alpha,\mu,\nu_n} \Sigma_{\alpha\mu}(iv_n) G_{\mu\alpha}(iv_n) = \sum_{\alpha\rho\gamma\delta} U_{[\alpha\rho]\gamma\delta} \langle c_\alpha^\dagger c_\rho^\dagger c_\delta c_\gamma \rangle \quad (\text{B.35})$$

and with the definition (3.13) of the antisymmetrized U , whose second term requires an

exchange of creators to agree with the order in $H_{\text{loc,int}}$, we finally arrive at the expression

$$\frac{1}{2\beta} \sum_{\alpha,\mu,\nu_n} \Sigma_{\alpha\mu}(i\nu_n) G_{\mu\alpha}(i\nu_n) = \sum_{\alpha\rho\gamma\delta} \frac{U_{\alpha\rho\gamma\delta}}{2} \langle c_\alpha^\dagger c_\rho^\dagger c_\delta c_\gamma \rangle = \langle H_{\text{loc,int}} \rangle \quad (\text{B.36})$$

for the potential energy.

Acknowledgments

The accomplishment of this thesis would not have been possible without the support of various people. Most importantly, I am very grateful to my supervisor Giorgio Sangiovanni for giving me the opportunity to work in his group on interesting topics from the world of strong correlations, for answering numerous questions in spite of his usually busy schedule, and for providing a lot of helpful feedback on my work and writing.

I thank Karsten Held and the members of his group for their hospitality and interesting discussions during my visit to Vienna and his students Patrik Gunacker and Josef Kaufmann in particular for our extensive and productive collaboration on CT-HYB developments and improvements to the *w2dynamics* code, illuminating discussions about technical as well as physical aspects and the latter also for writing a user-friendly package for analytical continuation and sharing his knowledge about the subject. Markus Wallerberger also helpfully answered my occasional questions on details of the *w2dynamics* code, provided feedback on changes, and discussed interesting ideas for potential developments.

To Luca de' Medici I am grateful for many discussions in the context of our collaborations on the Hubbard model with Hund's coupling and for his feedback on the related section of this thesis, and to his group members Maria Chatzieleftheriou, Matteo Crispino, and Karla Baumann for related collaborations or discussions.

As far as the physics of two-particle quantities is concerned, I thank Thomas Schäfer, Matthias Reitner, Alessandro Toschi, and Lorenzo Del Re for helpful discussions and explanations particularly in relation to our common project and Georg Rohringer for an interesting introductory seminar talk and personal discussions on related topics.

For our pleasant and motivating work environment and occasional discussions about physics and other things I am grateful to current and former fellow group members and office mates, including Andi, Michael, Martin, Philipp, Domenico, Marius, Severino, Niklas, Stefan, Lorenzo, and Max. In particular, I thank Andreas Hausoel for initiating the project on improved sampling I started working on for my Master's thesis and explanations of as well as long-time collaboration on the development of the *w2dynamics* code, Lorenzo Crippa for helping me with the use of the *EDIPack* package, and Michael Karolak and Domenico Di Sante for providing the DFT results for some of our projects and helpfully responding to any questions about them.

I am grateful to Angelo Valli for feedback on a section of this thesis and to him and Marc Philipp Bahlke for discussions on our Kondo project, and of course also to all collaborators on any of my projects not explicitly mentioned so far.

Finally, I would like to thank my family for their support during all my years of study.

Bibliography

Please note that potentially available supplemental material published together with a listed item should be considered implicitly included in the corresponding bibliography entry and is not listed separately.

- ¹P. A. M. Dirac, "Quantum mechanics of many-electron systems," *Proceedings of the Royal Society of London. Series A, Containing Papers of a Mathematical and Physical Character* **123**, 714–733 (1929) (cit. on p. 9).
- ²J. Dongarra, "Trends in high performance computing: a historical overview and examination of future developments," *IEEE Circuits and Devices Magazine* **22**, 22–27 (2006) (cit. on p. 9).
- ³H. Lin, J. Gubernatis, H. Gould, and J. Tobochnik, "Exact Diagonalization Methods for Quantum Systems," *Computers in Physics* **7**, 400–407 (1993) (cit. on p. 9).
- ⁴M. Caffarel and W. Krauth, "Exact diagonalization approach to correlated fermions in infinite dimensions: Mott transition and superconductivity," *Phys. Rev. Lett.* **72**, 1545–1548 (1994) (cit. on pp. 9, 15, 18, 129).
- ⁵K. Capelle and V. L. Campo, "Density functionals and model Hamiltonians: Pillars of many-particle physics," *Physics Reports, Density functionals and model Hamiltonians: Pillars of many-particle physics* **528**, 91–159 (2013) (cit. on p. 9).
- ⁶R. O. Jones and O. Gunnarsson, "The density functional formalism, its applications and prospects," *Rev. Mod. Phys.* **61**, 689–746 (1989) (cit. on pp. 9, 34).
- ⁷R. O. Jones, "Density functional theory: Its origins, rise to prominence, and future," *Rev. Mod. Phys.* **87**, 897–923 (2015) (cit. on pp. 9, 10).
- ⁸P. A. M. Dirac, "Note on Exchange Phenomena in the Thomas Atom," *Mathematical Proceedings of the Cambridge Philosophical Society* **26**, 376–385 (1930) (cit. on p. 9).
- ⁹L. H. Thomas, "The calculation of atomic fields," *Mathematical Proceedings of the Cambridge Philosophical Society* **23**, 542–548 (1927) (cit. on p. 9).
- ¹⁰E. Fermi, "Eine statistische Methode zur Bestimmung einiger Eigenschaften des Atoms und ihre Anwendung auf die Theorie des periodischen Systems der Elemente," *Z. Physik* **48**, 73–79 (1928) (cit. on p. 9).

- ¹¹D. R. Hartree, “The Wave Mechanics of an Atom with a Non-Coulomb Central Field. Part I. Theory and Methods,” *Mathematical Proceedings of the Cambridge Philosophical Society* **24**, 89–110 (1928) (cit. on p. 9).
- ¹²D. R. Hartree, “The Wave Mechanics of an Atom with a Non-Coulomb Central Field. Part II. Some Results and Discussion,” *Mathematical Proceedings of the Cambridge Philosophical Society* **24**, 111–132 (1928) (cit. on p. 9).
- ¹³V. Fock, “Näherungsmethode zur Lösung des quantenmechanischen Mehrkörperproblems,” *Z. Physik* **61**, 126–148 (1930) (cit. on p. 9).
- ¹⁴J. C. Slater, “Note on Hartree’s Method,” *Phys. Rev.* **35**, 210–211 (1930) (cit. on p. 9).
- ¹⁵P. Hohenberg and W. Kohn, “Inhomogeneous Electron Gas,” *Phys. Rev.* **136**, B864–B871 (1964) (cit. on pp. 9, 34).
- ¹⁶W. Kohn and L. J. Sham, “Self-Consistent Equations Including Exchange and Correlation Effects,” *Phys. Rev.* **140**, A1133–A1138 (1965) (cit. on pp. 9, 34).
- ¹⁷W. Kohn, “Nobel Lecture: Electronic structure of matter—wave functions and density functionals,” *Rev. Mod. Phys.* **71**, 1253–1266 (1999) (cit. on p. 10).
- ¹⁸G. R. Stewart, “Non-Fermi-liquid behavior in *d*- and *f*-electron metals,” *Rev. Mod. Phys.* **73**, 797–855 (2001) (cit. on p. 10).
- ¹⁹G. Kotliar, S. Y. Savrasov, K. Haule, V. S. Oudovenko, O. Parcollet, and C. A. Marianetti, “Electronic structure calculations with dynamical mean-field theory,” *Rev. Mod. Phys.* **78**, 865–951 (2006) (cit. on pp. 10, 34).
- ²⁰A. Georges, L. de’Medici, and J. Mravlje, “Strong Correlations from Hund’s Coupling,” *Annual Review of Condensed Matter Physics* **4**, 137–178 (2013) (cit. on pp. 10, 15, 32, 51, 126–128).
- ²¹N. F. Mott, “The transition to the metallic state,” *Philos. Mag.* **6**, 287–309 (1961) (cit. on pp. 10, 33, 124).
- ²²D. B. McWhan, A. Menth, J. P. Remeika, W. F. Brinkman, and T. M. Rice, “Metal-Insulator Transitions in Pure and Doped V_2O_3 ,” *Phys. Rev. B* **7**, 1920–1931 (1973) (cit. on p. 10).
- ²³M. Imada, A. Fujimori, and Y. Tokura, “Metal-insulator transitions,” *Rev. Mod. Phys.* **70**, 1039–1263 (1998) (cit. on pp. 10, 32, 120, 126, 128).
- ²⁴J. G. Bednorz and K. A. Müller, “Possible high T_c superconductivity in the Ba–La–Cu–O system,” *Z. Physik B - Condensed Matter* **64**, 189–193 (1986) (cit. on p. 10).
- ²⁵M. Capone, M. Fabrizio, C. Castellani, and E. Tosatti, “Strongly Correlated Superconductivity,” *Science* **296**, 2364–2366 (2002) (cit. on p. 10).

- ²⁶P. A. Lee, N. Nagaosa, and X.-G. Wen, “Doping a Mott insulator: Physics of high-temperature superconductivity,” *Rev. Mod. Phys.* **78**, 17–85 (2006) (cit. on p. 10).
- ²⁷Y. Kamihara, T. Watanabe, M. Hirano, and H. Hosono, “Iron-Based Layered Superconductor $\text{La}[\text{O}_{1-x}\text{F}_x]\text{FeAs}$ ($x = 0.05\text{--}0.12$) with $T_c = 26\text{ K}$,” *J. Am. Chem. Soc.* **130**, 3296–3297 (2008) (cit. on pp. 10, 126).
- ²⁸J. Kondo, “Resistance Minimum in Dilute Magnetic Alloys,” *Prog. Theor. Phys.* **32**, 37–49 (1964) (cit. on pp. 10, 73, 74, 98, 110).
- ²⁹Z. Fisk, H. R. Ott, T. M. Rice, and J. L. Smith, “Heavy-electron metals,” *Nature* **320**, 124–129 (1986) (cit. on p. 10).
- ³⁰A. P. Ramirez, “Colossal magnetoresistance,” *J. Phys.: Condens. Matter* **9**, 8171 (1997) (cit. on p. 10).
- ³¹J. Hubbard, “Electron correlations in narrow energy bands,” *Proc. R. Soc. Lond. A* **276**, 238–257 (1963) (cit. on pp. 10, 13, 18, 32, 124).
- ³²P. W. Anderson, “Localized Magnetic States in Metals,” *Phys. Rev.* **124**, 41–53 (1961) (cit. on pp. 10, 13).
- ³³A. Georges, G. Kotliar, W. Krauth, and M. J. Rozenberg, “Dynamical mean-field theory of strongly correlated fermion systems and the limit of infinite dimensions,” *Rev. Mod. Phys.* **68**, 13–125 (1996) (cit. on pp. 10, 13, 32, 33, 37, 124, 132, 135, 160, 165, 168, 174–176, 178–180, 193).
- ³⁴P. Werner, A. Comanac, L. de’Medici, M. Troyer, and A. J. Millis, “Continuous-Time Solver for Quantum Impurity Models,” *Phys. Rev. Lett.* **97**, 076405 (2006) (cit. on pp. 10, 17, 18, 20, 23, 28, 29, 94, 129).
- ³⁵P. Werner, E. Gull, M. Troyer, and A. J. Millis, “Spin Freezing Transition and Non-Fermi-Liquid Self-Energy in a Three-Orbital Model,” *Phys. Rev. Lett.* **101**, 166405 (2008) (cit. on pp. 10, 51–54, 119, 127, 128, 161).
- ³⁶E. Gull, A. J. Millis, A. I. Lichtenstein, A. N. Rubtsov, M. Troyer, and P. Werner, “Continuous-time Monte Carlo methods for quantum impurity models,” *Rev. Mod. Phys.* **83**, 349–404 (2011) (cit. on pp. 13, 15, 17, 18, 21, 22, 28, 29, 31, 41, 50, 56, 57, 64, 65, 74, 129).
- ³⁷F. Aryasetiawan, K. Karlsson, O. Jepsen, and U. Schönberger, “Calculations of Hubbard U from first-principles,” *Phys. Rev. B* **74**, 125106 (2006) (cit. on pp. 14, 78, 119).
- ³⁸E. Şaşıoğlu, C. Friedrich, and S. Blügel, “Effective Coulomb interaction in transition metals from constrained random-phase approximation,” *Phys. Rev. B* **83**, 121101 (2011) (cit. on pp. 14, 78, 104, 106, 119).

- ³⁹M. Karolak, “Electronic Correlation Effects in Transition Metal Systems: From Bulk Crystals to Nanostructures,” PhD thesis (Universität Hamburg, 2013) (cit. on pp. 14, 15, 78, 93, 95, 104).
- ⁴⁰M. Wallerberger, A. Hausoel, P. Gunacker, A. Kowalski, N. Parragh, F. Goth, K. Held, and G. Sangiovanni, “W2dynamics: Local one- and two-particle quantities from dynamical mean field theory,” *Computer Physics Communications* **235**, 388–399 (2019) (cit. on pp. 14, 15, 23, 24, 34, 35, 51, 66, 103, 119, 129, 167, 185).
- ⁴¹J. Kanamori, “Electron Correlation and Ferromagnetism of Transition Metals,” *Prog. Theor. Phys.* **30**, 275–289 (1963) (cit. on pp. 15, 32, 77).
- ⁴²F. Hund, “Zur Deutung verwickelter Spektren, insbesondere der Elemente Scandium bis Nickel,” *Z. Physik* **33**, 345–371 (1925) (cit. on pp. 15, 126).
- ⁴³J. W. Negele and H. Orland, *Quantum many-particle systems* (Perseus Books, Reading, MA, 1998) (cit. on pp. 15, 16, 36, 152).
- ⁴⁴T. Matsubara, “A New Approach to Quantum-Statistical Mechanics,” *Prog. Theor. Phys.* **14**, 351–378 (1955) (cit. on p. 16).
- ⁴⁵A. Abrikosov, L. Gorkov, and I. Dzyaloshinskii, “On the application of quantum-field-theory methods to problems of quantum statistics at finite temperatures,” *Sov. Phys. JETP* **9**, 636–641 (1959) (cit. on p. 16).
- ⁴⁶A. A. Abrikosov, L. P. Gorkov, and I. E. Dzyaloshinski, *Methods of quantum field theory in statistical physics*, Rev. English ed. (Dover Publications, New York, 1975) (cit. on pp. 16, 36).
- ⁴⁷H. Bruus and K. Flensberg, *Many-body quantum theory in condensed matter physics: an introduction*, Oxford graduate texts (Oxford University Press, Oxford ; New York, 2004) (cit. on pp. 16, 17, 20, 36, 37, 39, 40, 57, 60, 124, 135, 150, 168, 175, 203, 207).
- ⁴⁸G. C. Wick, “The Evaluation of the Collision Matrix,” *Phys. Rev.* **80**, 268–272 (1950) (cit. on p. 17).
- ⁴⁹A. N. Rubtsov and A. I. Lichtenstein, “Continuous-time quantum Monte Carlo method for fermions: Beyond auxiliary field framework,” *Jetp Lett.* **80**, 61–65 (2004) (cit. on pp. 17, 18).
- ⁵⁰E. Gull, “Continuous-Time Quantum Monte Carlo Algorithms for Fermions,” Doctoral Thesis (ETH Zurich, 2008) (cit. on pp. 17, 25, 31).
- ⁵¹J. E. Hirsch and R. M. Fye, “Monte Carlo Method for Magnetic Impurities in Metals,” *Phys. Rev. Lett.* **56**, 2521–2524 (1986) (cit. on p. 17).
- ⁵²R. L. Stratonovich, “On a method of calculating quantum distribution functions,” *Sov. Phys. Dokl.* **2**, 416–419 (1957) (cit. on p. 17).

- ⁵³J. Hubbard, "Calculation of Partition Functions," *Phys. Rev. Lett.* **3**, 77–78 (1959) (cit. on p. 17).
- ⁵⁴S. R. White, "Density matrix formulation for quantum renormalization groups," *Phys. Rev. Lett.* **69**, 2863–2866 (1992) (cit. on p. 18).
- ⁵⁵U. Schollwöck, "The density-matrix renormalization group," *Rev. Mod. Phys.* **77**, 259–315 (2005) (cit. on p. 18).
- ⁵⁶Y. Núñez Fernández and K. Hallberg, "Solving the Multi-site and Multi-orbital Dynamical Mean Field Theory Using Density Matrix Renormalization," *Frontiers in Physics* **6**, 13 (2018) (cit. on p. 18).
- ⁵⁷K. G. Wilson, "The renormalization group: Critical phenomena and the Kondo problem," *Rev. Mod. Phys.* **47**, 773–840 (1975) (cit. on pp. 18, 74, 82, 114, 120).
- ⁵⁸R. Bulla, T. A. Costi, and T. Pruschke, "Numerical renormalization group method for quantum impurity systems," *Rev. Mod. Phys.* **80**, 395–450 (2008) (cit. on pp. 18, 129).
- ⁵⁹K. Held, "Electronic structure calculations using dynamical mean field theory," *Advances in Physics* **56**, 829–926 (2007) (cit. on pp. 18, 34).
- ⁶⁰K. Yosida and K. Yamada, "Perturbation Expansion for the Anderson Hamiltonian," *Prog. Theor. Phys. Suppl.* **46**, 244–255 (1970) (cit. on p. 18).
- ⁶¹K. Yosida and K. Yamada, "Perturbation Expansion for the Anderson Hamiltonian. III," *Prog. Theor. Phys.* **53**, 1286–1301 (1975) (cit. on p. 18).
- ⁶²K. Yamada, "Perturbation Expansion for the Anderson Hamiltonian. II," *Prog. Theor. Phys.* **53**, 970–986 (1975) (cit. on p. 18).
- ⁶³N. Read and D. M. Newns, "A new functional integral formalism for the degenerate Anderson model," *J. Phys. C: Solid State Phys.* **16**, L1055 (1983) (cit. on p. 18).
- ⁶⁴P. Coleman, "New approach to the mixed-valence problem," *Phys. Rev. B* **29**, 3035–3044 (1984) (cit. on p. 18).
- ⁶⁵A. I. Lichtenstein and M. I. Katsnelson, "Ab initio calculations of quasiparticle band structure in correlated systems: LDA++ approach," *Phys. Rev. B* **57**, 6884–6895 (1998) (cit. on pp. 18, 34, 76).
- ⁶⁶J. Hubbard, "Electron correlations in narrow energy bands III. An improved solution," *Proc. R. Soc. Lond. A* **281**, 401–419 (1964) (cit. on pp. 18, 124).
- ⁶⁷N. E. Bickers, "Review of techniques in the large- N expansion for dilute magnetic alloys," *Rev. Mod. Phys.* **59**, 845–939 (1987) (cit. on p. 18).
- ⁶⁸T. Pruschke and N. Grewe, "The Anderson model with finite Coulomb repulsion," *Z. Physik B - Condensed Matter* **74**, 439–449 (1989) (cit. on p. 18).

- ⁶⁹K. Haule, S. Kirchner, J. Kroha, and P. Wölfle, “Anderson impurity model at finite Coulomb interaction U : Generalized noncrossing approximation,” *Phys. Rev. B* **64**, 155111 (2001) (cit. on p. 18).
- ⁷⁰A. Georges and G. Kotliar, “Hubbard model in infinite dimensions,” *Phys. Rev. B* **45**, 6479–6483 (1992) (cit. on pp. 18, 33, 124).
- ⁷¹P. Werner and A. J. Millis, “Hybridization expansion impurity solver: General formulation and application to Kondo lattice and two-orbital models,” *Phys. Rev. B* **74**, 155107 (2006) (cit. on pp. 18, 20, 25, 28, 29).
- ⁷²K. Haule, “Quantum Monte Carlo impurity solver for cluster dynamical mean-field theory and electronic structure calculations with adjustable cluster base,” *Phys. Rev. B* **75**, 155113 (2007) (cit. on pp. 18, 26, 28–31, 45, 67).
- ⁷³H. Shinaoka, M. Dolfi, M. Troyer, and P. Werner, “Hybridization expansion Monte Carlo simulation of multi-orbital quantum impurity problems: matrix product formalism and improved sampling,” *J. Stat. Mech.* **2014**, P06012 (2014) (cit. on pp. 18, 23, 25, 26, 31, 48, 51, 67).
- ⁷⁴P. Gunacker, M. Wallerberger, E. Gull, A. Hausoel, G. Sangiovanni, and K. Held, “Continuous-time quantum Monte Carlo using worm sampling,” *Phys. Rev. B* **92**, 155102 (2015) (cit. on pp. 18, 25–28, 67, 167, 185).
- ⁷⁵N. V. Prokof’ev, B. V. Svistunov, and I. S. Tupitsyn, “Exact quantum Monte Carlo process for the statistics of discrete systems,” *Jetp Lett.* **64**, 911–916 (1996) (cit. on p. 18).
- ⁷⁶N. V. Prokof’ev and B. V. Svistunov, “Polaron Problem by Diagrammatic Quantum Monte Carlo,” *Phys. Rev. Lett.* **81**, 2514–2517 (1998) (cit. on pp. 18, 25).
- ⁷⁷A. N. Rubtsov, “Quantum Monte Carlo determinantal algorithm without Hubbard-Stratonovich transformation: a general consideration,” *arXiv:cond-mat/0302228* (2003) (cit. on p. 18).
- ⁷⁸H. Shinaoka, E. Gull, and P. Werner, “Continuous-time hybridization expansion quantum impurity solver for multi-orbital systems with complex hybridizations,” *Computer Physics Communications* **215**, 128–136 (2017) (cit. on p. 20).
- ⁷⁹F. James, “Monte Carlo theory and practice,” *Rep. Prog. Phys.* **43**, 1145 (1980) (cit. on pp. 20, 21).
- ⁸⁰W. Krauth, *Statistical mechanics: algorithms and computations*, Oxford master series in physics Statistical, computational, and theoretical physics 13 (Oxford Univ. Press, Oxford, 2006) (cit. on pp. 20, 21).

- ⁸¹D. P. Landau and K. Binder, *A guide to Monte Carlo simulations in statistical physics*, Fourth edition (Cambridge University Press, Cambridge, United Kingdom, 2015) (cit. on p. 20).
- ⁸²N. Metropolis, A. W. Rosenbluth, M. N. Rosenbluth, A. H. Teller, and E. Teller, “Equation of State Calculations by Fast Computing Machines,” *J. Chem. Phys.* **21**, 1087–1092 (1953) (cit. on p. 22).
- ⁸³W. K. Hastings, “Monte Carlo Sampling Methods Using Markov Chains and Their Applications,” *Biometrika* **57**, 97–109 (1970) (cit. on pp. 22, 23).
- ⁸⁴A. D. Sokal, *Monte Carlo Methods in Statistical Mechanics: Foundations and New Algorithms: Lectures from the Cargese Summer School on Functional Integration: Basics and Applications*, tech. rep. (Department of Physics, New York University, 1996) (cit. on p. 22).
- ⁸⁵H. Suwa and S. Todo, “Markov Chain Monte Carlo Method without Detailed Balance,” *Phys. Rev. Lett.* **105**, 120603 (2010) (cit. on p. 23).
- ⁸⁶E. P. Bernard, W. Krauth, and D. B. Wilson, “Event-chain Monte Carlo algorithms for hard-sphere systems,” *Phys. Rev. E* **80**, 056704 (2009) (cit. on p. 23).
- ⁸⁷W. Krauth, “Event-Chain Monte Carlo: Foundations, Applications, and Prospects,” *Frontiers in Physics* **9** (2021) (cit. on p. 23).
- ⁸⁸R. G. Miller, “The Jackknife—A Review,” *Biometrika* **61**, 1–15 (1974) (cit. on p. 23).
- ⁸⁹B. Efron, “Bootstrap Methods: Another Look at the Jackknife,” *Ann. Statist.* **7**, 1–26 (1979) (cit. on p. 23).
- ⁹⁰B. Efron, “Better Bootstrap Confidence Intervals,” *Journal of the American Statistical Association* **82**, 171–185 (1987) (cit. on p. 23).
- ⁹¹M. Wallerberger, “W2dynamics: continuous time quantum Monte Carlo calculations of one- and two-particle propagators,” Thesis (Technische Universität Wien, Wien, 2016) (cit. on pp. 24, 28–31, 44, 59, 65).
- ⁹²P. Sémon, G. Sordi, and A.-M. S. Tremblay, “Ergodicity of the hybridization-expansion Monte Carlo algorithm for broken-symmetry states,” *Phys. Rev. B* **89**, 165113 (2014) (cit. on p. 23).
- ⁹³P. Seth, I. Krivenko, M. Ferrero, and O. Parcollet, “TRIQS/CTHYB: A Continuous-Time Quantum Monte Carlo Hybridization Expansion Solver for Quantum Impurity Problems,” *Computer Physics Communications* **200**, 274–284 (2016) (cit. on pp. 23, 29, 30).

- ⁹⁴A. I. Poteryaev, J. M. Tomczak, S. Biermann, A. Georges, A. I. Lichtenstein, A. N. Rubtsov, T. Saha-Dasgupta, and O. K. Andersen, “Enhanced crystal-field splitting and orbital-selective coherence induced by strong correlations in V_2O_3 ,” *Phys. Rev. B* **76**, 085127 (2007) (cit. on p. 25).
- ⁹⁵F. Wang and D. P. Landau, “Efficient, Multiple-Range Random Walk Algorithm to Calculate the Density of States,” *Phys. Rev. Lett.* **86**, 2050–2053 (2001) (cit. on p. 25).
- ⁹⁶F. Wang and D. P. Landau, “Determining the density of states for classical statistical models: A random walk algorithm to produce a flat histogram,” *Phys. Rev. E* **64**, 056101 (2001) (cit. on p. 25).
- ⁹⁷M. Troyer, S. Wessel, and F. Alet, “Flat Histogram Methods for Quantum Systems: Algorithms to Overcome Tunneling Problems and Calculate the Free Energy,” *Phys. Rev. Lett.* **90**, 120201 (2003) (cit. on p. 25).
- ⁹⁸A. I. Poteryaev, M. Ferrero, A. Georges, and O. Parcollet, “Effect of crystal-field splitting and interband hybridization on the metal-insulator transitions of strongly correlated systems,” *Phys. Rev. B* **78**, 045115 (2008) (cit. on p. 25).
- ⁹⁹E. Burovski, N. Prokof’ev, B. Svistunov, and M. Troyer, “The Fermi–Hubbard model at unitarity,” *New J. Phys.* **8**, 153 (2006) (cit. on p. 25).
- ¹⁰⁰E. Gull, D. R. Reichman, and A. J. Millis, “Bold-line diagrammatic Monte Carlo method: General formulation and application to expansion around the noncrossing approximation,” *Phys. Rev. B* **82**, 075109 (2010) (cit. on p. 25).
- ¹⁰¹C. Melnick, P. Sémon, K. Yu, N. D’Imperio, A.-M. Tremblay, and G. Kotliar, “Accelerated impurity solver for DMFT and its diagrammatic extensions,” *Computer Physics Communications* **267**, 108075 (2021) (cit. on p. 26).
- ¹⁰²A. Hausoel, M. Wallerberger, J. Kaufmann, K. Held, and G. Sangiovanni, *Aberration of the Green’s function estimator in hybridization expansion continuous-time quantum Monte Carlo*, (Nov. 2022) arXiv:2211.06266 [cond-mat] (cit. on pp. 26, 28).
- ¹⁰³P. Sémon, C.-H. Yee, K. Haule, and A.-M. S. Tremblay, “Lazy skip-lists: An algorithm for fast hybridization-expansion quantum Monte Carlo,” *Phys. Rev. B* **90**, 075149 (2014) (cit. on pp. 26, 31, 67).
- ¹⁰⁴A. Dutt and V. Rokhlin, “Fast Fourier Transforms for Nonequispaced Data,” *SIAM J. Sci. Comput.* **14**, 1368–1393 (1993) (cit. on p. 27).
- ¹⁰⁵J. Keiner, S. Kunis, and D. Potts, “Using NFFT 3—A Software Library for Various Nonequispaced Fast Fourier Transforms,” *ACM Trans. Math. Softw.* **36**, 19:1–19:30 (2009) (cit. on p. 27).

- ¹⁰⁶P. Staar, T. A. Maier, and T. C. Schulthess, “Efficient non-equidistant FFT approach to the measurement of single- and two-particle quantities in continuous time Quantum Monte Carlo methods,” *J. Phys.: Conf. Ser.* **402**, 012015 (2012) (cit. on p. 27).
- ¹⁰⁷A. N. Rubtsov, V. V. Savkin, and A. I. Lichtenstein, “Continuous-time quantum Monte Carlo method for fermions,” *Phys. Rev. B* **72**, 035122 (2005) (cit. on p. 28).
- ¹⁰⁸E. Gull, P. Staar, S. Fuchs, P. Nukala, M. S. Summers, T. Pruschke, T. C. Schulthess, and T. Maier, “Submatrix updates for the continuous-time auxiliary-field algorithm,” *Phys. Rev. B* **83**, 075122 (2011) (cit. on p. 28).
- ¹⁰⁹J. Sherman and W. J. Morrison, “Adjustment of an Inverse Matrix Corresponding to a Change in One Element of a Given Matrix,” *The Annals of Mathematical Statistics* **21**, 124–127 (1950) (cit. on p. 29).
- ¹¹⁰M. A. Woodbury, *Inverting modified matrices* (Princeton University, Princeton, N. J., 1950) (cit. on p. 29).
- ¹¹¹W. Hager, “Updating the Inverse of a Matrix,” *SIAM Rev.* **31**, 221–239 (1989) (cit. on p. 29).
- ¹¹²G. Fano, F. Ortolani, and F. Semeria, “Preliminary group analysis of a 4 x 4 two dimensional hubbard model,” *Int. J. Mod. Phys. B* **03**, 1845–1852 (1989) (cit. on p. 29).
- ¹¹³P. Thunström, I. Di Marco, and O. Eriksson, “Electronic Entanglement in Late Transition Metal Oxides,” *Phys. Rev. Lett.* **109**, 186401 (2012) (cit. on p. 29).
- ¹¹⁴N. Parragh, “Strongly Correlated Multi-Orbital Systems : A Continuous-Time Quantum Monte Carlo Analysis,” PhD thesis (Universität Würzburg, 2013) (cit. on pp. 29, 30).
- ¹¹⁵N. Parragh, A. Toschi, K. Held, and G. Sangiovanni, “Conserved quantities of SU(2)-invariant interactions for correlated fermions and the advantages for quantum Monte Carlo simulations,” *Phys. Rev. B* **86**, 155158 (2012) (cit. on pp. 30, 95).
- ¹¹⁶A. M. Läuchli and P. Werner, “Krylov implementation of the hybridization expansion impurity solver and application to 5-orbital models,” *Phys. Rev. B* **80**, 235117 (2009) (cit. on p. 31).
- ¹¹⁷A. Kowalski, A. Hausoel, M. Wallerberger, P. Gunacker, and G. Sangiovanni, “State and superstate sampling in hybridization-expansion continuous-time quantum Monte Carlo,” *Phys. Rev. B* **99**, 155112 (2019) (cit. on pp. 31, 43, 47, 49).
- ¹¹⁸M. C. Gutzwiller, “Effect of Correlation on the Ferromagnetism of Transition Metals,” *Phys. Rev. Lett.* **10**, 159–162 (1963) (cit. on p. 32).
- ¹¹⁹J. Hubbard, “Electron Correlations in Narrow Energy Bands. II. The Degenerate Band Case,” *Proc. R. Soc. Lond. A* **277**, 237–259 (1964) (cit. on pp. 32, 124).

- ¹²⁰F. Bloch, "Über die Quantenmechanik der Elektronen in Kristallgittern," *Z. Physik* **52**, 555–600 (1929) (cit. on p. 32).
- ¹²¹J. C. Slater, "A Simplification of the Hartree-Fock Method," *Phys. Rev.* **81**, 385–390 (1951) (cit. on p. 32).
- ¹²²E. Müller-Hartmann, "Fermions on a lattice in high dimensions," *Int. J. Mod. Phys. B* **03**, 2169–2187 (1989) (cit. on p. 32).
- ¹²³W. Metzner and D. Vollhardt, "Correlated Lattice Fermions in $d=\infty$ Dimensions," *Phys. Rev. Lett.* **62**, 324–327 (1989) (cit. on pp. 32, 178).
- ¹²⁴E. Müller-Hartmann, "Correlated fermions on a lattice in high dimensions," *Z. Physik B - Condensed Matter* **74**, 507–512 (1989) (cit. on p. 32).
- ¹²⁵E. Müller-Hartmann, "The Hubbard model at high dimensions: some exact results and weak coupling theory," *Z. Physik B - Condensed Matter* **76**, 211–217 (1989) (cit. on p. 32).
- ¹²⁶L. M. Falicov and J. C. Kimball, "Simple Model for Semiconductor-Metal Transitions: SmB_6 and Transition-Metal Oxides," *Phys. Rev. Lett.* **22**, 997–999 (1969) (cit. on p. 32).
- ¹²⁷U. Brandt and C. Mielsch, "Thermodynamics and correlation functions of the Falicov-Kimball model in large dimensions," *Z. Physik B - Condensed Matter* **75**, 365–370 (1989) (cit. on p. 32).
- ¹²⁸U. Brandt and C. Mielsch, "Thermodynamics of the Falicov-Kimball model in large dimensions II," *Z. Physik B - Condensed Matter* **79**, 295–299 (1990) (cit. on p. 32).
- ¹²⁹U. Brandt and C. Mielsch, "Free energy of the Falicov-Kimball model in large dimensions," *Z. Physik B - Condensed Matter* **82**, 37–41 (1991) (cit. on p. 32).
- ¹³⁰P. G. J. van Dongen and D. Vollhardt, "Exact mean-field Hamiltonian for fermionic lattice models in high dimensions," *Phys. Rev. Lett.* **65**, 1663–1666 (1990) (cit. on p. 32).
- ¹³¹V. Janiš, "A new construction of thermodynamic mean-field theories of itinerant fermions: application to the Falicov-Kimball model," *Z. Physik B - Condensed Matter* **83**, 227–235 (1991) (cit. on p. 32).
- ¹³²F. J. Ohkawa, "Heavy Electrons in the Mott-Transition Region," *Prog. Theor. Phys. Suppl.* **106**, 95–107 (1991) (cit. on p. 33).
- ¹³³F. J. Ohkawa, "Electron Correlation in the Hubbard Model in $d=\infty$ Dimension," *J. Phys. Soc. Jpn.* **60**, 3218–3221 (1991) (cit. on p. 33).
- ¹³⁴M. Jarrell, "Hubbard model in infinite dimensions: A quantum Monte Carlo study," *Phys. Rev. Lett.* **69**, 168–171 (1992) (cit. on pp. 33, 124).

- ¹³⁵A. Georges and W. Krauth, “Numerical solution of the $d=\infty$ Hubbard model: Evidence for a Mott transition,” *Phys. Rev. Lett.* **69**, 1240–1243 (1992) (cit. on pp. 33, 124, 126).
- ¹³⁶A. Georges and W. Krauth, “Physical properties of the half-filled Hubbard model in infinite dimensions,” *Phys. Rev. B* **48**, 7167–7182 (1993) (cit. on pp. 33, 125, 126).
- ¹³⁷T. Pruschke, D. L. Cox, and M. Jarrell, “Hubbard model at infinite dimensions: Thermodynamic and transport properties,” *Phys. Rev. B* **47**, 3553–3565 (1993) (cit. on p. 33).
- ¹³⁸T. Pruschke, D. L. Cox, and M. Jarrell, “Transport Properties of the Infinite-Dimensional Hubbard Model,” *EPL* **21**, 593–598 (1993) (cit. on p. 33).
- ¹³⁹M. J. Rozenberg, X. Y. Zhang, and G. Kotliar, “Mott-Hubbard transition in infinite dimensions,” *Phys. Rev. Lett.* **69**, 1236–1239 (1992) (cit. on p. 33).
- ¹⁴⁰N. Marzari, A. A. Mostofi, J. R. Yates, I. Souza, and D. Vanderbilt, “Maximally localized Wannier functions: Theory and applications,” *Rev. Mod. Phys.* **84**, 1419–1475 (2012) (cit. on p. 34).
- ¹⁴¹V. I. Anisimov, A. I. Poteryaev, M. A. Korotin, A. O. Anokhin, and G. Kotliar, “First-principles calculations of the electronic structure and spectra of strongly correlated systems: dynamical mean-field theory,” *J. Phys.: Condens. Matter* **9**, 7359–7367 (1997) (cit. on p. 34).
- ¹⁴²K. Held, I. A. Nekrasov, N. Blümer, V. I. Anisimov, and D. Vollhardt, “Realistic modeling of strongly correlated electron systems: an introduction to the $\text{Lda}+\text{dmft}$ approach,” *Int. J. Mod. Phys. B* **15**, 2611–2625 (2001) (cit. on p. 34).
- ¹⁴³A. Georges, “Strongly Correlated Electron Materials: Dynamical Mean-Field Theory and Electronic Structure,” *AIP Conference Proceedings* **715**, 3–74 (2004) (cit. on p. 34).
- ¹⁴⁴K. Held, I. A. Nekrasov, G. Keller, V. Eyert, N. Blümer, A. K. McMahan, R. T. Scalettar, T. Pruschke, V. I. Anisimov, and D. Vollhardt, “Realistic investigations of correlated electron systems with $\text{LDA} + \text{DMFT}$,” *physica status solidi (b)* **243**, 2599–2631 (2006) (cit. on p. 34).
- ¹⁴⁵R. Žitko, “Convergence acceleration and stabilization of dynamical mean-field theory calculations,” *Phys. Rev. B* **80**, 125125 (2009) (cit. on pp. 35, 56, 131, 167, 199).
- ¹⁴⁶H. U. R. Strand, A. Sabashvili, M. Granath, B. Hellsing, and S. Östlund, “Dynamical mean field theory phase-space extension and critical properties of the finite temperature Mott transition,” *Phys. Rev. B* **83**, 205136 (2011) (cit. on pp. 35, 56, 131, 138, 167).
- ¹⁴⁷A. L. Fetter and J. D. Walecka, *Quantum theory of many-particle systems*, International series in pure and applied physics (McGraw-Hill, San Francisco, 1971) (cit. on pp. 36, 37).

- ¹⁴⁸V. M. Galitskii and A. B. Migdal, “Application of quantum field theory methods to the many body problem,” *Sov. Phys. JETP* **7**, 96–104 (1958) (cit. on pp. 36, 37, 39, 193, 207).
- ¹⁴⁹H. Lehmann, “Über Eigenschaften von Ausbreitungsfunktionen und Renormierungskonstanten quantisierter Felder,” *Nuovo Cim* **11**, 342–357 (1954) (cit. on pp. 36, 169).
- ¹⁵⁰P. Coleman, *Introduction to many body physics* (Cambridge University Press, New York, NY, 2015) (cit. on pp. 36, 40).
- ¹⁵¹J. Kaufmann and K. Held, “Ana_cont: Python package for analytic continuation,” *Computer Physics Communications* **282**, 108519 (2023) (cit. on pp. 37, 41).
- ¹⁵²V. M. Galitskii, “The energy spectrum of a non-ideal Fermi gas,” *Sov. Phys. JETP* **7**, 104–112 (1958) (cit. on p. 37).
- ¹⁵³D. Pines and D. Bohm, “A Collective Description of Electron Interactions: II. Collective vs Individual Particle Aspects of the Interactions,” *Phys. Rev.* **85**, 338–353 (1952) (cit. on p. 40).
- ¹⁵⁴J. M. Luttinger and P. Nozières, “Derivation of the Landau Theory of Fermi Liquids. II. Equilibrium Properties and Transport Equation,” *Phys. Rev.* **127**, 1431–1440 (1962) (cit. on p. 40).
- ¹⁵⁵L. D. Landau, “The Theory of a Fermi Liquid,” *Sov. Phys. JETP* **3**, 920–925 (1957) (cit. on p. 40).
- ¹⁵⁶V. P. Silin, “Theory of a Degenerate Electron Liquid,” *Sov. Phys. JETP* **6**, 387–391 (1958) (cit. on p. 40).
- ¹⁵⁷L. D. Landau, “On the Theory of the Fermi Liquid,” *Sov. Phys. JETP* **8**, 70–74 (1959) (cit. on p. 40).
- ¹⁵⁸P. Nozières and J. M. Luttinger, “Derivation of the Landau Theory of Fermi Liquids. I. Formal Preliminaries,” *Phys. Rev.* **127**, 1423–1431 (1962) (cit. on p. 40).
- ¹⁵⁹P. Nozières, “A “Fermi-liquid” description of the Kondo problem at low temperatures,” *J Low Temp Phys* **17**, 31–42 (1974) (cit. on pp. 40, 90).
- ¹⁶⁰L. De Leo, “Non-Fermi liquid behavior in multi-orbital Anderson impurity models and possible relevance for strongly correlated lattice models,” PhD thesis (SISSA, Oct. 2004) (cit. on p. 40).
- ¹⁶¹L. De Leo and M. Fabrizio, “Spectral properties of a two-orbital Anderson impurity model across a non-Fermi-liquid fixed point,” *Phys. Rev. B* **69**, 245114 (2004) (cit. on p. 40).
- ¹⁶²I. Affleck, “Non-Fermi Liquid Behavior in Kondo Models,” *J. Phys. Soc. Jpn.* **74**, 59–66 (2005) (cit. on p. 40).

- ¹⁶³J. M. Luttinger, “Analytic Properties of Single-Particle Propagators for Many-Fermion Systems,” *Phys. Rev.* **121**, 942–949 (1961) (cit. on p. 40).
- ¹⁶⁴A. V. Chubukov and D. L. Maslov, “First-Matsubara-frequency rule in a Fermi liquid. I. Fermionic self-energy,” *Phys. Rev. B* **86**, 155136 (2012) (cit. on pp. 40, 54, 90, 104).
- ¹⁶⁵J. Fei, C.-N. Yeh, and E. Gull, “Nevanlinna Analytical Continuation,” *Phys. Rev. Lett.* **126**, 056402 (2021) (cit. on p. 41).
- ¹⁶⁶Z. Huang, E. Gull, and L. Lin, “Robust analytic continuation of Green’s functions via projection, pole estimation, and semidefinite relaxation,” *Phys. Rev. B* **107**, 075151 (2023) (cit. on p. 41).
- ¹⁶⁷H.-B. Schüttler and D. J. Scalapino, “Monte Carlo Studies of the Dynamics of Quantum Many-Body Systems,” *Phys. Rev. Lett.* **55**, 1204–1207 (1985) (cit. on p. 41).
- ¹⁶⁸M. Jarrell and J. E. Gubernatis, “Bayesian inference and the analytic continuation of imaginary-time quantum Monte Carlo data,” *Physics Reports* **269**, 133–195 (1996) (cit. on pp. 41, 89, 107, 143).
- ¹⁶⁹R. N. Silver, J. E. Gubernatis, D. S. Sivia, and M. Jarrell, “Spectral densities of the symmetric Anderson model,” *Phys. Rev. Lett.* **65**, 496–499 (1990) (cit. on p. 41).
- ¹⁷⁰R. N. Silver, D. S. Sivia, and J. E. Gubernatis, “Maximum-entropy method for analytic continuation of quantum Monte Carlo data,” *Phys. Rev. B* **41**, 2380–2389 (1990) (cit. on pp. 41, 89, 107).
- ¹⁷¹J. E. Gubernatis, M. Jarrell, R. N. Silver, and D. S. Sivia, “Quantum Monte Carlo simulations and maximum entropy: Dynamics from imaginary-time data,” *Phys. Rev. B* **44**, 6011–6029 (1991) (cit. on p. 41).
- ¹⁷²C. E. Shannon, “A mathematical theory of communication,” *The Bell System Technical Journal* **27**, 379–423 (1948) (cit. on p. 41).
- ¹⁷³R. K. Bryan, “Maximum entropy analysis of oversampled data problems,” *Eur Biophys J* **18**, 165–174 (1990) (cit. on pp. 41, 89, 107).
- ¹⁷⁴R. Levy, J. P. F. LeBlanc, and E. Gull, “Implementation of the Maximum Entropy Method for Analytic Continuation,” *Computer Physics Communications* **215**, 149–155 (2017) (cit. on pp. 41, 89, 107, 143).
- ¹⁷⁵D. Bergeron and A.-M. S. Tremblay, “Algorithms for optimized maximum entropy and diagnostic tools for analytic continuation,” *Phys. Rev. E* **94**, 023303 (2016) (cit. on p. 41).
- ¹⁷⁶J. Kaufmann, “Local and Nonlocal Correlations in Interacting Electron Systems,” PhD Thesis (TU Wien, Wien, 2021) (cit. on pp. 41, 56).

- ¹⁷⁷Y. Motoyama, K. Yoshimi, and J. Otsuki, “Robust analytic continuation combining the advantages of the sparse modeling approach and the Padé approximation,” *Phys. Rev. B* **105**, 035139 (2022) (cit. on p. 41).
- ¹⁷⁸K. Yoshimi, J. Otsuki, Y. Motoyama, M. Ohzeki, and H. Shinaoka, “SpM: Sparse modeling tool for analytic continuation of imaginary-time Green’s function,” *Computer Physics Communications* **244**, 319–323 (2019) (cit. on p. 41).
- ¹⁷⁹J. Otsuki, M. Ohzeki, H. Shinaoka, and K. Yoshimi, “Sparse modeling approach to analytical continuation of imaginary-time quantum Monte Carlo data,” *Phys. Rev. E* **95**, 061302 (2017) (cit. on p. 41).
- ¹⁸⁰H. J. Vidberg and J. W. Serene, “Solving the Eliashberg equations by means of N-point Padé approximants,” *J Low Temp Phys* **29**, 179–192 (1977) (cit. on p. 41).
- ¹⁸¹A. Kowalski, “Improved Sampling in Continuous-Time Quantum Monte Carlo Algorithms for Fermions,” Master’s thesis (Julius-Maximilians-Universität Würzburg, Würzburg, Sept. 2017) (cit. on p. 43).
- ¹⁸²M. P. Bahlke, M. Karolak, and C. Herrmann, “Interplay between strong correlation and adsorption distances: Co on Cu(001),” *Phys. Rev. B* **97**, 035119 (2018) (cit. on pp. 44, 49, 75–77, 102, 117).
- ¹⁸³A. Valli, M. P. Bahlke, A. Kowalski, M. Karolak, C. Herrmann, and G. Sangiovanni, “Kondo screening in Co adatoms with full Coulomb interaction,” *Phys. Rev. Research* **2**, 033432 (2020) (cit. on pp. 44, 49, 73, 77, 103, 104).
- ¹⁸⁴K. Haule and G. Kotliar, “Coherence–incoherence crossover in the normal state of iron oxypnictides and importance of Hund’s rule coupling,” *New J. Phys.* **11**, 025021 (2009) (cit. on pp. 51, 127, 128).
- ¹⁸⁵Z. P. Yin, K. Haule, and G. Kotliar, “Fractional power-law behavior and its origin in iron-chalcogenide and ruthenate superconductors: Insights from first-principles calculations,” *Phys. Rev. B* **86**, 195141 (2012) (cit. on p. 51).
- ¹⁸⁶J. Mravlje, M. Aichhorn, T. Miyake, K. Haule, G. Kotliar, and A. Georges, “Coherence-Incoherence Crossover and the Mass-Renormalization Puzzles in Sr_2RuO_4 ,” *Phys. Rev. Lett.* **106**, 096401 (2011) (cit. on pp. 51, 127, 128).
- ¹⁸⁷L. de’Medici, J. Mravlje, and A. Georges, “Janus-Faced Influence of Hund’s Rule Coupling in Strongly Correlated Materials,” *Phys. Rev. Lett.* **107**, 256401 (2011) (cit. on pp. 51, 52, 126, 127, 135).

- ¹⁸⁸F. Hardy, A. E. Böhmer, D. Aoki, P. Burger, T. Wolf, P. Schweiss, R. Heid, P. Adelman, Y. X. Yao, G. Kotliar, J. Schmalian, and C. Meingast, “Evidence of Strong Correlations and Coherence-Incoherence Crossover in the Iron Pnictide Superconductor KFe_2As_2 ,” *Phys. Rev. Lett.* **111**, 027002 (2013) (cit. on pp. 51, 127, 128).
- ¹⁸⁹A. Horvat, R. Žitko, and J. Mravlje, “Low-energy physics of three-orbital impurity model with Kanamori interaction,” *Phys. Rev. B* **94**, 165140 (2016) (cit. on pp. 52, 54).
- ¹⁹⁰K. Stadler, G. Kotliar, A. Weichselbaum, and J. von Delft, “Hundness versus Mottness in a three-band Hubbard–Hund model: On the origin of strong correlations in Hund metals,” *Annals of Physics* **405**, 365–409 (2019) (cit. on pp. 52, 127).
- ¹⁹¹K. M. Stadler, Z. P. Yin, J. von Delft, G. Kotliar, and A. Weichselbaum, “Dynamical Mean-Field Theory Plus Numerical Renormalization-Group Study of Spin-Orbital Separation in a Three-Band Hund Metal,” *Phys. Rev. Lett.* **115**, 136401 (2015) (cit. on pp. 52, 54, 127).
- ¹⁹²X. Deng, K. M. Stadler, K. Haule, A. Weichselbaum, J. von Delft, and G. Kotliar, “Signatures of Mottness and Hundness in archetypal correlated metals,” *Nature Communications* **10**, 2721 (2019) (cit. on pp. 52, 53, 80, 82, 127).
- ¹⁹³M. Chatzieftheriou, A. Kowalski, M. Berović, A. Amaricci, M. Capone, L. De Leo, G. Sangiovanni, and L. de’Medici, “Mott Quantum Critical Points at Finite Doping,” *Phys. Rev. Lett.* **130**, 066401 (2023) (cit. on pp. 52, 123, 167).
- ¹⁹⁴A. Kowalski, M. Reitner, L. Del Re, M. Chatzieftheriou, A. Amaricci, A. Toschi, L. de’Medici, G. Sangiovanni, and T. Schäfer, *Thermodynamic stability at the two-particle level*, Sept. 20, 2023, arXiv:2309.11108 [cond-mat] (cit. on pp. 52, 163).
- ¹⁹⁵L. Gaspard and J. M. Tomczak, *Timescale of local moment screening across and above the Mott transition*, (Dec. 2021) arXiv:2112.02881 [cond-mat] (cit. on pp. 54, 82).
- ¹⁹⁶C. Watzenböck, M. Feller, K. Held, and A. Toschi, “Long-term memory magnetic correlations in the Hubbard model: A dynamical mean-field theory analysis,” *SciPost Physics* **12**, 184 (2022) (cit. on pp. 54, 82).
- ¹⁹⁷N. Dasari, N. S. Vidhyadhiraja, M. Jarrell, and R. H. McKenzie, “Quantum critical local spin dynamics near the Mott metal-insulator transition in infinite dimensions,” *Phys. Rev. B* **95**, 165105 (2017) (cit. on pp. 54, 128).
- ¹⁹⁸J. Kaufmann, P. Gunacker, A. Kowalski, G. Sangiovanni, and K. Held, “Symmetric improved estimators for continuous-time quantum Monte Carlo,” *Phys. Rev. B* **100**, 075119 (2019) (cit. on pp. 56, 61, 62, 207).
- ¹⁹⁹E. Gull, P. Werner, A. Millis, and M. Troyer, “Performance analysis of continuous-time solvers for quantum impurity models,” *Phys. Rev. B* **76**, 235123 (2007) (cit. on p. 56).

- ²⁰⁰H. Hafermann, K. R. Patton, and P. Werner, “Improved estimators for the self-energy and vertex function in hybridization-expansion continuous-time quantum Monte Carlo simulations,” *Phys. Rev. B* **85**, 205106 (2012) (cit. on pp. 56–60, 64, 66, 207).
- ²⁰¹L. Boehnke, H. Hafermann, M. Ferrero, F. Lechermann, and O. Parcollet, “Orthogonal polynomial representation of imaginary-time Green’s functions,” *Phys. Rev. B* **84**, 075145 (2011) (cit. on p. 57).
- ²⁰²M. Potthoff, T. Wegner, and W. Nolting, “Interpolating self-energy of the infinite-dimensional Hubbard model: Modifying the iterative perturbation theory,” *Phys. Rev. B* **55**, 16132–16142 (1997) (cit. on p. 57).
- ²⁰³X. Wang, H. T. Dang, and A. J. Millis, “High-frequency asymptotic behavior of self-energies in quantum impurity models,” *Phys. Rev. B* **84**, 073104 (2011) (cit. on p. 57).
- ²⁰⁴G. Li and W. Hanke, “Efficient treatment of the high-frequency tail of the self-energy function and its relevance for multiorbital models,” *Phys. Rev. B* **85**, 115103 (2012) (cit. on pp. 57, 64).
- ²⁰⁵N. Wentzell, G. Li, A. Tagliavini, C. Taranto, G. Rohringer, K. Held, A. Toschi, and S. Andergassen, “High-frequency asymptotics of the vertex function: Diagrammatic parametrization and algorithmic implementation,” *Phys. Rev. B* **102**, 085106 (2020) (cit. on p. 57).
- ²⁰⁶J. Kaufmann, P. Gunacker, and K. Held, “Continuous-time quantum Monte Carlo calculation of multiorbital vertex asymptotics,” *Phys. Rev. B* **96**, 035114 (2017) (cit. on pp. 57, 65).
- ²⁰⁷M. Han and H. J. Choi, “Causal optimization method for imaginary-time Green’s functions in interacting electron systems,” *Phys. Rev. B* **104**, 115112 (2021) (cit. on p. 57).
- ²⁰⁸H. Hafermann, “Self-energy and vertex functions from hybridization-expansion continuous-time quantum Monte Carlo for impurity models with retarded interaction,” *Phys. Rev. B* **89**, 235128 (2014) (cit. on pp. 57, 58).
- ²⁰⁹P. Gunacker, M. Wallerberger, T. Ribic, A. Hausoel, G. Sangiovanni, and K. Held, “Worm-improved estimators in continuous-time quantum Monte Carlo,” *Phys. Rev. B* **94**, 125153 (2016) (cit. on pp. 57–59, 65, 66).
- ²¹⁰G. Górski and J. Mizia, “Equation of motion solutions to Hubbard model retaining Kondo effect,” *Physica B: Condensed Matter* **427**, 42–46 (2013) (cit. on p. 57).
- ²¹¹R. Bulla, A. C. Hewson, and T. Pruschke, “Numerical renormalization group calculations for the self-energy of the impurity Anderson model,” *J. Phys.: Condens. Matter* **10**, 8365–8380 (1998) (cit. on pp. 58, 60, 129).

- ²¹²R. P. Feynman, “Space-Time Approach to Quantum Electrodynamics,” *Phys. Rev.* **76**, 769–789 (1949) (cit. on pp. 59, 164).
- ²¹³A. Moutenet, W. Wu, and M. Ferrero, “Determinant Monte Carlo algorithms for dynamical quantities in fermionic systems,” *Phys. Rev. B* **97**, 085117 (2018) (cit. on p. 60).
- ²¹⁴G. Rohringer, A. Valli, and A. Toschi, “Local electronic correlation at the two-particle level,” *Phys. Rev. B* **86**, 125114 (2012) (cit. on pp. 64, 65, 165, 168, 169, 174–177, 203, 204).
- ²¹⁵O. Gunnarsson, T. Schäfer, J. P. F. LeBlanc, J. Merino, G. Sangiovanni, G. Rohringer, and A. Toschi, “Parquet decomposition calculations of the electronic self-energy,” *Phys. Rev. B* **93**, 245102 (2016) (cit. on pp. 65, 166, 167, 181).
- ²¹⁶G. Rohringer, H. Hafermann, A. Toschi, A. A. Katanin, A. E. Antipov, M. I. Katsnelson, A. I. Lichtenstein, A. N. Rubtsov, and K. Held, “Diagrammatic routes to nonlocal correlations beyond dynamical mean field theory,” *Rev. Mod. Phys.* **90**, 025003 (2018) (cit. on pp. 65, 167).
- ²¹⁷W. J. de Haas, J. de Boer, and G. J. van den Berg, “The electrical resistance of gold, copper and lead at low temperatures,” *Physica* **1**, 1115–1124 (1934) (cit. on p. 73).
- ²¹⁸K. Yosida, “Bound State Due to the s-d Exchange Interaction,” *Phys. Rev.* **147**, 223–227 (1966) (cit. on p. 74).
- ²¹⁹A. Okiji, “Bound State due to the s-d Exchange Interaction: Effect of the Higher Order Perturbation,” *Progress of Theoretical Physics* **36**, 712–725 (1966) (cit. on p. 74).
- ²²⁰K. Yosida, “Ground State Energy of Conduction Electrons Interacting with a Localized Spin,” *Progress of Theoretical Physics* **36**, 875–886 (1966) (cit. on p. 74).
- ²²¹A. Yoshimori, “Closed-Form Solution for the Collective Bound State due to the s-d Exchange Interaction,” *Phys. Rev.* **168**, 493–494 (1968) (cit. on p. 74).
- ²²²A. A. Abrikosov, “Electron scattering on magnetic impurities in metals and anomalous resistivity effects,” *Physics Physique Fizika* **2**, 5–20 (1965) (cit. on pp. 74, 98).
- ²²³H. Suhl, “Dispersion Theory of the Kondo Effect,” *Phys. Rev.* **138**, A515–A523 (1965) (cit. on pp. 74, 98, 110).
- ²²⁴Y. Nagaoka, “Self-Consistent Treatment of Kondo’s Effect in Dilute Alloys,” *Phys. Rev.* **138**, A1112–A1120 (1965) (cit. on pp. 74, 98, 110).
- ²²⁵A. C. Hewson, *The Kondo problem to heavy fermions*, Cambridge studies in magnetism 2 (Cambridge University Press, Cambridge ; New York, 1993) (cit. on pp. 74, 103).
- ²²⁶P. W. Anderson, “A poor man’s derivation of scaling laws for the Kondo problem,” *J. Phys. C: Solid State Phys.* **3**, 2436–2441 (1970) (cit. on p. 74).

- ²²⁷H. C. Manoharan, C. P. Lutz, and D. M. Eigler, “Quantum mirages formed by coherent projection of electronic structure,” *Nature* **403**, 512–515 (2000) (cit. on pp. 74, 99).
- ²²⁸N. Knorr, M. A. Schneider, L. Diekhöner, P. Wahl, and K. Kern, “Kondo Effect of Single Co Adatoms on Cu Surfaces,” *Phys. Rev. Lett.* **88**, 096804 (2002) (cit. on pp. 74, 75, 80, 100).
- ²²⁹N. Néel, J. Kröger, L. Limot, K. Palotas, W. A. Hofer, and R. Berndt, “Conductance and Kondo Effect in a Controlled Single-Atom Contact,” *Phys. Rev. Lett.* **98**, 016801 (2007) (cit. on pp. 74, 75, 80, 82, 99).
- ²³⁰L. Vitali, R. Ohmann, S. Stepanow, P. Gambardella, K. Tao, R. Huang, V. S. Stepanyuk, P. Bruno, and K. Kern, “Kondo Effect in Single Atom Contacts: The Importance of the Atomic Geometry,” *Phys. Rev. Lett.* **101**, 216802 (2008) (cit. on pp. 74, 75).
- ²³¹V. Madhavan, W. Chen, T. Jamneala, M. F. Crommie, and N. S. Wingreen, “Tunneling into a Single Magnetic Atom: Spectroscopic Evidence of the Kondo Resonance,” *Science* **280**, 567–569 (1998) (cit. on pp. 74, 98, 99).
- ²³²P. Wahl, L. Diekhöner, M. A. Schneider, L. Vitali, G. Wittich, and K. Kern, “Kondo Temperature of Magnetic Impurities at Surfaces,” *Phys. Rev. Lett.* **93**, 176603 (2004) (cit. on pp. 74, 75, 80).
- ²³³J. Li, W.-D. Schneider, R. Berndt, and B. Delley, “Kondo Scattering Observed at a Single Magnetic Impurity,” *Phys. Rev. Lett.* **80**, 2893–2896 (1998) (cit. on pp. 74, 98, 99).
- ²³⁴L. Kouwenhoven and L. Glazman, “Revival of the Kondo effect,” *Phys. World* **14**, 33–38 (2001) (cit. on pp. 74, 98).
- ²³⁵U. Fano, “Sullo spettro di assorbimento dei gas nobili presso il limite dello spettro d’arco,” *Nuovo Cim* **12**, 154–161 (1935) (cit. on pp. 74, 99).
- ²³⁶U. Fano, “Effects of Configuration Interaction on Intensities and Phase Shifts,” *Phys. Rev.* **124**, 1866–1878 (1961) (cit. on pp. 74, 99, 114).
- ²³⁷O. Újsághy, J. Kroha, L. Szunyogh, and A. Zawadowski, “Theory of the Fano Resonance in the STM Tunneling Density of States due to a Single Kondo Impurity,” *Phys. Rev. Lett.* **85**, 2557–2560 (2000) (cit. on pp. 74, 99).
- ²³⁸S. Frank and D. Jacob, “Orbital signatures of Fano-Kondo line shapes in STM adatom spectroscopy,” *Phys. Rev. B* **92**, 235127 (2015) (cit. on p. 74).
- ²³⁹H. T. Dang, M. dos Santos Dias, A. Liebsch, and S. Lounis, “Strong correlation effects in theoretical STM studies of magnetic adatoms,” *Phys. Rev. B* **93**, 115123 (2016) (cit. on pp. 74–76, 109).

- ²⁴⁰J. Bouaziz, F. S. Mendes Guimarães, and S. Lounis, “A new view on the origin of zero-bias anomalies of Co atoms atop noble metal surfaces,” *Nat Commun* **11**, 6112 (2020) (cit. on pp. 74, 109).
- ²⁴¹A. B. Shick, M. Tchaplianka, and A. I. Lichtenstein, “Spin-orbit coupling and Kondo resonance in the Co adatom on the Cu(100) surface: DFT plus exact diagonalization study,” *Phys. Rev. B* **106**, 245115 (2022) (cit. on pp. 74, 109).
- ²⁴²F. Friedrich, A. Odobesko, J. Bouaziz, S. Lounis, and M. Bode, “Evidence for spinarons in Co adatoms,” *Nat. Phys.*, 1–6 (2023) (cit. on pp. 74, 109).
- ²⁴³P. Huang and E. A. Carter, “Ab Initio Explanation of Tunneling Line Shapes for the Kondo Impurity State,” *Nano Letters* **8**, 1265–1269 (2008) (cit. on pp. 74, 75, 77, 78, 86).
- ²⁴⁴D. Jacob, “Towards a full ab initio theory of strong electronic correlations in nanoscale devices,” *J. Phys.: Condens. Matter* **27**, 245606 (2015) (cit. on pp. 74, 75, 77, 78, 84, 88–90, 93, 95, 103).
- ²⁴⁵P. P. Baruselli, R. Requist, A. Smogunov, M. Fabrizio, and E. Tosatti, “Co adatoms on Cu surfaces: Ballistic conductance and Kondo temperature,” *Phys. Rev. B* **92**, 045119 (2015) (cit. on pp. 74, 75, 78, 86, 88, 89).
- ²⁴⁶J. Kliewer, R. Berndt, and S. Crampin, “Controlled Modification of Individual Adsorbate Electronic Structure,” *Phys. Rev. Lett.* **85**, 4936–4939 (2000) (cit. on p. 75).
- ²⁴⁷T. Uchihashi, J. Zhang, J. Kröger, and R. Berndt, “Quantum modulation of the Kondo resonance of Co adatoms on Cu/Co/Cu(100): Low-temperature scanning tunneling spectroscopy study,” *Phys. Rev. B* **78**, 033402 (2008) (cit. on pp. 75, 99).
- ²⁴⁸J. R. Schrieffer, “The Kondo Effect—The Link Between Magnetic and Nonmagnetic Impurities in Metals?” *Journal of Applied Physics* **38**, 1143–1150 (1967) (cit. on p. 75).
- ²⁴⁹A. H. Nevidomskyy and P. Coleman, “Kondo Resonance Narrowing in *d*- and *f*-Electron Systems,” *Phys. Rev. Lett.* **103**, 147205 (2009) (cit. on pp. 75, 79, 85, 88, 96).
- ²⁵⁰M. D. Daybell and W. A. Steyert, “Localized Magnetic Impurity States In Metals: Some Experimental Relationships,” *Rev. Mod. Phys.* **40**, 380–389 (1968) (cit. on pp. 75, 80).
- ²⁵¹B. Surer, M. Troyer, P. Werner, T. O. Wehling, A. M. Läuchli, A. Wilhelm, and A. I. Lichtenstein, “Multiorbital Kondo physics of Co in Cu hosts,” *Phys. Rev. B* **85**, 085114 (2012) (cit. on pp. 75, 76, 103, 104).
- ²⁵²E. Gorelov, T. O. Wehling, A. N. Rubtsov, M. I. Katsnelson, and A. I. Lichtenstein, “Relevance of the complete Coulomb interaction matrix for the Kondo problem: Co impurities in Cu hosts,” *Phys. Rev. B* **80**, 155132 (2009) (cit. on pp. 75, 77, 103, 104).

- ²⁵³O. Gunnarsson, O. K. Andersen, O. Jepsen, and J. Zaanen, "Density-functional calculation of the parameters in the Anderson model: Application to Mn in CdTe," *Phys. Rev. B* **39**, 1708–1722 (1989) (cit. on p. 76).
- ²⁵⁴P. Lucignano, R. Mazzarello, A. Smogunov, M. Fabrizio, and E. Tosatti, "Kondo conductance in an atomic nanocontact from first principles," *Nature Mater* **8**, 563–567 (2009) (cit. on p. 76).
- ²⁵⁵D. Jacob, K. Haule, and G. Kotliar, "Kondo Effect and Conductance of Nanocontacts with Magnetic Impurities," *Phys. Rev. Lett.* **103**, 016803 (2009) (cit. on p. 76).
- ²⁵⁶G. Kresse and J. Furthmüller, "Efficient iterative schemes for ab initio total-energy calculations using a plane-wave basis set," *Phys. Rev. B* **54**, 11169–11186 (1996) (cit. on pp. 76, 101, 115).
- ²⁵⁷G. Kresse and D. Joubert, "From ultrasoft pseudopotentials to the projector augmented-wave method," *Phys. Rev. B* **59**, 1758–1775 (1999) (cit. on pp. 76, 101, 115).
- ²⁵⁸P. E. Blöchl, "Projector augmented-wave method," *Phys. Rev. B* **50**, 17953–17979 (1994) (cit. on pp. 76, 101, 115).
- ²⁵⁹R. W. G. Wyckoff, *Crystal structures*, 2nd ed. (Interscience Publishers, New York, 1963) (cit. on p. 77).
- ²⁶⁰B. Amadon, F. Lechermann, A. Georges, F. Jollet, T. O. Wehling, and A. I. Lichtenstein, "Plane-wave based electronic structure calculations for correlated materials using dynamical mean-field theory and projected local orbitals," *Phys. Rev. B* **77**, 205112 (2008) (cit. on pp. 77, 78, 102, 103, 117, 119).
- ²⁶¹M. Karolak, T. O. Wehling, F. Lechermann, and A. I. Lichtenstein, "General DFT++ method implemented with projector augmented waves: electronic structure of SrVO₃ and the Mott transition in Ca_{2-x}Sr_xRuO₄," *J. Phys.: Condens. Matter* **23**, 085601 (2011) (cit. on pp. 77, 102, 117).
- ²⁶²J. C. Slater, "The Theory of Complex Spectra," *Phys. Rev.* **34**, 1293–1322 (1929) (cit. on pp. 78, 93).
- ²⁶³J. C. Slater, *Quantum theory of atomic structure*, International series in pure and applied physics (McGraw-Hill, New York, 1960) (cit. on pp. 78, 93).
- ²⁶⁴Y. Tanabe and S. Sugano, "On the Absorption Spectra of Complex Ions II," *J. Phys. Soc. Jpn.* **9**, 766–779 (1954) (cit. on pp. 78, 95).
- ²⁶⁵F. M. F. de Groot, J. C. Fuggle, B. T. Thole, and G. A. Sawatzky, "2p x-ray absorption of 3d transition-metal compounds: An atomic multiplet description including the crystal field," *Phys. Rev. B* **42**, 5459–5468 (1990) (cit. on pp. 78, 95).

- ²⁶⁶R. E. Watson, "Iron Series Hartree-Fock Calculations," *Phys. Rev.* **118**, 1036–1045 (1960) (cit. on pp. 78, 95).
- ²⁶⁷I. Schnell, G. Czycholl, and R. C. Albers, "Unscreened Hartree-Fock calculations for metallic Fe, Co, Ni, and Cu from ab initio Hamiltonians," *Phys. Rev. B* **68**, 245102 (2003) (cit. on pp. 78, 95).
- ²⁶⁸A. Hausoel, M. Karolak, E. Şaşıoğlu, A. Lichtenstein, K. Held, A. Katanin, A. Toschi, and G. Sangiovanni, "Local magnetic moments in iron and nickel at ambient and Earth's core conditions," *Nat Commun* **8**, 16062 (2017) (cit. on pp. 78, 82, 104, 119).
- ²⁶⁹E. Şaşıoğlu, C. Friedrich, and S. Blügel, "Strength of the Effective Coulomb Interaction at Metal and Insulator Surfaces," *Phys. Rev. Lett.* **109**, 146401 (2012) (cit. on pp. 78, 104, 106, 119).
- ²⁷⁰D.-J. Choi, P. Abufager, L. Limot, and N. Lorente, "From tunneling to contact in a magnetic atom: The non-equilibrium Kondo effect," *The Journal of Chemical Physics* **146**, 092309 (2016) (cit. on p. 78).
- ²⁷¹T. Pruschke and R. Bulla, "Hund's coupling and the metal-insulator transition in the two-band Hubbard model," *Eur. Phys. J. B* **44**, 217–224 (2005) (cit. on pp. 78, 126, 135).
- ²⁷²A. Liebsch, "Novel Mott Transitions in a Nonisotropic Two-Band Hubbard Model," *Phys. Rev. Lett.* **95**, 116402 (2005) (cit. on p. 78).
- ²⁷³P. Nozières and A. Blandin, "Kondo effect in real metals," *J. Phys. France* **41**, 193–211 (1980) (cit. on pp. 80, 103).
- ²⁷⁴D. L. Cox and A. Zawadowski, "Exotic Kondo effects in metals: Magnetic ions in a crystalline electric field and tunnelling centres," *Advances in Physics* **47**, 599–942 (1998) (cit. on p. 80).
- ²⁷⁵O. Y. Kolesnychenko, R. de Kort, M. I. Katsnelson, A. I. Lichtenstein, and H. van Kempen, "Real-space imaging of an orbital Kondo resonance on the Cr(001) surface," *Nature* **415**, 507–509 (2002) (cit. on p. 80).
- ²⁷⁶P. Jarillo-Herrero, J. Kong, H. S. J. van der Zant, C. Dekker, L. P. Kouwenhoven, and S. De Franceschi, "Orbital Kondo effect in carbon nanotubes," *Nature* **434**, 484–488 (2005) (cit. on p. 80).
- ²⁷⁷S. Sasaki, S. De Franceschi, J. M. Elzerman, W. G. van der Wiel, M. Eto, S. Tarucha, and L. P. Kouwenhoven, "Kondo effect in an integer-spin quantum dot," *Nature* **405**, 764–767 (2000) (cit. on p. 80).
- ²⁷⁸W. Pauli, "Über Gasentartung und Paramagnetismus," *Z. Physik* **41**, 81–102 (1927) (cit. on p. 80).

- ²⁷⁹P. Weiss, “L’hypothèse du champ moléculaire et la propriété ferromagnétique,” *J. Phys. Theor. Appl.* **6**, 661–690 (1907) (cit. on p. 80).
- ²⁸⁰S. Burdin, A. Georges, and D. R. Grempel, “Coherence Scale of the Kondo Lattice,” *Phys. Rev. Lett.* **85**, 1048–1051 (2000) (cit. on p. 80).
- ²⁸¹A. Amaricci, L. de’Medici, G. Sordi, M. J. Rozenberg, and M. Capone, “Path to poor coherence in the periodic Anderson model from Mott physics and hybridization,” *Phys. Rev. B* **85**, 235110 (2012) (cit. on p. 80).
- ²⁸²X. Deng, K. M. Stadler, K. Haule, S.-S. B. Lee, A. Weichselbaum, J. von Delft, and G. Kotliar, “Reply to: “Extracting Kondo temperature of strongly-correlated systems from the inverse local magnetic susceptibility,”” *Nature Communications* **12**, 1445 (2021) (cit. on p. 80).
- ²⁸³A. Toschi, R. Arita, P. Hansmann, G. Sangiovanni, and K. Held, “Quantum dynamical screening of the local magnetic moment in Fe-based superconductors,” *Phys. Rev. B* **86**, 064411 (2012) (cit. on pp. 82, 84).
- ²⁸⁴L. de’Medici, “Hund’s coupling and its key role in tuning multiorbital correlations,” *Phys. Rev. B* **83**, 205112 (2011) (cit. on pp. 88, 127).
- ²⁸⁵L. Fanfarillo and E. Bascones, “Electronic correlations in Hund metals,” *Phys. Rev. B* **92**, 075136 (2015) (cit. on pp. 88, 127).
- ²⁸⁶N. Néel, J. Kröger, M. Schüler, B. Shao, T. O. Wehling, A. Kowalski, and G. Sangiovanni, “Single-Co Kondo effect in atomic Cu wires on Cu(111),” *Phys. Rev. Research* **2**, 023309 (2020) (cit. on p. 98).
- ²⁸⁷F. Patthey, B. Delley, W.-D. Schneider, and Y. Baer, “Low-Energy Excitations in α - and γ -Ce Observed by Photoemission,” *Phys. Rev. Lett.* **55**, 1518–1521 (1985) (cit. on p. 98).
- ²⁸⁸F. Patthey, W.-D. Schneider, Y. Baer, and B. Delley, “High-temperature collapse of the Kondo resonance in CeSi₂ observed by photoemission,” *Phys. Rev. Lett.* **58**, 2810–2813 (1987) (cit. on p. 98).
- ²⁸⁹F. Patthey, J.-M. Imer, W.-D. Schneider, H. Beck, Y. Baer, and B. Delley, “High-resolution photoemission study of the low-energy excitations in 4f-electron systems,” *Phys. Rev. B* **42**, 8864–8881 (1990) (cit. on p. 98).
- ²⁹⁰C. Laubschat, E. Weschke, C. Holtz, M. Domke, O. Strebel, and G. Kaindl, “Surface-electronic structure of α -like Ce compounds,” *Phys. Rev. Lett.* **65**, 1639–1642 (1990) (cit. on p. 98).
- ²⁹¹E. Weschke, C. Laubschat, T. Simmons, M. Domke, O. Strebel, and G. Kaindl, “Surface and bulk electronic structure of Ce metal studied by high-resolution resonant photoemission,” *Phys. Rev. B* **44**, 8304–8307 (1991) (cit. on p. 98).

- ²⁹²D. Ehm, S. Hufner, F. Reinert, J. Kroha, P. Wölfle, O. Stockert, C. Geibel, and H. v. Löhneysen, “High-resolution photoemission study on low- T_K Ce systems: Kondo resonance, crystal field structures, and their temperature dependence,” *Phys. Rev. B* **76**, 045117 (2007) (cit. on p. 98).
- ²⁹³E. Wuilloud, H. R. Moser, W.-D. Schneider, and Y. Baer, “Electronic structure of γ - and α -Ce,” *Phys. Rev. B* **28**, 7354–7357 (1983) (cit. on p. 98).
- ²⁹⁴M. Ternes, A. J. Heinrich, and W.-D. Schneider, “Spectroscopic manifestations of the Kondo effect on single adatoms,” *J. Phys.: Condens. Matter* **21**, 053001 (2008) (cit. on p. 98).
- ²⁹⁵T. Komeda, “Spins of adsorbed molecules investigated by the detection of Kondo resonance,” *Surface Science* **630**, 343–355 (2014) (cit. on p. 98).
- ²⁹⁶M. Ternes, “Probing Magnetic Excitations and Correlations in Single and Coupled Spin Systems with Scanning Tunneling Spectroscopy,” *Progress in Surface Science* **92**, 83–115 (2017) (cit. on p. 98).
- ²⁹⁷J. Göres, D. Goldhaber-Gordon, S. Heemeyer, M. A. Kastner, H. Shtrikman, D. Mahalu, and U. Meirav, “Fano resonances in electronic transport through a single-electron transistor,” *Phys. Rev. B* **62**, 2188–2194 (2000) (cit. on p. 99).
- ²⁹⁸P. Wahl, P. Simon, L. Diekhöner, V. S. Stepanyuk, P. Bruno, M. A. Schneider, and K. Kern, “Exchange Interaction between Single Magnetic Adatoms,” *Phys. Rev. Lett.* **98**, 056601 (2007) (cit. on p. 99).
- ²⁹⁹A. F. Otte, M. Ternes, S. Loth, C. P. Lutz, C. F. Hirjibehedin, and A. J. Heinrich, “Spin Excitations of a Kondo-Screened Atom Coupled to a Second Magnetic Atom,” *Phys. Rev. Lett.* **103**, 107203 (2009) (cit. on p. 99).
- ³⁰⁰S. Meierott, N. Néel, and J. Kröger, “Kondo effect of single Co atoms on Au(110),” *Phys. Rev. B* **91**, 201111 (2015) (cit. on p. 99).
- ³⁰¹V. Iancu, A. Deshpande, and S.-W. Hla, “Manipulation of the Kondo Effect via Two-Dimensional Molecular Assembly,” *Phys. Rev. Lett.* **97**, 266603 (2006) (cit. on p. 99).
- ³⁰²V. Iancu, A. Deshpande, and S.-W. Hla, “Manipulating Kondo Temperature via Single Molecule Switching,” *Nano Lett.* **6**, 820–823 (2006) (cit. on p. 99).
- ³⁰³J. Kügel, M. Karolak, J. Senkpiel, P.-J. Hsu, G. Sangiovanni, and M. Bode, “Relevance of Hybridization and Filling of 3d Orbitals for the Kondo Effect in Transition Metal Phthalocyanines,” *Nano Lett.* **14**, 3895–3902 (2014) (cit. on p. 99).
- ³⁰⁴T. Knaak, M. Gruber, C. Lindström, M.-L. Bocquet, J. Heck, and R. Berndt, “Ligand-Induced Energy Shift and Localization of Kondo Resonances in Cobalt-Based Complexes on Cu(111),” *Nano Lett.* **17**, 7146–7151 (2017) (cit. on p. 99).

- ³⁰⁵L. Limot and R. Berndt, "Kondo effect and surface-state electrons," *Applied Surface Science, Proceedings of the Seventh International Symposium on Atomically Controlled Surfaces, Interfaces and Nanostructures* **237**, 572–576 (2004) (cit. on p. 99).
- ³⁰⁶Q. L. Li, C. Zheng, R. Wang, B. F. Miao, R. X. Cao, L. Sun, D. Wu, Y. Z. Wu, S. C. Li, B. G. Wang, and H. F. Ding, "Role of the surface state in the Kondo resonance width of a Co single adatom on Ag(111)," *Phys. Rev. B* **97**, 035417 (2018) (cit. on p. 99).
- ³⁰⁷N. Néel, J. Kröger, R. Berndt, T. O. Wehling, A. I. Lichtenstein, and M. I. Katsnelson, "Controlling the Kondo Effect in CoCu_n Clusters Atom by Atom," *Phys. Rev. Lett.* **101**, 266803 (2008) (cit. on pp. 99–101).
- ³⁰⁸L. Limot, J. Kröger, R. Berndt, A. Garcia-Lekue, and W. A. Hofer, "Atom Transfer and Single-Adatom Contacts," *Phys. Rev. Lett.* **94**, 126102 (2005) (cit. on p. 99).
- ³⁰⁹J. A. Stroscio, F. Tavazza, J. N. Crain, R. J. Celotta, and A. M. Chaka, "Electronically Induced Atom Motion in Engineered CoCu_n Nanostructures," *Science* **313**, 948–951 (2006) (cit. on p. 99).
- ³¹⁰J. Lagoute, C. Nacci, and S. Fölsch, "Doping of Monatomic Cu Chains with Single Co Atoms," *Phys. Rev. Lett.* **98**, 146804 (2007) (cit. on p. 99).
- ³¹¹J. P. Perdew, K. Burke, and M. Ernzerhof, "Generalized Gradient Approximation Made Simple," *Phys. Rev. Lett.* **77**, 3865–3868 (1996) (cit. on pp. 101, 115).
- ³¹²T. Ribic, E. Assmann, A. Tóth, and K. Held, "Cubic interaction parameters for t_{2g} Wannier orbitals," *Phys. Rev. B* **90**, 165105 (2014) (cit. on p. 104).
- ³¹³A. C. Hewson, "The Strong Coupling Fixed-Point Revisited," *J. Phys. Soc. Jpn.* **74**, 8–15 (2005) (cit. on p. 104).
- ³¹⁴K. Edwards and A. C. Hewson, "A new renormalization group approach for systems with strong electron correlation," *J. Phys.: Condens. Matter* **23**, 045601 (2011) (cit. on p. 104).
- ³¹⁵K. Palotás, G. Mándi, and L. Szunyogh, "Orbital-dependent electron tunneling within the atom superposition approach: Theory and application to W(110)," *Phys. Rev. B* **86**, 235415 (2012) (cit. on p. 109).
- ³¹⁶A. Odobesko, D. Di Sante, A. Kowalski, S. Wilfert, F. Friedrich, R. Thomale, G. Sangiovanni, and M. Bode, "Observation of tunable single-atom Yu-Shiba-Rusinov states," *Phys. Rev. B* **102**, 174504 (2020) (cit. on pp. 110, 112, 114).
- ³¹⁷L. Yu, "Bound state in superconductors with paramagnetic impurities," *Acta Phys. Sin.* **21**, 75 (1965) (cit. on p. 110).
- ³¹⁸H. Shiba, "Classical Spins in Superconductors," *Prog. Theor. Phys.* **40**, 435–451 (1968) (cit. on pp. 110, 114, 115).

- ³¹⁹A. I. Rusinov, "Superconductivity near a paramagnetic impurity," *Jetp Lett.* **9**, 85–87 (1969) (cit. on pp. 110, 114, 115).
- ³²⁰A. V. Balatsky, I. Vekhter, and J.-X. Zhu, "Impurity-induced states in conventional and unconventional superconductors," *Rev. Mod. Phys.* **78**, 373–433 (2006) (cit. on p. 110).
- ³²¹A. A. Abrikosov, "Influence of impurity ferromagnetism and of the external magnetic field on the resistance of a metal with magnetic impurities," *Physics Physique Fizika* **2**, 61–69 (1965) (cit. on p. 110).
- ³²²S. Nadj-Perge, I. K. Drozdov, B. A. Bernevig, and A. Yazdani, "Proposal for realizing Majorana fermions in chains of magnetic atoms on a superconductor," *Phys. Rev. B* **88**, 020407 (2013) (cit. on pp. 110, 121).
- ³²³F. Pientka, L. I. Glazman, and F. von Oppen, "Topological superconducting phase in helical Shiba chains," *Phys. Rev. B* **88**, 155420 (2013) (cit. on p. 110).
- ³²⁴B. Braunecker and P. Simon, "Interplay between Classical Magnetic Moments and Superconductivity in Quantum One-Dimensional Conductors: Toward a Self-Sustained Topological Majorana Phase," *Phys. Rev. Lett.* **111**, 147202 (2013) (cit. on p. 110).
- ³²⁵J. Klinovaja, P. Stano, A. Yazdani, and D. Loss, "Topological Superconductivity and Majorana Fermions in RKKY Systems," *Phys. Rev. Lett.* **111**, 186805 (2013) (cit. on p. 110).
- ³²⁶M. M. Vazifeh and M. Franz, "Self-Organized Topological State with Majorana Fermions," *Phys. Rev. Lett.* **111**, 206802 (2013) (cit. on p. 110).
- ³²⁷Y. Kim, M. Cheng, B. Bauer, R. M. Lutchyn, and S. Das Sarma, "Helical order in one-dimensional magnetic atom chains and possible emergence of Majorana bound states," *Phys. Rev. B* **90**, 060401 (2014) (cit. on p. 110).
- ³²⁸S. Nadj-Perge, I. K. Drozdov, J. Li, H. Chen, S. Jeon, J. Seo, A. H. MacDonald, B. A. Bernevig, and A. Yazdani, "Observation of Majorana fermions in ferromagnetic atomic chains on a superconductor," *Science* **346**, 602–607 (2014) (cit. on pp. 110, 121).
- ³²⁹H. Kim, A. Palacio-Morales, T. Posske, L. Rózsa, K. Palotás, L. Szunyogh, M. Thorwart, and R. Wiesendanger, "Toward tailoring Majorana bound states in artificially constructed magnetic atom chains on elemental superconductors," *Science Advances* **4**, eaar5251 (2018) (cit. on p. 110).
- ³³⁰A. Kamlapure, L. Cornils, J. Wiebe, and R. Wiesendanger, "Engineering the spin couplings in atomically crafted spin chains on an elemental superconductor," *Nat Commun* **9**, 3253 (2018) (cit. on pp. 110, 111).
- ³³¹A. Y. Kitaev, "Unpaired Majorana fermions in quantum wires," *Phys.-Usp.* **44**, 131 (2001) (cit. on p. 111).

- ³³²C. Nayak, S. H. Simon, A. Stern, M. Freedman, and S. Das Sarma, “Non-Abelian anyons and topological quantum computation,” *Rev. Mod. Phys.* **80**, 1083–1159 (2008) (cit. on p. 111).
- ³³³T. Matsuura, S. Ichinose, and Y. Nagaoka, “Theory of Kondo Effect in Superconductors. I. Transition Temperature and Upper Critical Field,” *Prog. Theor. Phys.* **57**, 713–733 (1977) (cit. on p. 111).
- ³³⁴M. R. Buitelaar, T. Nussbaumer, and C. Schönenberger, “Quantum Dot in the Kondo Regime Coupled to Superconductors,” *Phys. Rev. Lett.* **89**, 256801 (2002) (cit. on p. 111).
- ³³⁵M. I. Salkola, A. V. Balatsky, and J. R. Schrieffer, “Spectral properties of quasiparticle excitations induced by magnetic moments in superconductors,” *Phys. Rev. B* **55**, 12648–12661 (1997) (cit. on pp. 111, 114).
- ³³⁶N. Hatter, B. W. Heinrich, D. Rolf, and K. J. Franke, “Scaling of Yu-Shiba-Rusinov energies in the weak-coupling Kondo regime,” *Nat Commun* **8**, 1–7 (2017) (cit. on p. 111).
- ³³⁷K. Satori, H. Shiba, O. Sakai, and Y. Shimizu, “Numerical Renormalization Group Study of Magnetic Impurities in Superconductors,” *J. Phys. Soc. Jpn.* **61**, 3239–3254 (1992) (cit. on pp. 111, 115).
- ³³⁸O. Sakai, Y. Shimizu, H. Shiba, and K. Satori, “Numerical Renormalization Group Study of Magnetic Impurities in Superconductors. II. Dynamical Excitation Spectra and Spatial Variation of the Order Parameter,” *J. Phys. Soc. Jpn.* **62**, 3181–3197 (1993) (cit. on pp. 111, 115).
- ³³⁹R. Žitko, O. Bodensiek, and T. Pruschke, “Effects of magnetic anisotropy on the sub-gap excitations induced by quantum impurities in a superconducting host,” *Phys. Rev. B* **83**, 054512 (2011) (cit. on pp. 111, 115).
- ³⁴⁰K. J. Franke, G. Schulze, and J. I. Pascual, “Competition of Superconducting Phenomena and Kondo Screening at the Nanoscale,” *Science* **332**, 940–944 (2011) (cit. on pp. 111, 112, 114, 115).
- ³⁴¹L. Schneider, M. Steinbrecher, L. Rózsa, J. Bouaziz, K. Palotás, M. dos Santos Dias, S. Lounis, J. Wiebe, and R. Wiesendanger, “Magnetism and in-gap states of 3d transition metal atoms on superconducting Re,” *npj Quantum Mater.* **4**, 1–8 (2019) (cit. on pp. 111, 121).
- ³⁴²S. Kezilebieke, R. Žitko, M. Dvorak, T. Ojanen, and P. Liljeroth, “Observation of Coexistence of Yu-Shiba-Rusinov States and Spin-Flip Excitations,” *Nano Lett.* **19**, 4614–4619 (2019) (cit. on p. 111).

- ³⁴³H. Huang, R. Drost, J. Senkpiel, C. Padurariu, B. Kubala, A. L. Yeyati, J. C. Cuevas, J. Ankerhold, K. Kern, and C. R. Ast, “Quantum phase transitions and the role of impurity-substrate hybridization in Yu-Shiba-Rusinov states,” *Commun Phys* **3**, 1–9 (2020) (cit. on p. 111).
- ³⁴⁴A. B. Odobesko, S. Haldar, S. Wilfert, J. Hagen, J. Jung, N. Schmidt, P. Sessi, M. Vogt, S. Heinze, and M. Bode, “Preparation and electronic properties of clean superconducting Nb(110) surfaces,” *Phys. Rev. B* **99**, 115437 (2019) (cit. on p. 111).
- ³⁴⁵S. Twomey, “On the Numerical Solution of Fredholm Integral Equations of the First Kind by the Inversion of the Linear System Produced by Quadrature,” *J. ACM* **10**, 97–101 (1963) (cit. on p. 112).
- ³⁴⁶R. C. Dynes, V. Narayanamurti, and J. P. Garno, “Direct Measurement of Quasiparticle-Lifetime Broadening in a Strong-Coupled Superconductor,” *Phys. Rev. Lett.* **41**, 1509–1512 (1978) (cit. on p. 112).
- ³⁴⁷D.-J. Choi, C. Rubio-Verdú, J. de Bruijckere, M. M. Ugeda, N. Lorente, and J. I. Pascual, “Mapping the orbital structure of impurity bound states in a superconductor,” *Nat Commun* **8**, 15175 (2017) (cit. on p. 112).
- ³⁴⁸M. E. Flatté and J. M. Byers, “Local electronic structure of defects in superconductors,” *Phys. Rev. B* **56**, 11213–11231 (1997) (cit. on p. 114).
- ³⁴⁹M. E. Flatté and J. M. Byers, “Local Electronic Structure of a Single Magnetic Impurity in a Superconductor,” *Phys. Rev. Lett.* **78**, 3761–3764 (1997) (cit. on p. 114).
- ³⁵⁰L. Cornils, A. Kamlapure, L. Zhou, S. Pradhan, A. A. Khajetoorians, J. Fransson, J. Wiebe, and R. Wiesendanger, “Spin-Resolved Spectroscopy of the Yu-Shiba-Rusinov States of Individual Atoms,” *Phys. Rev. Lett.* **119**, 197002 (2017) (cit. on p. 114).
- ³⁵¹J. Bauer, J. I. Pascual, and K. J. Franke, “Microscopic resolution of the interplay of Kondo screening and superconducting pairing: Mn-phthalocyanine molecules adsorbed on superconducting Pb(111),” *Phys. Rev. B* **87**, 075125 (2013) (cit. on p. 115).
- ³⁵²R. Žitko, J. S. Lim, R. López, and R. Aguado, “Shiba states and zero-bias anomalies in the hybrid normal-superconductor Anderson model,” *Phys. Rev. B* **91**, 045441 (2015) (cit. on p. 115).
- ³⁵³A. Villas, R. L. Klees, H. Huang, C. R. Ast, G. Rastelli, W. Belzig, and J. C. Cuevas, “Interplay between Yu-Shiba-Rusinov states and multiple Andreev reflections,” *Phys. Rev. B* **101**, 235445 (2020) (cit. on p. 115).
- ³⁵⁴D. M. Eigler and E. K. Schweizer, “Positioning single atoms with a scanning tunnelling microscope,” *Nature* **344**, 524–526 (1990) (cit. on p. 115).

- ³⁵⁵M. Getzlaff, J. Bansmann, and G. Schönhense, “Oxygen on Fe(110): magnetic properties of the adsorbate system,” *Journal of Magnetism and Magnetic Materials* **192**, 458–466 (1999) (cit. on p. 115).
- ³⁵⁶F. Passek and M. Donath, “Magnetic surface state becomes nonmagnetic by oxygen adsorption,” *Phys. Rev. Lett.* **71**, 2122–2125 (1993) (cit. on p. 115).
- ³⁵⁷D. N. McIlroy, C. Waldfried, D. Li, J. Pearson, S. D. Bader, D.-J. Huang, P. D. Johnson, R. F. Sabiryanov, S. S. Jaswal, and P. A. Dowben, “Oxygen Induced Suppression of the Surface Magnetization of Gd(0001),” *Phys. Rev. Lett.* **76**, 2802–2805 (1996) (cit. on p. 115).
- ³⁵⁸P. Limelette, A. Georges, D. Jérôme, P. Wzietek, P. Metcalf, and J. M. Honig, “Universality and Critical Behavior at the Mott Transition,” *Science* **302**, 89–92 (2003) (cit. on p. 120).
- ³⁵⁹J. Kügel, M. Karolak, A. Krönlein, D. Serrate, M. Bode, and G. Sangiovanni, “Reversible magnetic switching of high-spin molecules on a giant Rashba surface,” *npj Quant Mater* **3**, 1–7 (2018) (cit. on p. 120).
- ³⁶⁰M. Chatzieftheriou, “Charge instabilities, Mott transition and transport in Hund metals,” PhD Thesis (Université Paris Sciences & Lettres, July 2021) (cit. on pp. 123, 157).
- ³⁶¹N. F. Mott, “The Basis of the Electron Theory of Metals, with Special Reference to the Transition Metals,” *Proc. Phys. Soc. A* **62**, 416–422 (1949) (cit. on p. 124).
- ³⁶²N. Blümer, “Mott Hubbard metal insulator transition and optical conductivity in high dimensions,” PhD thesis (Universität Augsburg, Aachen, 2002) (cit. on p. 125).
- ³⁶³L. de’Medici, “Hund’s Induced Fermi-Liquid Instabilities and Enhanced Quasiparticle Interactions,” *Phys. Rev. Lett.* **118**, 167003 (2017) (cit. on pp. 125, 127, 128, 147, 148, 163, 199).
- ³⁶⁴J. C. Slater, “Magnetic Effects and the Hartree-Fock Equation,” *Phys. Rev.* **82**, 538–541 (1951) (cit. on p. 124).
- ³⁶⁵M. J. Rozenberg, G. Kotliar, and X. Y. Zhang, “Mott-Hubbard transition in infinite dimensions. II,” *Phys. Rev. B* **49**, 10181–10193 (1994) (cit. on pp. 125, 126).
- ³⁶⁶W. Krauth, “Coexistence of solutions in dynamical mean-field theory of the Mott transition,” *Phys. Rev. B* **62**, 6860–6861 (2000) (cit. on pp. 126, 130).
- ³⁶⁷M. J. Rozenberg, G. Moeller, and G. Kotliar, “The Metal-Insulator Transition in the Hubbard Model at Zero Temperature II,” *Mod. Phys. Lett. B* **08**, 535–543 (1994) (cit. on p. 126).

- ³⁶⁸G. Moeller, Q. Si, G. Kotliar, M. Rozenberg, and D. S. Fisher, “Critical Behavior near the Mott Transition in the Hubbard Model,” *Phys. Rev. Lett.* **74**, 2082–2085 (1995) (cit. on p. 126).
- ³⁶⁹G. Kotliar, S. Murthy, and M. J. Rozenberg, “Compressibility Divergence and the Finite Temperature Mott Transition,” *Phys. Rev. Lett.* **89**, 046401 (2002) (cit. on pp. 126, 163).
- ³⁷⁰M. J. Rozenberg, “Integer-filling metal-insulator transitions in the degenerate Hubbard model,” *Phys. Rev. B* **55**, R4855–R4858 (1997) (cit. on pp. 126, 135).
- ³⁷¹Y. Ōno, M. Potthoff, and R. Bulla, “Mott transitions in correlated electron systems with orbital degrees of freedom,” *Phys. Rev. B* **67**, 035119 (2003) (cit. on pp. 126, 138).
- ³⁷²K. Hallberg, D. J. García, P. S. Cornaglia, J. I. Facio, and Y. Núñez-Fernández, “State-of-the-art techniques for calculating spectral functions in models for correlated materials,” *EPL* **112**, 17001 (2015) (cit. on pp. 126, 135).
- ³⁷³C.-H. Yee and L. Balents, “Phase Separation in Doped Mott Insulators,” *Phys. Rev. X* **5**, 021007 (2015) (cit. on p. 126).
- ³⁷⁴V. J. Emery, S. A. Kivelson, and H. Q. Lin, “Phase separation in the t-J model,” *Phys. Rev. Lett.* **64**, 475–478 (1990) (cit. on pp. 126, 161).
- ³⁷⁵M. Grilli, R. Raimondi, C. Castellani, C. Di Castro, and G. Kotliar, “Superconductivity, phase separation, and charge-transfer instability in the $U=\infty$ limit of the three-band model of the CuO_2 planes,” *Phys. Rev. Lett.* **67**, 259–262 (1991) (cit. on pp. 126, 161).
- ³⁷⁶N. Furukawa and M. Imada, “Two-Dimensional Hubbard Model —Metal Insulator Transition Studied by Monte Carlo Calculation—,” *Journal of the Physical Society of Japan* **61**, 3331–3354 (1992) (cit. on pp. 126, 161).
- ³⁷⁷V. J. Emery and S. A. Kivelson, “Frustrated electronic phase separation and high-temperature superconductors,” *Physica C: Superconductivity* **209**, 597–621 (1993) (cit. on p. 126).
- ³⁷⁸C. Castellani, C. Di Castro, and M. Grilli, “Singular Quasiparticle Scattering in the Proximity of Charge Instabilities,” *Phys. Rev. Lett.* **75**, 4650–4653 (1995) (cit. on p. 126).
- ³⁷⁹P. W. Anderson, “The Resonating Valence Bond State in La_2CuO_4 and Superconductivity,” *Science* **235**, 1196–1198 (1987) (cit. on p. 126).
- ³⁸⁰F. C. Zhang and T. M. Rice, “Effective Hamiltonian for the superconducting Cu oxides,” *Phys. Rev. B* **37**, 3759–3761 (1988) (cit. on p. 126).
- ³⁸¹M. Eckstein, M. Kollar, K. Byczuk, and D. Vollhardt, “Hopping on the Bethe lattice: Exact results for densities of states and dynamical mean-field theory,” *Phys. Rev. B* **71**, 235119 (2005) (cit. on p. 126).

- ³⁸²Z. P. Yin, K. Haule, and G. Kotliar, “Kinetic frustration and the nature of the magnetic and paramagnetic states in iron pnictides and iron chalcogenides,” *Nature Materials* **10**, 932–935 (2011) (cit. on p. 126).
- ³⁸³L. de’Medici, G. Giovannetti, and M. Capone, “Selective Mott Physics as a Key to Iron Superconductors,” *Phys. Rev. Lett.* **112**, 177001 (2014) (cit. on pp. 126, 161).
- ³⁸⁴P. Werner, E. Gull, and A. J. Millis, “Metal-insulator phase diagram and orbital selectivity in three-orbital models with rotationally invariant Hund coupling,” *Phys. Rev. B* **79**, 115119 (2009) (cit. on p. 126).
- ³⁸⁵H. Ishida and A. Liebsch, “Fermi-liquid, non-Fermi-liquid, and Mott phases in iron pnictides and cuprates,” *Phys. Rev. B* **81**, 054513 (2010) (cit. on p. 127).
- ³⁸⁶J. Steinbauer, L. de’Medici, and S. Biermann, “Doping-driven metal-insulator transition in correlated electron systems with strong Hund’s exchange coupling,” *Phys. Rev. B* **100**, 085104 (2019) (cit. on pp. 127, 145, 147).
- ³⁸⁷L. de’Medici, S. R. Hassan, M. Capone, and X. Dai, “Orbital-Selective Mott Transition out of Band Degeneracy Lifting,” *Phys. Rev. Lett.* **102**, 126401 (2009) (cit. on p. 127).
- ³⁸⁸N. Lanatà, H. U. R. Strand, G. Giovannetti, B. Hellsing, L. de’Medici, and M. Capone, “Orbital selectivity in Hund’s metals: The iron chalcogenides,” *Phys. Rev. B* **87**, 045122 (2013) (cit. on p. 127).
- ³⁸⁹M. Yi, Z.-K. Liu, Y. Zhang, R. Yu, J.-X. Zhu, J. J. Lee, R. G. Moore, F. T. Schmitt, W. Li, S. C. Riggs, J.-H. Chu, B. Lv, J. Hu, M. Hashimoto, S.-K. Mo, Z. Hussain, Z. Q. Mao, C. W. Chu, I. R. Fisher, Q. Si, Z.-X. Shen, and D. H. Lu, “Observation of universal strong orbital-dependent correlation effects in iron chalcogenides,” *Nature Communications* **6**, 7777 (2015) (cit. on p. 127).
- ³⁹⁰A. Isidori, M. Berović, L. Fanfarillo, L. de’Medici, M. Fabrizio, and M. Capone, “Charge Disproportionation, Mixed Valence, and Janus Effect in Multiorbital Systems: A Tale of Two Insulators,” *Phys. Rev. Lett.* **122**, 186401 (2019) (cit. on p. 127).
- ³⁹¹M. Edelmann, G. Sangiovanni, M. Capone, and L. de’Medici, “Chromium analogs of iron-based superconductors,” *Phys. Rev. B* **95**, 205118 (2017) (cit. on pp. 127, 128, 147).
- ³⁹²M. Chatzieftheriou, M. Berović, P. Villar Arribi, M. Capone, and L. de’Medici, “Enhancement of charge instabilities in Hund’s metals by breaking of rotational symmetry,” *Phys. Rev. B* **102**, 205127 (2020) (cit. on pp. 127, 128, 147, 148, 157, 160).
- ³⁹³T. Misawa and M. Imada, “Superconductivity and its mechanism in an ab initio model for electron-doped LaFeAsO,” *Nat Commun* **5**, 1–11 (2014) (cit. on p. 127).

- ³⁹⁴P. Villar Arribi and L. de'Medici, "Hund-Enhanced Electronic Compressibility in FeSe and its Correlation with T_c ," *Phys. Rev. Lett.* **121**, 197001 (2018) (cit. on pp. 127, 128, 147).
- ³⁹⁵P. Villar Arribi and L. de'Medici, "Hund's metal crossover and superconductivity in the 111 family of iron-based superconductors," *Phys. Rev. B* **104**, 125130 (2021) (cit. on pp. 127, 128, 147).
- ³⁹⁶L. de'Medici, A. Georges, and S. Biermann, "Orbital-selective Mott transition in multi-band systems: Slave-spin representation and dynamical mean-field theory," *Phys. Rev. B* **72**, 205124 (2005) (cit. on pp. 128, 147).
- ³⁹⁷S. R. Hassan and L. de'Medici, "Slave spins away from half filling: Cluster mean-field theory of the Hubbard and extended Hubbard models," *Phys. Rev. B* **81**, 035106 (2010) (cit. on pp. 128, 147).
- ³⁹⁸L. de'Medici and M. Capone, "Modeling many-body physics with Slave-Spin Mean-Field: Mott and Hund's physics in Fe-superconductors," arXiv:1607.08468 [cond-mat], Springer Series in Solid-State Sciences **186**, 115–185 (2017) (cit. on pp. 128, 147–149, 152).
- ³⁹⁹I. I. Mazin, D. J. Singh, M. D. Johannes, and M. H. Du, "Unconventional Superconductivity with a Sign Reversal in the Order Parameter of $\text{LaFeAsO}_{1-x}\text{F}_x$," *Phys. Rev. Lett.* **101**, 057003 (2008) (cit. on p. 128).
- ⁴⁰⁰P. Werner, M. Casula, T. Miyake, F. Aryasetiawan, A. J. Millis, and S. Biermann, "Satellites and large doping and temperature dependence of electronic properties in hole-doped BaFe_2As_2 ," *Nature Phys* **8**, 331–337 (2012) (cit. on p. 128).
- ⁴⁰¹F. Rullier-Albenque, "Influence of the electronic structure on the transport properties of some iron pnictides," *Comptes Rendus Physique, Iron-based superconductors / Supraconducteurs à base de fer* **17**, 164–187 (2016) (cit. on p. 128).
- ⁴⁰²P. J. Hirschfeld, "Using gap symmetry and structure to reveal the pairing mechanism in Fe-based superconductors," *Comptes Rendus Physique, Iron-based superconductors / Supraconducteurs à base de fer* **17**, 197–231 (2016) (cit. on p. 128).
- ⁴⁰³M. Vojta, "Quantum phase transitions," *Rep. Prog. Phys.* **66**, 2069–2110 (2003) (cit. on p. 128).
- ⁴⁰⁴S. Sachdev, "Quantum Criticality: Competing Ground States in Low Dimensions," *Science* **288**, 475–480 (2000) (cit. on p. 128).
- ⁴⁰⁵H. Terletska, J. Vučičević, D. Tanasković, and V. Dobrosavljević, "Quantum Critical Transport near the Mott Transition," *Phys. Rev. Lett.* **107**, 026401 (2011) (cit. on p. 128).

- ⁴⁰⁶J. Vučičević, H. Terletska, D. Tanasković, and V. Dobrosavljević, “Finite-temperature crossover and the quantum Widom line near the Mott transition,” *Phys. Rev. B* **88**, 075143 (2013) (cit. on p. 128).
- ⁴⁰⁷T. Furukawa, K. Miyagawa, H. Taniguchi, R. Kato, and K. Kanoda, “Quantum criticality of Mott transition in organic materials,” *Nature Phys* **11**, 221–224 (2015) (cit. on p. 128).
- ⁴⁰⁸J. Vučičević, D. Tanasković, M. J. Rozenberg, and V. Dobrosavljević, “Bad-Metal Behavior Reveals Mott Quantum Criticality in Doped Hubbard Models,” *Phys. Rev. Lett.* **114**, 246402 (2015) (cit. on p. 128).
- ⁴⁰⁹A. Pustogow, M. Bories, A. Löhle, R. Rösslhuber, E. Zhukova, B. Gorshunov, S. Tomić, J. A. Schlueter, R. Hübner, T. Hiramatsu, Y. Yoshida, G. Saito, R. Kato, T.-H. Lee, V. Dobrosavljević, S. Fratini, and M. Dressel, “Quantum spin liquids unveil the genuine Mott state,” *Nature Mater* **17**, 773–777 (2018) (cit. on p. 128).
- ⁴¹⁰H. Eisenlohr, S.-S. B. Lee, and M. Vojta, “Mott quantum criticality in the one-band Hubbard model: Dynamical mean-field theory, power-law spectra, and scaling,” *Phys. Rev. B* **100**, 155152 (2019) (cit. on p. 128).
- ⁴¹¹A. Sokol and D. Pines, “Toward a unified magnetic phase diagram of the cuprate superconductors,” *Phys. Rev. Lett.* **71**, 2813–2816 (1993) (cit. on p. 128).
- ⁴¹²C. Castellani, C. Di Castro, and M. Grilli, “Non-Fermi-liquid behavior and d-wave superconductivity near the charge-density-wave quantum critical point,” *Z. Phys. B - Condensed Matter* **103**, 137–144 (1996) (cit. on p. 128).
- ⁴¹³C. M. Varma, “Non-Fermi-liquid states and pairing instability of a general model of copper oxide metals,” *Phys. Rev. B* **55**, 14554–14580 (1997) (cit. on p. 128).
- ⁴¹⁴G. Aeppli, T. E. Mason, S. M. Hayden, H. A. Mook, and J. Kulda, “Nearly Singular Magnetic Fluctuations in the Normal State of a High- T_c Cuprate Superconductor,” *Science* **278**, 1432–1435 (1997) (cit. on p. 128).
- ⁴¹⁵J. L. Tallon, J. W. Loram, G. V. M. Williams, J. R. Cooper, I. R. Fisher, J. D. Johnson, M. P. Staines, and C. Bernhard, “Critical Doping in Overdoped High- T_c Superconductors: a Quantum Critical Point?” *physica status solidi (b)* **215**, 531–540 (1999) (cit. on p. 128).
- ⁴¹⁶C. M. Varma, “Pseudogap Phase and the Quantum-Critical Point in Copper-Oxide Metals,” *Phys. Rev. Lett.* **83**, 3538–3541 (1999) (cit. on p. 128).
- ⁴¹⁷D. M. Broun, “What lies beneath the dome?” *Nature Phys* **4**, 170–172 (2008) (cit. on p. 128).

- ⁴¹⁸N. S. Vidhyadhiraja, A. Macridin, C. Şen, M. Jarrell, and M. Ma, “Quantum Critical Point at Finite Doping in the 2D Hubbard Model: A Dynamical Cluster Quantum Monte Carlo Study,” *Phys. Rev. Lett.* **102**, 206407 (2009) (cit. on p. 128).
- ⁴¹⁹K. Mielson, E. Khatami, D. Galanakis, A. Macridin, J. Moreno, and M. Jarrell, “Thermodynamics of the quantum critical point at finite doping in the two-dimensional Hubbard model studied via the dynamical cluster approximation,” *Phys. Rev. B* **80**, 140505 (2009) (cit. on p. 128).
- ⁴²⁰S. Sachdev, “Where is the quantum critical point in the cuprate superconductors?” *physica status solidi (b)* **247**, 537–543 (2010) (cit. on p. 128).
- ⁴²¹E. Khatami, K. Mielson, D. Galanakis, A. Macridin, J. Moreno, R. T. Scalettar, and M. Jarrell, “Quantum criticality due to incipient phase separation in the two-dimensional Hubbard model,” *Phys. Rev. B* **81**, 201101 (2010) (cit. on pp. 128, 161).
- ⁴²²D. Galanakis, E. Khatami, K. Mielson, A. Macridin, J. Moreno, D. A. Browne, and M. Jarrell, “Quantum criticality and incipient phase separation in the thermodynamic properties of the Hubbard model,” *Phil. Trans. R. Soc. A.* **369**, 1670–1686 (2011) (cit. on pp. 128, 161).
- ⁴²³K. B. Efetov, H. Meier, and C. Pépin, “Pseudogap state near a quantum critical point,” *Nature Phys* **9**, 442–446 (2013) (cit. on p. 128).
- ⁴²⁴W. Xu, G. Kotliar, and A. M. Tsvelik, “Quantum critical point revisited by dynamical mean-field theory,” *Phys. Rev. B* **95**, 121113 (2017) (cit. on p. 128).
- ⁴²⁵B. Michon, C. Girod, S. Badoux, J. Kačmarčík, Q. Ma, M. Dragomir, H. A. Dabkowska, B. D. Gaulin, J.-S. Zhou, S. Pyon, T. Takayama, H. Takagi, S. Verret, N. Doiron-Leyraud, C. Marcenat, L. Taillefer, and T. Klein, “Thermodynamic signatures of quantum criticality in cuprate superconductors,” *Nature* **567**, 218–222 (2019) (cit. on p. 128).
- ⁴²⁶A. Weichselbaum and J. von Delft, “Sum-Rule Conserving Spectral Functions from the Numerical Renormalization Group,” *Phys. Rev. Lett.* **99**, 076402 (2007) (cit. on p. 129).
- ⁴²⁷R. Žitko and T. Pruschke, “Energy resolution and discretization artifacts in the numerical renormalization group,” *Phys. Rev. B* **79**, 085106 (2009) (cit. on p. 129).
- ⁴²⁸A. Amaricci, L. Crippa, A. Scazzola, F. Petocchi, G. Mazza, L. de’Medici, and M. Capone, “EDĪpack: A parallel exact diagonalization package for quantum impurity problems,” *Computer Physics Communications* **273**, 108261 (2022) (cit. on p. 129).
- ⁴²⁹N.-H. Tong, S.-Q. Shen, and F.-C. Pu, “Mott-Hubbard transition in infinite dimensions,” *Phys. Rev. B* **64**, 235109 (2001) (cit. on pp. 130, 138).

- ⁴³⁰J. Clerk-Maxwell, “On the Dynamical Evidence of the Molecular Constitution of Bodies,” *Nature* **11**, 357–359 (1875) (cit. on p. 130).
- ⁴³¹D. D. Johnson, “Modified Broyden’s method for accelerating convergence in self-consistent calculations,” *Phys. Rev. B* **38**, 12807–12813 (1988) (cit. on pp. 131, 167).
- ⁴³²K. Inaba, A. Koga, S.-i. Suga, and N. Kawakami, “Finite-temperature Mott transitions in the multiorbital Hubbard model,” *Phys. Rev. B* **72**, 085112 (2005).
- ⁴³³J. E. Han, M. Jarrell, and D. L. Cox, “Multiorbital Hubbard model in infinite dimensions: Quantum Monte Carlo calculation,” *Phys. Rev. B* **58**, R4199–R4202 (1998) (cit. on p. 135).
- ⁴³⁴E. G. C. P. van Loon, “Two-particle correlations and the metal-insulator transition: Iterated perturbation theory revisited,” *Phys. Rev. B* **105**, 245104 (2022) (cit. on p. 138).
- ⁴³⁵C. Castellani, C. Di Castro, D. Feinberg, and J. Ranninger, “New Model Hamiltonian for the Metal-Insulator Transition,” *Phys. Rev. Lett.* **43**, 1957–1960 (1979) (cit. on pp. 138, 146).
- ⁴³⁶M. J. Rozenberg, R. Chitra, and G. Kotliar, “Finite Temperature Mott Transition in the Hubbard Model in Infinite Dimensions,” *Phys. Rev. Lett.* **83**, 3498–3501 (1999) (cit. on pp. 138, 146).
- ⁴³⁷F. N. Fritsch and J. Butland, “A Method for Constructing Local Monotone Piecewise Cubic Interpolants,” *SIAM J. Sci. and Stat. Comput.* **5**, 300–304 (1984) (cit. on p. 142).
- ⁴³⁸P. Virtanen, R. Gommers, T. E. Oliphant, M. Haberland, T. Reddy, D. Cournapeau, E. Burovski, P. Peterson, W. Weckesser, J. Bright, S. J. van der Walt, M. Brett, J. Wilson, K. J. Millman, N. Mayorov, A. R. J. Nelson, E. Jones, R. Kern, E. Larson, C. J. Carey, Í. Polat, Y. Feng, E. W. Moore, J. VanderPlas, D. Laxalde, J. Perktold, R. Cimrman, I. Henriksen, E. A. Quintero, C. R. Harris, A. M. Archibald, A. H. Ribeiro, F. Pedregosa, and P. van Mulbregt, “SciPy 1.0: fundamental algorithms for scientific computing in Python,” *Nat Methods* **17**, 261–272 (2020) (cit. on p. 142).
- ⁴³⁹H. B. Callen, *Thermodynamics and an introduction to thermostatistics*, 2nd ed. (Wiley, New York, 1985) (cit. on pp. 142, 192).
- ⁴⁴⁰L. D. Landau, “On the theory of phase transitions. I.,” *Zh. Eksp. Teor. Fiz.* **11**, 19 (1937) (cit. on pp. 147, 152).
- ⁴⁴¹A. B. Georgescu and S. Ismail-Beigi, “Generalized slave-particle method for extended Hubbard models,” *Phys. Rev. B* **92**, 235117 (2015) (cit. on p. 148).
- ⁴⁴²G. Kotliar and A. E. Ruckenstein, “New Functional Integral Approach to Strongly Correlated Fermi Systems: The Gutzwiller Approximation as a Saddle Point,” *Phys. Rev. Lett.* **57**, 1362–1365 (1986) (cit. on p. 148).

- ⁴⁴³F. Lechermann, A. Georges, G. Kotliar, and O. Parcollet, “Rotationally invariant slave-boson formalism and momentum dependence of the quasiparticle weight,” *Phys. Rev. B* **76**, 155102 (2007) (cit. on p. 148).
- ⁴⁴⁴S. Florens and A. Georges, “Slave-rotor mean-field theories of strongly correlated systems and the Mott transition in finite dimensions,” *Phys. Rev. B* **70**, 035114 (2004) (cit. on p. 148).
- ⁴⁴⁵H. Nishimori and G. Ortiz, *Elements of phase transitions and critical phenomena*, Oxford graduate texts (Oxford University Press, New York, 2011) (cit. on p. 152).
- ⁴⁴⁶L. D. Landau and E. M. Lifšic, *Quantum mechanics: non-relativistic theory*, 3rd ed., rev. and enl., Course of theoretical physics (Pergamon Press, Oxford, 1989) (cit. on p. 155).
- ⁴⁴⁷J. I. Facio, V. Vildosola, D. J. García, and P. S. Cornaglia, “On the nature of the Mott transition in multiorbital systems,” *Phys. Rev. B* **95**, 085119 (2017) (cit. on p. 157).
- ⁴⁴⁸M. Capone, M. Fabrizio, C. Castellani, and E. Tosatti, “Strongly Correlated Superconductivity and Pseudogap Phase near a Multiband Mott Insulator,” *Phys. Rev. Lett.* **93**, 047001 (2004) (cit. on p. 157).
- ⁴⁴⁹L. de’Medici, private communication, Apr. 2022 (cit. on p. 157).
- ⁴⁵⁰S. Raghu, X.-L. Qi, C.-X. Liu, D. J. Scalapino, and S.-C. Zhang, “Minimal two-band model of the superconducting iron oxypnictides,” *Phys. Rev. B* **77**, 220503 (2008) (cit. on pp. 159, 200).
- ⁴⁵¹T. Miyake, K. Nakamura, R. Arita, and M. Imada, “Comparison of Ab initio Low-Energy Models for LaFePO, LaFeAsO, BaFe₂As₂, LiFeAs, FeSe, and FeTe: Electron Correlation and Covalency,” *J. Phys. Soc. Jpn.* **79**, 044705 (2010) (cit. on p. 160).
- ⁴⁵²A. I. Lichtenstein and M. I. Katsnelson, “Antiferromagnetism and d-wave superconductivity in cuprates: A cluster dynamical mean-field theory,” *Phys. Rev. B* **62**, R9283–R9286 (2000) (cit. on p. 160).
- ⁴⁵³M. H. Hettler, A. N. Tahvildar-Zadeh, M. Jarrell, T. Pruschke, and H. R. Krishnamurthy, “Nonlocal dynamical correlations of strongly interacting electron systems,” *Phys. Rev. B* **58**, R7475–R7479 (1998) (cit. on p. 161).
- ⁴⁵⁴G. Kotliar, S. Y. Savrasov, G. Pálsson, and G. Biroli, “Cellular Dynamical Mean Field Approach to Strongly Correlated Systems,” *Phys. Rev. Lett.* **87**, 186401 (2001) (cit. on p. 161).
- ⁴⁵⁵T. Maier, M. Jarrell, T. Pruschke, and M. H. Hettler, “Quantum cluster theories,” *Rev. Mod. Phys.* **77**, 1027–1080 (2005) (cit. on p. 161).

- ⁴⁵⁶M. Ferrero, P. S. Cornaglia, L. De Leo, O. Parcollet, G. Kotliar, and A. Georges, “Valence bond dynamical mean-field theory of doped Mott insulators with nodal/antinodal differentiation,” *Europhys. Lett.* **85**, 57009 (2009) (cit. on p. 161).
- ⁴⁵⁷G. Sordi, K. Haule, and A.-M. S. Tremblay, “Finite Doping Signatures of the Mott Transition in the Two-Dimensional Hubbard Model,” *Phys. Rev. Lett.* **104**, 226402 (2010) (cit. on p. 161).
- ⁴⁵⁸S.-X. Yang, H. Fotsos, S.-Q. Su, D. Galanakis, E. Khatami, J.-H. She, J. Moreno, J. Zanen, and M. Jarrell, “Proximity of the Superconducting Dome and the Quantum Critical Point in the Two-Dimensional Hubbard Model,” *Phys. Rev. Lett.* **106**, 047004 (2011) (cit. on p. 161).
- ⁴⁵⁹G. Sordi, K. Haule, and A.-M. S. Tremblay, “Mott physics and first-order transition between two metals in the normal-state phase diagram of the two-dimensional Hubbard model,” *Phys. Rev. B* **84**, 075161 (2011) (cit. on pp. 161, 192).
- ⁴⁶⁰G. Sordi, P. Sémon, K. Haule, and A.-M. S. Tremblay, “Strong Coupling Superconductivity, Pseudogap, and Mott Transition,” *Phys. Rev. Lett.* **108**, 216401 (2012) (cit. on p. 161).
- ⁴⁶¹G. Sordi, P. Sémon, K. Haule, and A.-M. S. Tremblay, “Pseudogap temperature as a Widom line in doped Mott insulators,” *Sci Rep* **2**, 547 (2012) (cit. on p. 161).
- ⁴⁶²G. Sordi, P. Sémon, K. Haule, and A.-M. S. Tremblay, “*c*-axis resistivity, pseudogap, superconductivity, and Widom line in doped Mott insulators,” *Phys. Rev. B* **87**, 041101 (2013) (cit. on p. 161).
- ⁴⁶³C.-D. Hébert, P. Sémon, and A.-M. S. Tremblay, “Superconducting dome in doped quasi-two-dimensional organic Mott insulators: A paradigm for strongly correlated superconductivity,” *Phys. Rev. B* **92**, 195112 (2015) (cit. on p. 161).
- ⁴⁶⁴L. Fratino, P. Sémon, G. Sordi, and A.-M. S. Tremblay, “An organizing principle for two-dimensional strongly correlated superconductivity,” *Sci Rep* **6**, 22715 (2016) (cit. on p. 161).
- ⁴⁶⁵L. Fratino, P. Sémon, G. Sordi, and A.-M. S. Tremblay, “Pseudogap and superconductivity in two-dimensional doped charge-transfer insulators,” *Phys. Rev. B* **93**, 245147 (2016) (cit. on p. 161).
- ⁴⁶⁶P. Werner, S. Hoshino, and H. Shinaoka, “Spin-freezing perspective on cuprates,” *Phys. Rev. B* **94**, 245134 (2016) (cit. on pp. 161, 162).
- ⁴⁶⁷D. Springer, P. Chalupa, S. Ciuchi, G. Sangiovanni, and A. Toschi, “Interplay between local response and vertex divergences in many-fermion systems with on-site attraction,” *Phys. Rev. B* **101**, 155148 (2020) (cit. on pp. 165–167, 181, 188, 189).

- ⁴⁶⁸V. Zlatić and B. Horvatić, “The local approximation for correlated systems on high dimensional lattices,” *Solid State Communications* **75**, 263–267 (1990) (cit. on pp. 165, 178).
- ⁴⁶⁹O. Gunnarsson, G. Rohringer, T. Schäfer, G. Sangiovanni, and A. Toschi, “Breakdown of Traditional Many-Body Theories for Correlated Electrons,” *Phys. Rev. Lett.* **119**, 056402 (2017) (cit. on pp. 166, 167, 181).
- ⁴⁷⁰T. Schäfer, G. Rohringer, O. Gunnarsson, S. Ciuchi, G. Sangiovanni, and A. Toschi, “Divergent Precursors of the Mott-Hubbard Transition at the Two-Particle Level,” *Phys. Rev. Lett.* **110**, 246405 (2013) (cit. on pp. 166, 167, 181).
- ⁴⁷¹P. Chalupa, T. Schäfer, M. Reitner, D. Springer, S. Andergassen, and A. Toschi, “Fingerprints of the Local Moment Formation and its Kondo Screening in the Generalized Susceptibilities of Many-Electron Problems,” *Phys. Rev. Lett.* **126**, 056403 (2021) (cit. on pp. 166, 167, 192).
- ⁴⁷²E. Kozik, M. Ferrero, and A. Georges, “Nonexistence of the Luttinger-Ward Functional and Misleading Convergence of Skeleton Diagrammatic Series for Hubbard-Like Models,” *Phys. Rev. Lett.* **114**, 156402 (2015) (cit. on p. 166).
- ⁴⁷³A. Stan, P. Romaniello, S. Rigamonti, L. Reining, and J. A. Berger, “Unphysical and physical solutions in many-body theories: from weak to strong correlation,” *New J. Phys.* **17**, 093045 (2015) (cit. on p. 166).
- ⁴⁷⁴R. Rossi and F. Werner, “Skeleton series and multivaluedness of the self-energy functional in zero space-time dimensions,” *J. Phys. A: Math. Theor.* **48**, 485202 (2015) (cit. on p. 166).
- ⁴⁷⁵W. Tarantino, P. Romaniello, J. A. Berger, and L. Reining, “Self-consistent Dyson equation and self-energy functionals: An analysis and illustration on the example of the Hubbard atom,” *Phys. Rev. B* **96**, 045124 (2017) (cit. on p. 166).
- ⁴⁷⁶P. Thunström, O. Gunnarsson, S. Ciuchi, and G. Rohringer, “Analytical investigation of singularities in two-particle irreducible vertex functions of the Hubbard atom,” *Phys. Rev. B* **98**, 235107 (2018) (cit. on p. 166).
- ⁴⁷⁷A. J. Kim and V. Sacksteder, “Multivaluedness of the Luttinger-Ward functional in the fermionic and bosonic system with replicas,” *Phys. Rev. B* **101**, 115146 (2020) (cit. on p. 166).
- ⁴⁷⁸V. Janiš and V. Pokorný, “Critical metal-insulator transition and divergence in a two-particle irreducible vertex in disordered and interacting electron systems,” *Phys. Rev. B* **90**, 045143 (2014) (cit. on p. 166).

- ⁴⁷⁹T. Schäfer, S. Ciuchi, M. Wallerberger, P. Thunström, O. Gunnarsson, G. Sangiovanni, G. Rohringer, and A. Toschi, “Nonperturbative landscape of the Mott-Hubbard transition: Multiple divergence lines around the critical endpoint,” *Phys. Rev. B* **94**, 235108 (2016) (cit. on pp. 166, 167, 181, 191).
- ⁴⁸⁰T. Ribic, G. Rohringer, and K. Held, “Nonlocal correlations and spectral properties of the Falicov-Kimball model,” *Phys. Rev. B* **93**, 195105 (2016) (cit. on p. 166).
- ⁴⁸¹P. Chalupa, P. Gunacker, T. Schäfer, K. Held, and A. Toschi, “Divergences of the irreducible vertex functions in correlated metallic systems: Insights from the Anderson impurity model,” *Phys. Rev. B* **97**, 245136 (2018) (cit. on pp. 166, 167, 191).
- ⁴⁸²J. Vučičević, N. Wentzell, M. Ferrero, and O. Parcollet, “Practical consequences of the Luttinger-Ward functional multivaluedness for cluster DMFT methods,” *Phys. Rev. B* **97**, 125141 (2018) (cit. on pp. 167, 190).
- ⁴⁸³O. Gunnarsson, T. Schäfer, J. P. F. LeBlanc, E. Gull, J. Merino, G. Sangiovanni, G. Rohringer, and A. Toschi, “Fluctuation Diagnostics of the Electron Self-Energy: Origin of the Pseudogap Physics,” *Phys. Rev. Lett.* **114**, 236402 (2015) (cit. on p. 167).
- ⁴⁸⁴R. Rossi, F. Werner, N. Prokof’ev, and B. Svistunov, “Shifted-action expansion and applicability of dressed diagrammatic schemes,” *Phys. Rev. B* **93**, 161102 (2016) (cit. on p. 167).
- ⁴⁸⁵F. B. Kugler and J. v. Delft, “Derivation of exact flow equations from the self-consistent parquet relations,” *New J. Phys.* **20**, 123029 (2018) (cit. on p. 167).
- ⁴⁸⁶F. Krien, A. Valli, and M. Capone, “Single-boson exchange decomposition of the vertex function,” *Phys. Rev. B* **100**, 155149 (2019) (cit. on p. 167).
- ⁴⁸⁷K. Van Houcke, E. Kozik, R. Rossi, Y. Deng, and F. Werner, *Physical and unphysical regimes of self-consistent many-body perturbation theory*, (Feb. 2021) arXiv:2102.04508 [cond-mat] (cit. on p. 167).
- ⁴⁸⁸P. Chalupa-Gantner, “The nonperturbative feats of local electronic correlation: The physics of irreducible vertex divergences,” Thesis (Technische Universität Wien, 2022) (cit. on p. 167).
- ⁴⁸⁹C. Melnick and G. Kotliar, “Fermi-liquid theory and divergences of the two-particle irreducible vertex in the periodic Anderson lattice,” *Phys. Rev. B* **101**, 165105 (2020) (cit. on p. 167).
- ⁴⁹⁰R. Nourafkan, M. Côté, and A.-M. S. Tremblay, “Charge fluctuations in lightly hole-doped cuprates: Effect of vertex corrections,” *Phys. Rev. B* **99**, 035161 (2019) (cit. on p. 167).

- ⁴⁹¹M. Reitner, P. Chalupa, L. Del Re, D. Springer, S. Ciuchi, G. Sangiovanni, and A. Toschi, “Attractive Effect of a Strong Electronic Repulsion: The Physics of Vertex Divergences,” *Phys. Rev. Lett.* **125**, 196403 (2020) (cit. on pp. 167, 171, 181, 188, 189, 199, 200).
- ⁴⁹²N. V. Prokof’ev, B. V. Svistunov, and I. S. Tupitsyn, “Exact, complete, and universal continuous-time worldline Monte Carlo approach to the statistics of discrete quantum systems,” *J. Exp. Theor. Phys.* **87**, 310–321 (1998) (cit. on pp. 167, 185).
- ⁴⁹³N. V. Prokof’ev, B. V. Svistunov, and I. S. Tupitsyn, ““Worm” algorithm in quantum Monte Carlo simulations,” *Physics Letters A* **238**, 253–257 (1998) (cit. on pp. 167, 185).
- ⁴⁹⁴P. Gunacker, “Diagrammatic quantum Monte-Carlo with worm-sampling,” *Diplomarbeit* (TU Wien, Wien, 2014) (cit. on pp. 167, 185).
- ⁴⁹⁵G. Rohringer, “New routes towards a theoretical treatment of nonlocal electronic correlations,” *PhD thesis* (TU Wien, Wien, 2013) (cit. on pp. 168, 176).
- ⁴⁹⁶E. G. C. P. van Loon, H. Hafermann, A. I. Lichtenstein, and M. I. Katsnelson, “Thermodynamic consistency of the charge response in dynamical mean-field based approaches,” *Phys. Rev. B* **92**, 085106 (2015) (cit. on p. 171).
- ⁴⁹⁷L. Del Re, private communication, May 2021 (cit. on pp. 177, 178).
- ⁴⁹⁸T. F. Chan, “An Improved Algorithm for Computing the Singular Value Decomposition,” *ACM Trans. Math. Softw.* **8**, 72–83 (1982) (cit. on p. 181).
- ⁴⁹⁹M. Baer, *Findiff*, 2018 (cit. on p. 182).
- ⁵⁰⁰A. Lee, “Centrohermitian and skew-centrohermitian matrices,” *Linear Algebra Appl., Special Volume Dedicated to Alson S. Householder* **29**, 205–210 (1980) (cit. on p. 188).
- ⁵⁰¹M. Reitner, private communication, Feb. 2023 (cit. on p. 193).
- ⁵⁰²E. Noether, “Invariante Variationsprobleme,” *Nachrichten von der Gesellschaft der Wissenschaften zu Göttingen, Mathematisch-Physikalische Klasse* **1918**, 235–257 (1918) (cit. on p. 204).